Final Report
on the
SURFACE ELECTRICAL PROPERTIES EXPERIMENT

NASA Contract NAS-11540

CSR TR-74-1

March 15, 1974

CENTER FOR SPACE RESEARCH
MASSACHUSETTS INSTITUTE OF TECHNOLOGY

Final Report
on the
SURFACE ELECTRICAL PROPERTIES EXPERIMENT

NASA Contract NAS-11540

CSR TR-74-1

March 15, 1974

FINAL REPORT

ON

THE SURFACE ELECTRICAL PROPERTIES EXPERIMENT

Contract # NAS-11540

To: Johnson Space Center
National Aeronautics and Space Administration
Houston, Texas 77058

From: Center for Space Research
and
Department of Earth and Planetary Sciences
Massachusetts Institute of Technology
Cambridge, Massachusetts 02139

Gene Simmons
Principal Investigator

15 March 1974.

TABLE OF CONTENTS

SUMMARY

The Surface Electrical Properties Experiment (SEP) was flown to the Moon in December 1972 on Apollo 17 and used to explore a portion of the Taurus-Littrow region. SEP used a relatively new technique, termed Radio Frequency Interferometry (RFI). Electromagnetic waves were radiated from two orthogonal, horizontal electric dipole antennas on the surface of the Moon at frequencies of 1, 2, 4, 8, 16, and 32 Mhz.

The field strength of the EM waves was measured as a function of distance with a receiver mounted on the Lunar Roving Vehicle and using three orthogonal, electrically small, loops. The interference pattern produced by the waves that travelled above the Moon's surface and those that travelled below the surface was recorded on magnetic tape. The tape was returned to Earth for analysis and interpretation.

Data were obtained during EVA 2 on the traverse from the SEP-site (near the landing point) towards Station 2 for a distance of about 2 1/2 km. Unfortunately, data were not obtained during the remainder of EVA 2 because the SEP receiver overheated. Neither were data obtained during EVA 3 because a switch was placed in the standby-position rather than the on-position for the early portion of the EVA and the SEP receiver then overheated. Thus our analysis of the electrical structure of the Taurus-Littrow site is restricted to the vicinity of the traverse from the SEP-site to Station 2.

Because the lower frequency waves penetrate deeper into the Moon than the higher frequency waves, we use the 1 MHz interference pattern to infer the electrical properties at depth. We use the 32MHz pattern to estimate the properties near the surface. In one model, the relative dielectric constant increases from a value of 3 1/2 near the surface to a value of about 6 - 7 at a depth of 100m and then decreases slightly. In another model, a near-surface, sloping interface between material of slightly differing dielectric constant satisfies some of the constraints imposed by the observed data. We have not yet obtained any model that satisfies most of the constraints provided by the large quantity of data for the lunar traverse.

Despite the lack of a model that does satisfy most of the observed data, we believe that the gross electrical features of the Taurus-Littrow site are these: (1) the relative dielectric constant increases with depth (from about 3 1/2 at the surface to 6 - 7 at depth), (2) the dielectric constant is rather constant over the depth interval of 100 meters to at least 2 1/2 km, (3) the loss tangent is no larger than 0.05 and possibly as small as 0.002, (4) no significant quantity of water is present within 2 1/2 km of the Moon's surface at Taurus-Littrow, (5) electromagnetic scattering at frequences of 1 - 32 MHz is absent at Taurus-Littrow which implies that subsurface "boulders" of dimensions in the range of 10 - 300m and with contrasting dielectric constant, are not present

within 1 - 2 km of the surface.

In this final report, we include several reprints, preprints, and an initial draft of the first publication of the SEP results. These documents provide a rather complete account of the details of the theory of the RFI technique, of the terrestrial tests of the technique, and of the present state of our interpretation of the Apollo 17 data.

ELECTRICAL STRUCTURE AT TAURUS-LITTROW

This section is a preliminary draft of the initial manuscript to be submitted to any scientific journal describing the SEP experiment and the scientific results obtained from the experiment. This initial draft, prepared by Strangway, Annan, Redman, Rossiter and Watts, will be modified before submission to a journal. The list and sequence of authors' names have not yet been determined.

(REVISED)

Introduction

The Surface Electrical Properties (SEP) Experiment was flown to the Taurus-Littrow region of the moon on Apollo 17. The experiment used megahertz radio frequencies in order to determine (i) electrical layering at the landing site, (ii) the dielectric properties of the surface material *in situ*, and (iii) the presence of scattering bodies.

In order to sound into the surface layers a relatively new technique, called radio frequency interferometry (RFI), had been developed for the lunar experiment and had been tested extensively on earth. A transmitter was set out on the lunar surface and a receiver was carried on the Lunar Roving Vehicle. As the Rover moved along its traverse, the received magnetic field strength and the Rover's position with respect to the transmitter were recorded.

At any point on the traverse several waves reach the receiver, and these waves interfere, as shown in Figure 1. The interference pattern is diagnostic both of the physical properties and of the structure of the upper layers. Field strength data for six frequencies and six combinations of receiving and transmitting antenna orientation, along with position, calibration, and temperature information, were recorded on a magnetic tape which was returned to earth.

The basis for the interferometry concept and details of the SEP Experiment have been given elsewhere (Annan, 1973; Rossiter *et al.*, 1973; Simmons *et al.*, 1972; Kong, Tsang, and Simmons, 1974; the SEP Team, 1974). In the present paper we

will outline briefly the basis for our interpretation, present the lunar SEP data, and describe our most recent evaluation of the results.

Background Material

Because radio interferometry is a relatively new technique, most of our background experience with it was built up explicitly for the lunar experiment. This study had three main facets: (i) theoretical evaluation of the EM fields surrounding a dipole antenna over a dielectric medium; (ii) experimental work using an analogue scale model; and, (iii) field work on several different glaciers for full scale experiments.

Although the integral expressions for the EM fields surrounding a dipole over a half-space have been known for some time (e.g. Banõs, 1966), their evaluation for layered media with with completely general electrical properties is far from trivial. Straight numerical integration is prohibitively expensive (Tsang, Brown, Kong, and Simmons, 1974). Therefore three complementary approximate methods were used - a geometric optics approach, the theory of normal modes and fast Fourier transform (FFT) techniques. The geometric optics formulation (Annan, 1970, 1973; Kong, 1972; Tsang et al., 1973) is most accurate for "optically thick" layers, and becomes invalid for distances less than about a wavelength. Theoretical cures are most easily calculated with the normal mode formulation for thin layers in which only a few modes propagate. The use of the FFT technique (Tsang, Brown, Kong, and Simmons, 1974) allows us

to calculate theoretical interference patterns for models in which the electrical properties vary continuously with depth.

In order to check these calculations, and to be able to study cases too complex for theoretical treatment, a scale model was constructed in which we used microwave frequencies (Waller, 1973; Annan et al., 1974). The model consisted of a layer of dielectric oil in which a reflecting plate could be set up in many different orientations. A typical suite of model curves for the layered case of a dielectric over a perfect reflector is shown in Figure 2, along with the corresponding theoretical curves. The inaccuracy of the geometric optics solution for thin layers is readily apparent.

Field experience with the RFI technique was gained on trips to the Gorner and Athabasca Glaciers (Rossiter et al., 1973; Strangway et al., 1974), and to the Juneau Icefields, using lunar hardware at various stages of development. Because most of the glaciers were known, from independent work, to approximate plane layered media, we were able to match observed data with curves obtained from the geometric optics formulation for layered media. In the analysis of the glacier field data, we compared, by trial-and-error suites of theoretical curves with field data. Attempts at formal inversion are currently underway (Watts, 1974).

A typical set of field profiles for the glacier tests and their corresponding "best-fit" theoretical curves are shown in Figure 3. No single frequency or component was uniquely indicative of the parameters (dielectric constant, loss tangent,

and depth to reflector). However, if we accepting only parameter sets that give consistent, good (but not perfect) fits for all frequencies, and for both of the maximum-coupled components for which we have theoretical solutions, then we can always find an "acceptable" interpretation.

SEP Operational History

The SEP experiment was done at the Apollo 17 Taurus-Littrow landing site. The transmitting dipole antennas were deployed by the astronaut about 150 meters east of the Lunar Module in a north-south and in an east-west direction (see Figure 4). During EVA-II SEP data are recorded as the Rover moved in a westerly direction away from the SEP transmitter towards Station #2. The traverse as reconstructed from the SEP-LRV navigation data is given in Figure 5.

From the SEP transmitter out to a range of 1.7 km the receiver operated normally. Between the range of 1.7 km and 4.3 km the receiver operated in an acquisition mode, attempting to acquire a synchronization signal from the transmitter. In this mode only partial data is collected. At a range of 4.3 km, because of the low received field strength, the receiver obtained a false resynchronizing pulse, causing an incorrect realignment of the receiver and transmitter timing, and a subsequent loss of field strength data from that point. At Station #2 the receiver was turned off to aid in cooling. The receiver was operating again between Stations #4 and #5; however,

the signal levels were too low to allow a resynchronization with the transmitter. At the beginning of the Station #5 stop the receiver was turned off, and, although the receiver was turned on again at the end of the station stop, because the internal receiver temperature was above a safe limit a thermal switch prevented it from operating for the remainder of EVA-II.

Data were to have been recorded during EVA-III from the SEP transmitter to Station #6 but the astronauts failed to turn on the receiver. Therefore, the data which are used as a basis for this discussion are those taken from the SEP transmitter west to a range of 4.3 km.

SEP Data and Discussion

The configuration of the SEP transmitting and receiving antennas is shown in Figure 6. Electromagnetic waves of six frequencies, 1, 2, 4, 8, 16 and 32 MHz, are transmitted sequentially by two orthogonal horizontal dipole antennas and received by three orthogonal selectrically small, loop antennas, resulting in 36 readings of the field strength during each measurement cycle.

Positional information from the Rover navigation system is recorded as increments and decrements of 1° in bearing, and 100 m in range, and as odometer pulses, each equivalent to a .49 meter change in position for the right-front and left-rear wheels of the Rover.

The Rover traverse derived from SEP data is compared in Table 1 with traverse data produced by the U.S.G.S. (ALGIT, 1974) and with the traverse reconstruction created from the Goddard Very Long Baseline Interferometry Data (I. Salzberg, personal communication, January 1974). The VLBI data have an absolute accuracy of approximately 40 m. The U.S.G.S. traverse is taken from photographic pans made at station stops, and are accurate to approximately 10 m for EP-4, LRV-1, and Station 2, and to about 50 m for LRV-2 and 3.

The three traverses are plotted in Figure 7. The maximum differences are about 500 m at stops LRV-2 and 3. The differences between USGS and VLBI traverses are larger than expected, and later adjustments of the data may improve the agreement among the three sets. For the first 2 km, all three reconstructions are in good agreement.

TABLE 1. COMPARISON OF EVA-II TRAVERSE STOPS FROM USGS, VLBI and SEP-LRV NAVIGATION DATA (See Figure 7).

STATION	RANGE (Km)			BEARING		
	VLBI	USGS	SEP-LRV NAV DATA	VLBI	USGS	SEP-LRV NAV DATA
EP-4	.500	.538	.508	80.4	80	83
LRV-1	2.603	2.603	2.645	80.9	78	82
LRV-2	3.750	3.729	3.811	81.4	86	83
LRV-3	4.248	4.253	4.325	80.2	87	82
HOLE IN THE WALL	5.638		5.683	79.5		81
STN. #2		7.46	7.6		68	71

A set of SEP field strength data is shown in Figure 8. Each

plot contains either the endfire or the broadside components for one frequency, plotted as a function of range, in free-space wavelengths. The data are plotted for a maximum distance of 1.7 km or to 20 free-space wavelengths.

For each frequency, six components are measured. Three components - H_ϕ endfire, and H_ρ and H_z broadside are maximum-coupled for a plane layered geometry, while the other three are minimum-coupled to the transmitted signal. For all six frequencies the maximum-coupled components have an average level from 5 to 15 dB greater than the minimum-coupled components. These results are in direct contrast to our glacial observations. For all our glacier runs the max and min components were approximately equal in level at 16 and 32 MHz (Strangway, et al., 1974). We attributed this rough equality of signal level to the presence of random scatterers (e.g. crevasses) in the ice with dimensions on the order of a wavelength. On this basis then, infer that few scattering bodies are present in the subsurface near the lunar SEP site, with typical sizes of 10 to 300 m and contrasting dielectric properties. Scattering experiments both in the scale model and on glaciers support this conclusion.

Further confirmation is obtained, by an examination of the H_ϕ endfire component. This component has a near-surface wave so large that it effectively masks any interference. However, if near-surface scattering is important, this component becomes erratic. As can be seen from Figure 8, this component is relatively smooth at all SEP frequencies. The residual peaks and

nulls correlate well with those in the H_ρ-broadside component. Therefore we believe that these two components are slightly mixed because the traverse was not completely east-west (i.e. not directly off the end of the endfire antenna).

The other two maximum-coupled components (H_ρ and H_z broadside) have been the most important for interpretation (see Figure 9). At 16 and 32 MHz the number of peaks and troughs per free space wavelength of range is fairly low, indicating a dielectric constant of about 2 to 5. However, the lower frequencies show somewhat higher beating rates, indicating a dielectric constant of about 6 to 8, and certainly less than 10. These observations imply that the dielectric constant of the near-surface material is lower than that of deeper material. These results are consistent with the dielectric properties of a soil layer over solid rock, as measured on returned samples (e.g. Olhoeft et al., 1973).

The loss tangent is estimated from the sharpness of the peaks and nulls in the two major components and from the average decay of the field strength with distance. Our analysis indicates that the average loss tangent of the sub-surface material to a depth of several hundred meters is less than 0.05 and possibly as low as 0.002. The fact that the higher frequencies have strong signal levels for many tens of wavelengths from the transmitter, while the lower frequencies die out relatively quickly, indicates that the loss tangent of the near surface material is 0.01 or less. These low loss values confirm that no liquid water is present in the outer kilometer of the moon.

Structure is more difficult to determine unambiguously. By comparing the two major components with suites of theoretical curves for a plane two-layer geometry (i.e. dielectric layer over a dielectric half-space), no single set of parameters has been found that gives theoretical curves in satisfactory agreement with the data at all frequencies. Several perturbations from the two-layer model have therefore been suggested.

One possible variation is sketched in Figure 10 (a), showing a thinning layer of soil over rock. The layer is 20 m thick near the SEP site, with dielectric constant of 3 to 4, and thins to 15 m a few hundred meters to the west. The lower material has a dielectric constant of 6 to 7. Results from the Lunar Seismic Profiling Experiment, conducted over the same region, show good agreement with this model (Watkins and Kovach, 1973). The chief basis for this interpretation is the curve for 2 MHz broadside (Figure 9 (b)), which shows little interference out to about 4 wavelengths range, but then has several dramatic peaks. This behaviour suggests that the layer is just thick enough near the transmitter that little energy is transmitted either through the layer or through the subsurface. However, further from the transmitter the layer becomes so thin that it is essentially transparent. Although we have not obtained theoretical formulations for sloping interfaces, we have observed interference patterns for sloping glacier

interfaces and for the microwave model that resemble the lunar pattern.

Table 2 lists the parameters of a three-layer model, sketched in Figure 10 (b). In this model we assume, (i) that layer 1 is so thin that it is essentially transparent to all frequencies but 16 and 32 MHz; and, (ii) that the boundary between layers 2 and 3 is too deep to have much effect on the 16 and 32 MHz patterns. Theoretical curves for this model are shown for comparison with the data in Figure 9. Although the major features of the data are present also in the theoretical curves, the details are not always in good agreement. This lack of agreement may be due to slight adjustments in loss tangent (the particular features in most curves are very dependent on the loss tangent), or due to slight dipping of the interfaces (as mentioned above).

TABLE 2. PARAMETERS FOR 3-LAYER MODEL

(See Figures 9 and 10(b)).

	Depth (m)	Dielectric constant	Loss tangent
Layer 1	7 ± 1	3.8 ± 0.2	0.008 ± 0.004
Layer 2	100 ± 10	7.5 ± 0.5	0.035 ± 0.025
Layer 3	00	9 ?	?

Another model that fits reasonably well, the observed data is shown in Figure 11 and several theoretical curves, obtained with the FFT formulation of Tsang, Brown, Kong and Simmons (1974) are shown in Figure 12.

Conclusions

Despite our present inability to match the lunar SEP observations with the theoretical curves calculated for various models, we believe that the gross electrical properties of the Taurus-Littrow region have been obtained. At the present stage of our analysis of the lunar data, we are confident of the following conclusions:

(1) The loss tangent of the lunar material in situ is less than 0.05 and possibly as low as 0.002, to depths of 2 to 3 kilometer.

(2) No liquid water is present at Taurus-Littrow to a depth of 2 to 3 kilometers.

(3) Electromagnetic scattering is not important at any of the SEP frequencies.

(4) Scattering bodies with sizes of 10 to 300 meters are not present in the vicinity of the traverse from the SEP-site to Station 2.

(5) The relative dielectric constant is about 3 1/2 near the surface and increases with depth to a value of 6 to 8 at about 100 meters. These values are consistent with the values expected for lunar soil overlying rock.

(6) No model consisting of plane layers has been found that fits the observations accurately. Some features of a thinning layer, a three-layer model and continuously increasing dielectric properties match some of the features of the observed interference patterns.

(7) The Rover navigation data recorded on EVA II to Station 2 is in good agreement with VLBI and USGS traverse reconstructions.

Acknowledgements

Financial support was provided by the National Aeronautics and Space Administration through Contract NAS -11540 with subcontract to University of Toronto. The lunar hardware was built by Raytheon. Technical and administrative support was provided by the Center for Space Research and the C. S. Draper Laboratory.

We thank Mssrs. J. Proctor and J. Rylaarsdam for computational and data processing assistance. Mr. G. Wagner designed and built the data reduction systems. Much of the data reduction was carried out at the Johnson Space Center and at the Lunar Science Institute, Houston, Texas.

References

Annan, A.P., "Radio Interferometry Depth Sounding", M. Sc. thesis, Dept. of Physics, U. Of Toronto, 1970.

Annan, A.P., "Radio Interferometry Depth Sounding"; Part I - Theoretical Discussion", Geophysics, v. 38, PP. 557-580, 1973.

Annan, A.P., Waller, W.M., Strangway, D.W., Rossiter, J.R., and Redman, J.D., "The Electromagnetic Response of a Two-Layer Dielectric Earth Excited by a Horizontal Electric Dipole", submitted to Geophysics, 1974.

Apollo Lunar Geology Investigation Team, (U.S.G.S.), "Preliminary Geological Analysis of the Apollo 17 Site", Apollo 17 Preliminary Science Report, 1974.

Baños, A., "Dipole Radiation in the Presence of a Conducting Half-space", Pergamon Press, New York, 1966.

Kong, J.A., "Electromagnetic Fields due to Dipole Antennas over Stratified Anisotropic Media", Geophysics, v. 37, pp. 985-996, 1972.

Olhoeft, G. R., Strangway, D.W., and Frisillo, A.L., "Lunar Sample Electrical Properties", Proc. Fourth Lunar Sci. Conf., (Suppl. 4, Geochim. Cosmochim. Acta), v. 3, pp. 3133-3149, 1973.

Rossiter, J.R., LaTorraca, G.A., Annan, A.P., Strangway, D.W., and Simmons, G., "Radio Interferometry Depth Sounding; Part II - Experimental Results", Geophysics, v. 38, pp. 581-599, 1973

Rossiter, J.R., Strangway, D.W., Annan, A.P., Watts, R.D., and Redman, J.D., "Detection of Thin Layers by Radio Interferometry", submitted to Geophysics, 1974.

Simmons, G., Strangway, D.W., Bannister, L., Baker, R., Cubley, D., LaTorraca, G., and Watts, R., "The Surface Electrical Properties Experiment", in Kopal, Z. and Strangway, D., eds., Lunar Geophysics, Proceedings of a Conference at the Lunar Science Institute, Houston, Texas, 18-21 October, 1971, D. Reidel, Dordrecht, PP. 258-271, 1972.

Strangway, D.W., Simmons, Gene, LaTorraca, G., Watts, R., Bannister, L., Baker, R., Redman, D., and Rossiter, J., "Radio-Frequency Interferometry - A New Technique for studying Glaciers", J. Glaciology, in press, 1974.

Surface Electrical Properties Team, "The Surface Electrical Properties Experiment", Apollo 17 Preliminary Science Report, in press, 1974.

Tsang, L., Kong, J.A., and Simmons, G., "Interference Patterns of a Horizontal Electric Dipole over Layered Dielectric Media", J. Geophys. Res., v. 78, pp. 3287-3300, 1973.

Waller, W. M., "Surface Electrical Properties Simulation Model", Lockheed Electronics Co. Final Report LEC/PESD 634-TR-139 for contract NAS 9-122200, NASA-JSC, Houston, 1973.

Watkins, J.S., and Kovach, R.L., "Seismic Investigation of the Lunar Regolith", Proc. Fourth Lunar Sci. Conf. (Suppl. 4, Geochim. Cosmochim. Acta), v. 3, pp. 2561-2574, 1973

Watts, R.D., "Line-Source Radiation over a Layered Dielectric: Inversion of Radio Interferometry Data", J. Geophys. Res., in press, 1974.

Figure Captions

Fig. 1. The three main waves used in radio interferometry. The surface wave travels above the surface of the dielectric and the subsurface wave travels just below it. Because these two waves travel at different velocities, their beat frequency is a function of the dielectric constant. Any reflected waves from a subsurface horizon also influence the interference pattern.

Fig. 2 Theoretical solutions and scale model data for a dielectric over a perfect reflector. The inaccuracy of the geometric optics approach for thin layers is readily apparent.

Fig. 3. Typical RFI data for the Athabasca Glacier and a set of theoretical curves.

Fig. 4. Photograph of the Taurus-Littrow site with superimposed information that shows the locations of traverses, major station stops, SEP transmitter site, and the explosive package (EP-4). SEP data were collected for a distance of 4 km along the traverse from SEP-site towards Station 2.

Dig. 5. Map of the EVA-II traverse, based on LRV navigation data, from the SEP site to Station 2. The Rover stops are indicated by LRV-1, -2, and -3.

Fig. 6 Notation of the field components. Three orthogonal magnetic field components are measured for each transmitting antenna. One transmitting antenna was approximately broadside to the traverse, the other was endfire to the traverse.

Fig. 7a,b,c. EVA-II traverse reconstruction as compiled from (i) LRV navigation data recorded by SEP; (ii) Goddard Very Long Baseline Interferometry; and (iii) U.S.G.S. traverse reconstruction from photographic information. The three independent reconstructions compare favorably to a distance of 3 km, although they disagree more than expected near LRV-2 and 3 (see Table 1).

Fig. 8 (a-l). The surface Electrical Properties Experiment data for all 36 "components". Each component has been plotted as a function of free space wavelength, out to 1.7 km or 20 wavelengths (whichever is smaller). The vertical scale is in dB, with a reference at -90 dBm, as shown. The component is labelled at the end of the curve; H_ϕ endfire, H_ρ and H_z broadside are maximum coupled; the others, minimum coupled. The pattern has been corrected for a 360° turn of the Rover at the position of the EP-4 deployment.

Fig. 9 Comparison of the theoretical curves (dashed lines) with observed data (solid lines) for H_ρ and H_z broadside. The parameters for this model are given in Table 2.

Fig. 10 The model with a sloping interface.

Fig. 11 Model C11.

Fig. 12 Typical comparison of theoretical curves for Model C11 with observed date.

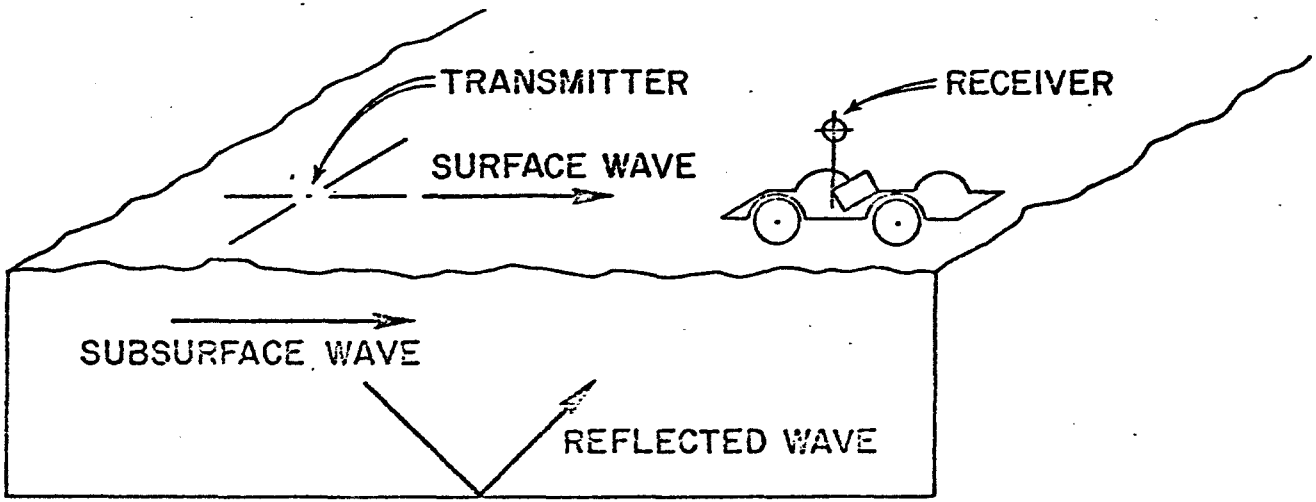
TRANSMITTER
RECEIVER
SURFACE WAVE
SUBSURFACE WAVE
REFLECTED WAVE

1(a)

Fig 1.

Fig 7.

THEORETICAL SOLUTIONS AND SCALE - MODEL RESULTS

PLANE LAYERED GEOMETRY, VARIOUS DEPTHS TO REFLECTOR

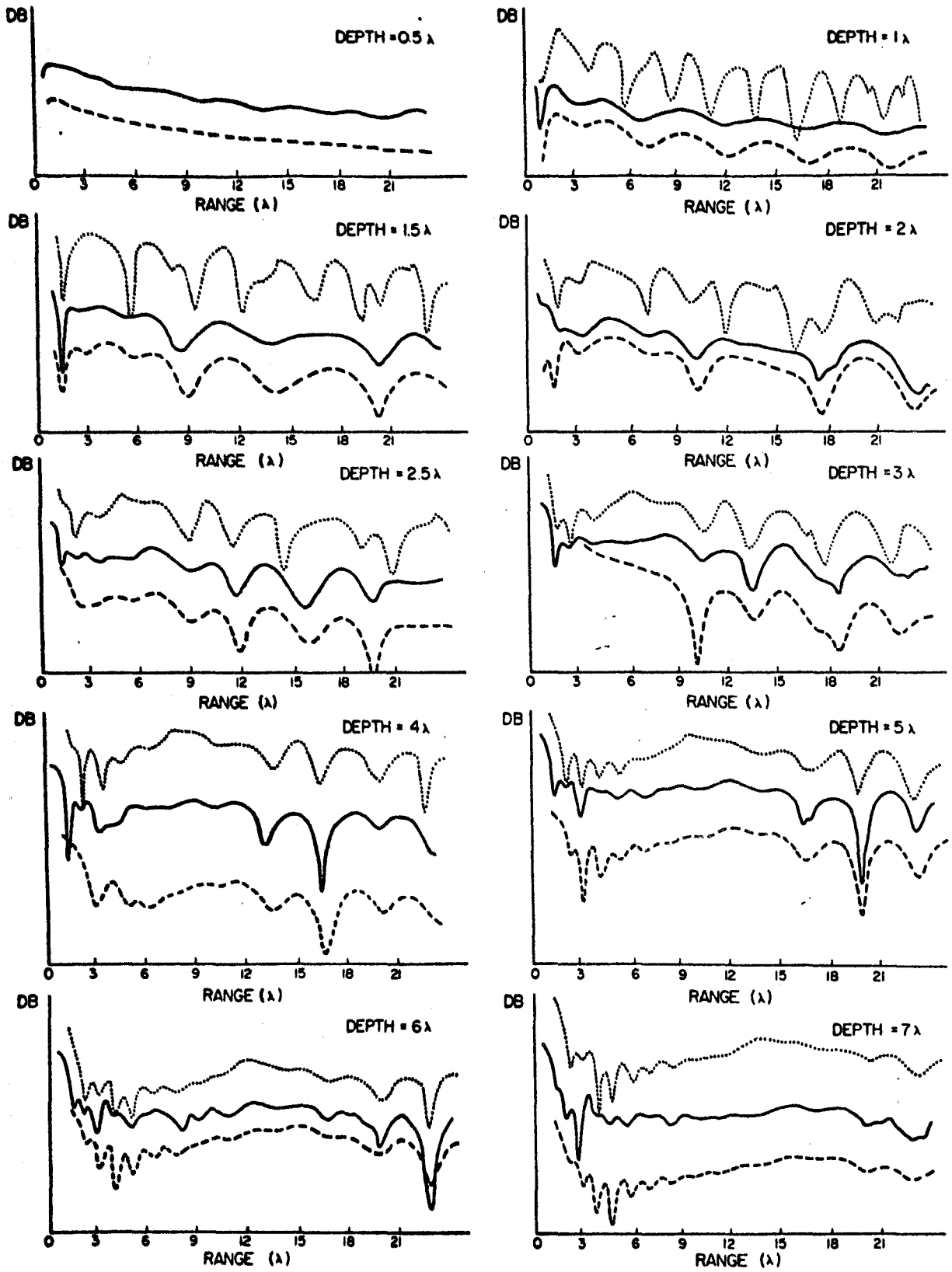

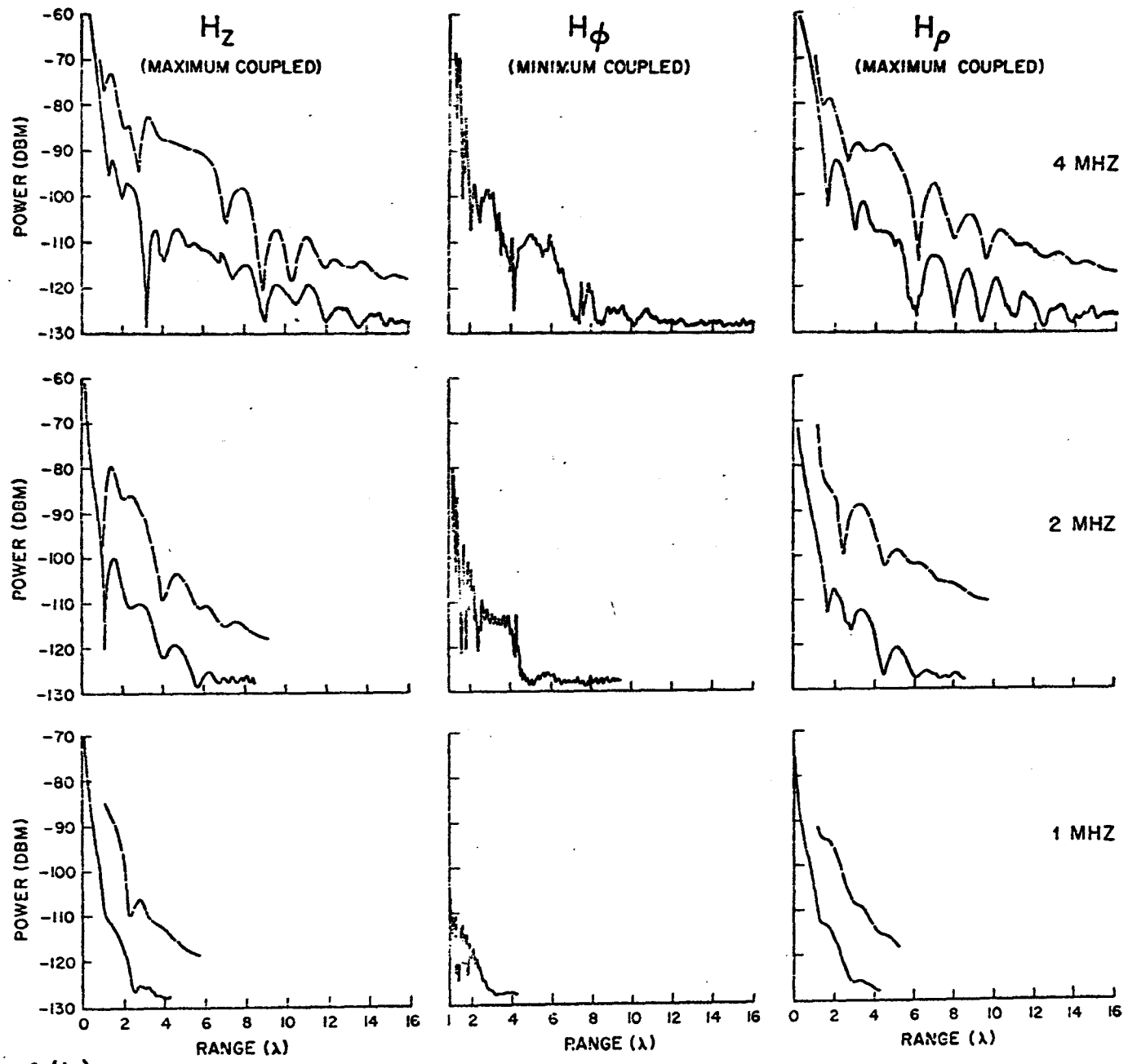
H_z
(MAXIMUM COUPLED)
H_ϕ
(MINIMUM COUPLED)
H_ρ
(MAXIMUM COUPLED)
4 MHZ
2 MHZ
1 MHZ
POWER (DBM)
-60
-70
-80
-90
-100
-110
-120
-130
0 2 4 6 8 10 12 14 16
RANGE (λ)

4(b)

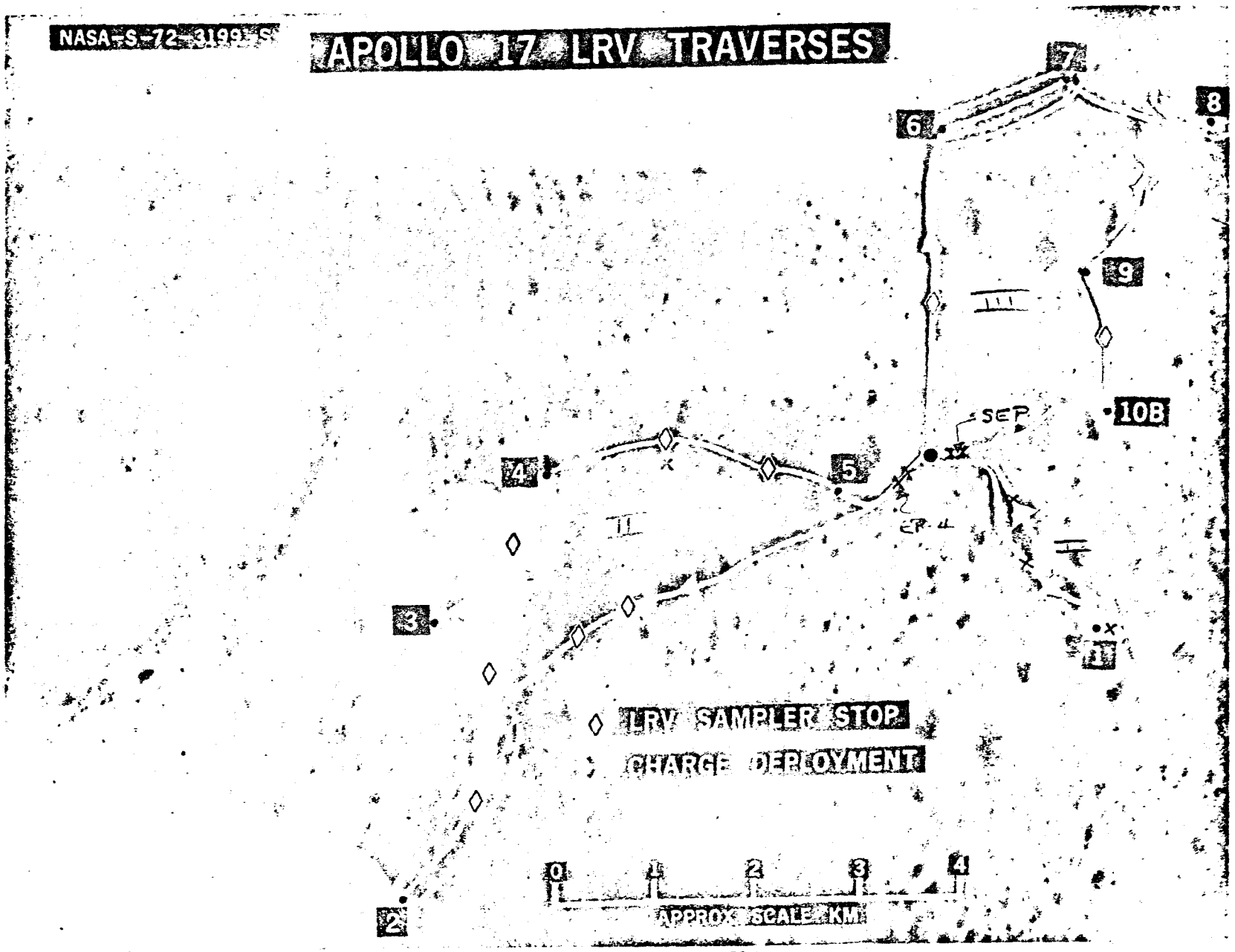

Fig. 17B - Pictorial view of the LRV traverses

FIG. #3

FIG. #3 EVA-II TRAVERSE RECONSTRUCTION FROM SEP-LRV NAVIGATION DATA

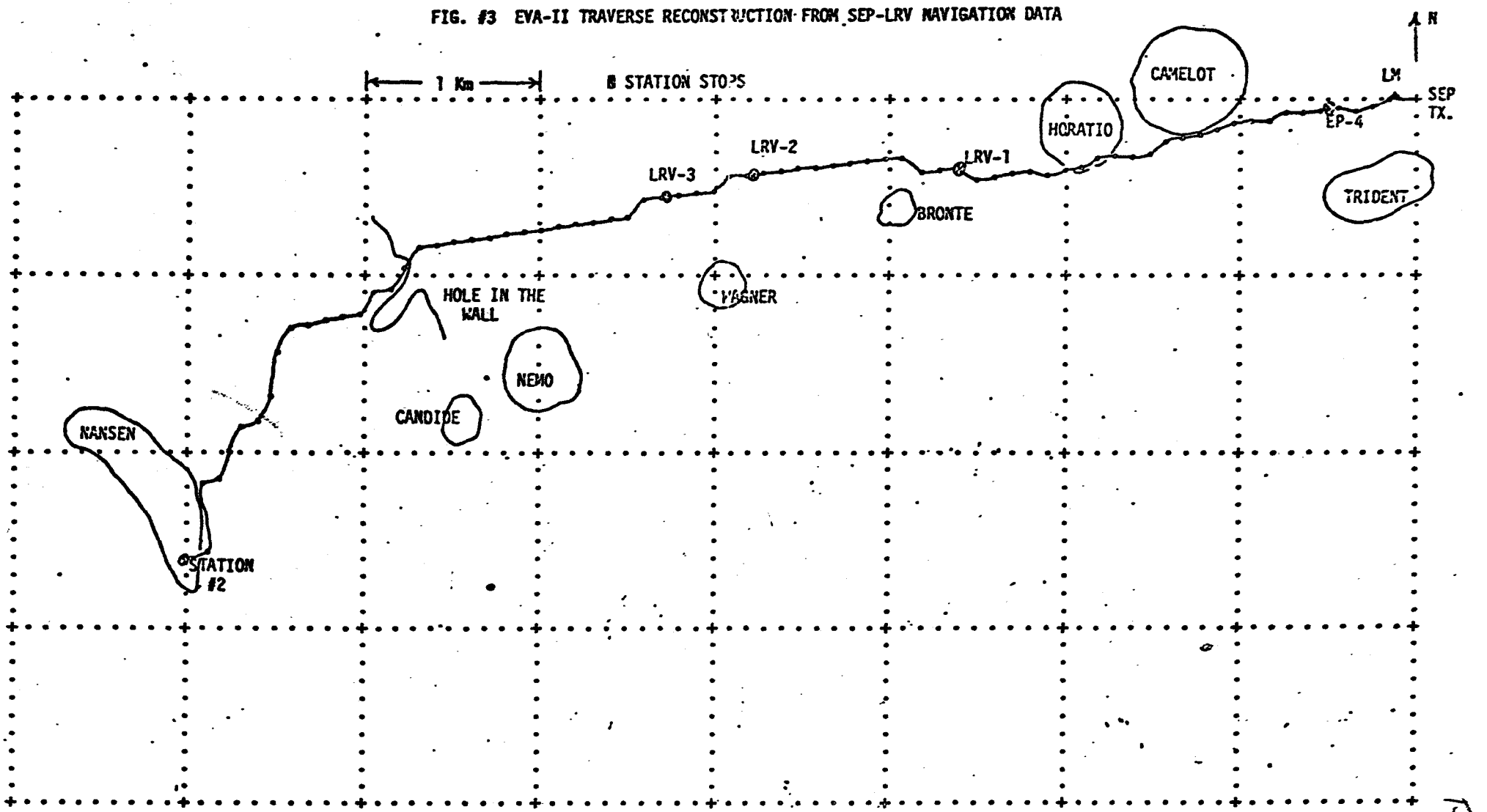

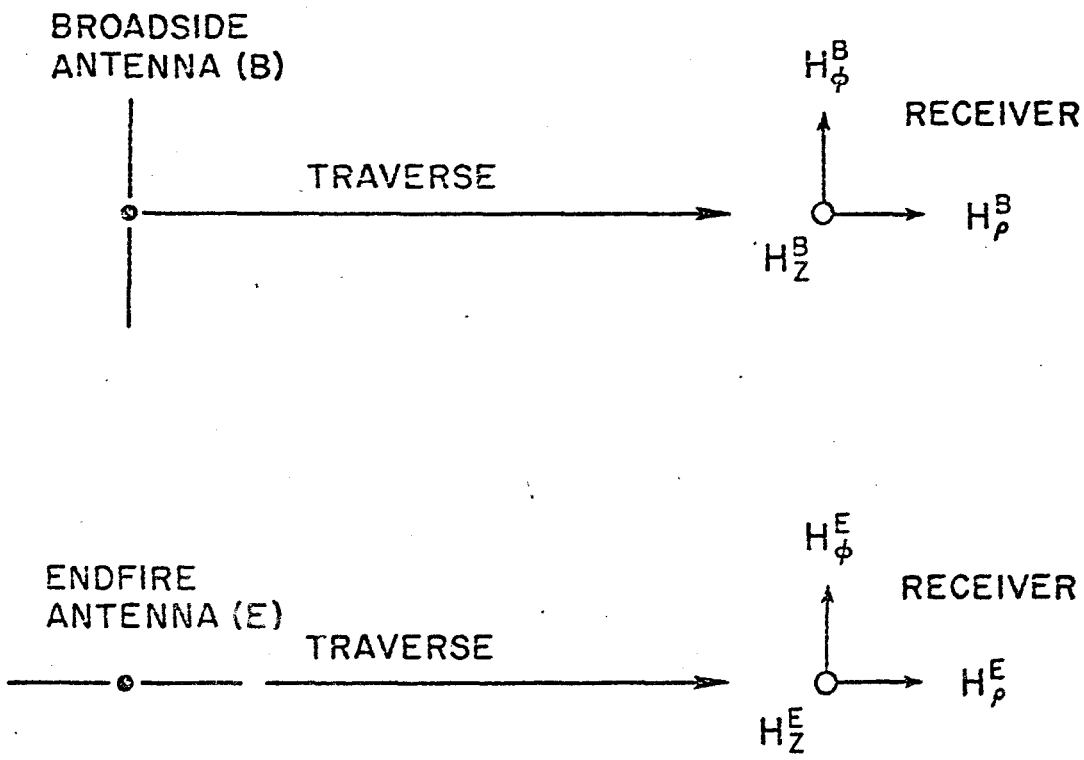
BROADSIDE
ANTENNA (B)
TRAVERSE
H_ϕ^B
RECEIVER
H_ρ^B
H_Z^B
ENDFIRE
ANTENNA (E)
TRAVERSE
H_ϕ^E
RECEIVER
H_ρ^E
H_Z^E

1(b)

Fig. 6

FIG. #4(a) COMPARISON OF EVA-II TRAVERSE RECONSTRUCTION FROM SEP-LRV NAVIGATION DATA WITH VLBI AND USGS TRAVERSE DATA

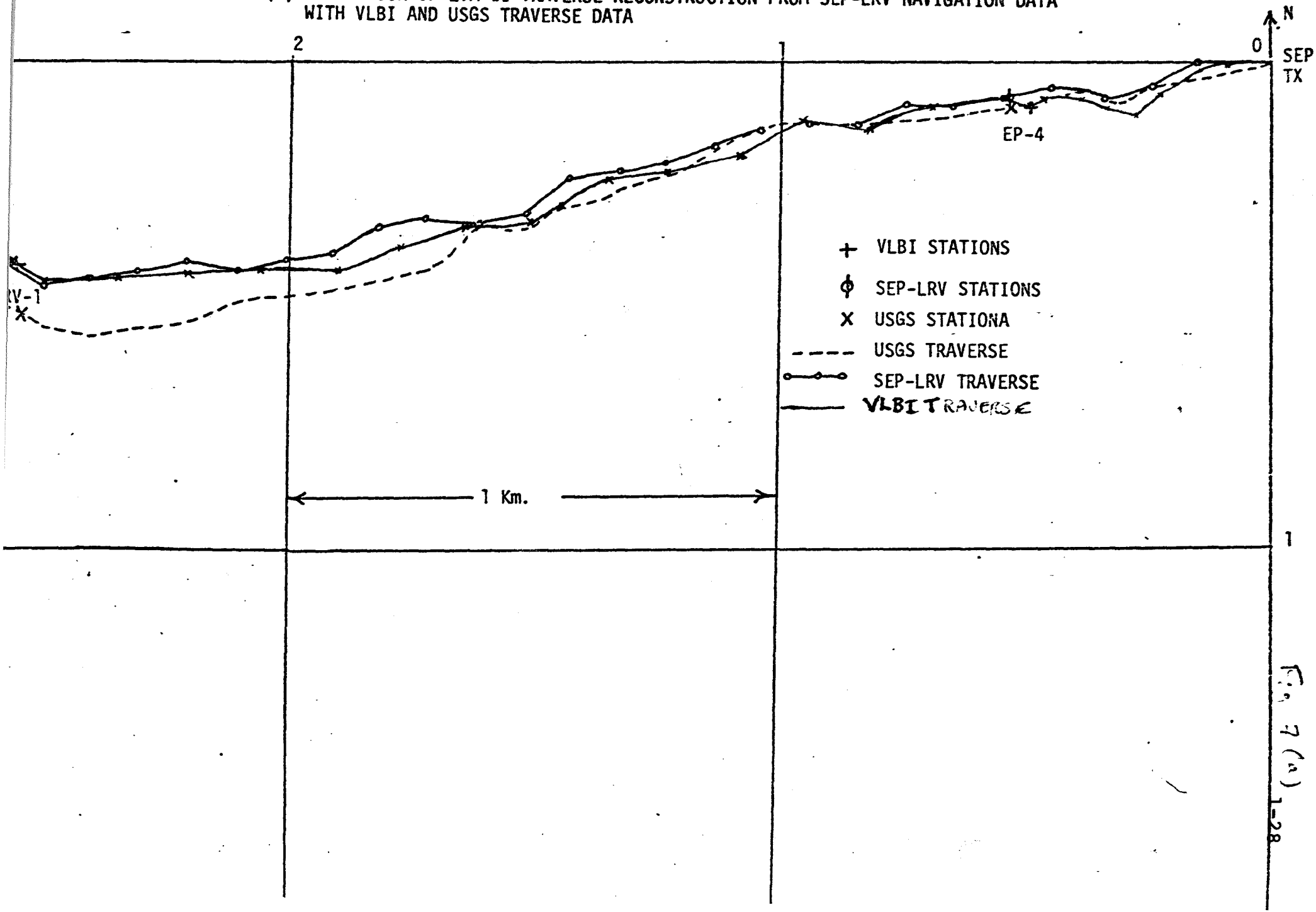

Fig. 7(a)

FIG. # 4(b)

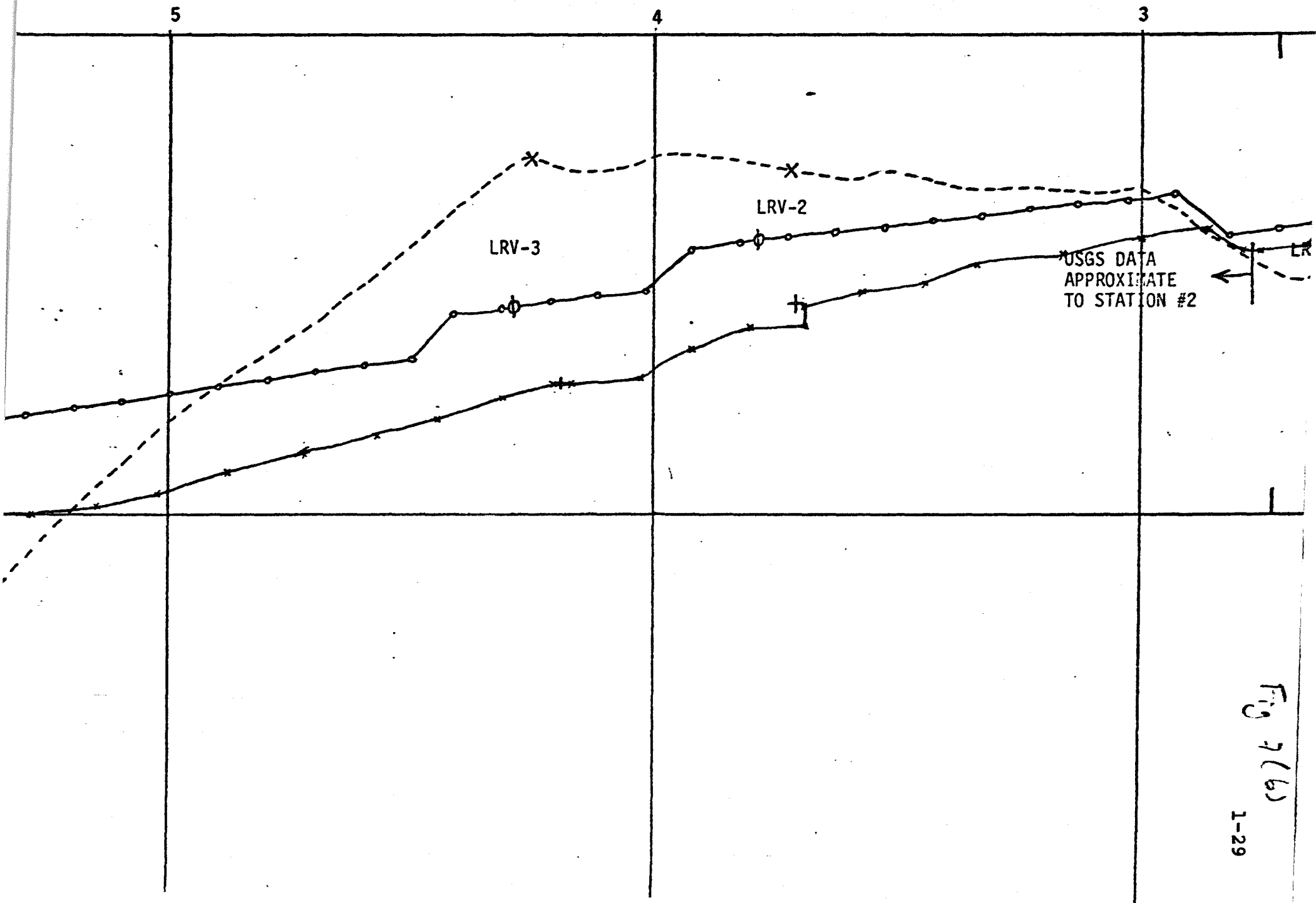

Fig 4(b)

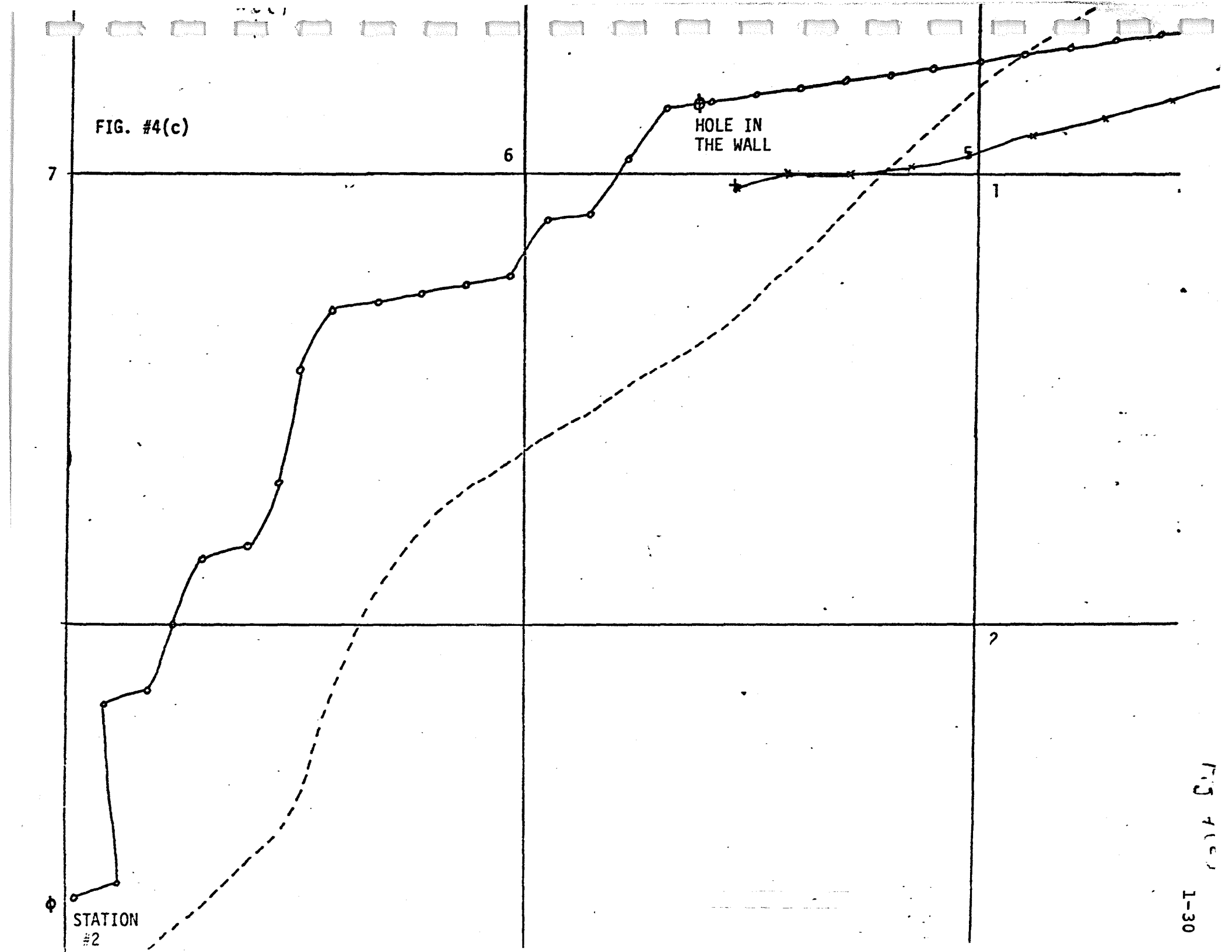
FIG. #4(c)
HOLE IN
THE WALL
7
6
5
1
2
STATION
#2

Fig 8(a)

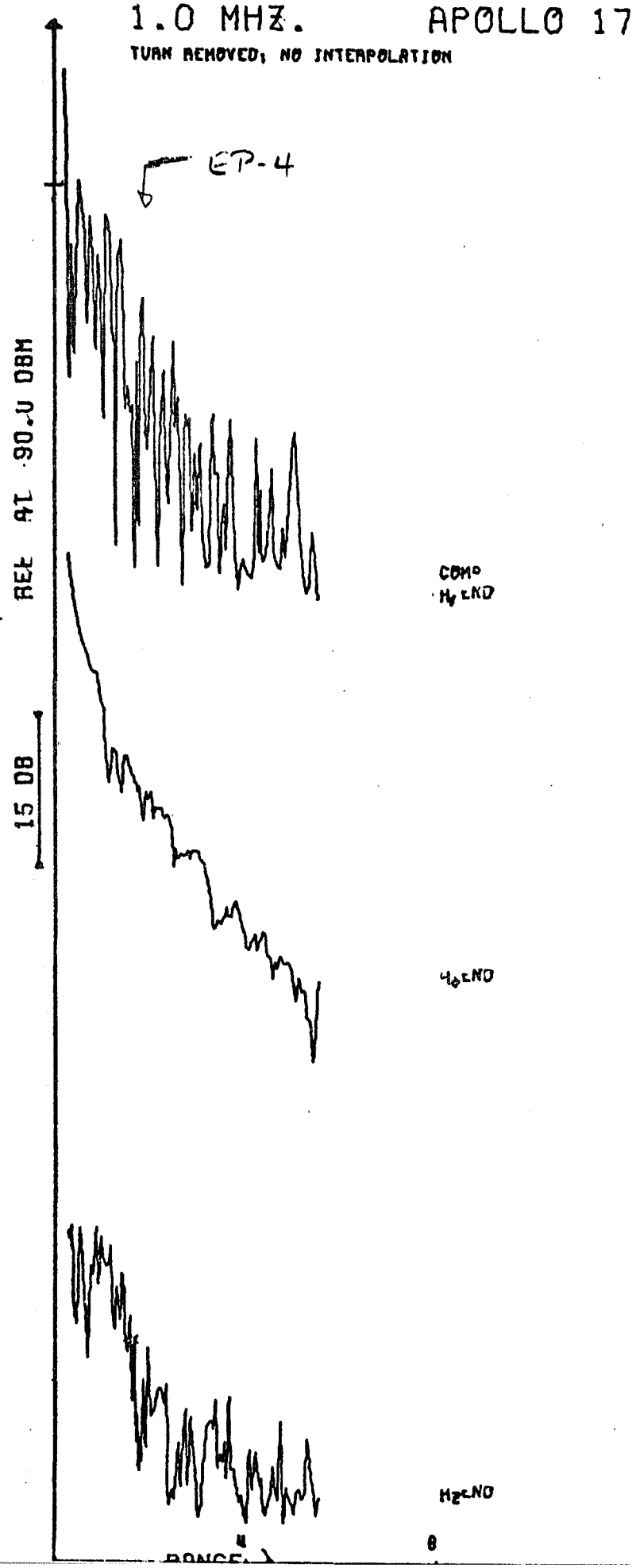
1.0 MHZ.
APOLLO 17
TVAN REMOVED; NO INTERPOLATION
EP-4
REL AT -90.0 DBM
15 DB
COMP
Hy END
Hφ END
Hz END
RANGE

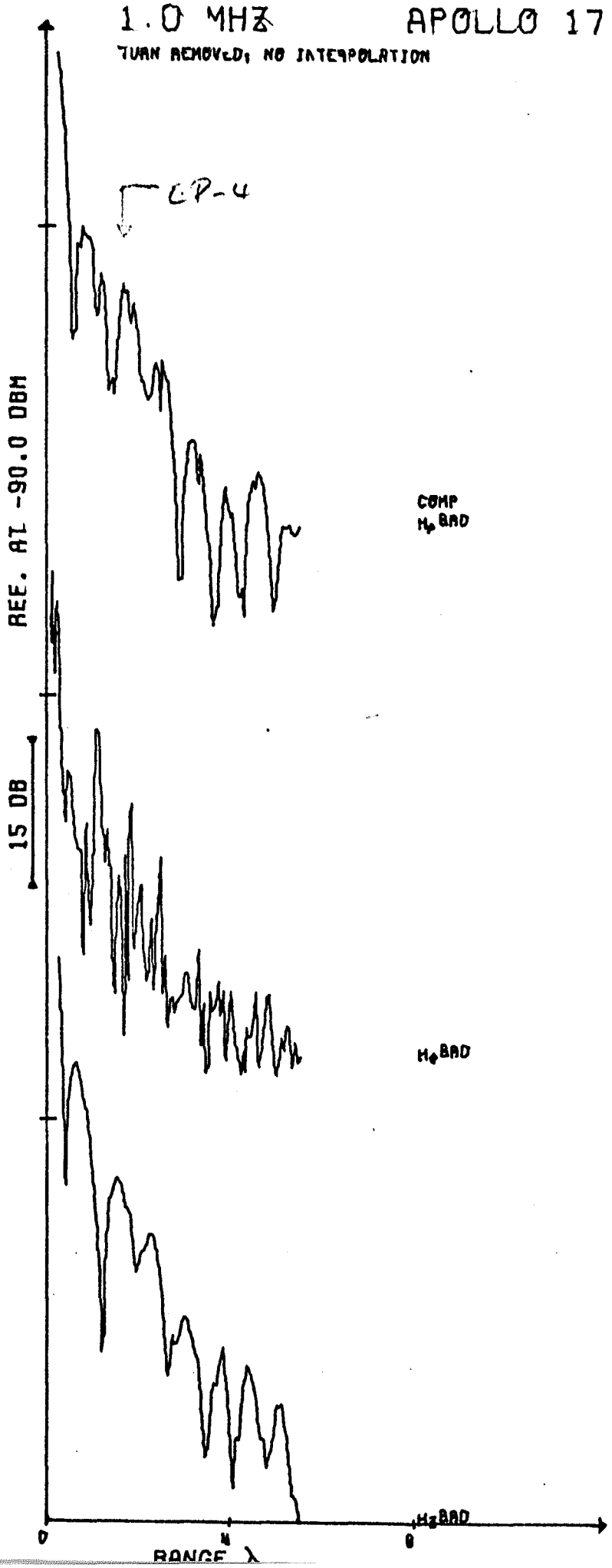
1.0 MHZ
APOLLO 17
TURN REMOVED; NO INTERPOLATION
CP-4
REF. AT -90.0 DBM
15 DB
COMP
Hφ BAD
Hφ BAD
Hz BAD
0
N
0
RANGE λ

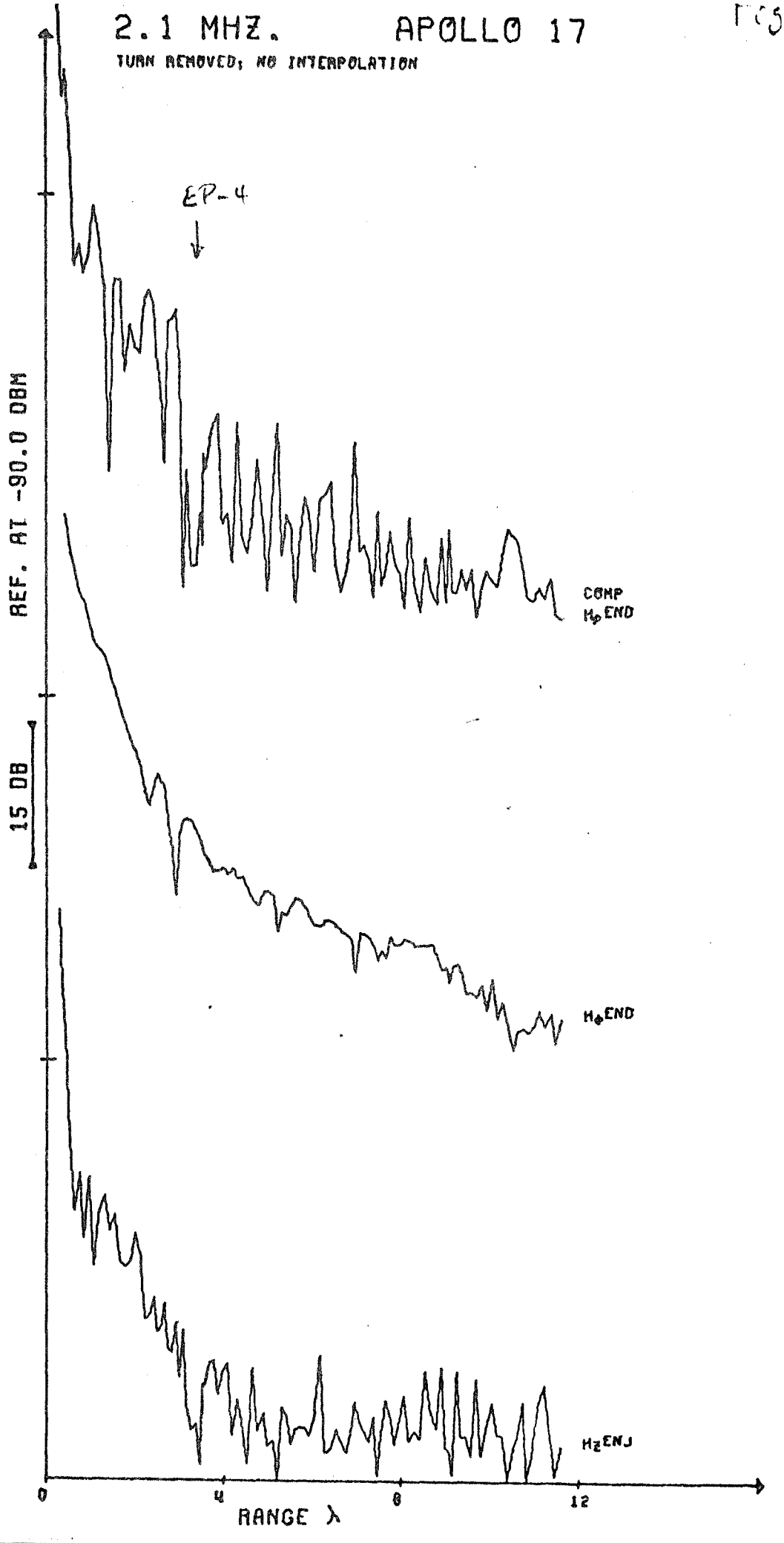
2.1 MHZ. APOLLO 17
TURN REMOVED; NO INTERPOLATION
EP-4
REF. AT -90.0 DBM
15 DB
COMP
H_ϕ END
H_ϕ END
H_Z ENJ
0
4
8
12
RANGE λ

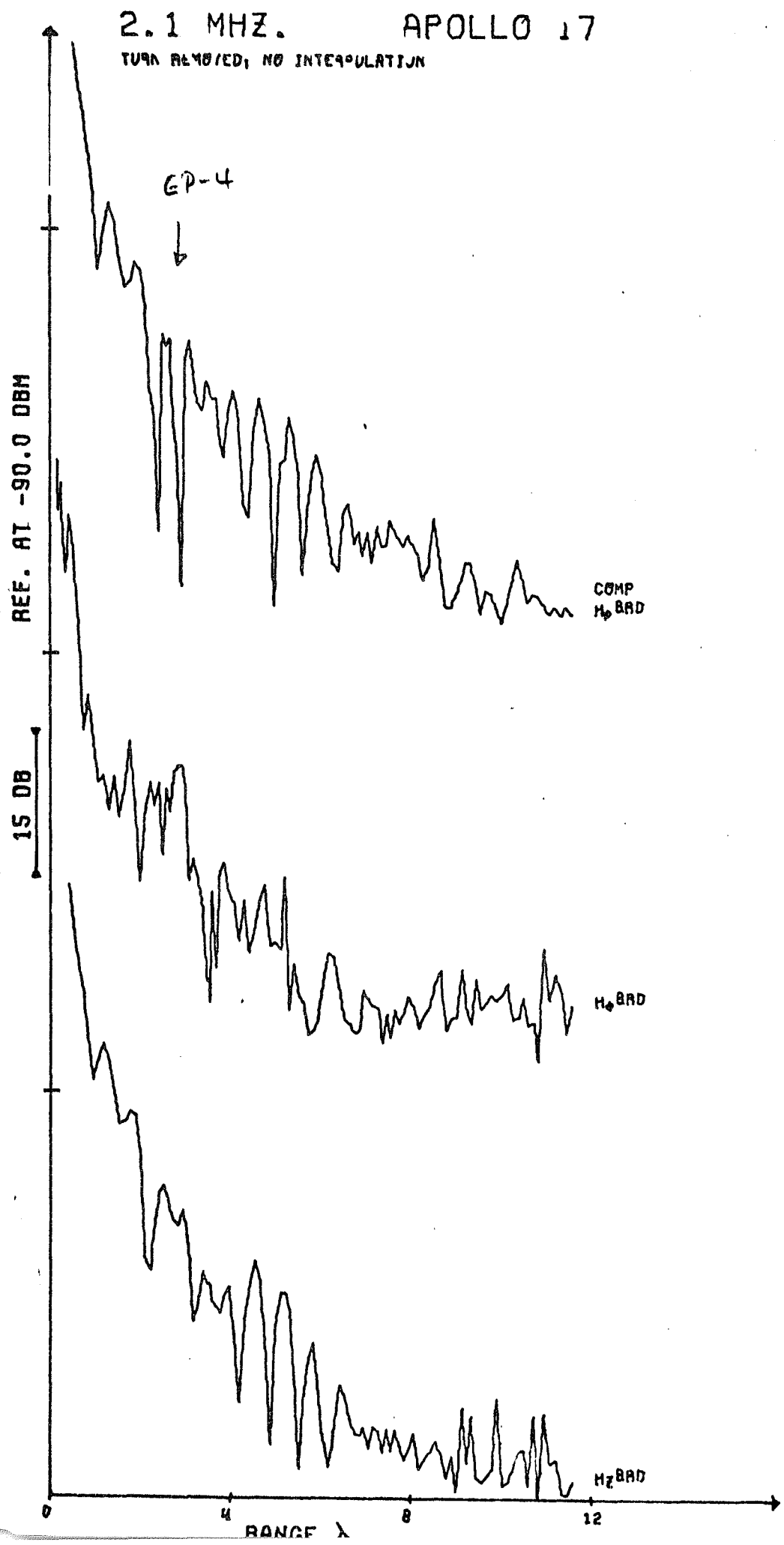
2.1 MHZ. APOLLO 17
TURN RENORMED; NO INTERPOLATION
GP-4
REF. AT -90.0 DBM
15 DB
COMP
Hφ BAD
Hφ BAD
Hz BAD
0
4
8
12
RANGE λ

Fig 8(e)

4.0 MHZ. APOLLO 17

TURN REMOVED; NO INTERPOLATION

EP-4

REF. AT -90.0 DBM

15 DB

COMP H_ϕ END

H_ϕ END

H_z END

0 4 8 12 16 20

RANGE λ

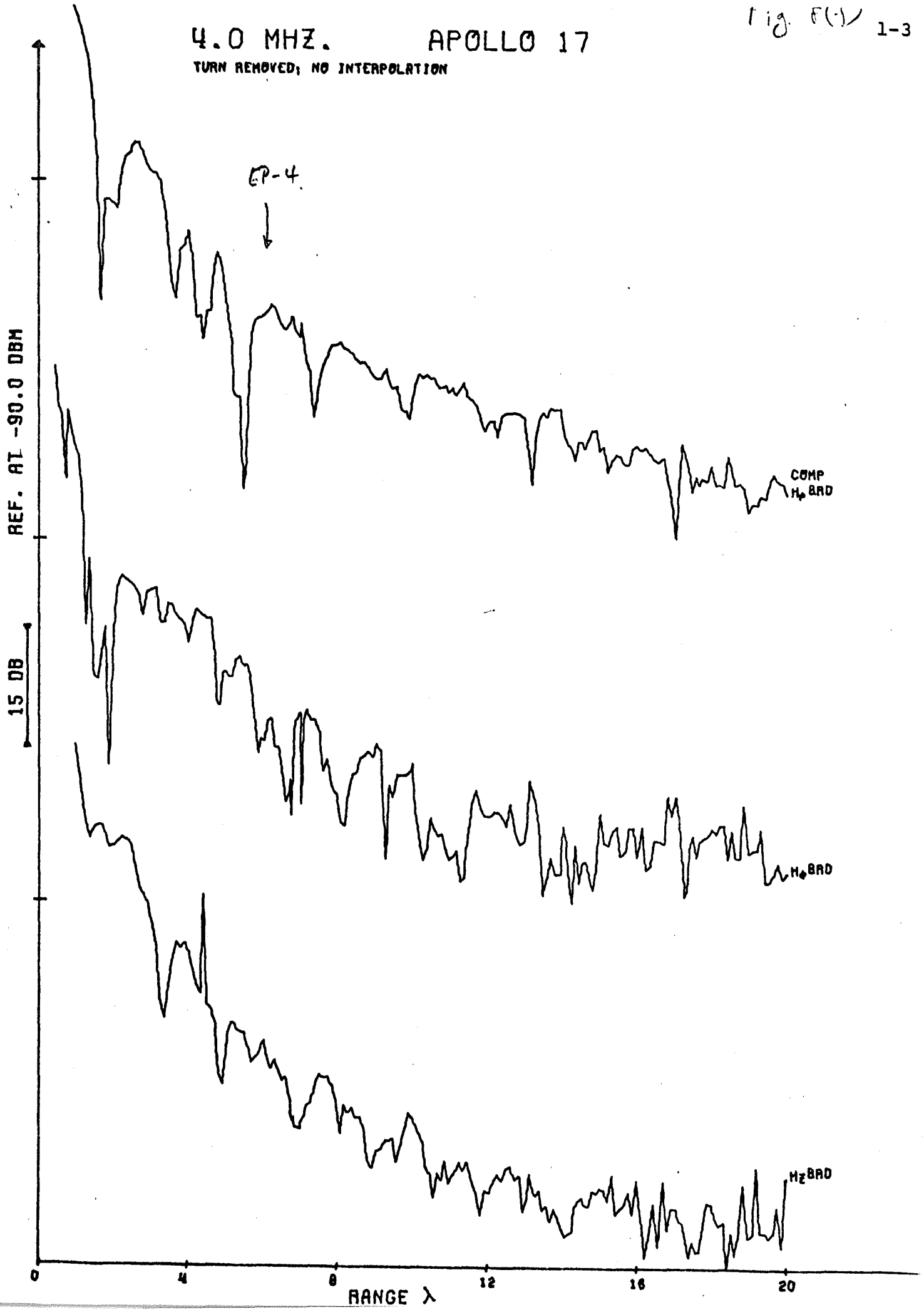
4.0 MHZ. APOLLO 17
TURN REMOVED; NO INTERPOLATION
EP-4
REF. AT -90.0 DBM
15 DB
COMP
H_ϕ BRD
H_ϕ BRD
H_Z BRD
0
4
8
12
16
20
RANGE λ

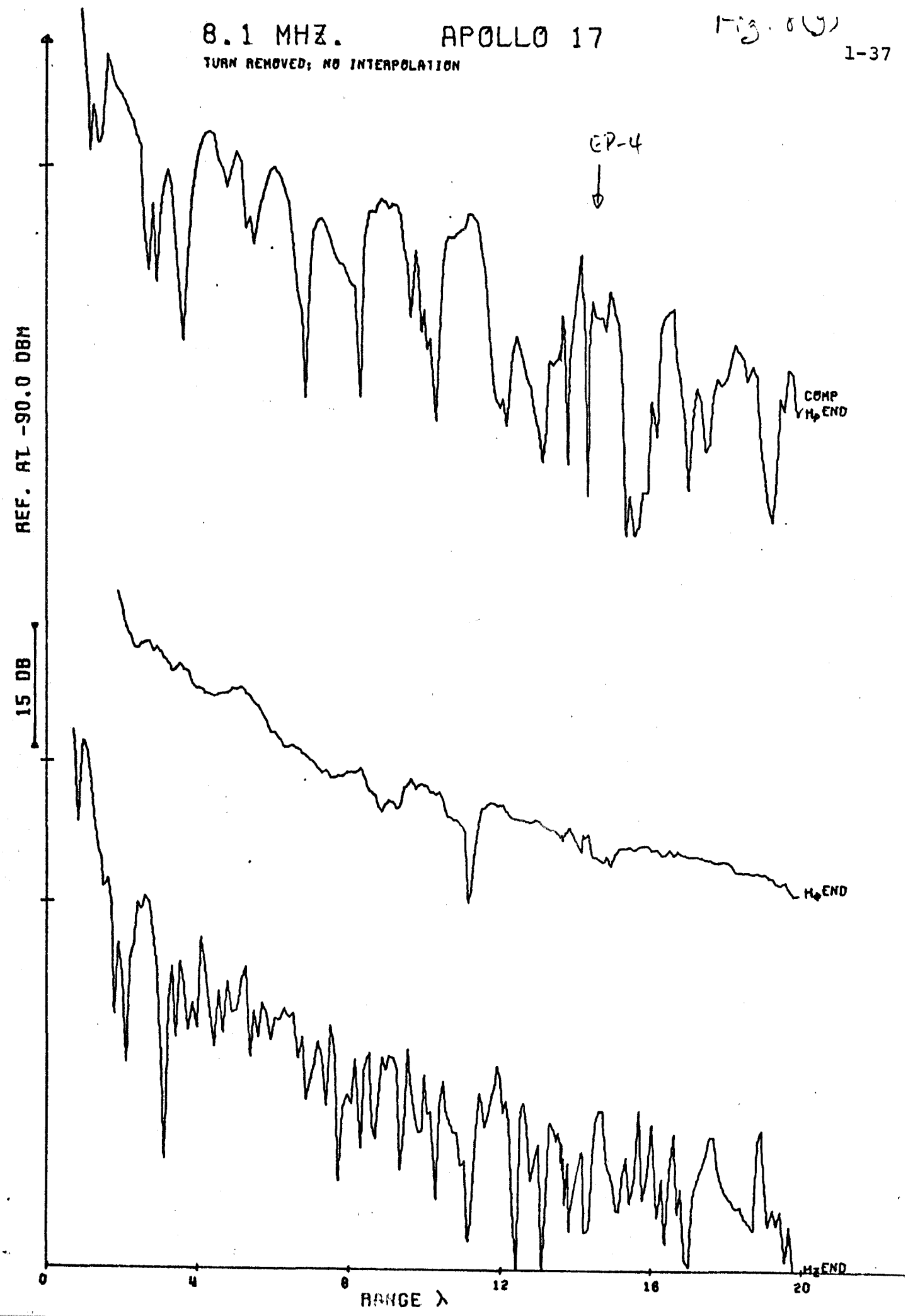
8.1 MHZ. APOLLO 17
TURN REMOVED; NO INTERPOLATION
EP-4
REF. AT -90.0 DBM
15 DB
COMP
H_ϕ END
H_ϕ END
H_z END
0
4
8
12
16
20
RANGE λ

Fig 8(a)

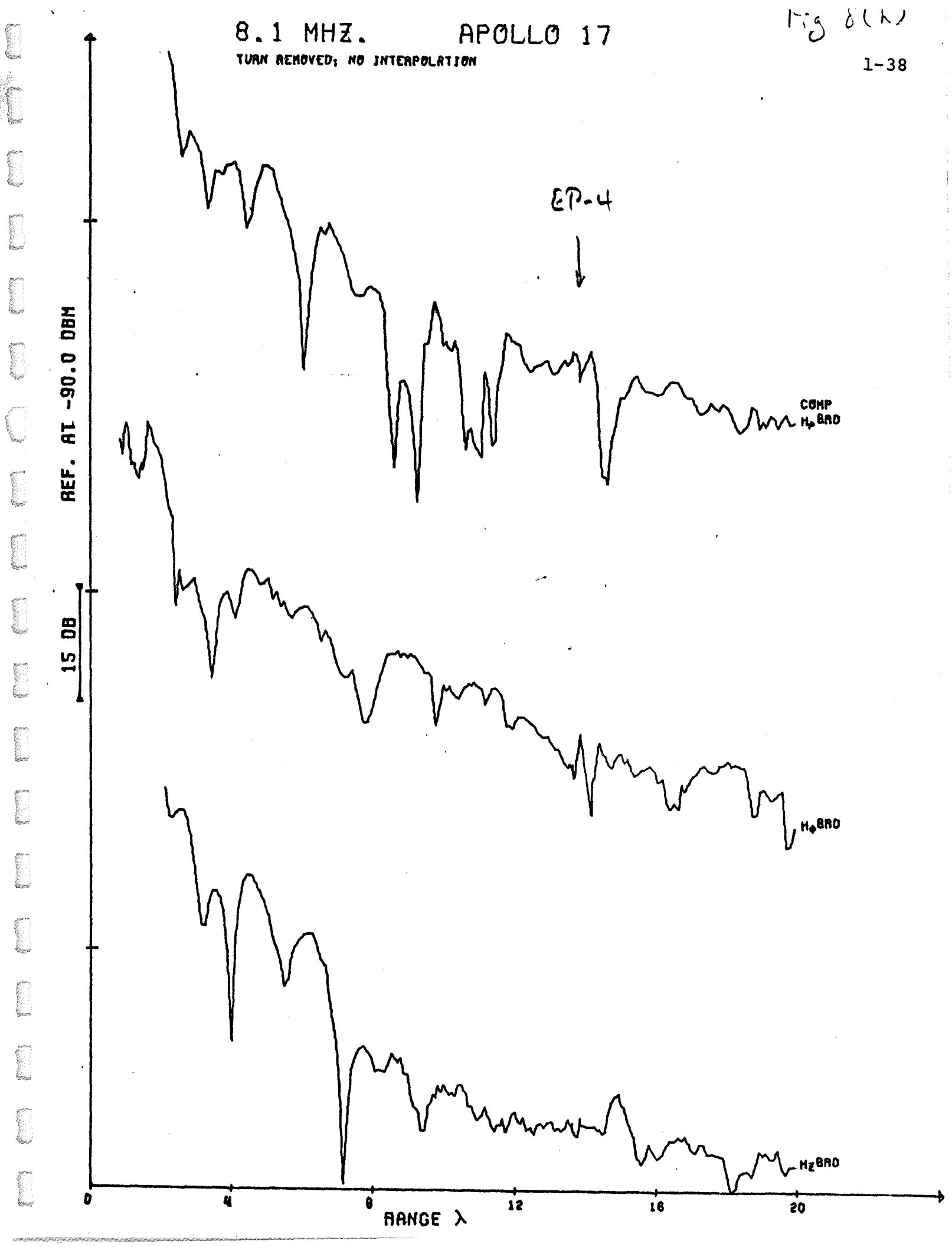
8.1 MHZ. APOLLO 17
TURN REMOVED; NO INTERPOLATION
EP-4
REF. AT -90.0 DBM
15 DB
COMP
H_ϕ BRD
H_ϕ BRD
H_Z BRD
0
4
8
12
16
20
RANGE λ

16.0 MHZ. APOLLO 17

TURN REMOVED; NO INTERPOLATION

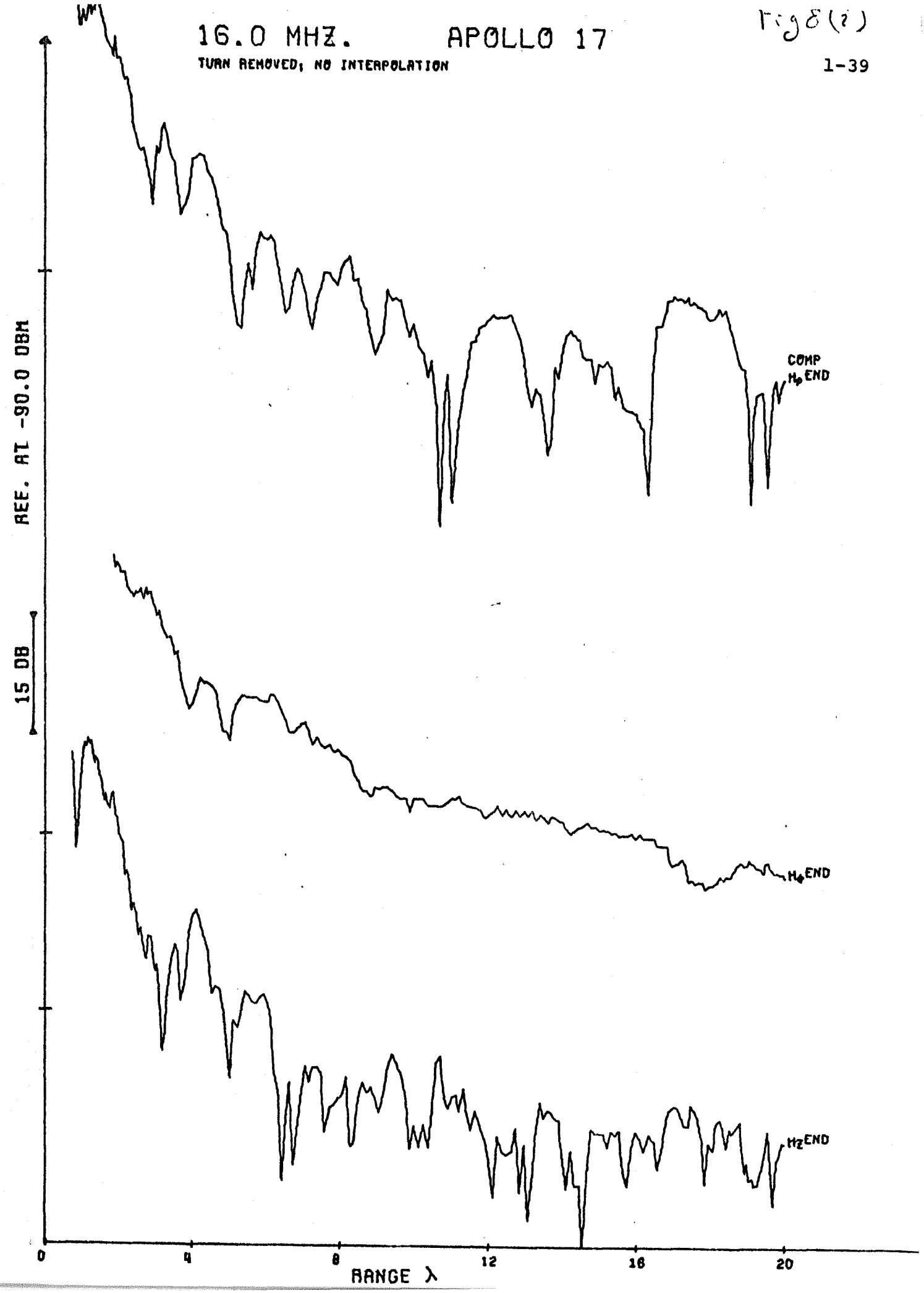

16.0 MHz. APOLLO 17

TURN REMOVED; NO INTERPOLATION

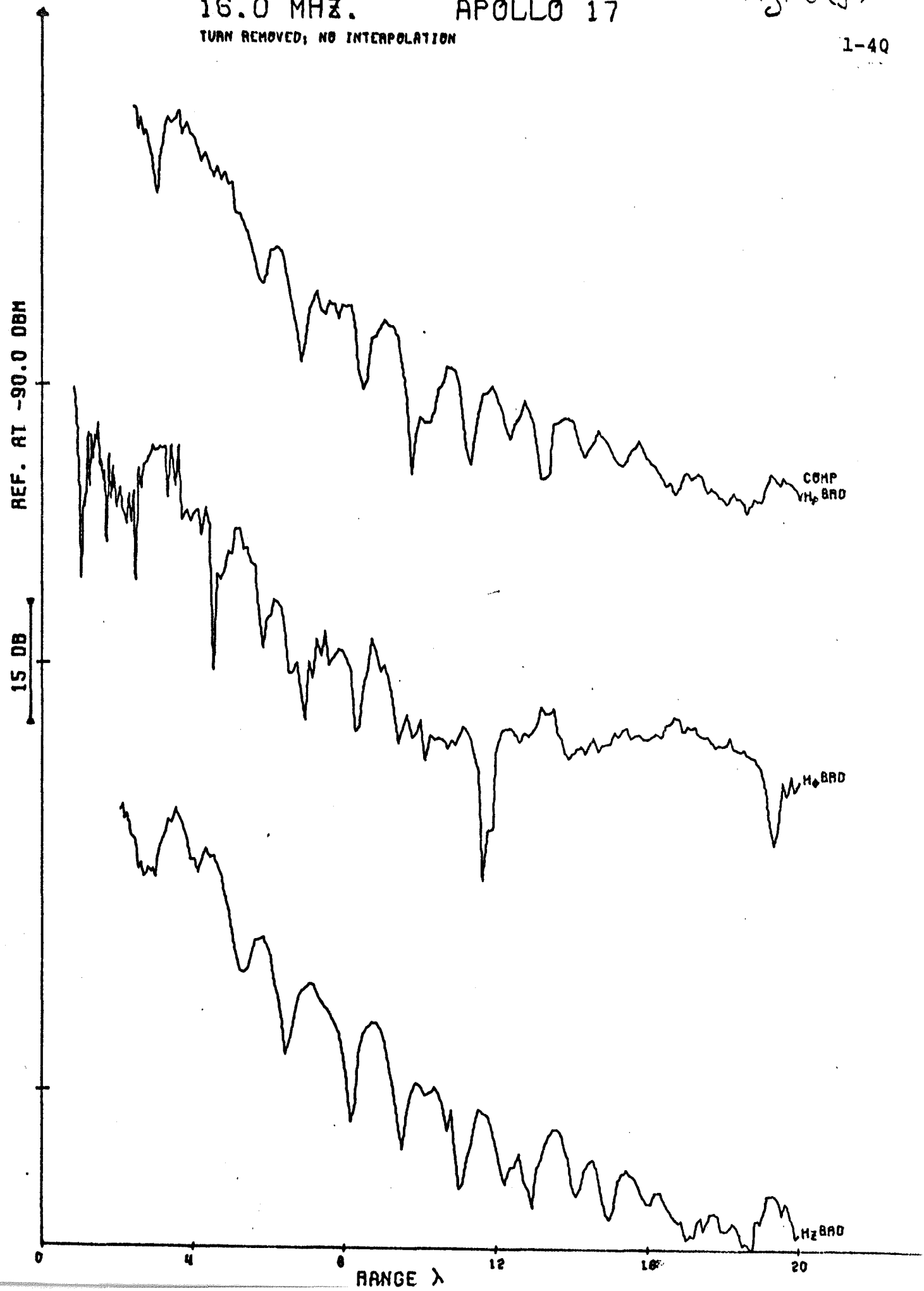

Fig. 8(J)

16.0 MHZ. APOLLO 17

TURN REMOVED; NO INTERPOLATION

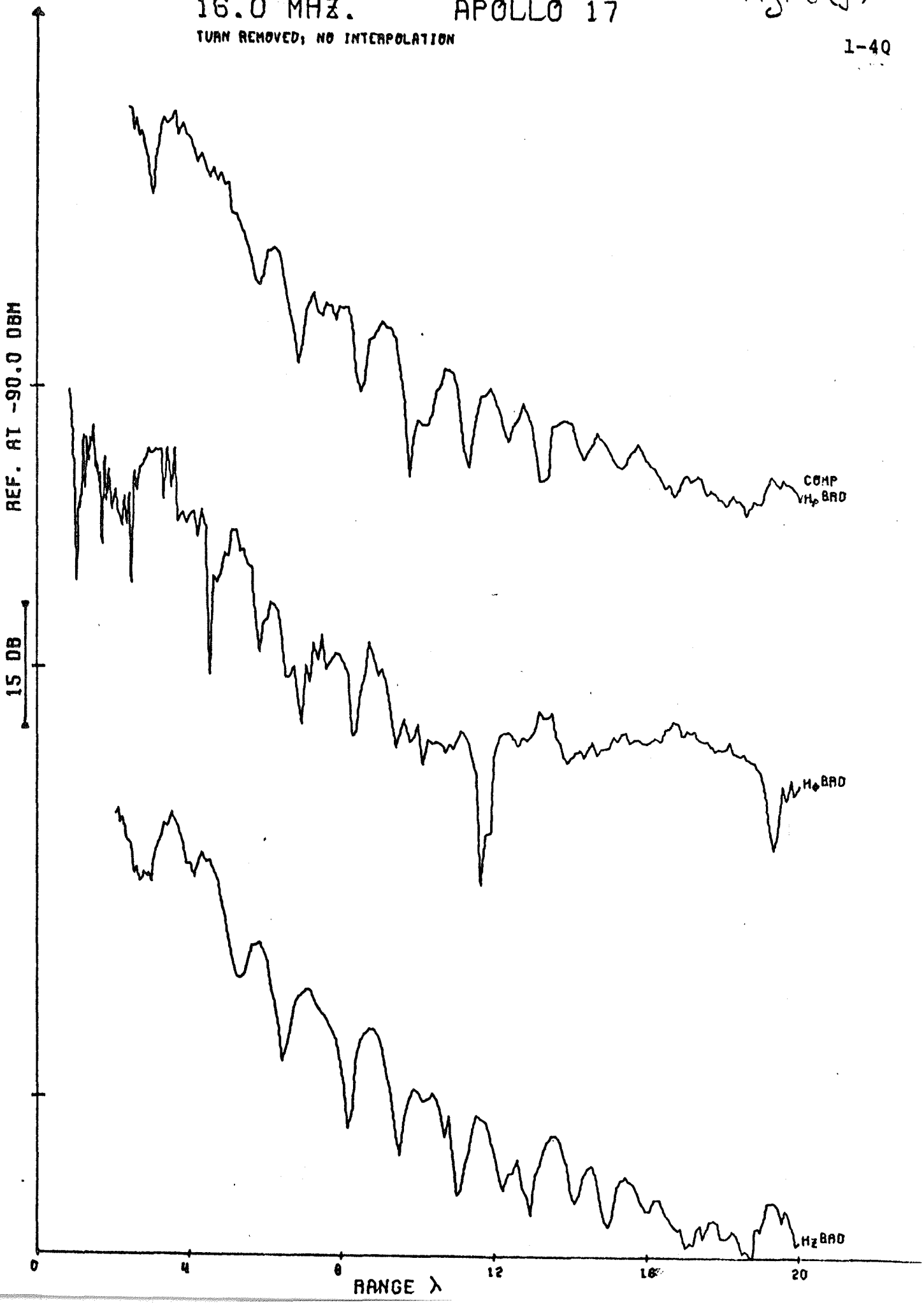

Fig 8 (k)

1-41

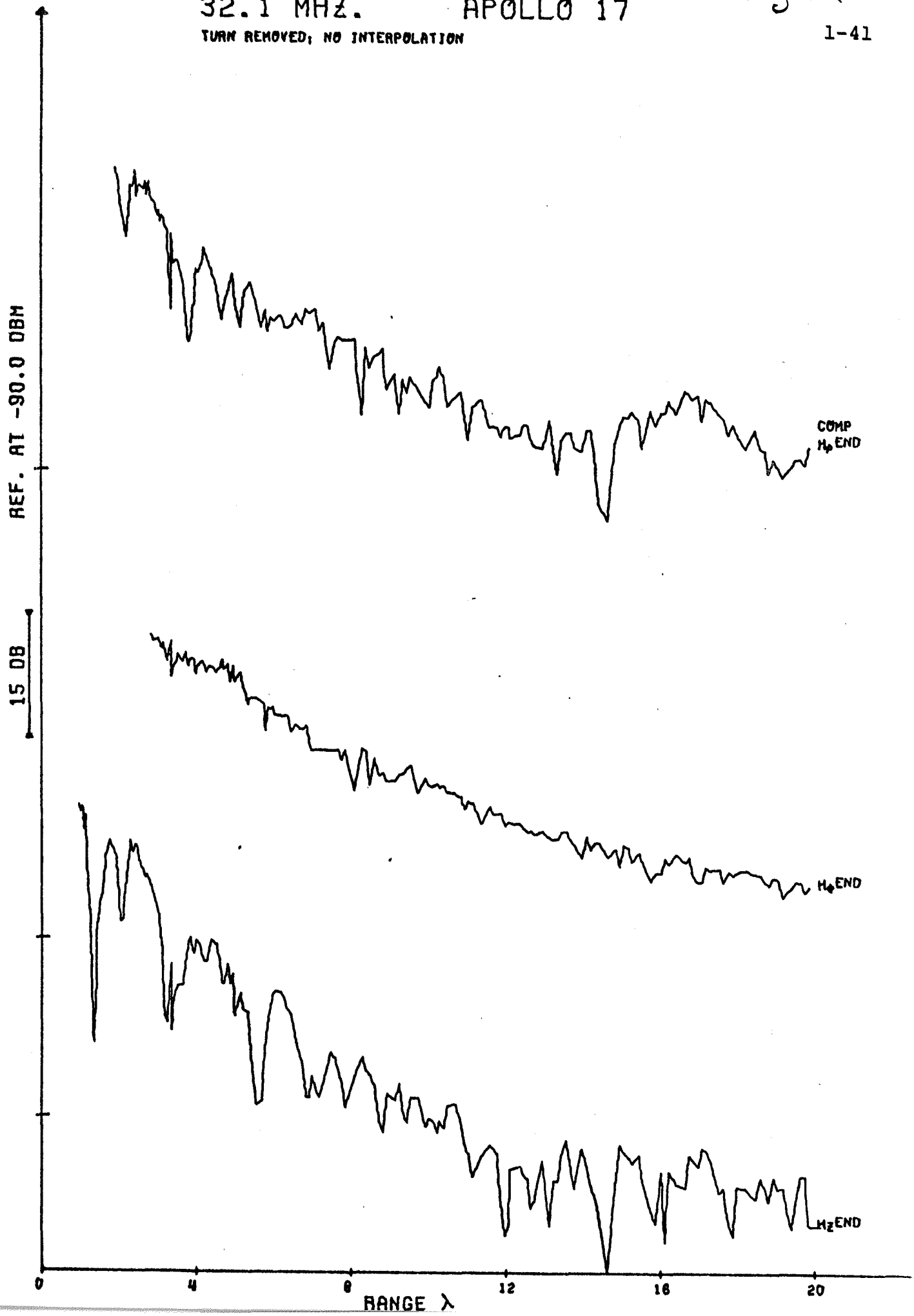
32.1 MHZ. APOLLO 17
TURN REMOVED; NO INTERPOLATION
REF. AT -90.0 DBM
15 DB
COMP
H_ϕ END
H_ϕ END
H_z END
0
4
8
12
16
20
RANGE λ

Fig 5(a)

32.1 MHZ. APOLLO 17

TURN REMOVED; NO INTERPOLATION

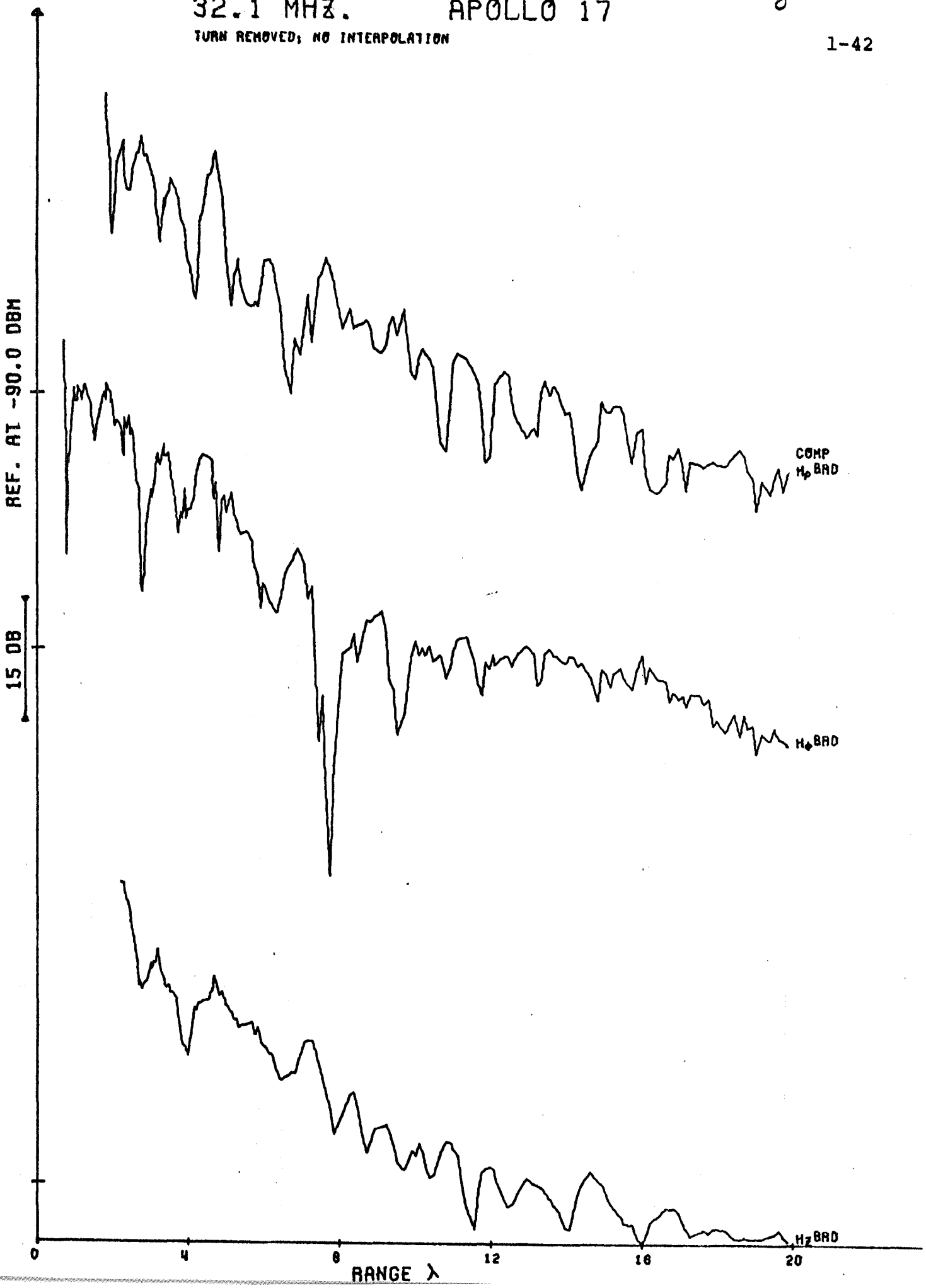

Fig 9(a)

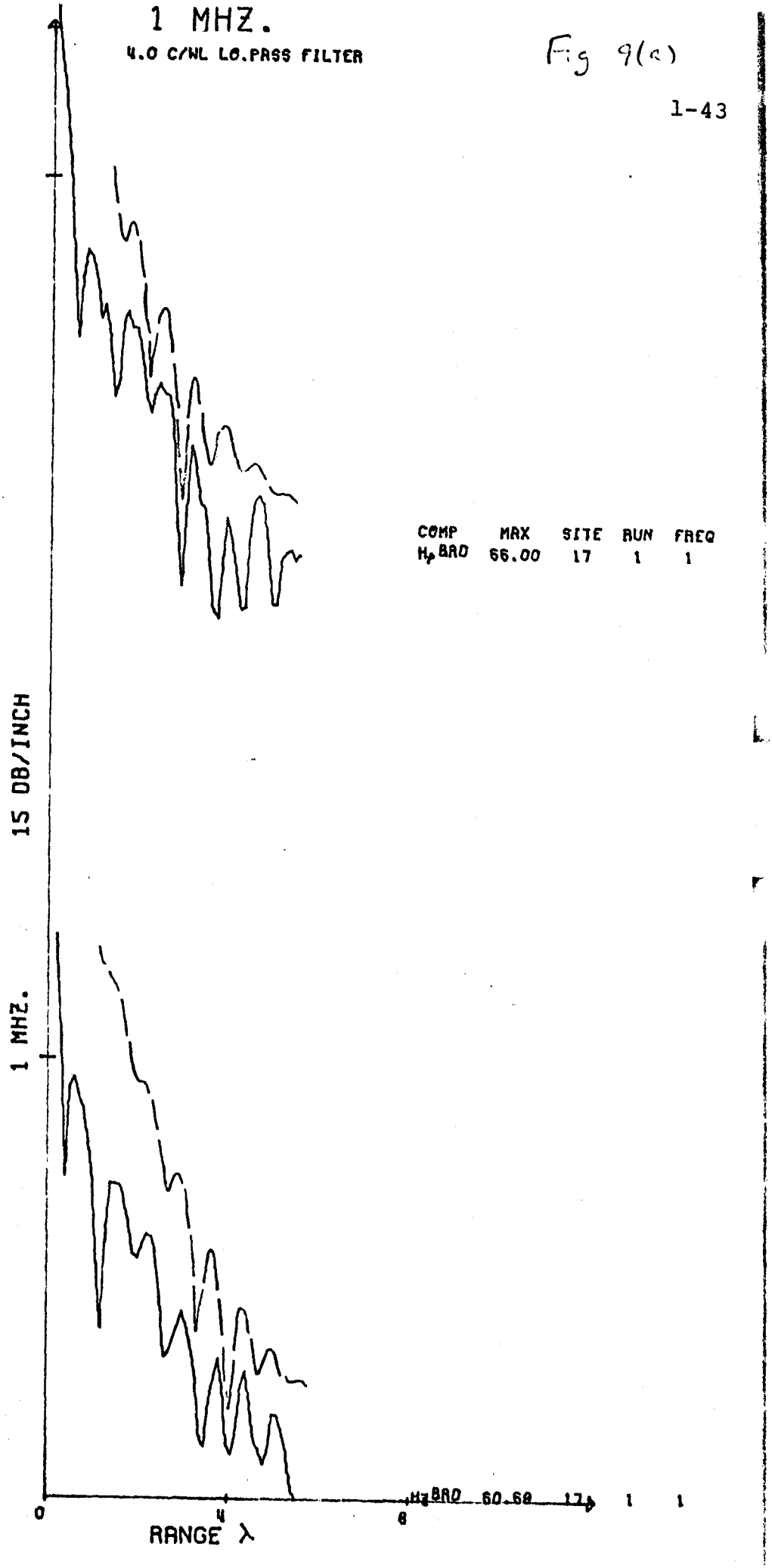
1 MHZ.
4.0 C/WL LO.PASS FILTER
COMP MAX SITE RUN FREQ
Hp BRD 66.00 17 1 1
15 DB/INCH
1 MHZ.
Hz BRD 60.60 17 1 1
0
4
8
RANGE λ

Fig 9(b)

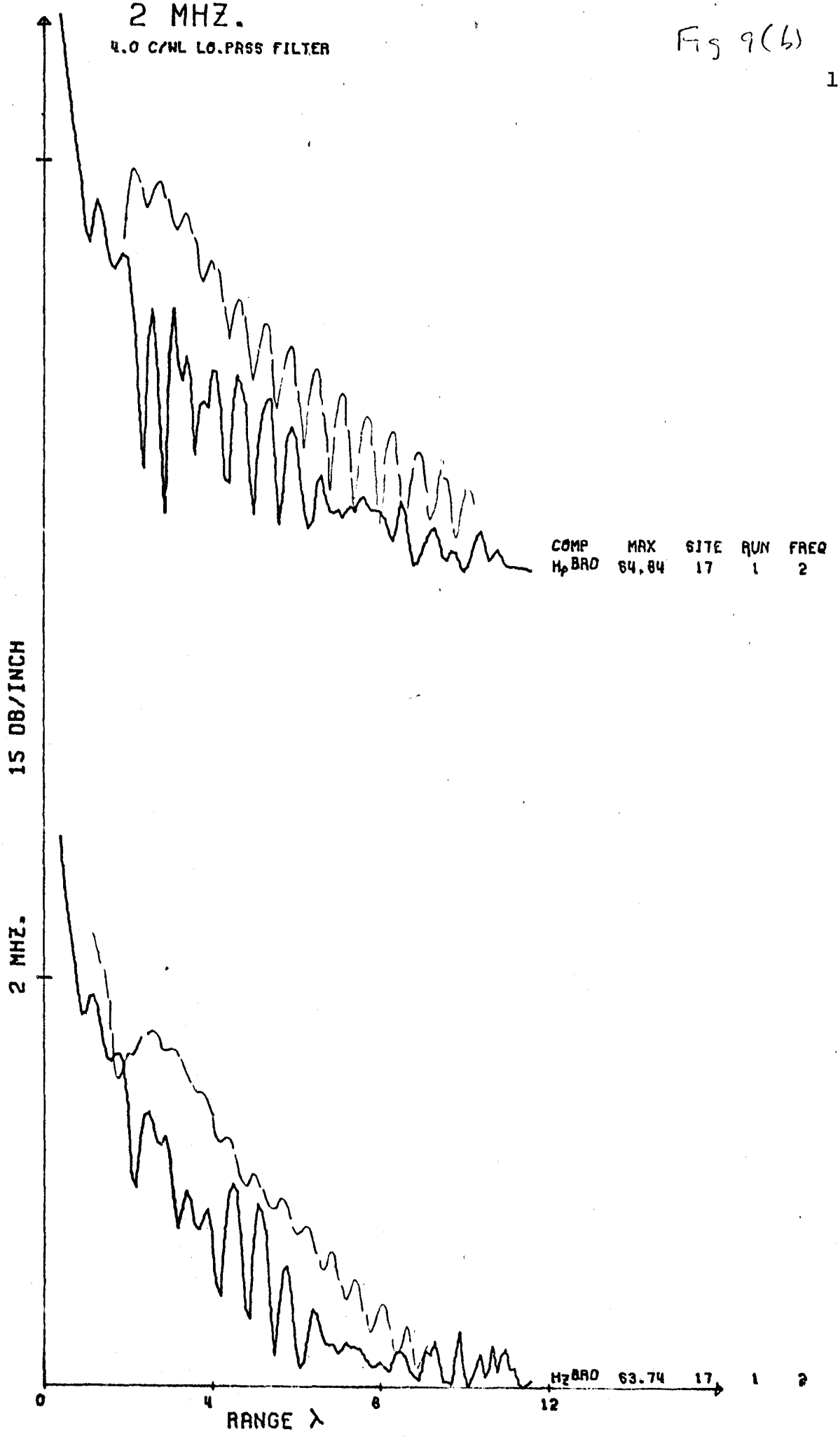
2 MHZ.
4.0 C/WL LO.PASS FILTER
COMP MAX SITE RUN FREQ
Hp BRD 64.84 17 1 2
15 DB/INCH
2 MHZ.
Hz BRD 63.74 17 1 2
0
4
8
12
RANGE λ

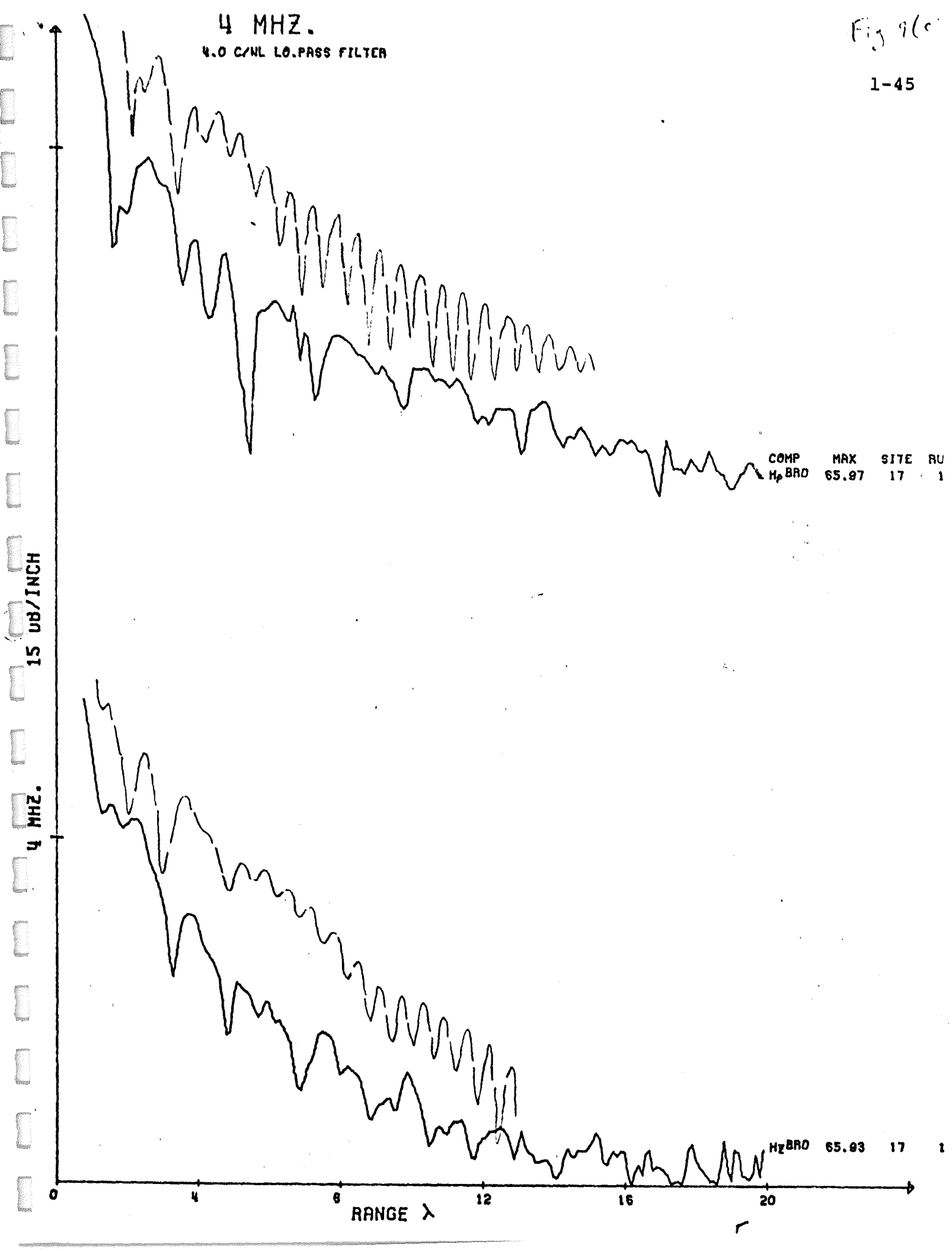
4 MHZ.
4.0 C/WL LO.PASS FILTER
COMP MAX SITE RU
Hφ BRD 65.97 17 1
15 UB/INCH
4 MHZ.
HZ BRD 65.93 17 1
0
4
8
12
16
20
RANGE λ

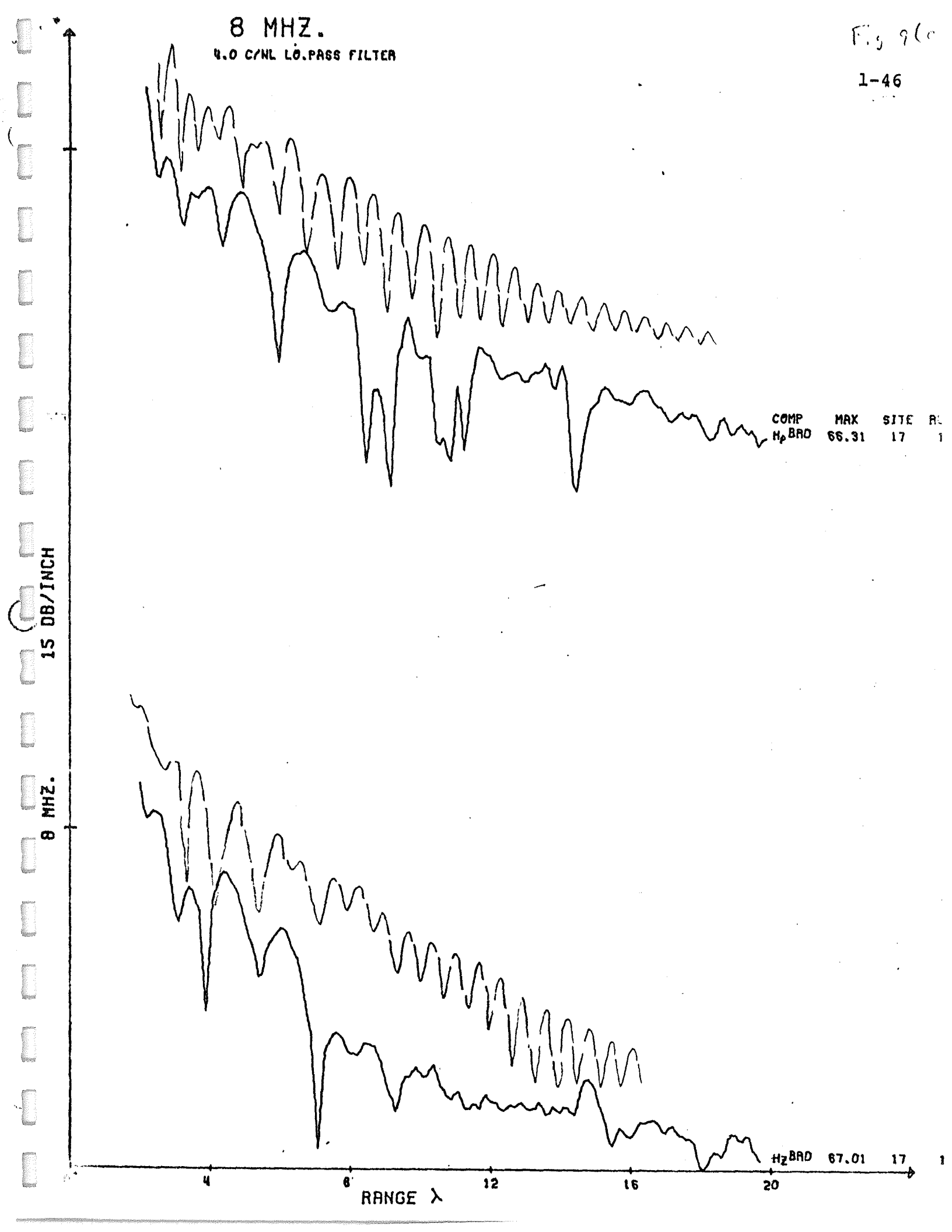
8 MHZ.
4.0 C/NL LO.PASS FILTER
COMP MAX SITE R
Hρ BAD 66.31 17 1
Hz BAD 67.01 17 1
15 DB/INCH
8 MHZ.
4
8
12
16
20
RANGE λ

Fig 9(c

1-46

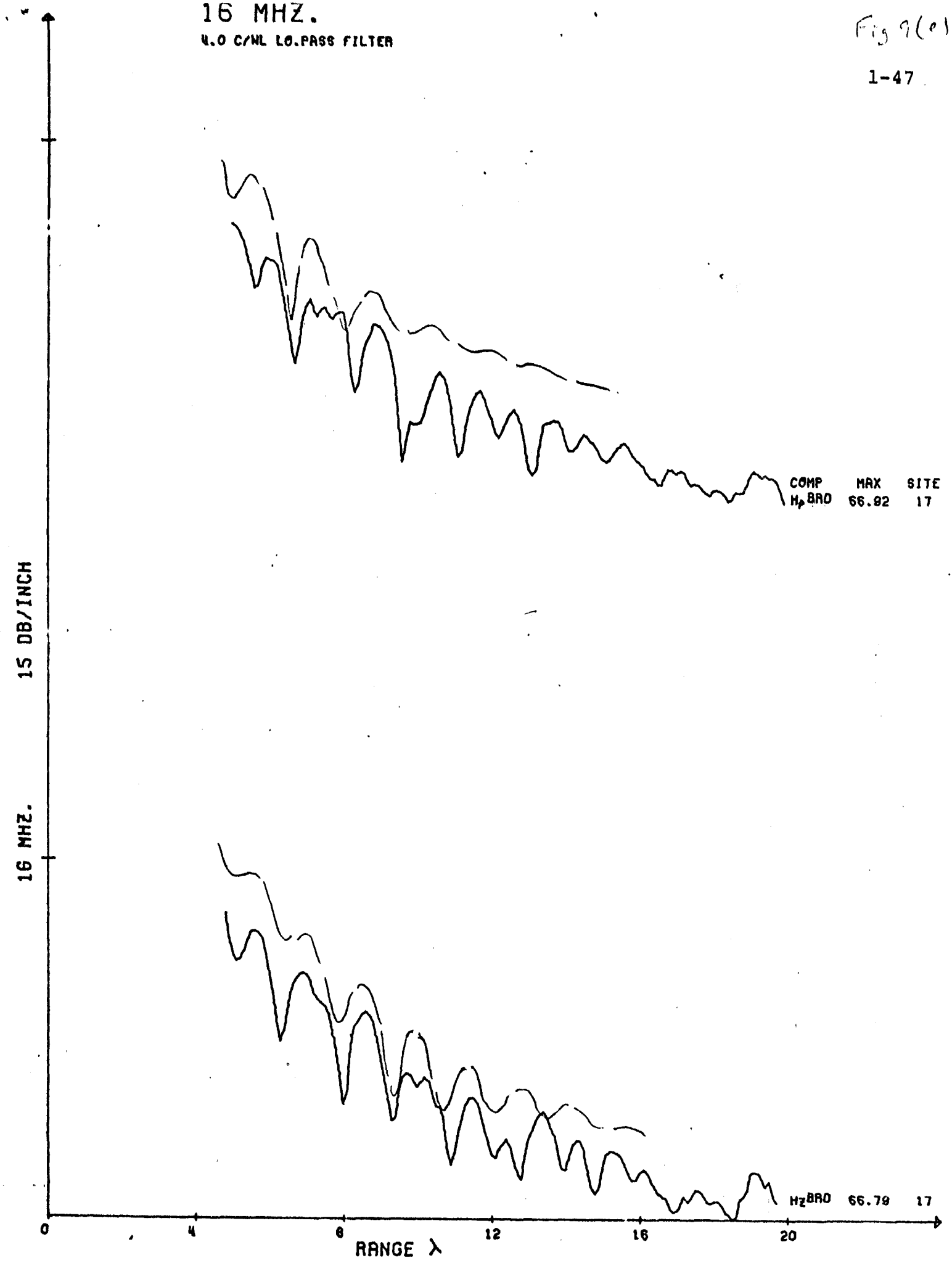
16 MHZ.
4.0 C/NL LO.PASS FILTER
15 DB/INCH
16 MHZ.
COMP MAX SITE
Hφ BRO 66.92 17
Hz BRO 66.79 17
0
4
8
12
16
20
RANGE λ

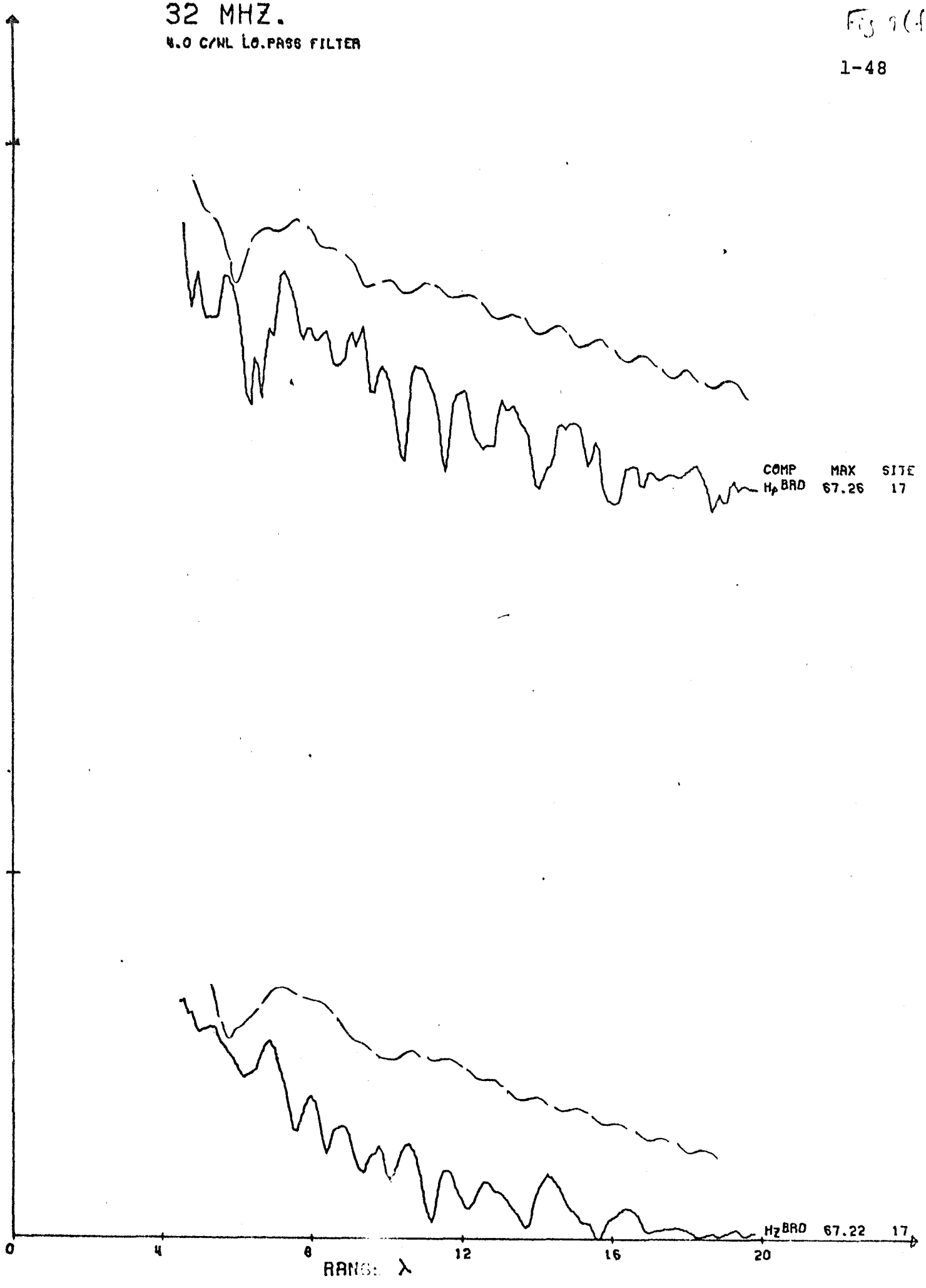
32 MHZ.
4.0 C/WL LO.PASS FILTER
COMP MAX SITE
Hρ BRD 67.26 17
Hz BRD 67.22 17
15 DB/INCH
32 MHZ.
0
4
8
12
16
20
RANGE λ

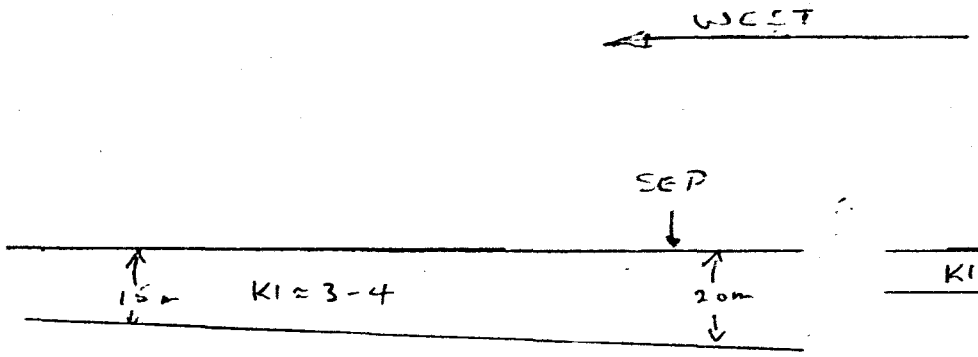

10 (a)

Sloping interface model.

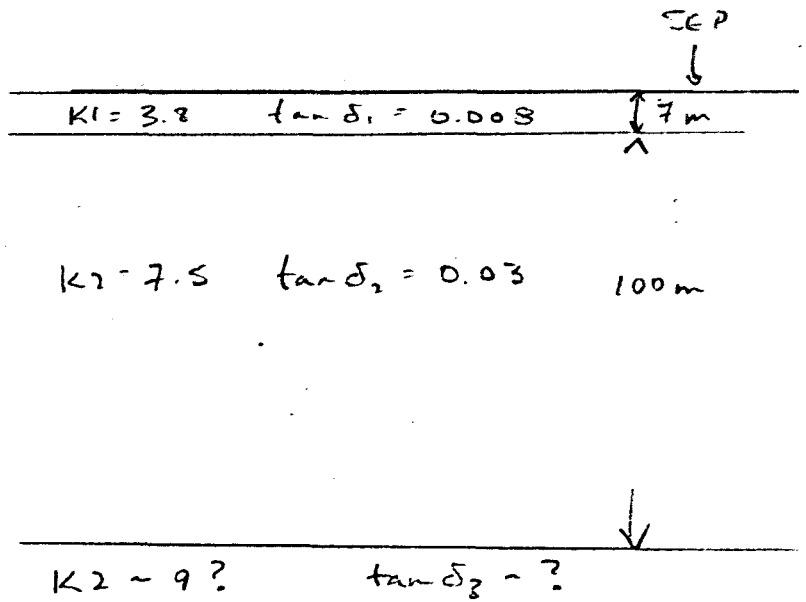

10 (b).

Three-layer model.

Fig 10.

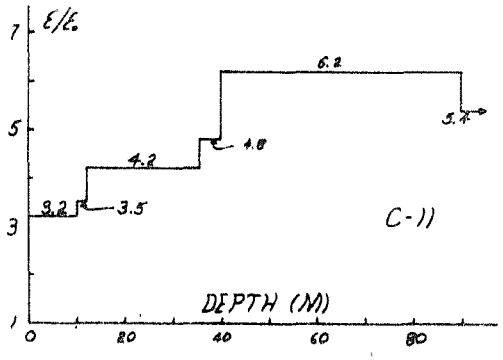
ε/ε₀
7
5
3
1
6.2
5.4
4.8
4.2
3.5
3.2
C-11
DEPTH (M)
0
20
40
60
80

Fig. 11

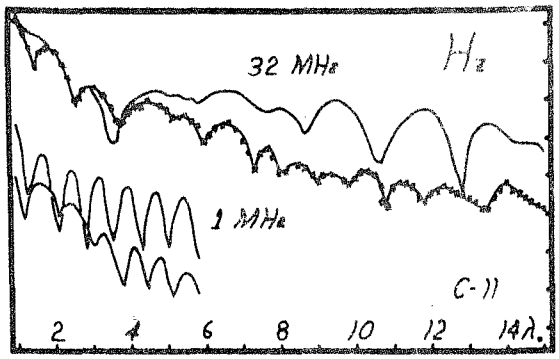
32 MHz
Hz
1 MHz
C-11
2
4
6
8
10
12
14λ.

Fig. 12

THE SURFACE ELECTRICAL PROPERTIES EXPERIMENT

GENE SIMMONS
Dept. of Earth and Planetary Sciences, MIT, Cambridge, Mass. 02139, U.S.A.

DAVID W. STRANGWAY
Geophysics Branch, NASA-Manned Spacecraft Center, Houston, Tex. 77058, U.S.A.

L. BANNISTER and R. BAKER
Laboratory for Space Experiments, Center for Space Research, MIT, Cambridge, Mass. 02139, U.S.A.

D. CUBLEY
Engineering and Development Directorate, NASA-Manned Spacecraft Center, Houston, Tex. 77058, U.S.A.

G. LATORRACA
Dept. of Earth and Planetary Sciences, MIT, Cambridge, Mass. 02139, U.S.A.

and

R. WATTS
Dept. of Physics, University of Toronto, Toronto, Canada, and Lunar Science Institute, Houston, Tex. 77058, U.S.A.

Abstract. The surface electrical properties experiment is presently planned for Apollo 17. It uses two orthogonal, electric dipole antennas laid on the surface, each 70 m long (tip-to-tip), to transmit at frequencies of 1, 2.1, 4, 8.1, 16 and 32.1 MHz. The signals are received by three mutually perpendicular coils mounted on the lunar Rover which traverses away from the transmitter. Information from the Rover navigation system is also recorded so that it will be possible to construct profiles at each frequency as a function of distance from the transmitter and for each transmitter and each receiving coil. Interferences between waves propagating just above and just below the surface will give a measure of the dielectric constant and loss tangent of the upper layer. Reflections from either layers or lateral inhomogeneities can also be detected and studied.

One version of the system has been constructed and tested on the Athabasca glacier. Analysis of the results shows that at 32 MHz, 16 MHz and 8 MHz scattering dominates the results suggesting that scattering bodies of 35 m or less in size are numerous. At 4 MHz, the ice was found to have a dielectric constant of about 3.3 and a loss tangent of 0.10, both values typical for ice. The depth of the ice was found to be around 265 m, a value typical for this glacier. At 2 MHz and 1 MHz the losses are much higher but the dielectric constant is still clearly determined as 3.3.

1. Introduction

In this paper we describe the general nature of the Surface Electrical Properties experiment now planned for the Apollo 17 mission. This experiment has been designed specifically to operate in the lunar environment where there is believed to be essentially no moisture present. Electromagnetic experiments on the Earth have a long history in the exploration for minerals, but because of the presence of moisture in the pore spaces in rocks resistivities greater than about 5×10^4 Ω-m are rare. The net result is that almost all work on the Earth has concentrated on using audio frequencies to get significant depths of penetration. The response parameter for electromagnetic waves is given as $(\varepsilon\mu\omega^2 + i\sigma\mu\omega)^{1/2}$ where

ε – dielectric constant – farads/m.
μ – magnetic permeability – henries/m.
ω – rotational frequency ($= 2\pi f$ – frequency in Hz)
σ – conductivity – mhos/m.

For most Earth applications $\sigma\mu\omega \gg \varepsilon\mu\omega^2$ so that the problem becomes entirely one of diffusion and no propagation takes place. In environments where the resistivity is very high, however, $\varepsilon\mu\omega^2 \gg \sigma\mu\omega$ and the problem becomes one of propagation with all the attendant phenomena of diffraction, interference, etc. Early attempts to penetrate the Earth at radio frequencies met with little success simply because the penetration depth (given by $\sqrt{(2/\sigma\mu\omega)}$ for the diffusive case and $(3 \times 10^8)/(\pi f\sqrt{K}\tan\delta)$ for the propagation case where $K =$ relative dielectric constant and $\tan\delta =$ loss tangent) was too small. In recent years, experiments on glaciers have shown that it is possible to get radio-frequency reflections from very great depths (Rinker and Mock, 1967; Harrison, 1970) and radar has been used to map the outline of salt domes (Unterberger *et al.*, 1970; Holster *et al.*, 1970). The reason for success in penetrating significant distances in these two media is that they both have very high resistivities, on the order of 10^{+6} Ω-m or more. Lunar soils and rocks have been shown to have very high values of resistivity and accordingly it would appear that the lunar environment is particularly suited to depth sounding using radio frequencies (Strangway, 1969; St. Amant and Strangway, 1970; Katsube and Collet, 1971; Chung *et al.*, 1971).

The properties of typical dielectrics have been reviewed by many workers but for those of interest to us, the dielectric constant ranges from about 3 for powders to about 10 for solids. Equally important is the general phenomenon that the loss tangent is nearly independent of frequency provided there are no relaxations. This was indeed found to be the case for the lunar samples (Katsube and Collet, 1971; Chung, 1972) so that the lunar materials behave precisely like those earth rocks which have no hydrous minerals (St. Amant and Strangway, 1970). The loss tangent may be converted to a variety of equivalent parameters. Since it is a measure of the imaginary part of the dielectric constant it is also a measure of the real part of the conductivity ($\tan\delta = K\omega\,\sigma_{app.}$). If there is a finite conductivity, however, this can be converted to an equivalent penetration depth ($\sqrt{(2/\sigma_{app.}\,\mu\omega)}$). For a frequency-independent loss tangent this relation is illustrated in Figure 1. Typically, the lunar rocks have values of $\sqrt{(K\tan\delta)}$ of about 0.05 to about 0.2 and the soils have values less by a factor of about 4 or 5 (see Table I). At 1 MHz the penetration depth in lunar materials is typically a few kilometers while at 30 MHz it is typically a few hundred meters.

The experimental results to be discussed in this paper were measured on glaciers which is almost the only environment on Earth in which a suitable analogue experiment can be conducted. The analogy is not perfect, since ice has a relaxation loss that occurs in the audio frequency part of the spectrum. The tail of this relaxation spectrum still affects the loss tangent in the range of frequencies of importance in the Surface Electrical Properties experiment with the result that the loss tangent decreases from 1 MHz to 32 MHz (Evans, 1965) in such a way that the product $f \cdot \tan\delta$ is approximately constant. The precise value is temperature-dependent but typically it has values of around 0.2 to

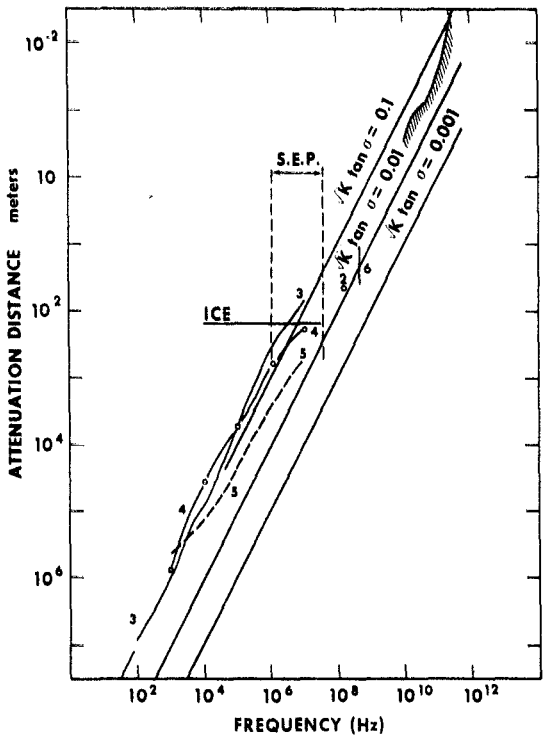

Fig. 1. Attenuation distance as a function of frequency from lunar samples and from remote lunar sensing.
Straight lines show theoretical values for typical dielectrics which have a loss tangent which is independent of frequency.
(1) Weaver (1965) – thermal emission and radar observations; (2) Tyler (1968) – bistatic radar; (3) Chung *et al.* (1971) – lunar igneous sample 12002; (4) Collett and Katsube (1971) – lunar breccia sample 10065; (5) Collett and Katsube (1971) – lunar fines sample 10084; (6) Gold *et al.* (1971) – lunar fines.

0.5. if the frequency, f, is given in MHz. This effect is illustrated schematically in Figure 1: the attenuation depth in ice is essentially frequency-independent with a value of a few hundred meters. Ice therefore, is not an optimum analogue for what we expect in the lunar case, but at least it is fairly transparent over part of the frequency range.

2. Experiment Concept

The concept of the SEP experiment is illustrated in Figure 2. An electric dipole transmitter is laid on the surface and transmits at six frequencies from 1 MHz to 32 MHz. Energy is propagated in three ways: (a) above the surface with the speed of light in vacuum, (b) below the surface along the interface with the velocity of light in the medium and (c) by reflection from layering or other inhomogeneities in the surface. These various waves interfere with each other as a function of position along the surface. Interference between the surface and subsurface wave gives a measure of the

TABLE I

Dielectric properties of lunar samples and of ice

		Rocks				Soil		
		10017	10065	12002	12002	10084	12070	Ice (near 0°C)
Dielectric constant	1 MHz	8.8	7.3	8.3	7.8	3.8	3.0	3.2
	10 MHz	9.3	7.3	8.3	8.8	3.8	3.0	3.2
	30 MHz	–	–	–	–	–	–	3.2
Loss tangent	1 MHz	0.075	0.063	0.051	0.056	0.0175	0.025	0.3
	10 MHz	0.021	0.019	0.0158	0.0114	0.0089	0.0053	0.03
	30 MHz	–	–	–	–	–	–	0.01

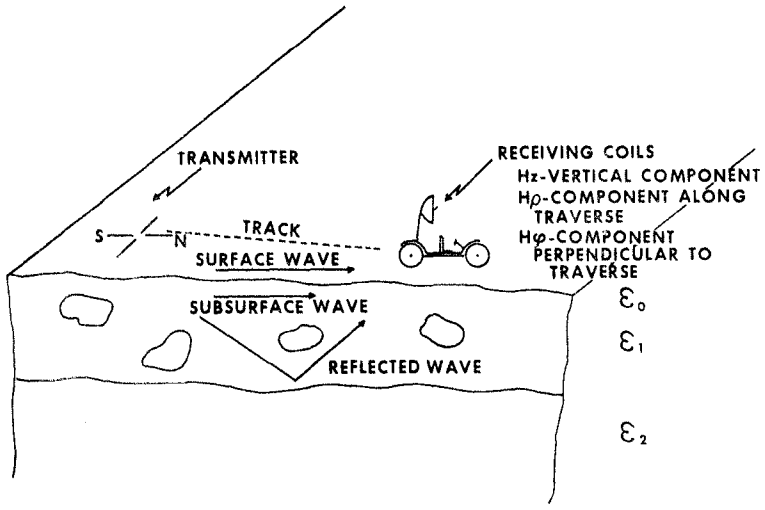

Fig. 2. Sketch illustrating operation of surface electrical properties experiment and various waves expected to be transmitted through and above lunar surface.

dielectric constant according to the formula $\varepsilon = (1 + \Delta K)^2$ where ΔK is the interference frequency. The rate of decay of the interferences gives a measure of the loss tangent. The receiver is mounted on the Rover and measures the field strength as a function of range so that the interference frequency can be measured. In addition, reflections from subsurface features can be detected as they interfere with the other waves. Transmission is done sequentially from a pair of orthogonal dipoles and the receiver consists of three orthogonal loops to measure the field strength of three independent components.

3. Instrumentation

Detailed descriptions of the experiment hardwave are planned for future papers so we will give only a brief description of the hardware in this section.

The transmitter is powered by solar cells and transmits sequentially at 1. 2.1, 4, 8.1, 16 and 32.1 MHz, each transmission at each frequency from one antenna lasting for 101.25 ms. The pair of orthogonal dipoles, each of which is 70 m long (tip-to-tip), are powered alternately. These dipoles are half-wave dipoles at 2.1, 4, 8.1, 16 and 32.1 MHz. A pair of wires is used for the experiment and a set of traps and supressors are built into the wires such that the transmitter 'sees' a half-wave resonant dipole at each of the frequencies. At 1 MHz the antenna is not a half-wave dipole but loading is used to compensate this. Precise matching of the antenna impedance with that of the Moon is difficult because of our ignorance of the exact value of the dielectric constant but we have designed the antenna for a value of 3.3 which is consistent with the bistatic radar results of Howard and Tyler (1972). On the ice, the antenna can be adjusted to make the antenna optimum at each frequency. The power radiated is 3.75 W at 1 MHz and 2.0 W at the other frequencies. The transmission sequence is shown in Figure 3 and provides about 10 samples per wavelength per component at 2.1, 4, 8.1, 16 and 32.1 MHz and 20 samples per wavelength per component at 1 MHz at a vehicle speed of 8 km h^{-1}.

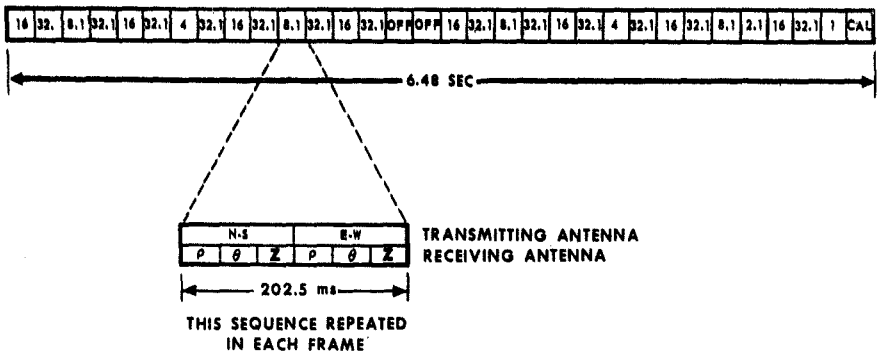

Fig. 3. Format: two frames marked OFF are used to monitor the background external noise at all frequencies and to measure the internal noise. The frame marked cal. is used for synchronizing transmitter and receiver and to record the internal temperature of the receiver.

The receiving antenna consists of three orthogonal coils which are mounted on the Rover. The reception of each coil is examined for 33 ms and in sequence. The signals are demodulated in the receiver and are frequency-coded by a voltage controlled oscillator. This oscillator operates over the frequency range of 300 to 3000 Hz, corresponding to a dynamic range in the instrument of -35 dbm to -135 dbm. This large dynamic range allows accurate field strength recording over a broad distance range from the transmitter. The output of the voltage-controlled oscillator is recorded on a recoverable tape recorder. With six transmission frequencies, two alternate transmitting antennas and three receiving antennas we record a total of 36 separate pieces of information.

In the lunar system, navigation data will be recorded in two different ways. On each

wheel there is a pulse generated every 0.245 m. We will record every second pulse from two separate wheels, for redundancy and as a check on wheel slippage. This means that the traverse can be reconstructed in increments of about 0.5 m. These same wheel pulses and a gyro-stabilized compass provide the basic input to the Rover navigation computer which displays range, bearing, heading, and distance travelled. The bearing and heading are computed in increments of 1° and the range and distance travelled are computed in increments of 100 meters. We will record the bearing every time it changes by ±1° (except in the immediate vicinity of the LM) and as a redundant check we will record the range in 100 m increments. The range is computed using the third slowest wheel, so we will have a separate measure of the wheel slip and an internal range check at 100 m increments. Finally, since there may be errors that will accumulate in both the range and bearing measurements we will use the known stop points to correct the traverse. Since these stops are likely to be in increments of one or two kilometers, we will have frequent updates to our traverse map. On the basis of this information we expect to be able to reconstruct the traverse to an accuracy of about 1% of the range and to reconstruct range *differences* over a few hundred meters to about 1 m or better.

For the glacier tests, we have used a simple odometer circuit connected to one of the drive-wheels which generates signals every 1.5 m. These signals are recorded independently on the tape recorder. These pulses have been used to determine the horizontal scale so that all the data discussed in this report have been plotted as field strength versus range.

4. Theoretical Work

We are reporting elsewhere the theory behind this experiment (Annan, 1972; Cooper, 1972; Sinha, 1972a, b, c) and have published a paper on some of the most preliminary glacier results, (Rossiter *et al.*, 1972). We will not, therefore, review all these results in the present paper. Rather we will only summarize a few points which are pertinent to the data analysis.

The transmitting antennas are crossed dipoles; in the simplest case the traverses are run broadside to one dipole and off the end of the other. The geometry is shown in Figure 2. The fields H_z and H_ϱ from the broadside antenna are both maximum-coupled and can be expected to show the interference patterns which are the basis of the experiment. Studies of the antenna patterns for these components show that the power above the surface is comparable to the power just below the surface so that significant interference between these two waves can be expected. In the case of the H_ϕ component off the end of the transmitter, however, power is transmitted above the surface but very little power is transmitted just below the surface. There is little interference, so this component is not as useful for determining the dielectric constant and loss tangent.

The other components (H_ϕ and H_ϱ broadside and H_z endfire) are minimum-coupled to the respective transmitters. These components are consequently useful in looking for energy scattered by either surface irregularities or subsurface inhomogeneities.

The radiation pattern of a electric field dipole at the interface between free space and

a semi-infinite dielectric medium contains a single lobe broadside of the antenna and two lobes endfire of the antenna as shown by Cooper (1972). The broadside or Transverse Electric (TE) radiation pattern and the endfire or Transverse Magnetic (TM) radiation pattern are illustrated in Figure 4 for a dipole over ice. The dipole is colinear with the X-axis in Cartesian coordinates. The angle between the vertical and the peak of the lobe is given by $\sin \beta = \sqrt{(\varepsilon_0/\varepsilon_1)}$ where ε_0 is the dielectric constant of free space

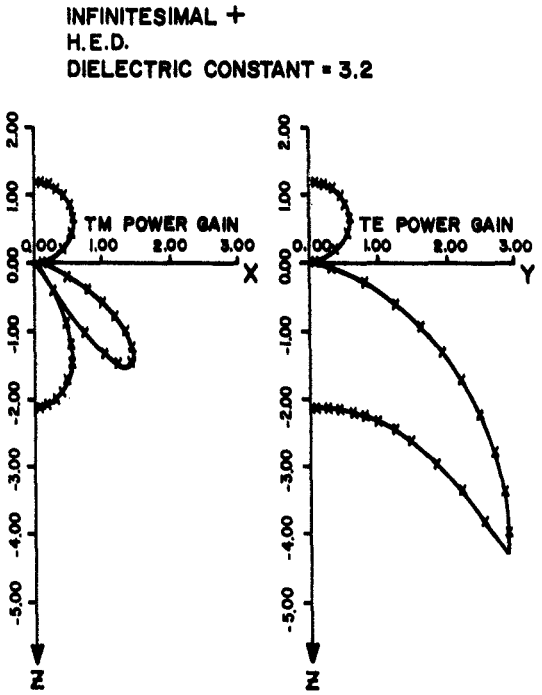

Fig. 4. Radiation pattern of horizontal electric dipole over ice. The dipole extends along the x-axis.

and ε_1 is the dielectric constant of the medium. In the case of ice where the ratio $\varepsilon_0/\varepsilon_1$ is given by 1/3.2 this angle is about 34°. The energy radiated downwards into the medium does not appear at the surface unless there is a reflecting horizon at depth. The presence of a horizontal reflector at depth d causes energy to appear at the surface at a distance $r \approx 2d \tan \beta$. For ice the depth to a reflector is given as $d = 0.8\ r$. In principle it is therefore possible to determine the dielectric constant and the loss tangent from the near-field interferences of the H_ϱ and H_z components from the broadside antenna. Reflections can be studied by the H_ϱ and H_z components from the broadside antenna and by the H_ϕ component from the endfire antenna.

5. Athabasca Glacier Data

Most of our work to data has been concentrated on the Athabasca glacier in westner

Canada (Figure 5a). It is a well-studied glacier and is very accessible. Previous studies based on gravity (Kanasewich, 1963), seismology and drilling (Paterson and Savage, 1963), and electrical sounding (Keller and Frischknecht, 1961) have been made and a map of approximate ice thickness is shown in Figure 5b. We have reported on earlier preliminary results (Rossiter *et al.*, 1972) and in this paper restrict ourselves to one set of data taken in the summer of 1971 with the evaluation model of the flight equipment which was described in this report. The profile discussed is shown in Figure 5b and is marked by the transmitter at the southern end. The ice thickness is approximately

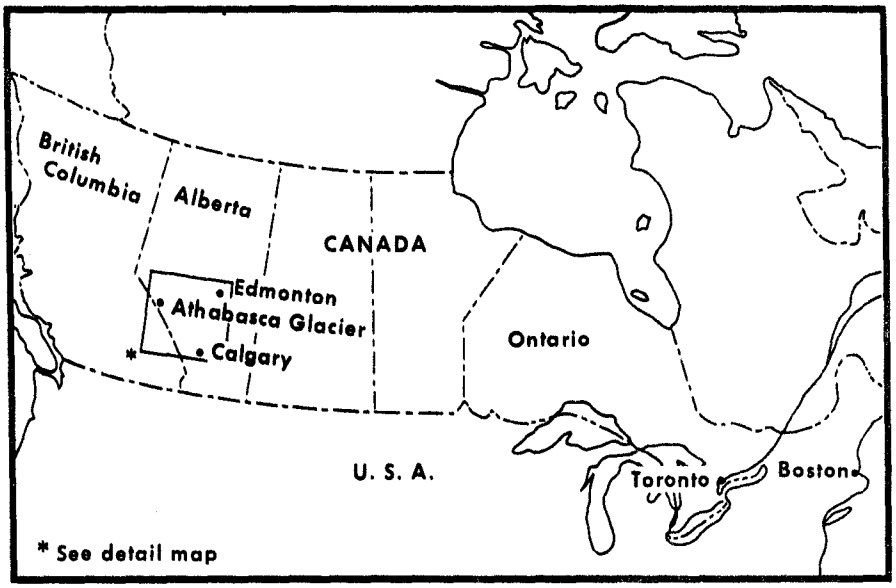

GENERAL LOCATION MAP

Figs. 5a–b. (a) Location map of the Athabasca glacier. (b) Sketch map of the Athabasca glacier, showing the location of the profile discussed in this report. Contours are the generalized thicknesses as determined from previous drilling and seismic studies.

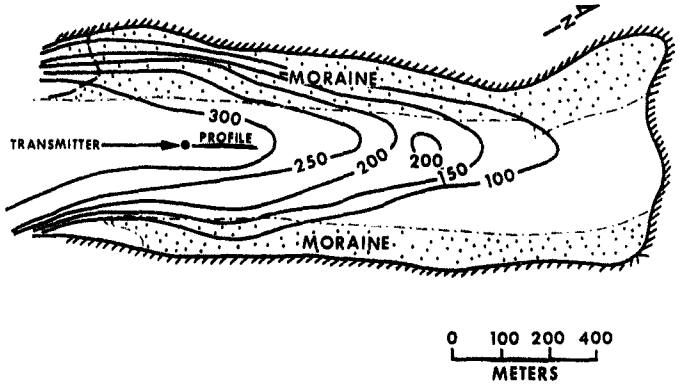

Fig. 5b.

300 m. The line was run from north to south and then repeated south to north with identical results.

The field strength data for all components at 4 MHz are shown in Figure 6 plotted as a logarithm of the power versus the distance in wavelengths. The length of the traverse was about seven wavelengths. Of particular interest and typical of all our runs at 4, 2 and 1 MHz is the fact that H_z and H_ϱ from the broadside antenna and H_ϕ from the endfire antenna are large and fairly smoothey varying functions. In particular the H_ϕ endfire component is quite smooth showing no surface and subsurface wave interference. H_z broadside, however, shows sharp nulls at about $1\text{-}\frac{1}{2}\lambda$, $2\text{-}\frac{1}{2}\lambda$

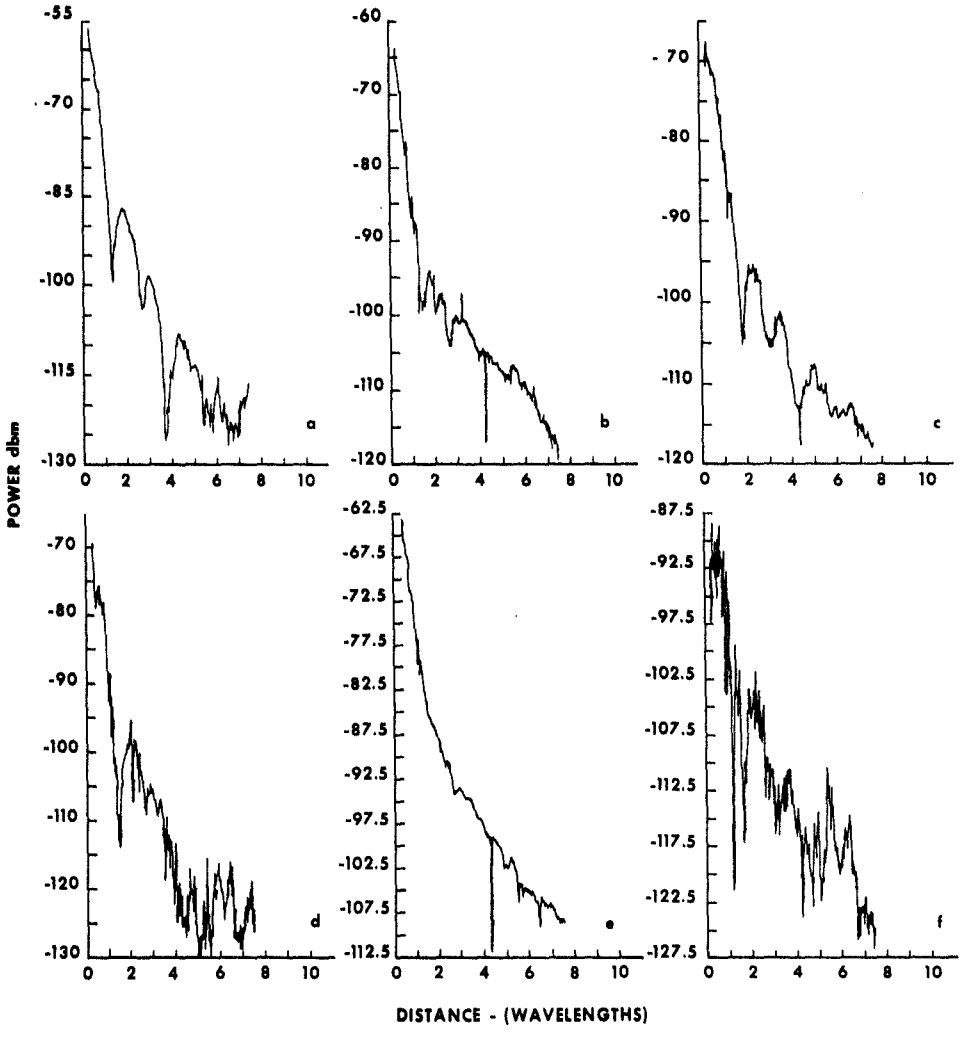

Fig. 6. Complete set of data at 4 MHz showing H_ϱ, H_ϕ and H_z from both the E-W (broadside) and the N-S (endfire) antenna. (a) E-W transmitter, H_z; (b) E-W transmitter, H_ϕ; (c) E-W transmitter, H_ϱ; (d) N-S transmitter, H_z, (e) N-S transmitter; H_ϕ; (f) N-S transmitter, H_ϱ.

and 3-$\frac{1}{2}\lambda$. These nulls are the interferences generated from the surface and subsurface waves as shown in Figure 7. Using the 4 MHz data, comparison with theoretical curves leads to a dielectric constant of about 3.3 and a loss tangent of 0.10.

Evidence in this particular subset of the data for reflected energy is not very strong but the simple curve is clearly disturbed at a distance of about 5 wavelengths from the source. We have compared this curve to a variety of theoretical curves and it appears that a depth of about 3.5 wavelengths for a reflector is indicated as shown in Figure 7b. This fact suggests a depth to the bottom of the ice of around 265 m. This depth is somewhat less than the predicted depth of about 300 m but the agreement is relatively good and it is possible that the ice thickness varies locally.

The other components are generally weaker and show very little character. This relation is to be expected for the minimum-coupled components and suggests that scattering at 4MHz (75 m) is minimal. At higher frequencies scattering becomes more significant and at 32 MHz and at 16 MHz the main structure is that due to scattering.

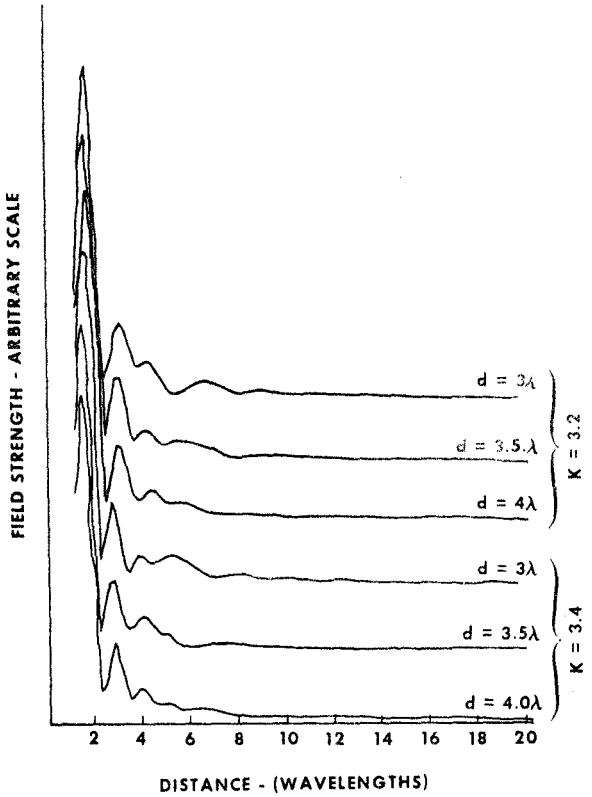

Figs. 7a–b. H_z component from E-W antenna. (a) theoretical curves showing effect of varying depth to the reflector and dielectric constant with a constant loss tangent of 0.10. (b) field data and theoretical curves showing effect of varying loss tangent and dielectric constant for a constant depth of 3.5 wavelengths.

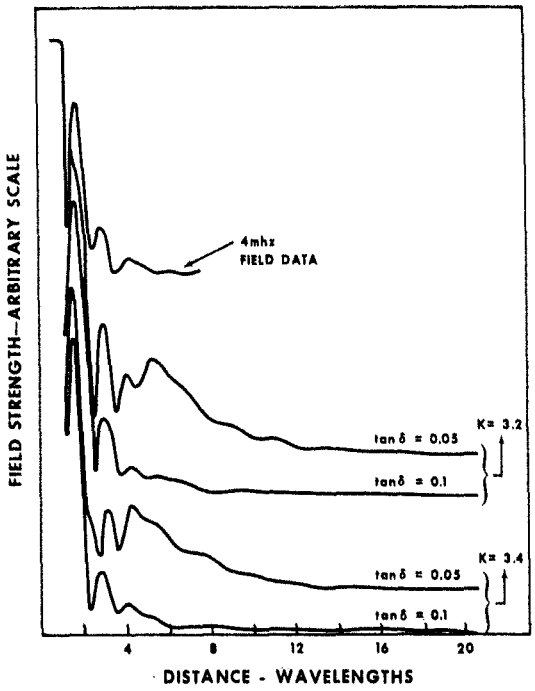

Fig. 7b.

In Figure 8 a set of data for all three components from the E-W transmitting antenna at 16 MHz is shown. The features to note in this plot are twofold. First, all components are about equal suggesting that as much energy is scattered into the minimum-coupled H_ϕ component as is present in the maximum-coupled H_ϱ and H_z components. Second is the erratic behaviour of the field components, which show a wide range of rapid variations on a scale that is smaller than a wavelength. We conclude therefore that scattering is a dominant process at 16 MHz, important at 8 MHz and relatively unimportant at 4 MHz. This observation suggests that the size of scatterers is typically about equal to the wavelength at 8 MHz which is about 35 m.

This result seems reasonable because this valley glacier is heavily crevassed and the typical size for the vertical and lateral extent of crevasses could be typically 30 m. These results are comparable to those of Gudmandsen and Christensen (1968) who had trouble doing airborne radio sounding at 35 MHz over valley glaciers in West Greenland. They attribute at least part of their difficulties to the presence of crevasses in the valley glaciers.

6. Conclusions

The radio frequency interference technique developed for the Apollo lunar program will be useful for measuring the dielectric constant and loss tangent of the upper layers of the moon in the frequency range from 1 MHz to 32 MHz. It will also be useful for

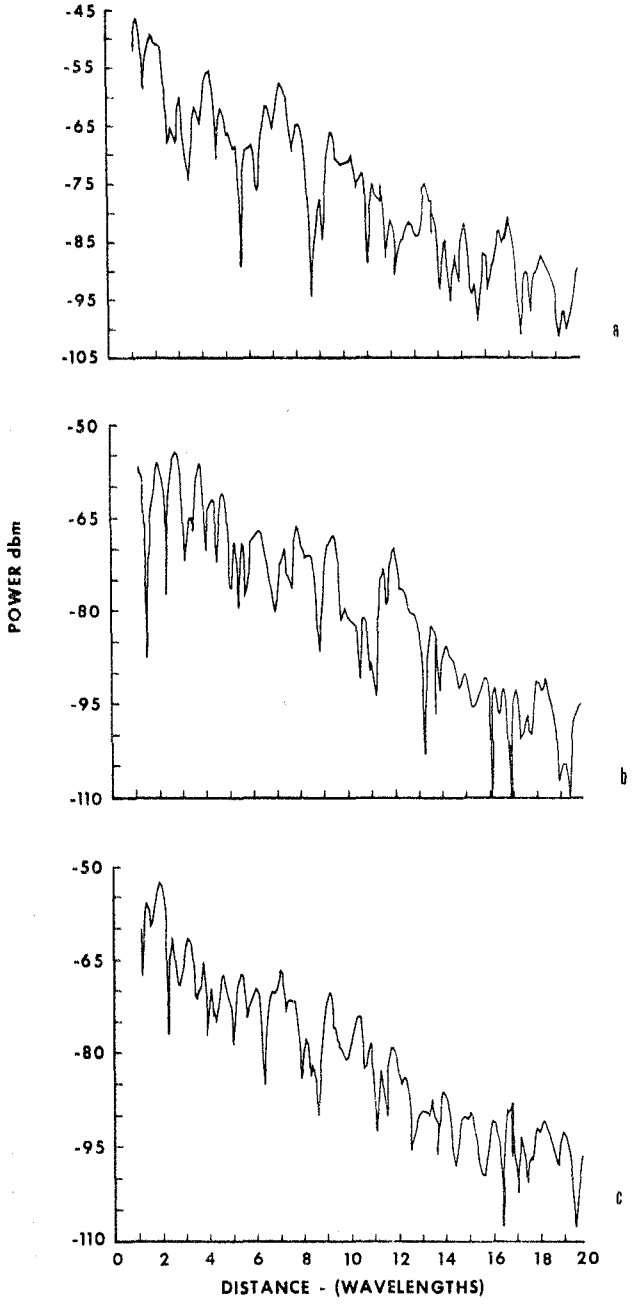

Fig. 8. Typical set of data taken at 16 MHz to illustrate scattering effect of glacier. All components H_z, H_ϕ and H_ϱ from the E-W transmitter are about equal.

detecting layering in the range from a few tens of meters to a few kilometers depending on the nature of the layers and of the electrical properties. In addition, it is likely to yield information on the presence of scattering bodies. This experiment has been tested on the Athabasca glacier. Here it was possible to measure the dielectric constant of ice as 3.3 and the loss tangent at 4 MHz as 0.10 giving a value of 0.4 for $f \cdot \tan \delta$. The depth of the ice was estinated to be about 265 m, a value in rough agreement with other determinations.

Acknowledgements

We would like to acknowledge permission from the Jasper National Park authorities to work on the Athabasca glacier.

This work was conducted under NASA Contract No. NAS 9-11540 at MIT and under a subcontract at the University of Toronto.

References

Annan, A. P.: 1970, Master of Science thesis, Department of Physics, University of Toronto.

Annan, A. P.: 1972, *Geophysics*, submitted for publication.

Chung, D. H.: 1972, this volume, p. 276.

Chung, D. H., Westphal, W. B., and Simmons, Gene: 1971, *Proceedings of the Second Lunar Science Conference* **3**, pp. 2381–90, MIT Press, Cambridge, Mass.

Cooper, William W.: 1972, 'TE/TM Patterns of Hertzian Dipole in Two- or Three-Layered Medium', submitted for publication.

Evans, S.: 1965, *J. Glaciol.* **5**, 773–92.

Gudmandsen, P. and Lintz Christensen, E.: 1968, 'Radioglaciology', interim report for EGIG of measurements in Greenland, May 1968, Laboratory of Electromagnetic Theory, The Technical University of Denmark, Lyngby, D 77.

Harrison, C. H.: 1970, *Geophysics* **35**, 1099–1115.

Holser, W. T., Brown, R. J. S., Roberts, F. A., Fredriksson, O. A., and Unterberger, R. R.: 1970, 'Radio Frequency Propagation in Salt Domes 2. Pulse Reflections from Salt Flanks', presented at SEG 40th Annual International Meeting, New Orleans.

Howard, H. L. and Tyler, G. L.: 'Bastatic-Radar Investigation', Apollo 15 Preliminary Science Report, NASA SP 289, 1972.

Kanasewich, E. R.: 1963, *J. Glaciol.* **4**, 617–31.

Katsube, T. J. and Collett, L. S.: 1971, *Proceedings of the Second Lunar Science Conference*, Vol. **3**, pp. 2367–79, MIT Press, Cambridge, Mass.

Keller, G. V. and Frischknecht, F. C.: 1961, in G. O. Raasch (ed.), *Geology of the Arctic* **2** (International Symposium), Toronto, University of Toronto, pp. 809–32.

Paterson, W. S. B. and Savage, J. C.: 1963, *J. Geophys. Res.* **68**, 4513–20.

Rinker, J. N. and Mock, S. J.: 1967, 'Radar Ice Thickness Profiles, Northwest Greenland', Special Report 103, U.S. Army Materiel Command, Cold Regions Research & Engineering Lab., Hanover, New Hampshire.

Rossiter, J. R., Annan, A. P., LaTorraca, G. A., Strangway, D. W. and Simmons, G.: 1972, 'Radio Interferometry Depth Sounding, Part II – Experimental Results', submitted for publication.

Saint-Amant, M. and Strangway, David W.: 1970, *Geophysics* **35**, 624–45.

Sinha, Ajit K.: 1972a, 'Fields from a Horizontal Electric Dipole over a Lossy Dielectric Medium and Its Applications in the Radio-Interferometry Method, Part I – The Half-Space,' submitted for publication.

Sinha, Ajit K.: 1972b, 'Fields from a Horizontal Electric Dipole over a Lossy Dielectric Medium and Its Application in the Radio-Interferometry Method, Part II – Layer over a Perfect Reflector', submitted for publication.

GEOPHYSICS, VOL. 37, NO. 6 (DECEMBER 1972), P. 985-996, 1 FIG.

ELECTROMAGNETIC FIELDS DUE TO DIPOLE ANTENNAS OVER STRATIFIED ANISOTROPIC MEDIA†

J. A. KONG*

Solutions to the problem of radiation of dipole antennas in the presence of a stratified anisotropic media are facilitated by decomposing a general wave field into transverse magnetic (TM) and transverse electric (TE) modes. Employing the propagation matrices, wave amplitudes in any region are related to those in any other regions. The reflection coefficients, which embed all the information about the geometrical configuration and the physical constituents of the medium, are obtained in closed form. In view of the general formulation, various special cases are discussed.

INTRODUCTION

The problem of radiation of a dipole source in the presence of stratified media has been studied extensively with application to geophysical exploration. An excellent review on the half-space case is contained in the book by Sommerfeld (1949) and in the monograph by Baños (1966). Propagation and radiation in stratified media are treated by Wait (1970) and Ward (1967). Wolf (1946) and Bhattacharya (1963) considered the case of dipoles on a two-layer earth. Wait (1951, 1953) solved the problem of electrical and magnetic dipoles over a stratified isotropic medium. The case of an anisotropic half space was studied by Chetaev (1963) and Wait (1966a). Praus (1965), Sinha and Bhattacharya (1967), and Sinha (1968, 1969) treated electric and magnetic dipoles over a two-layer anisotropic earth. Wait (1966b) formally solved the case of a horizontal dipole over a stratified anisotropic medium. All this work was carried out by means of Sommerfeld's Hertzian potential functions, and the primary interest is concentrated in the limits of high conductivity. Magnetic properties are almost entirely neglected, mainly because such model studies assume principal applications to the earth, where the permeability is nearly equal to that of vacuum, and the electric conductivity dominates at low frequencies. In events of other celestial bodies, such as the moon, where the lack of moisture renders very low conductivity to the medium, a study of contributions due to all electric and magnetic properties is important.

This paper is devoted to the case of radiation of various dipole sources in the presence of a stratified anisotropic medium. The anisotropic medium is uniaxial and possesses both tensor permittivities and permeabilities. The principal axes are all perpendicular to the boudaries separating different media. Solutions to the problem are facilitated by decomposing a general wave field into TM and TE modes, employing the concept of propagation matrices, and expressing the reflection coefficients in terms of continuous fractions. The primary excitation is separated entirely from contributions due to the medium. The reflection coefficients depend on the geometric configurations as well as the physical properties of the stratified medium.

In studying the theory of electromagnetic wave propagation, it has been appreciated both classically and quantum mechanically (Kong, 1970) that introduction of a potential function is not necessary and sometimes complicates the algebra, especially when anisotropic media are involved. With recognition of the fact that outside any source two scalar functions are sufficient to determine all field quantities, two components of the field vectors can be chosen as the fundamental scalar functions. In our case,

† Manuscript received by the Editor March 10, 1972; revised manuscript July 12, 1972.

* Massachusetts Institute of Technology, Cambridge, Massachusetts 02139.

the preferred field components for TM and TE decomposition are clearly those along the principal axis and normal to boundaries of stratification. With the aid of propagation matrices (Kong, 1971), wave amplitudes in any region are easily calculated in terms of those in any other region. Writing in the form of continuous fractions, we obtain a closed-form solution for the reflection coefficients. All field components are expressed in terms of integrals which are ready for direct numerical evaluation. A discussion is given for the various special cases.

TRANSVERSE ELECTRIC AND MAGNETIC WAVES

Governing equations for electromagnetic fields in a region outside any source are the Maxwell's source free equations,

$$\nabla \times \mathbf{E} = i\omega \bar{\bar{\mu}} \cdot \mathbf{H} \qquad \text{(1a)} \qquad \text{and} \qquad \nabla \times \mathbf{H} = -i\omega \bar{\bar{\epsilon}} \cdot \mathbf{E}, \qquad \text{(1b)}$$

where in (1a), $\bar{\bar{\mu}}$ is the permeability tensor of the media. The tensor $\bar{\bar{\epsilon}}$ in (1b) contains information about the dielectric constant and the conductivity of the medium. $\bar{\bar{\epsilon}} = \bar{\bar{\epsilon}}' + i\bar{\bar{\epsilon}}''$, where $\bar{\bar{\epsilon}}'$ is the permittivity tensor, and $\bar{\bar{\epsilon}}''$ is related to the conductivity tensor $\bar{\bar{\sigma}}$ by $\bar{\bar{\epsilon}}'' = \bar{\bar{\sigma}}/\omega$. Time harmonic excitations with time dependence $\exp(-i\omega t)$ have been assumed. The tensors $\bar{\bar{\epsilon}}$ and $\bar{\bar{\mu}}$ can be represented by hermitian matrices. In our case, we consider media which are uniaxially anisotropic, where

$$\bar{\bar{\epsilon}} = \begin{pmatrix} \epsilon & & \\ & \epsilon & \\ & & \epsilon_z \end{pmatrix} \qquad \text{(2a)} \qquad \text{and} \qquad \bar{\bar{\mu}} = \begin{pmatrix} \mu & & \\ & \mu & \\ & & \mu_z \end{pmatrix}. \qquad \text{(2b)}$$

We employ cylindrical coordinates, and the plane transverse to the $\hat{z}$ axis is characterized by ρ and ϕ. Longitudinal electric and magnetic components E_z and H_z are used to derive TE and TM waves. The wave equations to be satisfied by E_z and H_z are immediately derived from equations (1) and (2). If we take the $\hat{z}$ component of (1b) in view of $\bar{\bar{\epsilon}}$ given by (2a), employ (1a) to eliminate transverse magnetic field components, and use the fact that $\nabla \cdot \mathbf{E} = (1-a)\partial E_z/\partial z$, the equation for E_z is

$$\left(\nabla_t^2 + a\frac{\partial^2}{\partial z^2} + k^2 a\right) E_z = 0. \qquad \text{(3a)}$$

We also obtain the wave equation for H_z:

$$\left(\nabla_t^2 + b\frac{\partial^2}{\partial z^2} + k^2 b\right) H_z = 0. \qquad \text{(3b)}$$

In equations (3a) and (3b),

$$k = \omega\sqrt{\mu\epsilon}, \qquad \text{(4)} \qquad a = \epsilon_z/\epsilon, \qquad \text{(5a)} \qquad \text{and} \qquad b = \mu_z/\mu, \qquad \text{(5b)}$$

and

$$\nabla_t^2 = \frac{1}{\rho}\frac{\partial}{\partial \rho}\left(\rho\frac{\partial}{\partial \rho}\right) + \frac{1}{\rho^2}\frac{\partial^2}{\partial \phi^2} \qquad \text{(6)}$$

is the transverse Laplacian operator expressed in cylindrical coordinates. It is seen from equations (3) that E_z and H_z are decoupled, which would not be true if the $\bar{\bar{\epsilon}}$ and $\bar{\bar{\mu}}$ tensors possess off-diagonal elements. A unique decomposition of the total wave into a transverse-magnetic-field (TM) mode derivable from E_z and a transverse-electric-field (TE) mode derivable from H_z is, therefore, plausible. We note that a pair of vector wave equations can be derived from (1) and (2):

$$\nabla^2\mathbf{E} + k^2\mathbf{E} + (a-1)k^2 E_z\hat{z} + (a-1)\nabla(\partial E_z/\partial z) = 0 \qquad \text{(7a)}$$

and

$$\nabla^2\mathbf{H} + k^2\mathbf{H} + (b-1)k^2 H_z\hat{z} + (b-1)\nabla(\partial H_z/\partial z) = 0. \qquad \text{(7b)}$$

Equation (7a) is the vector wave equation for the electric fields of TM waves where $H_z = 0$, and (7b) is the wave equation for the magnetic fields of TE waves, where $E_z = 0$. The $\hat{z}$ component of the two vector equations (7) gives rise to equation (3).

Solutions of E_z and H_z to the wave equation (3) in cylindrical coordinates are well known. As a consequence of the Maxwell equations (1), all transverse-electric- and magnetic-field components can be expressed in terms of the longitudinal components E_z and H_z which, respectively, characterize the TM and the TE waves. In our problems we are interested in wave solutions which are outgoing in $\hat{\rho}$ direction and traveling or standing in $\hat{z}$ direction. Therefore, we obtain, for a fixed separation constant n,

$$\mathbf{E}^{TM} = \int_{-\infty}^{\infty} dk_\rho \begin{pmatrix} i\dfrac{k_z^{(e)}}{k_\rho}(-Ae^{-ik_z^{(e)}z} + Be^{ik_z^{(e)}z})H_n^{(1)\prime}(k_\rho\rho)S_n^{TM}(\phi) \\ i\dfrac{k_z^{(e)}}{k_\rho^2\rho}(-Ae^{-ik_z^{(e)}z} + Be^{ik_z^{(e)}z})H_n^{(1)}(k_\rho\rho)S_n^{TM\prime}(\phi) \\ [A(k_\rho)e^{-ik_z^{(e)}z} + B(k_\rho)e^{ik_z^{(e)}z}]H_n^{(1)}(k_\rho\rho)S_n^{TM}(\phi) \end{pmatrix}, \tag{8a}$$

$$\mathbf{H}^{TM} = \int_{-\infty}^{\infty} dk_\rho \begin{pmatrix} -i\dfrac{\omega\epsilon}{k_\rho^2\rho}(Ae^{-ik_z^{(e)}z} + Be^{ik_z^{(e)}z})H_n^{(1)}(k_\rho\rho)S_n^{TM\prime}(\phi) \\ i\dfrac{\omega\epsilon}{k_\rho}(Ae^{-ik_z^{(e)}z} + Be^{ik_z^{(e)}z})H_n^{(1)\prime}(k_\rho\rho)S_n^{TM}(\phi) \\ 0 \end{pmatrix}, \tag{8b}$$

$$\mathbf{E}^{TE} = \int_{-\infty}^{\infty} dk_\rho \begin{pmatrix} i\dfrac{\omega\mu}{k_\rho^2}(Ce^{-ik_z^{(m)}z} + De^{ik_z^{(m)}z})H_n^{(1)}(k_\rho\rho)S_n^{TE\prime}(\phi) \\ -i\dfrac{\omega\mu}{k_\rho}(Ce^{-ik_z^{(m)}z} + De^{ik_z^{(m)}z})H_n^{(1)\prime}(k_\rho\rho)S_n^{TE}(\phi) \\ 0 \end{pmatrix}, \tag{8c}$$

and

$$\mathbf{H}^{TE} = \int_{-\infty}^{\infty} dk_\rho \begin{pmatrix} i\dfrac{k_z^{(m)}}{k_\rho}(-Ce^{-ik_z^{(m)}z} + De^{ik_z^{(m)}z})H_n^{(1)\prime}(k_\rho\rho)S_n^{TE}(\phi) \\ i\dfrac{k_z^{(m)}}{k_\rho^2\rho}(-Ce^{-ik_z^{(m)}z} + De^{ik_z^{(m)}z})H_n^{(1)}(k_\rho\rho)S_n^{TE\prime}(\phi) \\ [C(k_\rho)e^{-ik_z^{(m)}z} + D(k_\rho)e^{ik_z^{(m)}z}]H_n^{(1)}(k_\rho\rho)S_n^{TE}(\phi) \end{pmatrix}, \tag{8d}$$

where superscripts TM and TE denote, respectively, TM and TE waves. We note that if the integrands for E_z and H_z are denoted, respectively, by $E_z(k_\rho)$ and $H_z(k_\rho)$ such that

$$E_z^{TM} = \int_{-\infty}^{\infty} dk_\rho E_z(k_\rho) \quad \text{and} \quad H_z^{TE} = \int_{-\infty}^{\infty} dk_\rho H_z(k_\rho),$$

then the integrands of the transverse components are related to $E_z(k_\rho)$ and $H_z(k_\rho)$ by the following relations:

$$E_t(k_\rho)^{TM} = \frac{1}{k_\rho^2}\nabla_t\{\partial E_z(k_\rho)/\partial z\}, \quad H_t(k_\rho)^{TM} = -i\frac{\omega\epsilon}{k_\rho^2}\nabla_t \times \mathbf{E}_z(k_\rho), \tag{9a}$$

and

$$H_t(k_\rho)^{TE} = \frac{1}{k_\rho^2}\nabla_t\{\partial H_z(k_\rho)/\partial z\}, \quad E_t(k_\rho)^{TE} = i\frac{\omega\mu}{k_\rho^2}\nabla_t \times \mathbf{H}_z(k_\rho), \tag{9b}$$

where

$$\mathbf{E}_z = \hat{z}E_z, \ \mathbf{H}_z = \hat{z}H_z, \quad \text{and} \quad \nabla_t = \hat{\rho}\frac{\partial}{\partial\rho} + \hat{\phi}\frac{1}{\rho}\frac{\partial}{\partial\rho}.$$

The fact that TM waves are extraordinary waves in the medium is signified in equation (8) by the superscript (e) on the $\hat{z}$-directed propagation constant $k_z^{(e)}$, which satisfies the dispersion relation

$$k_z^{(e)} = (k^2 - k_\rho^2/a)^{1/2}. \tag{10a}$$

TE waves are derived from H_z and satisfy the dispersion relation

$$K_z^{(m)} = (k^2 - k_\rho^2/b)^{1/2}, \tag{10b}$$

where the superscript (m) indicates the effect of magnetic anisotropy. In (8), the first element of the column matrices denotes the $\hat{\rho}$ component, the second element the $\hat{\phi}$ component, and the third element the $\hat{z}$ component. The Hankel functions $H_n^{(1)}$ of the first kind and nth order represent outgoing waves in ρ direction due to our choice of the time dependence $\exp(-i\omega t)$. $S_n(\phi)$ stands for sinusoidal functions of ϕ. Primes on $H_n^{(1)}(k_\rho\rho)$ and $S_n(\phi)$ denote differentiation with respect to the arguments. The k_ρ-dependent functions A, B, C, and D are to be determined by the appropriate boundary conditions.

PRIMARY EXCITATION

The explicit solutions to the problem of dipole radiation over a stratified medium depends on field excitations of the source and the geometrical configuration and physical constituents of the medium. In the absence of the stratified medium, the solution of electromagnetic fields in an isotropic medium due to a dipole antenna, which we refer to as the primary excitation, is well known (Adler et al, 1960). The solution is usually written in spherical coordinates. It can be transformed into cylindrical coordinates and represented by Hankel functions in the integral form. Writing in the general form, we have

$$E_z = \int_{-\infty}^{\infty} dk_\rho E_0(k_\rho)\begin{Bmatrix} e^{ik_z z} \\ e^{-ik_z z}\end{Bmatrix} H_n^{(1)}(k_\rho\rho)S_n^{TM}(\phi) \qquad \begin{matrix} z > 0 \\ z < 0 \end{matrix} \tag{11}$$

and

$$H_z = \int_{-\infty}^{\infty} dk_\rho H_0(k_\rho)\begin{Bmatrix} e^{ik_z z} \\ e^{-ik_z z}\end{Bmatrix} H_n^{(1)}(k_\rho\rho)S_n^{TE}(\phi) \qquad \begin{matrix} z > 0 \\ z < 0 \end{matrix}, \tag{12}$$

where E_0 and H_0 characterize the structure and excitation of the dipole. All field components follow from equation (8) with $B = D = 0$, $A = E_0$, $C = H_0$ for $z \lesssim 0$, and $A = C = 0$, $B = E_0$, $D = H_0$ for $z \gtrsim 0$.

For the elementary dipoles under consideration, we obtain (Appendix 1):

1) Vertical electric dipole: $n = 0$, $S_n^{TM}(\phi) = 1$,

$$E_0 = -\frac{Ilk_\rho^2}{8\pi\omega\epsilon k_z} \tag{13a}$$

and

$$H_0 = 0. \tag{13b}$$

2) Horizontal electric dipole along $\hat{x}$ direction,

$$E_0 = \pm\, i\frac{Ilk_\rho^2}{8\pi\omega\epsilon} z \gtrless 0 \qquad S_1^{TM} = \cos\phi \quad \text{and} \tag{14a}$$

$$H_0 = i\frac{Ilk_\rho^2}{8\pi k_z} \qquad S_1^{TE} = -\sin\phi. \tag{14b}$$

3) Vertical magnetic dipole: $n=0$, $S_n^{TE}(\phi)=1$,

$$H_0 = -i\frac{IAk_\rho^3}{8\pi k_z}, \tag{15a}$$

and

$$E_0 = 0. \tag{15b}$$

4) Horizontal magnetic dipole along $\hat{x}$ direction,

$$H_0 = \mp\frac{IAk_\rho^2}{8\pi} z \gtrless 0 \qquad S_1^{TM} = \cos\phi \quad \text{and} \tag{16a}$$

$$E_0 = -\frac{IA\omega\mu k_\rho^2}{8\pi k_z} \qquad S_1^{TE} = -\sin\phi. \tag{16b}$$

In equations (13)–(16) I is the current that drives the dipole, l is the equivalent length of the electric dipole, and A is the area of the current loop that constitutes the magnetic dipole. Horizontal dipoles can be obtained simply by a rotation of coordinates, which amounts to changing $\cos\phi$ to $\sin\phi$ and $\sin\phi$ to $-\cos\phi$. We note that a vertical electric dipole excites the TM wave only and a vertical magnetic dipole excites the TE wave only, both involve Hankel functions of zero order; whereas horizontal dipoles exicite both TM and TE waves and require Hankel functions of the first order. An arbitrarily oriented dipole can be treated as a linear combination of three dipoles along the $\hat{x}$, $\hat{y}$, and $\hat{z}$ axes.

DIPOLE ANTENNAS OVER STRATIFIED ANISOTROPIC MEDIA

Geometric configuration of the problem is shown in Figure 1. There are n slab regions, and the last region is numbered t instead of $n+1$, for the sake of simplification. In each region labeled i, solutions of electromagnetic field components take the form of equation (8) with all quantities subscripted by i. In the 0th region where we have the antennas, $A_0=E_0$ and $C_0=H_0$, which are known from (13)–(16) for the three types of antennas under consideration. The last region, namely region t, is semiinfinite, and we do not expect reflected waves, therefore, $B_t=D_t=0$.

Boundary conditions at all interfaces require all tangential electromagnetic field components be continuous for all ρ and ϕ (Appendix 2). Solutions can be facilitated by introducing propagation matrices (Kong, 1971). The upward propagation matrix for TM waves from the $(i+1)$th region to the ith region is defined to be

$$M_i^{i+1} = \frac{1}{2}\begin{pmatrix} \epsilon(+)_i^{i+1} e(+)_i^{(e)} & \epsilon(-)_i^{i+1} e(-)_i^{(e)} \\ \epsilon(-)_i^{i+1} e(+)_i^{(e)} & \epsilon(+)_i^{i+1} e(-)_i^{(e)} \end{pmatrix}, \tag{17}$$

where

$$\epsilon(\pm)_q^p = \left(\frac{\epsilon_p}{\epsilon_q} \pm \frac{k_{pz}^{(e)}}{k_{qz}^{(e)}}\right), \tag{18}$$

$$e(\pm)_i^{(e)} = \exp\left[\pm ik_{(i+1)z}^{(e)}(d_i - d_{i+1})\right], \quad \text{and} \tag{19}$$

$$k_{iz}^{(e)} = (k_i^2 - k_\rho^2/a)^{1/2}. \tag{20}$$

Matching boundary conditions at $z=-d_i$, we obtain

$$\begin{pmatrix} a_i \\ b_i \end{pmatrix} = M_i^{i+1}\begin{pmatrix} a_{i+1} \\ b_{i+1} \end{pmatrix}, \tag{21}$$

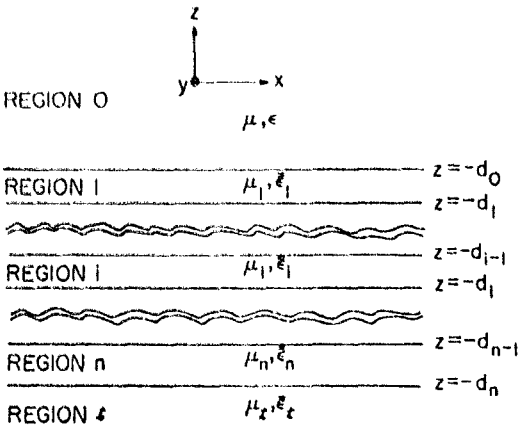

FIG. 1. Geometric configuration of the problem.

where

$$a_i = A_i \exp\left(ik_{iz}^{(a)} d_i\right) \tag{22a}$$

and

$$b_i = B_i \exp\left(-ik_{iz}^{(a)} d_i\right). \tag{22b}$$

Note that, with R^{TM} denoting reflection coefficients and T^{TM} denoting transmission coefficients, we can write

$$a_0 = E_0 \exp\left[ik_z^{(a)} d_0\right], \tag{23a}$$

$$b_0 = R^{TM} E_0 \exp\left[-ik_z^{(a)} d_0\right], \tag{23b}$$

and

$$a_t = T^{TM} E_0 \exp\left[ik_z^{(a)} d_t\right]. \tag{23c}$$

Also, $b_t = 0$, because there is no reflected wave in the last region. The parameter d_t in (23c) is introduced for convenience; it does not correspond to any distance and is always multipled by $e(-)_n^{(a)}$ to yield $\exp\left[ik_{nz}^{(a)} d_n\right]$. The definition of the propagation matrix is a useful one. Once wave amplitudes in any region are known, those in the regions above this one are all determined by (21). Thus the propagation matrix (17) propagates wave amplitudes upward. We can also define a propagation matrix M_{i+1}^{i} which propagates wave amplitudes downward.

$$M_{i+1}^{i} = \frac{1}{2}\begin{pmatrix} \epsilon(+)_{i+1}^{i} e(-)_i^{(a)} & \epsilon(-)_{i+1}^{i} e(-)_i^{(a)} \\ \epsilon(-)_{i+1}^{i} e(+)_i^{(a)} & \epsilon(+)_{i+1}^{i} e(+)_i^{(a)} \end{pmatrix} \tag{24a}$$

and

$$\begin{pmatrix} a_{i+1} \\ b_{i+1} \end{pmatrix} = M_{i+1}^{i} \begin{pmatrix} a_i \\ b_i \end{pmatrix}. \tag{24b}$$

It is easily shown that

$$M_i^{i+1} M_{i+1}^{i} = 1. \tag{25}$$

Following a parallel analysis of the above, we define a downward propagation matrix N_{i+1}^{i} for TE waves.

$$N_{i+1}^{i} = \frac{1}{2}\begin{pmatrix} \mu(+)_{i+1}^{i} e(-)_i^{(m)} & \mu(-)_{i+1}^{i} e(-)_i^{(m)} \\ \mu(-)_{i+1}^{i} e(+)_i^{(m)} & \mu(+)_{i+1}^{i} e(+)_i^{(m)} \end{pmatrix} \quad \text{and} \tag{26a}$$

$$\begin{pmatrix} c_{i+1} \\ d_{i+1} \end{pmatrix} = N_{i+1}^{i} \begin{pmatrix} c_i \\ d_i \end{pmatrix}. \tag{26b}$$

An upward propagation matrix N_i^{i+1} is defined as the inverse of N_{i+1}^{i}:

$$N_i^{i+1} = \frac{1}{2}\begin{pmatrix} \mu(+)_i^{i+1} e(+)_i^{(m)} & \mu(-)_i^{i+1} e(-)_i^{(m)} \\ \mu(-)_i^{i+1} e(+)_i^{(m)} & \mu(+)_i^{i+1} e(-)_i^{(m)} \end{pmatrix} \quad \text{and} \tag{27a}$$

$$\begin{pmatrix} c_i \\ d_i \end{pmatrix} = N_i^{i+1} \begin{pmatrix} c_{i+1} \\ d_{i+1} \end{pmatrix}. \tag{27b}$$

In (26) and (27),

$$\mu(\pm)_q^p = \frac{\mu_p}{\mu_q} \pm \frac{k_{pz}^{(m)}}{k_{qz}^{(m)}}, \qquad (28) \qquad c_i = C_i \exp\left[ik_{iz}^{(m)} d_i\right], \qquad (29a)$$

$$d_i = D_i \exp\left[-ik_{iz}^{(m)} d_i\right], \qquad (29b) \qquad \text{and} \qquad k_{iz}^{(m)} = (k_i^2 - k^2/b)^{1/2}. \qquad (29c)$$

Also $c_0 = H_0$, $d_0 = R^{TE} H_0$, $c_t = T^{TE} H_0$, and $d_t = 0$. We note that for vertical magnetic or electric dipoles, only the TM waves or the TE waves, respectively, are excited. In the case of either a horizontal electric dipole or a horizontal magnetic dipole, both TM and TE waves are excited.

REFLECTION COEFFICIENTS

In the interferometry method, our primary interest is the reflected wave fields. From the preceding section, we have established that when the wave amplitudes in region 0 are known, solutions in any other region can be determined by using the downward propagation matrices (24) and (26). In this section we derive a formula for the reflection coefficients which is expressed in continuous fractions. We observe from equation (23) that $b_t/a_t = 0$, and b_0/a_0 gives rise to the reflection coefficients R^{TM}. And from (21) an expression for b_i/a_i in terms of b_{i+1}/a_{i+1} can be established easily. In view of (17), (21) gives

$$\frac{b_i}{a_i} = \frac{\epsilon(+)_i^{i+1}}{\epsilon(-)_i^{i+1}} \left[1 - \frac{\epsilon(+)_i^{i+1}/\epsilon(-)_i^{i+1} - \epsilon(-)_i^{i+1}/\epsilon(+)_i^{i+1}}{\epsilon(+)_i^{i+1}/\epsilon(-)_i^{i+1} + (e(-)_i^{(e)})^2 (b_{i+1}/a_{i+1})} \right]. \qquad (30)$$

Making use of (30), we obtain a formula in continuous fraction for the reflection coefficient R^{TM}.

$$\begin{aligned} R^{TM} = {} & \exp\left(i2k_z^{(e)} d_0\right) \frac{\epsilon(+)_0^1}{\epsilon(-)_0^1} \left\{ 1 - \cfrac{\epsilon(+)_0^1/\epsilon(-)_0^1 - \epsilon(-)_0^1/\epsilon(+)_0^1}{\epsilon(+)_0^1/\epsilon(-)_0^1} \right. \\ & + \exp\left(i2k_{1z}^{(e)} (d_1 - d_0)\right) \frac{\epsilon(+)_1^2}{\epsilon(-)_1^2} \left[1 - \cfrac{\epsilon(+)_1^2/\epsilon(-)_1^2 - \epsilon(-)_1^2/\epsilon(+)_1^2}{\epsilon(+)_1^2/\epsilon(-)_1^2} \right. \\ & \left. \left. + \cdots + \exp\left(i2k_{nz}^{(e)} (d_n - d_{n-1})\right) \frac{\epsilon(-)_n^t}{\epsilon(+)_n^t} \cdots \right] \right\}. \end{aligned} \qquad (31)$$

In the same way we obtain the reflection coefficient for TE waves.

$$\begin{aligned} R^{TE} = {} & \exp\left(i2k_z^{(m)} d_0\right) \frac{\mu(+)_0^1}{\mu(-)_0^1} \left\{ 1 - \cfrac{\mu(+)_0^1/\mu(-)_0^1 - \mu(-)_0^1/\mu(+)_0^1}{\mu(+)_0^1/\mu(-)_0^1} \right. \\ & + \exp\left(i2k_{1z}^{(m)} (d_1 - d_0)\right) \frac{\mu(+)_1^2}{\mu(-)_1^2} \left[1 - \cfrac{\mu(+)_1^2/\mu(-)_1^2 - \mu(-)_1^2/\mu(+)_1^2}{\mu(+)_1^2/\mu(-)_1^2} \right. \\ & \left. \left. + \cdots + \exp\left(i2k_{nz}^{(m)} (d_n - d_{n-1})\right) \frac{\mu(-)_n^t}{\mu(+)_n^t} \cdots \right] \right\}. \end{aligned} \qquad (32)$$

Definitions of $\epsilon(\pm)_i^{i+1}$ and $\mu(\pm)_i^{i+1}$ are given in (18) and (28). The subscript n on R^{TM} and R^{TE} denotes the number of layers involved.

SUMMARY

With the reflection coefficients determined in the last section, we can now summarize the formulas for all field quantities in region 0, where interference patterns are calculated. We have decomposed total wave fields into a summation of the TM and TE wave modes.

$$\mathbf{E} = \mathbf{E}^{TM} + \mathbf{E}^{TE} \qquad (33) \qquad \text{and} \qquad \mathbf{H} = \mathbf{H}^{TM} + \mathbf{H}^{TE}. \qquad (34)$$

The TM and TE solutions are:

1) For a vertical electric dipole,

$$\mathbf{E}^{TM} = \int_{-\infty}^{\infty} dk_\rho \left(-\frac{I\ell}{8\pi\omega\epsilon}\right) \begin{bmatrix} ik_\rho^2 [\pm e^{\pm ik_z^{(e)} z} + R^{TM} e^{ik_z^{(e)} z}] H_0^{(1)'}(k_\rho \rho) \\ 0 \\ \dfrac{k_\rho^3}{k_z^{(e)}} [e^{\pm ik_z^{(e)} z} + R^{TM} e^{ik_z^{(e)} z}] H_0^{(1)}(k_\rho \rho) \end{bmatrix}, \qquad (35a)$$

$$\mathbf{H}^{TM} = \int_{-\infty}^{\infty} dk_\rho \left(-\frac{I\ell}{8\pi}\right) \begin{bmatrix} 0 \\ i \dfrac{k_\rho^2}{k_z^{(e)}} [e^{\pm ik_z^{(e)} z} + R^{TM} e^{ik_z^{(e)} z}] H_0^{(1)'}(k_\rho \rho) \\ 0 \end{bmatrix}, \qquad (35b)$$

and $\mathbf{E}^{TE} = \mathbf{H}^{TE} = 0$.

2) For a vertical magnetic dipole,

$$\mathbf{E}^{TE} = \int_{-\infty}^{\infty} dk_\rho \left(-i \frac{IA\omega\mu}{8\pi}\right) \begin{bmatrix} 0 \\ -i \dfrac{k_\rho^2}{k_z^{(m)}} (e^{\pm ik_z^{(m)} z} + R^{TE} e^{ik_z^{(m)} z}) H_0^{(1)'}(k_\rho \rho) \\ 0 \end{bmatrix}, \qquad (36a)$$

$$\mathbf{H}^{TE} = \int_{-\infty}^{\infty} dk_\rho \left(-i \frac{IA}{8\pi}\right) \begin{bmatrix} ik_\rho^2 (\pm e^{\pm ik_z^{(m)} z} + R^{TE} e^{ik_z^{(m)} z}) H_0^{(1)'}(k_\rho \rho) \\ 0 \\ \dfrac{k_\rho^3}{k_z^m} (e^{\pm ik_z^{(m)} z} + R^{TE} e^{ik_z^{(m)} z}) H_0^{(1)}(k_\rho \rho) \end{bmatrix}, \qquad (36b)$$

and $\mathbf{E}^{TM} = \mathbf{H}^{TM} = 0$.

3) For a horizontal electric dipole along $\hat{x}$ direction,

$$\mathbf{E}^{TM} = \int_{-\infty}^{\infty} dk_\rho \left(i \frac{I\ell}{8\pi\omega\epsilon}\right) \begin{bmatrix} ik_z^{(e)} k_\rho (e^{\pm ik_z^{(e)} z} - R^{TM} e^{ik_z^{(e)} z}) H_1^{(1)'}(k_\rho \rho) \cos\phi \\ -\dfrac{k_z^{(e)}}{\rho} (e^{\pm ik_z^{(e)} z} - R^{TM} e^{ik_z^{(e)} z}) H_1^{(1)}(k_\rho \rho) \sin\phi \\ k_\rho^2 (\pm e^{\pm ik_z^{(e)} z} - R^{TM} e^{ik_z^{(e)} z}) H_1^{(1)}(k_\rho \rho) \cos\phi \end{bmatrix}, \qquad (37a)$$

$$\mathbf{H}^{TM} = \int_{-\infty}^{\infty} dk_\rho \left(\frac{I\ell}{8\pi}\right) \begin{bmatrix} -\dfrac{1}{\rho} (\pm e^{\pm ik_z^{(e)} z} - R^{TM} e^{ik_z^{(e)} z}) H_1^{(1)}(k_\rho \rho) \sin\phi \\ -k_\rho (\pm e^{\pm ik_z^{(e)} z} - R^{TM} e^{ik_z^{(e)} z}) H_1^{(1)'}(k_\rho \rho) \cos\phi \\ 0 \end{bmatrix}, \qquad (37b)$$

$$\mathbf{E}^{TE} = \int_{-\infty}^{\infty} dk_\rho \left(\frac{I\ell\omega\mu}{8\pi}\right) \begin{bmatrix} -\dfrac{1}{k_z^{(m)}\rho}\,(e^{\pm ik_z^{(m)}z} + R^{TE}e^{ik_z^{(m)}z})H_1^{(1)}(k_\rho\rho)\cos\phi \\ \dfrac{k_\rho}{k_z^{(m)}}\,(e^{\pm ik_z^{(m)}z} + R^{TE}e^{ik_z^{(m)}z})H_1^{(1)\prime}(k_\rho\rho)\sin\phi \\ 0 \end{bmatrix}, \quad (37c)$$

$$\text{and} \quad \mathbf{H}^{TE} = \int_{-\infty}^{\infty} dk_\rho \left(i\frac{I\ell}{8\pi}\right) \begin{bmatrix} ik_\rho(\pm e^{\pm ik_z^{(m)}z} + R^{TE}e^{ik_z^{(m)}z})H_1^{(1)\prime}(k_\rho\rho)\sin\phi \\ \dfrac{i}{\rho}\,(\pm e^{\pm ik_z^{(m)}z} + R^{TE}e^{ik_z^{(m)}z})H_1^{(1)}(k_\rho\rho)\cos\phi \\ \dfrac{k_\rho^2}{k_z^{(m)}}\,(e^{\pm ik_z^{(m)}z} + R^{TE}e^{ik_z^{(m)}z})H_1^{(1)}(k_\rho\rho)\sin\phi \end{bmatrix}. \quad (37d)$$

4) For a horizontal magnetic dipole along $\hat{x}$ direction,

$$\mathbf{E}^{TM} = \int_{-\infty}^{\infty} dk_\rho \left(-\frac{IA\omega\mu}{8\pi}\right) \begin{bmatrix} ik_\rho(\pm e^{\pm ik_z^{(e)}z} + R^{TE}e^{ik_z^{(e)}z})H_1^{(1)\prime}(k_\rho\rho)\sin\phi \\ \dfrac{i}{\rho}\,(\pm e^{\pm ik_z^{(e)}z} + R^{TE}e^{ik_z^{(e)}z})H_1^{(1)}(k_\rho\rho)\cos\phi \\ -\dfrac{k_\rho^2}{k_z^{(e)}}\,(e^{\pm ik_z^{(e)}z} + R^{TE}e^{ik_z^{(e)}z})H_1^{(1)}(k_\rho\rho)\sin\phi \end{bmatrix}, \quad (38a)$$

$$\mathbf{H}^{TM} = \int_{-\infty}^{\infty} dk_\rho \left(-\frac{IAk^2}{8\pi}\right) \begin{bmatrix} -i\dfrac{1}{k_z^{(e)}\rho}\,(e^{\pm ik_z^{(e)}z} + R^{TE}e^{ik_z^{(e)}z})H_1^{(1)}(k_\rho\rho)\cos\phi \\ i\dfrac{k_\rho}{k_z^{(e)}}\,(e^{\pm ik_z^{(e)}z} + R^{TE}e^{ik_z^{(e)}z})H_1^{(1)\prime}(k_\rho\rho)\sin\phi \\ 0 \end{bmatrix}, \quad (38b)$$

$$\mathbf{E}^{TE} = \int_{-\infty}^{\infty} dk_\rho \left(i\frac{IA\omega u}{8\pi}\right) \begin{bmatrix} -\dfrac{1}{\rho}\,(\pm e^{\pm ik_z^{(m)}z} + R^{TE}e^{ik_z^{(m)}z})H_1^{(1)}(k_\rho\rho)\cos\phi \\ -k_\rho(\pm e^{\pm ik_z^{(m)}z} + R^{TE}e^{ik_z^{(m)}z})H_1^{(1)\prime}(k_\rho\rho)\cos\phi \\ 0 \end{bmatrix}, \quad (38c)$$

$$\text{and} \quad \mathbf{H}^{TE} = \int_{-\infty}^{\infty} dk_\rho \left(\frac{IA}{8\pi}\right) \begin{bmatrix} ik_z^{(m)}k_\rho(-e^{\pm ik_z^{(m)}z} + R^{TE}e^{ik_z^{(m)}z})H_1^{(1)\prime}(k_\rho\rho)\cos\phi \\ -i\dfrac{k_z^{(m)}}{\rho}\,(-e^{\pm ik_z^{(m)}z} + R^{TE}e^{ik_z^{(m)}z})H_1^{(1)}(k_\rho\rho)\sin\phi \\ k_\rho^2(\pm e^{\pm ik_z^{(m)}z} + R^{TE}e^{ik_z^{(m)}z})H_1^{(1)}(k_\rho\rho)\cos\phi \end{bmatrix}. \quad (38d)$$

DISCUSSIONS

The problem of radiation of various dipole antennas over a stratified anisotropic medium has been solved. In view of the general formalism presented, we can make the following observations:

1) All medium properties such as the constitutive parameters and the geometrical configuration are absorbed into the reflection coefficients R^{TM} and R^{TE}, which are readily computed by equations (31) and (32). Clearly, when all regions possess the same constitutive parameters, namely when there is no stratification, $R^{TM} = R^{TE} = 0$.

2) Since the anisotropy in permittivity appears only in $\epsilon(\pm)$, and the anisotropy in permeability appears only in $\mu(\pm)$, it is seen from (31)–(34) that R^{TM} does not depend on the magnetic anisotropy, and R^{TE} does not depend on the electric anisotropy. Both R^{TM} and R^{TE} are seen to be even functions of k_ρ.

3) It is obvious from (35)–(38) that a vertical electric dipole excites TM waves only, and a vertical magnetic dipole excites TE waves only, whereas both horizontal electric and magnetic dipoles excite both TM and TE waves. In the case when permeability is isotropic, the TM waves are extraordinary waves, and the TE waves are ordinary waves. A turnstile antenna, which consists of two dipoles perpendicular to each other and driven 90 degrees out of phase, also excites both TM and TE waves.

4) The above formulation can be compared with the potential approach for the various cases that exist. In the case of no stratified medium, the results are checked by using the identities

$$H_1^{(1)'} + \frac{1}{k_\rho \rho} H_1^{(1)} = H_0^{(1)} \tag{39}$$

and

$$\frac{i}{2}\int_{-\infty}^{\infty} dk_\rho e^{ik_z z} \frac{k_\rho}{k_z} H_0^{(1)}(k_\rho \rho) = \exp\left(ik\sqrt{\rho^2+z^2}\right)/\sqrt{\rho^2+z^2}, \tag{40}$$

where $r^2 = \rho^2 + z^2$ in spherical coordinates. We define the number of layers of a stratified medium equal to the number of boundaries. The medium below the nth boundary is called the tth layer.

5) The one-layer case (or half space) has been studied extensively. We obtain from (31) and (32)

$$R^{TM} = \frac{\epsilon(-)_0^1}{\epsilon(+)_0^1} \exp\left(i2k_z^{(e)} d_0\right) \quad \text{(41a)} \qquad \text{and} \qquad R^{TE} = \frac{\mu(-)_0^1}{\mu(+)_0^1} \exp\left(i2k_z^{(m)} d_0\right). \quad \text{(41b)}$$

In the case of a perfectly conducting half space, $\epsilon = \epsilon_3 \to \infty$. Equation (41) gives $R^{TM} = 1$ and $R^{TE} = -1$.

6) Observe that all contributions due to all layers below the first are lumped into the reflection coefficient R_{n-1}, such that

$$R_n^{TM} = \exp\left[i2k_z^{(e)} d_0\right] \frac{\epsilon(+)_0^1}{\epsilon(-)_0^1}\left(1 - \frac{\epsilon(+)_0^1/\epsilon(-)_0^1 - \epsilon(-)_0^1/\epsilon(+)_0^1}{\epsilon(+)_0^1/\epsilon(-)_0^1 + \exp\left[-i2k_{1z}^{(e)} d_0\right] R_{n-1}^{TM}}\right) \tag{42}$$

and

$$R_n^{TE} = \exp\left[i2k_z^{(m)} d_0\right] \frac{\mu(+)_0^1}{\mu(-)_0^1}\left(1 - \frac{\mu(+)_0^1/\mu(-)_0^1 - \mu(-)_0^1/\mu(+)_0^1}{\mu(+)_0^1/\mu(-)_0^1 + \exp\left[-i2k_{1z}^{(m)} d_0\right] R_{n-1}^{TE}}\right). \tag{43}$$

The definitions for R_{n-1}^{TM} and R_{n-1}^{TE} follow directly from (31) and (32).

7) The integrals as presented in (35)–(38) can be programmed directly with a computer or analyzed analytically. Asymptotic evaluations of the integrals and numerical results for the electromagnetic field quantities under various circumstances constitute topics of subsequent papers.

ACKNOWLEDGMENTS

I wish to thank Professor J. V. Harrington for providing me with the opportunity, the support, and the encouragement to pursue research in this field. This work is supported in part by the Joint Service Electronics Program (Contr. DAAB 07-71-C-0300) and NASA Contract NAS 9-11540. A portion of the research was done while the author was a visiting scientist at the Lunar Science Institute, which is operated by the Universities Space Research Association under Contract No. NSR 09-051-001 with the National Aeronautics and Space Administration.

REFERENCES

Adler, R. B., Chu, L. J., and Fano, R. M., 1960, Electromagnetic energy transmission and radiation, Chap. 10: New York, John Wiley and Sons, Inc.
Baños, A., 1966, Dipole radiation in the presence of a conducting half-space: New York, Pergamon Press.
Bhattacharyya, B. K., 1963, Electromagnetic fields of a vertical magnetic dipole placed above the earth's surface: Geophysics, v. 28, no. 3, p. 408–425.
Chetaev, D. N., 1963, On the field of a low-frequency electric dipole situated on the surface of a uniform anisotropic conducting half-space: Soviet Phys.–Tech. Phys., v. 7, no. 11, p. 991–995.
Kong, J. A., 1970, Quantization of electromagnetic waves in moving uniaxial media: J. Appl. Phys., v. 41, no. 2, p. 554–559.
——— 1971, Reflection and transmission of electromagnetic waves by stratified moving media: Can J. Phys., v. 49, no. 22, p. 2785–2792.
Praus, O., 1965, Field of electric dipole above two layer anisotropic medium: Stud. Geoph. et Geodaet., v. 9, p. 359–380.
Sinha, A. K., 1968, Electromagnetic fields of an oscillating magnetic dipole over an anisotropic earth: Geophysics, v. 33, no. 2, p. 346–353.
——— 1969, Vertical electric dipole over an inhomogeneous and anisotropic earth: Pure and Appl. Geophys., v. 72, no. 1, p. 123–147.
Sinha, A. K., and Bhattacharya, P. K., 1967, Electric dipole over an anisotropic and inhomogeneous earth: Geophysics, v. 32, no. 4, p. 652–667.
Sommerfeld, A., 1949, Partial differential equations in physics: New York, Academic Press Inc.
Wait, J. R., 1951, The magnetic dipole over the horizontally stratified earth: Can. J. Phys., v. 29, p. 577–592.
——— 1953, Radiation from a vertical electric dipole over a stratified ground: IEEE Trans. on Ant. and Prop., v. AP-1, p. 9–11.
——— 1966a, Fields of a horizontal dipole over a stratified anisotropic half-space: IEEE Trans. Ant. Prop., v. AP-14, p. 790–792.
——— 1966b, Fields of a horizontal dipole over an anisotropic half-space: Can. J. Phys., v. 44, p. 2387–2401.
——— 1970, Electromagnetic waves in stratified media: New York, Pergamon Press.
Ward, S. H., 1967, Electromagnetic theory for geophysical applications, *in* Mining geophysics, v. 2, part A: Tulsa, SEG, p. 10–196.
Wolf, A., 1946, Electric field of an oscillating dipole on the surface of a two-layer earth: Geophysics, v. 11, p. 518–534.

APPENDIX 1

In this appendix we derive equation (14) from well-known potential solutions for the dipole. Similar derivation, comparatively simpler, applies to equations (13), (15), and (16). The vector potential solution for the horizontal electric dipole is

$$\mathbf{A} = A\,(\hat{\rho}\cos\phi - \hat{\phi}\sin\phi), \quad \text{where} \quad A = \frac{I\ell}{4\pi} e^{ikr}/r.$$

The electromagnetic fields are obtained from

$$\mathbf{H} = \nabla \times \mathbf{A} \quad \text{and} \quad \mathbf{E} = i\frac{1}{\omega\epsilon}\left\{\nabla(\nabla\cdot\mathbf{A}) + k^2\mathbf{A}\right\}.$$

Using the identity (Sommerfeld, 1949)

$$\frac{e^{ikr}}{r} = \frac{i}{2}\int_{-\infty}^{\infty} dk_\rho \frac{k_\rho}{k_z} H_0^{(1)}(k_\rho\rho)e^{\pm ik_z z}.$$

The field components all can be written in the integral form. For the z component,

$$H_z = -\sin\phi\,\partial A/\partial\rho \quad \text{and} \quad E_z = i\frac{1}{\omega\epsilon}\cos\phi\,\partial^2 A/\partial\rho\partial z.$$

The results are equations (14a) and (14b).

APPENDIX 2

In this appendix, propagation matrices are derived from the boundary conditions. Consider the boundary at $z = -d_i$, the continuity of tangential electric fields and the continuity of tangential magnetic fields yields, for the TM waves,

$$k_{iz}^{(e)}\left\{-A_i e^{ik_{iz}^{(e)}d_i} + B_i e^{-ik_{iz}^{(e)}d_i}\right\} = k_{(i+1)z}^{(e)}\left\{-A_{i+1}e^{ik_{(i+1)z}^{(e)}d_i} + B_{i+1}e^{-ik_{(i+1)z}^{(e)}d_i}\right\} \quad \text{and} \tag{A1}$$

$$\epsilon_i\left\{A_i e^{ik_{iz}^{(e)}d_i} + B_i e^{-ik_{iz}^{(e)}d_i}\right\} = \epsilon_{i+1}\left\{A_{i+1}e^{ik_{(i+1)z}^{(e)}d_i} + B_{i+1}e^{-ik_{(i+1)z}^{(e)}d_i}\right\}. \tag{A2}$$

For the TE waves

$$\mu_i\left\{C_i e^{ik_{iz}^{(m)}d_i} + D_i e^{-ik_{iz}^{(m)}d_i}\right\} = \mu_{i+1}\left\{C_{i+1}e^{ik_{(i+1)z}^{(m)}d_i} + D_{i+1}e^{-ik_{(i+1)z}^{(m)}d_i}\right\} \quad \text{and} \tag{A3}$$

$$k_{iz}^{(m)}\left\{-C_i e^{ik_{iz}^{(m)}d_i} + D_i e^{-ik_{iz}^{(m)}d_i}\right\} = k_{(i+1)z}^{(m)}\left\{-C_{i+1}e^{ik_{(i+1)z}^{(m)}d_i} + D_{i+1}e^{-ik_{(i+1)z}^{(m)}d_i}\right\}. \tag{A4}$$

The reason that we can treat the TM and TE cases separately is that 1) for the vertical dipole case, only TM or TE is excited; 2) for the horizontal dipole case, although the total tangential field components consist of both TM and TE waves, the coefficients of $H_1^{(1)}$ and $H_1^{(1)'}$ separate TM and TE cases.

We now illustrate the derivation for the upward propagation matrix M_i^{i+1} for TM cases. From (A1) and (A2) it is straight-forward to solve for $A_i \exp ik_{iz}^{(e)}d_i$ and $B_i \exp -ik_{iz}^{(e)}d_i$, in terms of A_{i+1} and B_{i+1}. Using the definition (22) for a_i and b_i, we have

$$a_i = \frac{1}{2}\left\{\frac{\epsilon_{i+1}}{\epsilon_i} + \frac{k_{(i+1)z}^{(e)}}{k_{iz}^{(e)}}\right\} A_{i+1}e^{ik_{(i+1)z}^{(e)}d_i} + \frac{1}{2}\left\{\frac{\epsilon_{i+1}}{\epsilon_i} - \frac{k_{(i+1)z}^{(e)}}{k_{iz}^{(e)}}\right\} B_{i+1}e^{-ik_{(i+1)z}^{(e)}d_i} \quad \text{and} \tag{A5}$$

$$b_i = \frac{1}{2}\left\{\frac{\epsilon_{i+1}}{\epsilon_i} - \frac{k_{(i+1)z}^{(e)}}{k_{iz}^{(e)}}\right\} A_{i+1}e^{ik_{(i+1)z}^{(e)}d_i} + \frac{1}{2}\left\{\frac{\epsilon_{i+1}}{\epsilon_i} + \frac{k_{(i+1)z}^{(e)}}{k_{iz}^{(e)}}\right\} B_{i+1}e^{-ik_{(i+1)z}^{(e)}d_i}. \tag{A6}$$

Introducing definitions (18) and (19), we can write

$$a_i = \frac{1}{2}\left\{\epsilon(+)_i^{i+1}e(+)_i^{(e)}a_{i+1} + \epsilon(-)_i^{i+1}e(-)_i^{(e)}b_{i+1}\right\} \quad \text{and} \tag{A7}$$

$$b_i = \frac{1}{2}\left\{\epsilon(-)_i^{i+1}e(+)_i^{(e)}a_{i+1} + \epsilon(+)_i^{i+1}e(-)_i^{(e)}b_{i+1}\right\}. \tag{A8}$$

In view of the definition for propagation matrix (17), (A7) and (A8) are immediately cast into the form (21). The derivation for the downward propagation matrix involves a solution for A_{i+1}, B_{i+1} in terms of A_i and B_i; the result is equations (24a) and (24b). Similar procedure applied to (A3) and (A4) yields propagation matrices for TE waves.

GEOPHYSICS, VOL. 38, NO. 3 (JUNE 1973), P. 557–580, 10 FIGS., 7 TABLES

RADIO INTERFEROMETRY DEPTH SOUNDING: PART I—THEORETICAL DISCUSSION†

A. P. ANNAN*

Radio interferometry is a technique for measuring in-situ electrical properties and for detecting subsurface changes in electrical properties of geologic regions with very low electrical conductivity. Ice-covered terrestrial regions and the lunar surface are typical environments where this method can be applied. The field strengths about a transmitting antenna placed on the surface of such an environment exhibit interference maxima and minima which are characteristic of the subsurface electrical properties.

This paper (Part I) examines the theoretical wave nature of the electromagnetic fields about various types of dipole sources placed on the surface of a low-loss dielectric half-space and two-layer earth. Approximate expressions for the fields have been found using both normal mode analysis and the saddle-point method of integration. The solutions yield a number of important results for the radio interferometry depth-sounding method. The half-space solutions show that the interface modifies the directionality of the antenna. In addition, a regular interference pattern is present in the surface fields about the source. The introduction of a subsurface boundary modifies the surface fields with the interference pattern showing a wide range of possible behaviors. These theoretical results provide a basis for interpreting the experimental results described in Part II.

INTRODUCTION

The stimulus for this work was the interest in the measurement of lunar electrical properties in situ and the detection of subsurface layering, if any, by electromagnetic methods. Unlike most regions of the earth's surface, which are conductive largely due to the presence of water, the lunar surface is believed to be very dry and, therefore, to have a very low electrical conductivity (Strangway, 1969; Ward and Dey, 1971). Extensive experimental work on the electrical properties of dry geologic materials by Saint-Amant and Strangway (1970) indicates that these materials are low-loss dielectrics having dielectric constants in the range 3 to 15 and loss tangents considerably less than 1, in the Mhz frequency range. Analysis of the electrical properties of lunar samples by Katsube and Collett (1971) indicates that the lunar surface material has similar electrical properties.

Since electromagnetic methods commonly used in geophysics are designed for conductive earth problems, a method of depth sounding in a dominantly dielectric earth presented a very different problem. One possible method of detecting the presence of a boundary at depth in a dielectric is the radio interferometry technique, first suggested by Stern in 1927 (reported by Evans, 1963) as a method to measure the thickness of glaciers. The only reported application of the technique is the work of El-Said (1956), who attempted to sound the depth of the water table in the Egyptian desert. Although he successfully measured some interference maxima and minima, his method of interpretation of the data is open to question in light of the present work.

† Presented at the 39th Annual SEG International Meeting, September 18, 1969. Manuscript received by the Editor April 6, 1972; revised manuscript received September 22, 1972.

* University of Toronto, Toronto 181, Ontario, Canada.

The radio interferometry technique is conceptually quite simple. The essential features of the method are illustrated in Figure 1. A radio-frequency source placed on the surface of a dielectric earth radiates energy both into the air (or free space) above the earth and downward into the earth. Any subsurface contrast in electrical properties at depth will result in some energy being reflected back to the surface. As a result, there will be interference maxima and minima in the field strengths about the source due to waves traveling different paths. The spatial positions of the maxima and minima are characteristic of the electrical properties of the earth and can be used as a method of inferring the earth's electrical properties at depth.

The problem chosen for study in the theoretical work was that of the wave nature of the fields about various point-dipole sources placed on the surface of a two-layer earth. The mathematical solution to this type of boundary-value problem is found in numerous references. The general problem of electromagnetic waves in stratified media is extensively covered by Wait (1970), Brekhovskikh (1960), Budden (1961), Norton (1937), and Ott (1941, 1943). Although the solu-

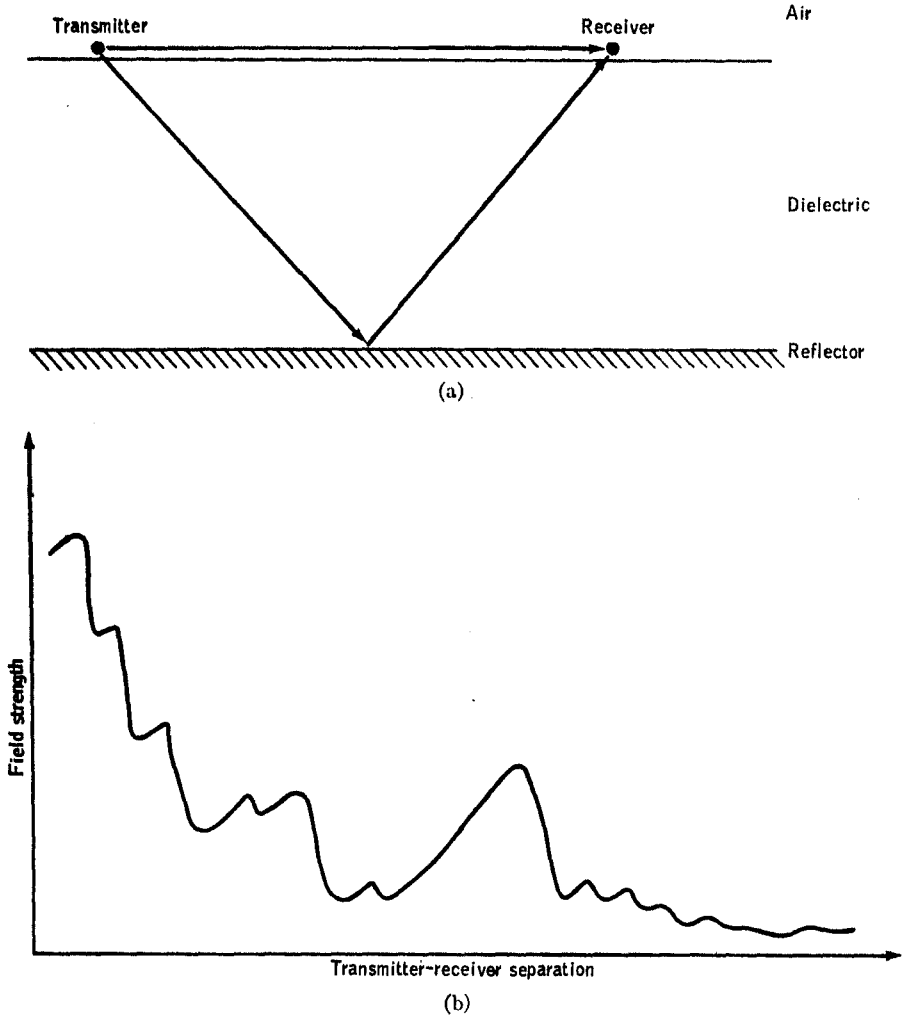

FIG. 1. (a) Transmitter-receiver configuration for radio interferometry, showing a direct wave and a reflected wave. (b) Schematic sketch of typical field-strength maxima and minima as the transmitter-receiver separation increases.

tion to the boundary-value problem can be found analytically, the integral expressions for fields cannot be evaluated exactly. In the radiation zone, approximate solutions to the integrals can be obtained by use of the theory of complex variables and special methods of contour integration. The preceding references, plus numerous others, discuss these techniques in detail. Since much of the detailed work in the mathematical development of these solutions is contained in the above references, the discussion of the solutions that follow will be primarily aimed at the radio interferometry application rather than the mathematical manipulations required to obtain them.

THEORETICAL BOUNDARY-VALUE PROBLEM

Although the various solutions of the boundary-value problem for horizontal and vertical electric and magnetic dipole sources over a two-layer earth appear in the literature, a complete and consistent tabulation of the solutions does not. Therefore, the boundary-value problem is outlined here, and a unified notation is used to express the solutions. This consistent notation is of considerable help in later discussions of the solutions.

The geometry and coordinate systems used in the boundary-value problem are shown in Figure 2. A point-dipole source is located at a height h on the z-axis above a two-layer earth, where the earth's surface is in the x–y-plane at $z=0$, and the subsurface boundary is at $z=-d$. The region $z\geq 0$ is taken as air or free space. The region $-d\leq z<0$ is a low-loss dielectric slab, and the region $z<-d$ is a half-space of arbitrary electrical properties. These regions are denoted 0, 1, and 2, respectively. K_i and M_i are the complex dielectric constant and relative permeability of each region, respectively. For consideration of vertical dipole sources, the dipole moments are taken aligned with the z-axis; for the horizontal dipole sources, the dipole moments are taken aligned parallel to the x-axis.

The solutions are most conveniently written and discussed using the electric and magnetic Hertz vector potential notation. On the assumption of a time dependence $e^{-i\omega t}$ and linear constitutive equations in Maxwell's equations, one obtains the following expressions for the electric and magnetic fields in terms of the Hertz vectors. For electric dipole sources, the electric Hertz vector satisfies the Helmholtz equation,

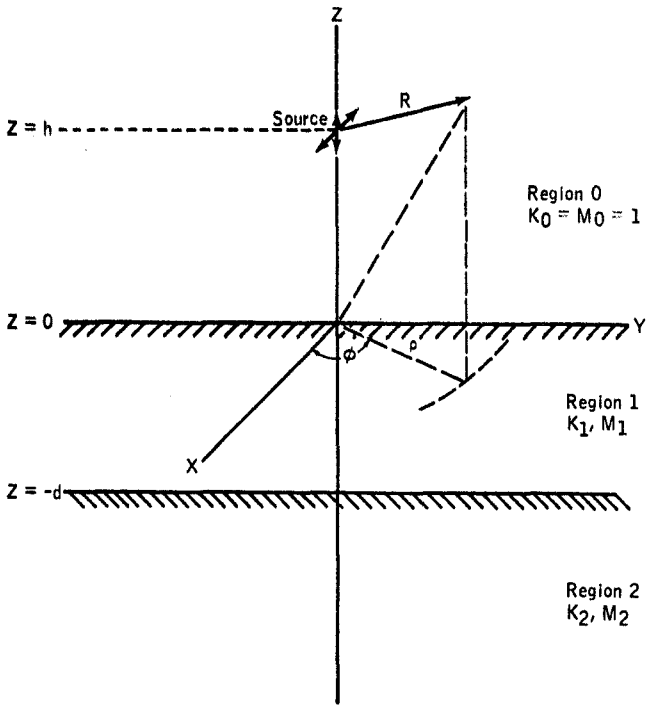

FIG. 2. Geometry of the boundary-value problem for a two-layer earth, showing notation used.

$$\nabla^2\Pi + k^2\Pi = -\frac{\mathbf{P}}{K\epsilon_0}, \tag{1}$$

with the electric and magnetic fields defined by

$$\mathbf{E} = k^2\Pi + \nabla\nabla\cdot\Pi, \tag{2}$$

and

$$\mathbf{H} = -i\omega K\epsilon_0\nabla\times\Pi \tag{3}$$

where k is the propagation constant. $\omega\sqrt{KM\epsilon_0\mu_0}$ and ϵ_0, μ_0 denote the permittivity and permeability of free space throughout. $\mathbf{P}$ is the electric dipole moment density distribution. Similarly, for magnetic dipole sources, the results for the magnetic Hertz vector are

$$\nabla^2\Pi + k^2\Pi = -\mathbf{M}, \tag{4}$$

and

$$\mathbf{H} = k^2\Pi + \nabla\nabla\cdot\Pi, \tag{5}$$

$$\mathbf{E} = i\omega M\mu_0\nabla\times\Pi, \tag{6}$$

where $\mathbf{M}$ is the magnetic dipole moment density distribution.

The dipole sources are taken as "unit" point dipole sources located in the region $z\geq 0$. The electric dipole moment density distribution is

$$\mathbf{P} = 4\pi\epsilon_0\delta(R)\mathbf{e}_j, \tag{7}$$

where $\mathbf{e}_j$ is a unit vector in the z-direction for a vertical electric dipole source and in the x-direction for the horizontal dipole source. $\delta(R)$ is the three-dimensional delta function, and $R=[x^2+y^2+(z-h)^2]^{1/2}$. Similarly for the magnetic dipole sources,

$$\mathbf{M} = 4\pi\delta(R)\mathbf{e}_j. \tag{8}$$

In the following discussions, no distinction between the electric and magnetic Hertz vectors is made. When we refer to electric dipole sources, the electric Hertz vector is implied; for magnetic dipole sources, the magnetic Hertz vector is implied. In addition, the free-space wavelength is taken as the scaling parameter for all length measurements. In other words, a distance, denoted ρ, is in free-space wavelengths, and the true length is $W\rho$, where W is the free-space wavelength:

$$W = \frac{2\pi}{\omega(\epsilon_0\mu_0)^{1/2}}. \tag{9}$$

This choice of scaling parameter makes all the following integral solutions dimensionless.

As shown by Sommerfeld (1909) for a half-space earth, and extended to a multilayered earth by Wait (1970), the Hertz vectors for the vertical dipole sources have only a z-component, while for the horizontal dipole sources, the Hertz vectors have both x- and z-components. The vertical dipole sources have solutions of the form

$$\Pi_z^0 = \frac{e^{ik_0R}}{R} + \frac{1}{2W}\int_{-\infty}^{\infty}\frac{\lambda}{P_0}a_0(\lambda)e^{-P_0(Z+h)}H_0^1(\lambda\rho)d\lambda, \tag{10}$$

$$\Pi_z^1 = \frac{1}{2W}\int_{-\infty}^{\infty}\frac{\lambda}{P_0}\left[a_1(\lambda)e^{P_1Z} + a_2(\lambda)e^{-P_1Z}\right]\cdot e^{-P_0h}H_0^1(\lambda\rho)d\lambda, \tag{11}$$

and

$$\Pi_z^2 = \frac{1}{2W}\int_{-\infty}^{\infty}\frac{\lambda}{P_0}a_3(\lambda)\cdot e^{P_2Z+(P_2-P_1)d-P_0h}H_0^1(\lambda\rho)d\lambda. \tag{12}$$

λ is the separation constant of the differential equation, and $p_j=(\lambda^2-k_j^2)^{1/2}$, with the sign of the root being chosen such that the solution satisfies the radiation condition. In the above form, after scaling by W, λ is a dimensionless parameter, and $k_j=2\pi(K_jM_j)^{1/2}$ is the relative propagation constant of each region. The $a_j(\lambda)$ are unknown functions of λ which are found by satisfying the boundary conditions that tangential $\mathbf{E}$ and $\mathbf{H}$ be continuous at $z=0$ and $z=-d$.

For horizontal dipole sources, the solutions for the Hertz vector take the form

$$\Pi_x^0 = \frac{e^{ik_0R}}{WR} + \frac{1}{2W}\int_{-\infty}^{\infty}\frac{\lambda}{P_0}b_0(\lambda)e^{-P_0(Z+h)}H_0^1(\lambda\rho)d\lambda, \tag{13}$$

and

$$\Pi_z^0 = \frac{\cos\phi}{2W}\int_{-\infty}^{\infty}\frac{\lambda^2}{P_0}c_0(\lambda)\cdot e^{-P_0(Z+h)}H_1^1(\lambda\rho)d\lambda \tag{14}$$

for region 0;

$$\Pi_x^1 = \frac{1}{2W}\int_{-\infty}^{\infty}\frac{\lambda}{P_0}\left[b_1(\lambda)e^{P_1 z} + b_2(\lambda)e^{-P_1 z}\right] \cdot e^{-P_0 h}H_0^1(\lambda\rho)d\lambda, \tag{15}$$

and

$$\Pi_z^1 = \frac{\cos\phi}{2W}\int_{-\infty}^{\infty}\frac{\lambda^2}{P_0}\left[c_1(\lambda)e^{P_1 z} + c_2(\lambda)e^{-P_1 z}\right] \cdot e^{-P_0 h}H_1^1(\lambda\rho)d\lambda \tag{16}$$

for region 1; and

$$\Pi_x^2 = \frac{1}{2W}\int_{-\infty}^{\infty}\frac{\lambda}{P_0}b_3(\lambda) \cdot e^{P_2 z + (P_2 - P_1)d - P_0 h}H_0^1(\lambda\rho)d\lambda, \tag{17}$$

and

$$\Pi_z^2 = \frac{\cos\phi}{2W}\int_{-\infty}^{\infty}\frac{\lambda^2}{P_0}c_3(\lambda) \cdot e^{P_2 z + (P_2 - P_1)d - P_0 h}H_1^1(\lambda\rho)d\lambda \tag{18}$$

for region 2.

The parameters λ and P_j are the same as for the vertical dipole solutions, and the coefficients $b_j(\lambda)$ and $c_j(\lambda)$ are found by satisfying the condition that tangential **E** and **H** be continuous at the boundaries.

The boundary conditions for the Hertz vectors and the resulting expressions for $a_j(\lambda)$, $b_j(\lambda)$, and $c_j(\lambda)$ are tabulated in Appendix A. The expressions for $a_j(\lambda)$, $b_j(\lambda)$, and $c_j(\lambda)$ are written in terms of the *TE* and *TM* Fresnel plane-wave reflection and transmission coefficients. Using this notation, the similarity of all the solutions is clearly emphasized and makes general discussion of the solutions possible rather than dealing with each source separately.

In discussing the approximate evaluation of the above integral expressions, extensive use is made of the plane-wave spectrum concept, since the wave nature of the problem is most clearly understood using this approach. A brief outline of the plane-wave spectrum notation used and approximate evaluation of integrals by the saddle-point method is given in Appendix B.

For radio interferometry applications, the fields at the earth's surface for the source placed at the earth's surface are of primary interest; this corresponds to setting both z and h equal to 0 in the preceding expressions for the Hertz vectors. In the following discussions, h is always set equal to 0, and, in most instances, z is assumed to be close to 0. The solutions are discussed in two parts; the half-space solutions and the two-layer earth solutions. The half-space solutions for the Hertz vectors are obtained by setting $K_1 = K_2$ and $M_1 = M_2$ in expressions (10) through (18). The half-space solution is of considerable interest since the fields about the source show interference maxima and minima without a subsurface reflector present. It also provides a base level for detection of reflections from depth.

APPROXIMATE SOLUTIONS

Half-space earth

The solution of the half-space problem is treated by numerous authors, and the wave nature of the fields is well defined. In the following discussions, the results of Ott (1941) and Brekhovskikh (1960) are followed quite closely, and detailed discussions of various aspects of the solutions can be found in these references. The wave nature of the fields about the source is illustrated in Figure 3. The wavefronts denoted A and B are spherical waves in the air and earth regions; wave C in the air is an inhomogeneous wave, and wave D in the earth has numerous names, the most common being head, flank, or lateral wave. Waves C and D exist only in a limited spatial region, which is defined as those points whose position vectors make an angle greater than α^c with the z-axis. The angle α^c is related to the critical angle of the boundary and is defined in Appendix B.

All the dipole sources exhibit the same wave nature. To demonstrate how the waves are derived from the integral expressions, the vertical magnetic dipole source is used for illustration. In the air, the Hertz vector is given by

$$\Pi_z^0 = \frac{e^{ik_0 R}}{WR} + \frac{ik_0}{2W}\int_c \sin\theta_0 R_{01}(\theta_0) \cdot e^{ik_0 z\cos\theta_0}H_0^1(k_0\rho\sin\theta_0)d\theta_0, \tag{19}$$

and in the earth by

$$\Pi_z^1 = \frac{ik_1}{2W}\int_c \sin\theta_1 T_{10}(\theta_1) \cdot e^{-ik_1 z\cos\theta_1}H_0^1(k_1\rho\sin\theta_1)d\theta_1. \tag{20}$$

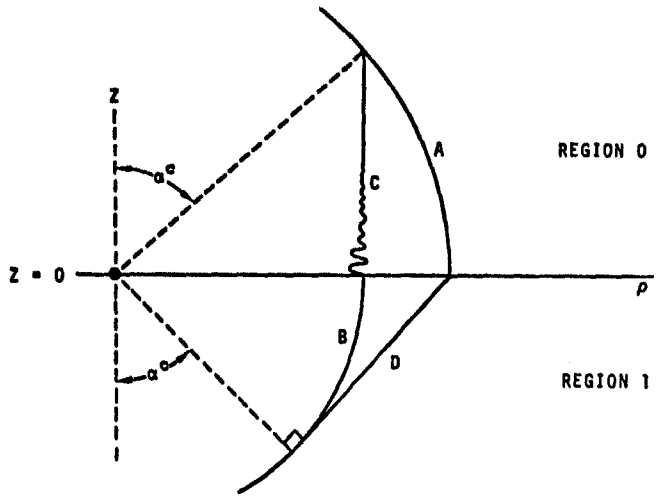

FIG. 3. Wavefronts about a dipole source on the surface of a half-space earth. A and B are spherical waves in the air and earth, respectively, wave C is an inhomogeneous wave in air, and D is the head wave in the earth.

With the aid of the Hankel transform identity (Sommerfeld, 1949),

$$\frac{e^{ik_0R}}{WR} = \frac{ik_0}{2W}\int_c \sin\theta_0 \cdot e^{ik_0|Z|\cos\theta_0} H_0^1(k_0\rho\sin\theta_0)\,d\theta_0, \tag{21}$$

and the relation $R_{ij} = T_{ij} - 1$ for the Fresnel coefficients, equation (19) becomes

$$\Pi_Z^0 = \frac{ik_0}{2W}\int_c \sin\theta_0 T_{01}(\theta_0) \cdot e^{ik_0|Z|\cos\theta_0} H_0^1(k_0\rho\sin\theta_0)\,d\theta_0. \tag{22}$$

Using the saddle-point method as discussed in Appendix B, the approximate solutions of the integral expressions (20) and (22) are

$$\Pi_Z^0 = \frac{e^{ik_0R}}{WR}\left\{T_{01}(\alpha) - \frac{i}{2k_0R}\left(T_{01}''(\alpha) + \cot\alpha T_{01}'(\alpha)\right)\right\}, \tag{23}$$

and

$$\Pi_Z^1 = \frac{e^{ik_1R}}{WR}\left\{T_{10}(\alpha) - \frac{i}{2k_1R}\left[T_{10}''(\alpha) + \cot\alpha T_{10}'(\alpha)\right]\right\}, \tag{24}$$

where $R = (\rho^2 + Z^2)^{1/2}$, and $\alpha = \tan^{-1}\rho/|Z|$. Expressions (23) and (24) correspond to the spherical waves A and B in Figure 3. The bracketed terms on the right may be interpreted as the modification to the directionality of the source due to the presence of the boundary.

The waves C and D are generated by crossing the branch points of T_{01} and T_{10} to obtain the saddle-point solutions (23) and (24) for angles $\alpha > \alpha^c$. As outlined in Appendix B, the contribution of the branch point can be approximately evaluated by the method of steepest descent as long as α is not close to the branch point. For $\alpha > \alpha^c$ the expressions

$$I_B^0 = \frac{2ik_1\eta_{01}(1 - \cot\alpha\tan\theta_{01}^c)^{-3/2}\, e^{ik_1\rho - (k_1^2 - k_0^2)^{\frac{1}{2}}Z}}{(k_1^2 - k_0^2)W\rho^2}, \tag{25}$$

and

$$I_B^1 = \frac{2ik_0\eta_{10}(1 - \cot\alpha \tan\theta_{10}^c)^{3/2} e^{ik_0\rho - i(k_1^2 - k_0^2)^{1/2}z}}{(k_1^2 - k_0^2)W\rho^2} \tag{26}$$

must be added to (23) and (24) in order that the solutions be correct. Expression (25) is readily identified as the inhomogeneous wave C, and (26) corresponds to the lateral wave D.

The asymptotic solutions have the form of the geometrical optics solution plus second-order correction terms. For a perfectly dielectric earth, expressions (24) and (26) become infinite as α approaches α^c. The singular behavior arises from the second-order terms which depend on the derivatives of $T_{10}(\theta_1)$. The first-order term which is the geometrical optics solution remains bounded. In this particular case, the angle α^c is the critical angle of $T_{10}(\theta_1)$. As a result, the saddle point and branch point coincide at $\alpha=\alpha^c$, and the approximate methods used to evaluate the integrals are no longer valid. The conical surface about the z-axis, defined by $\alpha=\alpha^c$, is the region where the lateral and spherical waves merge together. In this region the two waves cannot be considered separately; the combined effect of the saddle point and branch point must be evaluated. Detailed analysis of this region for integrals similar to expression (20) is given by Brekhovskikh (1960), who obtains an asymptotic solution with the geometrical optics solution, as the leading term plus a connection term which falls off as $(k_1R)^{-5/4}$ instead of $(k_1R)^{-2}$. This result indicates that the geometrical optics solution still describes the fields adequately for $\alpha\sim\alpha^c$ when $(k_1R)^{-1/4}\ll 1$. The correction terms given in (24) and (26), however, are not valid when α is close to α^c.

The fields at the earth's surface are of primary interest and are obtained by setting $z=0$ and $\alpha=\pi/2$ in (23), (24), (25), and (26). The solutions given are valid for this region provided the contrast in material properties is not extremely large. In the case of large contrasts, as occur in conductive earth problems, the transmission and reflection coefficients have a pole near $\theta_0=\pi/2$. The pole is located at $\theta_0=\pi-\theta_B$, where θ_B is the Brewster angle. The role of this pole in radio wave propagation over a conductive earth has been the subject of a tremendous amount of discussion since Sommerfeld (1909, 1949) equated the contribution of this pole to the Zenneck surface wave. Numerous people (Norton, 1937; Ott, 1943; Van der Waerden, 1951; Brekhovskikh, 1960; and Wait, 1970) have considered the problem since then using the modified saddle-point technique to evaluate the integrals for $\alpha\sim\pi/2$. While a true surface wave is not excited, the pole enhances the fields near the source in such a manner that they fall off approximately as $(kR)^{-1}$. At large distances from the source, the fields are those determined by the normal saddle-point method which have a $(kR)^{-2}$ fall off. The transition between the ranges is determined by the proximity of θ_B to $\pi/2$. In the radio interferometry application, the earth properties of interest are those of a low-loss dielectric which is assumed to have only moderate contrasts with the free-space properties. The pole in this case is well away from $\pi/2$ and does not affect the preceding solutions.

In the particular situation of an earth where $M_0=M_1$, the Hertz vector for a vertical magnetic dipole can be evaluated exactly for $z=h=0$. The result is

$$\Pi_Z^0=\Pi_Z^1=\frac{2}{(k_1^2-k_0^2)W\rho^2}\left[e^{ik_0\rho}\left(ik_0-\frac{1}{\rho}\right)-e^{ik_1\rho}\left(ik_1-\frac{1}{\rho}\right)\right], \tag{27}$$

as shown by Wait (1951). This provides a check on the approximate solution. The approximate solution, obtained by adding (23) and (25) or (24) and (26) for $\alpha=\pi/2$, is

$$\Pi_Z^0=\Pi_Z^1=\frac{2i}{(k_1^2-k_0^2)W\rho^2}\left[k_0e^{ik_0\rho}-k_1e^{ik_1\rho}\right], \tag{28}$$

which is the same as (27) if third-order terms are neglected.

The integral expressions for the Hertz vectors for the other dipole sources can be treated in the same manner as for the vertical magnetic dipole. For $z\sim 0$, in the air, they have the form

$$(-ik_0\cos\phi\sin\alpha)^n\frac{e^{ik_0R}}{WR}\left[G_1(\alpha)+\frac{G_2(\alpha)}{2k_0R}\right]+(\cos\phi)^n(1-\cot\alpha\tan\theta_{10}^c)^{-3/2} \tag{29}$$

$$\cdot G_3(\alpha)\,\frac{e^{ik_1\rho-(k_1^2-k_0^2)^{\frac{1}{2}}z}}{W\rho^2}.$$

The $G_i(\alpha)$ for the various sources are tabulated in Table 1. The electric and magnetic fields can be obtained by differentiation of the preceding solutions; the particular form of the integrals encountered permits interchange of the integration and differentiation steps.

The half-space solutions demonstrated that interference patterns will be observed in the field strengths even when there is no subsurface reflector. This is readily seen from equation (28). The fields at the earth's surface are composed of two propagating components with one having the phase velocity of the air, and the other the velocity of the earth. Another important feature of the half-space solutions is that the fields near the boundary fall off as the inverse square of the radial distance from the source at distances greater than two or three wavelengths from the source.

A convenient method of interpreting the solutions is to equate the radiation pattern of the source on the boundary to the first-order term in the preceding solutions. This technique demonstrates how the boundary modifies the directionality of the source. The radiation pattern is sharply peaked in the direction of the critical angle into the earth. A sketch of the radiation pattern for a vertical dipole source is shown in Figure 4. This directionality of the source is important when reflections from a subsurface boundary are considered.

Two-layer earth

The analysis of the integral expressions for the two-layer earth problem is carried out in two different ways. The depth of the subsurface boundary and the electromagnetic losses of the first layer determine which approach is more useful. The primary method of analysis is to treat the first layer of the earth as a leaky waveguide and use normal mode analysis. In certain cases the mode analysis is cumbersome, and these cases

Table 1. Coefficients $G_i(\alpha)$ for half-space earth solutions for various dipole sources.

Source	Hertz Vector	n	G_1	G_2	G_3
Vertical Magnetic Dipole	Magnetic Π_z^0	0	$T_{01}(\alpha)$	$-i(G_1''(\alpha)+G_1'(\alpha)\cot\alpha)$	$-\dfrac{2ik_1\eta_{01}}{k_1^2-k_0^2}$
Vertical Electric Dipole	Electric Π_z^0	0	$S_{01}(\alpha)$	$-i(G_1''(\alpha)+G_1'(\alpha)\cot\alpha)$	$-\dfrac{2ik_1\xi_{01}}{k_1^2-k_0^2}$
Horizontal Magnetic Dipole	Magnetic Π_x^0	0	$S_{01}(\alpha)$	$-i(G_1''(\alpha)+G_1'(\alpha)\cot\alpha)$	$-\dfrac{2ik_1\xi_{01}}{k_1^2-k_0^2}$
	Magnetic Π_z^0	1	$\dfrac{(\gamma_{01}-1)T_{01}(\alpha)S_{01}(\alpha)}{2P_0(\alpha)}$	$-i(G_1''(\alpha)+3G_1'(\alpha)\cot\alpha-2G_1(\alpha))$	$\dfrac{2ik_0^2(\xi_{10}+\eta_{10})}{k_1^2(k_0^2-k_1^2)^{1/2}}$
Horizontal Electric Dipole	Electric Π_x^0	0	$T_{01}(\alpha)$	$-i(G_1''(\alpha)+G_1'(\alpha)\cot\alpha)$	$-\dfrac{2ik_1\eta_{01}}{k_1^2-k^2}$
	Electric Π_z^0	1	$\dfrac{(\gamma_{01}-1)T_{01}(\alpha)S_{01}(\alpha)}{2P_0(\alpha)}$	$-i(G_1''(\alpha)+3G_1'(\alpha)\cot\alpha-2G_1(\alpha))$	$\dfrac{2ik_0^2(\eta_{10}+\xi_{10})}{k_1^2(k_0^2-k_1^2)^{1/2}}$

Definition: $G_1'(\alpha)=\left.\dfrac{dG_1(\theta_0)}{d\theta_0}\right|_{\theta_0=\alpha}$ $\qquad$ $G_1''=\left.\dfrac{d^2G_1(\theta_0)}{d\theta_0^2}\right|_{\theta_0=\alpha}$

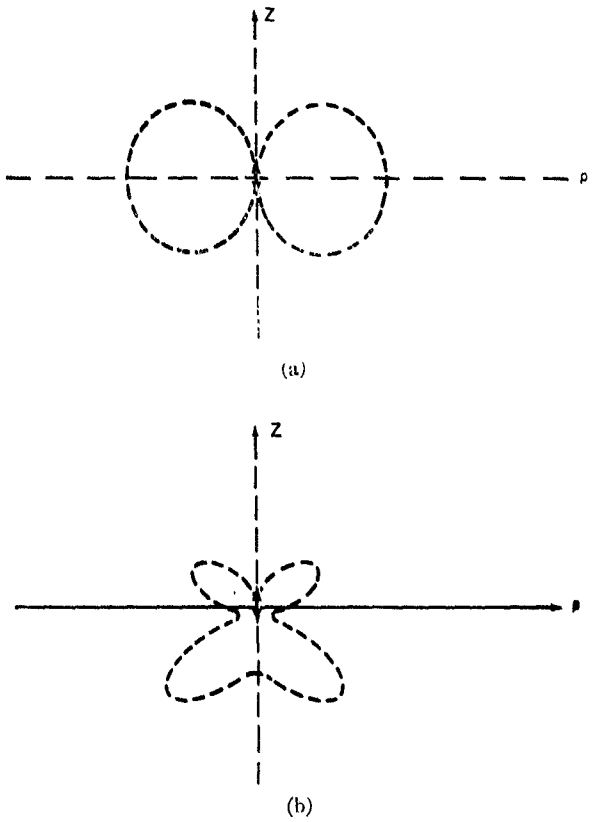

FIG. 4. Sketch showing how a dielectric boundary modifies the directionality of a vertical dipole source placed on the boundary. (a) No boundary present. (b) Boundary at $Z=0$.

yield more useful results when the integrals are solved approximately using the saddle-point method of integration.

The various dipole sources may all be treated in the same manner. For the purpose of illustrating the method of analysis, the horizontal electric dipole source solutions are used as an example. The x- and z-components of the electric Hertz vector in the air for this source are given by equations (13) and (14) where the coefficients b_0 and c_0 are listed in Table A-2.

For normal mode analysis, equation (13) is rewritten using the integral identity [equation (21)]. The components of the Hertz vector are given by

$$\Pi_x^0 = \frac{ik_1}{2W}\int_c \sin\theta_1 m_{10}(\theta_1)[1 + b_0(\theta_1)] \cdot e^{ik_0 Z\cos\theta_0} H_0^1(k_1\rho\sin\theta_1)\,d\theta_1, \tag{30}$$

and

$$\Pi_Z^0 = \cos\phi\,\frac{ik_1^2}{2W}\int_c \sin^2\theta_1 m_{10}(\theta_1)c_0(\theta_1) \cdot e^{ik_0\cos\theta_0 Z} H_1^1(k_1\rho\sin\theta_1)\,d\theta_1, \tag{31}$$

where the integration variable is θ_1, as defined in Appendix B. The singularities of the coefficients b_0 and c_0 determine the nature of the solutions to equations (30) and (31).

The expressions

$$m_{10}(1 + b_0) = \frac{\eta_0 T_{10}(1 + R_{12}\beta)}{1 - R_{10}R_{12}\beta}, \tag{32}$$

and

$$m_{10}c_0 = \frac{1}{2\rho_0} \cdot \left[\frac{(\gamma_{01}-1)\eta_{10}T_{10}(1+R_{12}\beta)S_{01}(1+X_{12}\beta)}{(1-X_{10}X_{12}\beta)(1-R_{10}R_{12}\beta)}\right.$$

$$\frac{(\gamma_{21}-1)\xi_{10}S_{10}S_{12}\gamma_{01}T_{01}\gamma_{12}T_{12}\beta}{(1-X_{10}X_{12}\beta)(1-R_{10}R_{12}\beta)}\Bigg] \quad (33)$$

have branch points at the two critical angles of the two boundaries in question. In addition, equation (32) has an infinite set of simple poles, and (33) has a doubly infinite set of poles on each Riemann surface. These poles are determined by the normal mode equations,

$$1 - R_{10}R_{12}\beta = 0, \quad (34)$$

and

$$1 - X_{10}X_{12}\beta = 0. \quad (35)$$

Equations (34) and (35) are the TE and TM normal mode equations, respectively. Both are transcendental equations with infinite sets of roots. The relation between the normal modes and multiple reflections is readily obtained by expanding the denominators of equations (32) and (33) into infinite geometric series. For example,

$$(1 - R_{10}R_{12}\beta) = \sum_{n=0}^{\infty} (R_{10}R_{12}\beta)^n. \quad (36)$$

The positions of the poles and branch points in the complex plane determine the wave nature of the solutions to equations (30) and (31). The normal mode solutions are obtained by deforming the contour of integration C to C', as schematically illustrated in Figure 5. The integral from $-(\pi/2)+i\infty$ to $\pi/2+i\infty$, and from $\pi/2+i\infty$ to $\pi/2-i\infty$ is identically zero. Along the first part of C' the integral is zero since the integrand is zero. Along the second part of the contour C' the integral is zero due to the asymmetry of the integrand about $\theta_1=\pi/2$. This result is common in mode analysis and has a wide range of applications as discussed in detail by Brekhovskikh (1960). The integral along C is equal to the residues of the poles crossed in deforming the contour to C', plus the integrals along contours C_1 and C_2 which run from $+i\infty$ around the branch points and back to $+i\infty$. The components of the Hertz vector are given by

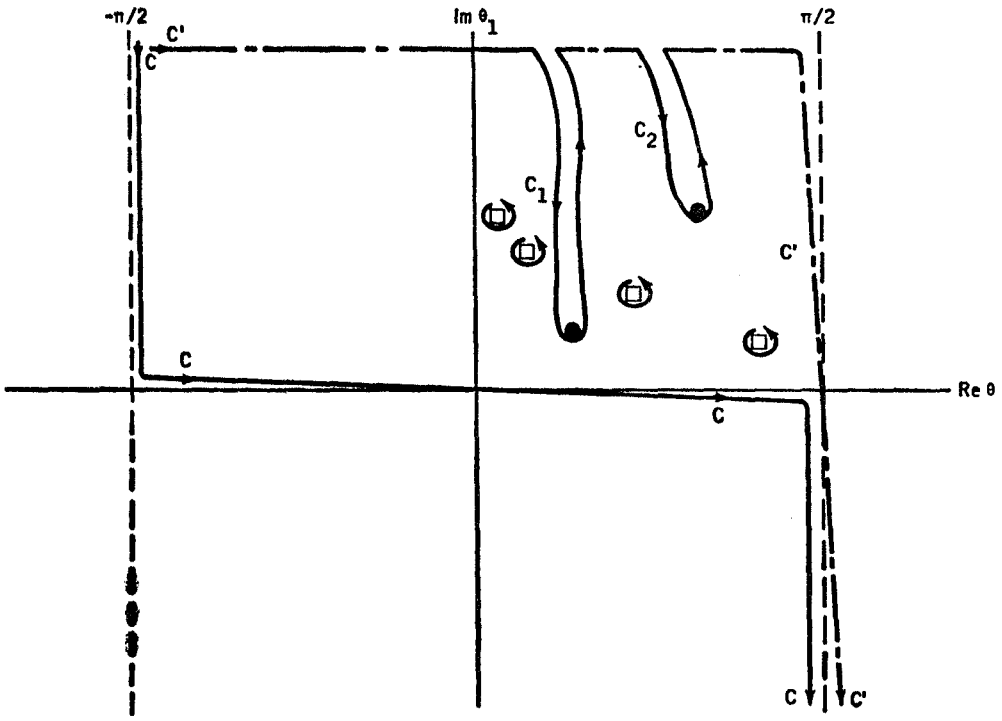

FIG. 5. Complex θ_1-plane showing how integration contour C is modified to C' in order to obtain normal mode solutions. Branch points denoted by solid circles and the poles by squares.

Table 2. Residues of poles for normal mode analysis for horizontal electric dipole.

Π_x^0 *TE* Mode Residue	$\dfrac{ik_1 \sin\theta_1^P \eta_{10} T_{10}(\theta_1^P)[1 + R_{12}(\theta_1^P)\beta(\theta_1^P)] e^{ik_0(1-\gamma_{10}\sin^2\theta_1^P)^{1/2}z}}{2W\left(i2k_1 d\cos\theta_1^P - \dfrac{\partial \ln R_{10}(\theta_1)R_{12}(\theta_1)}{\partial\theta_1}\right)\Big\vert_{\theta_1=\theta_1^P}} H_0^1(k_1\rho\sin\theta_1^P)$
Π_z^0 *TE* Mode Residue	$\dfrac{\cos\phi ik_1^2 \sin^2\theta_1^P l(\theta_1^P) e^{ik_0(1-\gamma_{10}\sin^2\theta_1^P)^{1/2}z}}{2W[1 - X_{10}(\theta_1^P)X_{12}(\theta_1^P)\beta(\theta_1^P)]\left(i2k_1 d\cos\theta_1^P - \dfrac{\partial \ln R_{10}(\theta_1)R_{12}(\theta_1)}{\partial\theta_1}\right)\Big\vert_{\theta_1=\theta_1^P}} H_1^1(k_1\rho\sin\theta_1^P)$
Π_z^0 *TM* Mode Residue	$\dfrac{\cos\phi ik_1^2 \sin^2\theta_1^P l(\theta_1^P) e^{ik_0(1-\gamma_{10}\sin^2\theta_1^P)^{1/2}z}}{2W[1 - R_{10}(\theta_1^P)R_{12}(\theta_1^P)\beta(\theta_1^P)]\left(i2k_1 d\cos\theta_1^P - \dfrac{\partial \ln X_{10}(\theta_1)X_{12}(\theta_1)}{\partial\theta_1}\right)\Big\vert_{\theta_1=\theta_1^P}} H_1^1(k_1\rho\sin\theta_1^P)$

where $l(\theta_1^P) = \dfrac{(\gamma_{01}-1)}{2P_0(\theta_1^P)}[\eta_{10}T_{10}(\theta_1^P)[1 + R_{12}(\theta_1^P)\beta(\theta_1^P)]S_{01}(1 + X_{12}(\theta_1^P)\beta(\theta_1^P))]$

$- \dfrac{(\gamma_{21}-1)}{2P_0(\theta_1^P)}[\xi_{10}S_{10}(\theta_1^P)S_{12}(\theta_1^P)\gamma_{01}T_{01}(\theta_1^P)\gamma_{12}T_{12}(\theta_1^P)\beta(\theta_1^P)]$

$$\Pi_x^0 = 2\pi i \sum (TE \text{ pole residues}) + I_1 + I_2, \tag{37}$$

and

$$\Pi_z^0 = 2\pi i \sum (TE \text{ pole residues}) + 2\pi i \sum (TM \text{ pole residues}) + I_3 + I_4, \tag{38}$$

where

$$I_1 = \frac{ik_1}{2W}\int_{c_1} \sin\theta_1 m_{10}(\theta_1)[1 + b_0(\theta_1)] \cdot e^{ik_0 z\cos\theta_0} H_0^1(k_1\rho\sin\theta_1)d\theta_1, \tag{39}$$

$$I_2 = \frac{ik_1}{2W}\int_{c_2} \sin\theta_1 m_{10}(\theta_1)[1 + b_0(\theta_1)] \cdot e^{ik_0 z\cos\theta_0} H_0^1(k_1\rho\sin\theta_1)d\theta_1, \tag{40}$$

$$I_3 = \cos\phi\,\frac{ik_1^2}{2W}\int_{c_1} \sin^2\theta_1 m_{10}(\theta_1)c_0(\theta_1) \cdot e^{ik_0 z\cos\theta_0} H_1^1(k_1\rho\sin\theta_1)d\theta_1, \tag{41}$$

$$I_4 = \cos\phi\,\frac{ik_1^2}{2W}\int_{c_2} \sin^2\theta_1 m_{10}(\theta_1)c_0(\theta_1) \cdot e^{ik_0 z\cos\theta_0} H_1^1(k_1\rho\sin\theta_1)d\theta_1. \tag{42}$$

The solutions (37) and (38) are completely general and valid provided a branch point and a pole, or a *TE* and *TM* pole, do not coincide. In the first situation, the pole and branch-point contributions must be considered together rather than separately, as indicated. In the other situation, (38) must include the residue of a second-order pole rather than the residues of two simple poles, as indicated. Since these situations rarely occur, they are not discussed further here.

The expressions for the residues in (37) and (38) are tabulated in Table 2. Approximate solutions to the branch cut integrals may be obtained by steepest-descent integration as discussed in Appendix B. The solutions are the second-order lateral and inhomogeneous waves generated at the boundaries. The approximate solutions are listed in Table 3.

The behavior of the fields at the earth's surface is very dependent on the position of the singular points in the complex θ_1 plane, which points are, in turn, determined by the material properties of the earth and the layer thickness d. The important features of the solutions are the radial dependences and the initial amplitudes of the various terms in the solutions. All the residues contain Hankel functions, which, for radial distances greater than one or two wavelengths, have the form

Table 3. Approximate steepest-descent solutions to branch-cut integrals for normal mode analysis of the horizontal electric dipole.

I_1	$\dfrac{2ik_0\eta_{10}^2(1+R_{12}(\theta_{10}^c)\beta(\theta_{10}^c))^2 e^{ik_0\rho}}{(k_1^2-k_0^2)(1-R_{12}(\theta_{10}^c)\beta(\theta_{10}^c))^2 W\rho^2}$
I_2	$\dfrac{2ik_1^2\eta_{20}T_{10}^2(\theta_{12}^c)(1-\cot\alpha_d\tan\theta_{12}^c)^{-3/2} e^{ik_0\rho-2d(k_2^2-k_1^2)^{1/2}-(k_2^2-k_0^2)^{1/2}Z}}{k_2(k_1^2-k_0^2)(1-R_{10}(\theta_{12}^c)\beta(\theta_{12}^c))^2 W\rho^2}$
I_3	$-\dfrac{\cos\phi k_0}{2(k_1^2-k_0^2)^{1/2}}\left[\dfrac{C_1(\theta_{10}^c)e^{ik_0\rho}}{W\rho^2}+\dfrac{(1-\cot\alpha_d\tan\theta_{10}^c)^{-3/2}C_2(\theta_{10}^c)e^{ik_0\rho+i2d(k_1^2-k_0^2)^{1/2}}}{W\rho^2}\right]$
I_4	$-\dfrac{\cos\phi k_2(1-\cot\alpha_d\tan\theta_{12}^c)^{-3/2}C_3(\theta_{12}^c)\, e^{ik_2\rho-(k_2^2-k_1^2)^{1/2}2d-(k_2^2-k_0^2)^{1/2}Z}}{2(k_1^2-k_2^2)^{1/2}W\rho^2}$
$C_1(\theta_{10}^c)$	$\dfrac{4i\gamma_{10}}{k_0}\left[\dfrac{\eta_{01}(1-R_{12}^2\beta^2)(1+X_{12}\beta)^2+\xi_{01}(1-X_{12}^2\beta^2)(1+R_{12}\beta)^2}{(1-X_{12}\beta)^2(1-R_{12}\beta)^2}\right]$
$C_2(\theta_{10}^c)$	$\dfrac{4i\gamma_{10}(1-\gamma_{12})\gamma_{01}S_{12}T_{12}[\eta_{01}(1+X_{12}\beta)(1-R_{12}\beta)+\xi_{01}(1-X_{12}\beta)(1+R_{12}\beta)]}{k_0(1-\gamma_{01})(1-X_{12}\beta)^2(1-R_{12}\beta)^2}$
$C_3(\theta_{12}^c)$	$\dfrac{2i\eta_{10}T_{10}S_{01}\sqrt{\gamma_{21}}\{(\gamma_{01}-1)[\xi_{12}S_{10}(1+T_{01}\beta-R_{10}\beta^2)+\eta_{12}T_{10}(1+S_{01}\beta-X_{10}\beta^2)]-2(1-\gamma_{12})\gamma_{01}\gamma_{12}[\xi_{21}(1+X_{10}\beta)(1-R_{10}\beta)+\eta_{21}(1-X_{10}\beta)(1+R_{10}\beta)]\}}{k_0(1-\gamma_{20})^{1/2}(1-\gamma_{21})^{1/2}(1-X_{10}\beta)^2(1-R_{12}\beta)^2}$
	$\sin\theta_{10}^c=\dfrac{k_0}{k_1}\qquad \sin\theta_{12}^c=\dfrac{k_2}{k_1}\qquad \alpha_d=\tan^{-1}\left\lvert\dfrac{2d}{\rho}\right\rvert$

$$\rho^{-1/2}e^{ik_1\rho\sin\theta_1^p}, \tag{43}$$

where θ_1^p is a pole defined by equations (34) and (35). The branch cut contributions, I_1 and I_3, fall off as ρ^{-2} with no exponential attenuation, while I_2 and I_4 fall off as ρ^{-2} and are exponentially attenuated when the earth is lossy. The amplitudes of the modes are largest for those poles in the vicinity of θ_{10}^c. This effect is related to the modified directionality of the source as discussed for the half-space fields. When the earth has a finite loss all terms in the solution except I_1 and the first term of I_3 have amplitudes which decay exponentially with increasing loss or increasing d.

The positions of the poles in the complex θ_1 plane for three idealized models are illustrated schematically in Figure 6. The earth consists of a perfect dielectric slab over a half-space, which is a perfect conductor in case (a), a perfect dielectric with $K_2>K_1$ in case (b), and a perfect dielectric with $K_2<K_1$ in case (c). In all cases $M_0=M_1=M_2$ is assumed since permeabilities of bulk earth materials vary little from the free-space value. The poles lie on the lines $|R_{10}R_{12}\beta|=1$ and $|X_{10}X_{12}\beta|=1$, with the density of distribution of the poles on these lines controlled by the slab thickness d. For d small, the poles are widely spaced with most of them lying high up the lines near the imaginary θ_1 axis. For increasing d, the poles move down the lines toward $\theta_1=\pi/2$ and are more closely packed. Unattenuated modes occur only when the θ_1^p lie on or close to the real θ_1 axis. In case (a), the pole contours lie on the real axis for $\theta_{10}^c\le\theta_1\le\pi/2$; unattenuated modes can be excited when θ_1 exceeds the critical angle of the free-space-earth interface. In case (c), the slab forms a dielectric waveguide when θ_1 is greater than the critical angles of both boundaries. For both (a) and (c), the modes with real θ_1^p less than the largest critical angle are highly damped due to energy leaking out of the slab. In

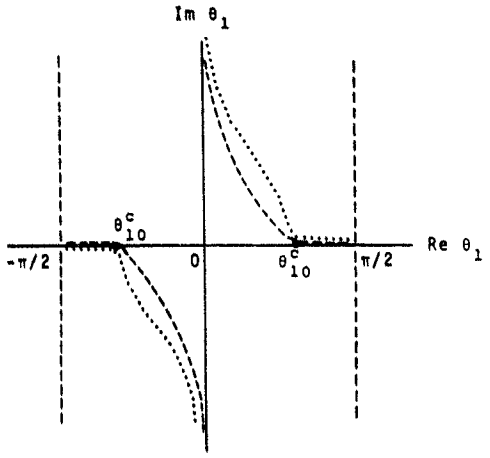

$K_0 = 1$	FREE SPACE
K_2	PERFECT DIELECTRIC
	PERFECT CONDUCTOR

(a)

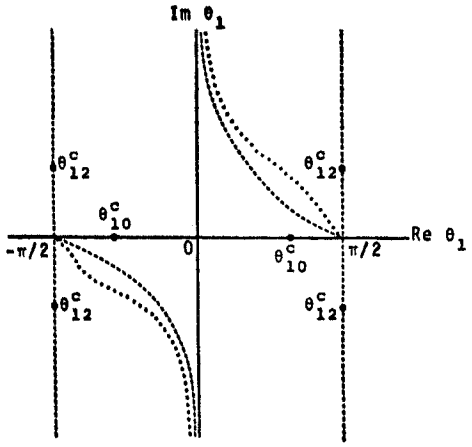

$K_0 = 1$	FREE SPACE
K_1	PERFECT DIELECTRIC
$K_2 > K_1$	PERFECT DIELECTRIC

(b)

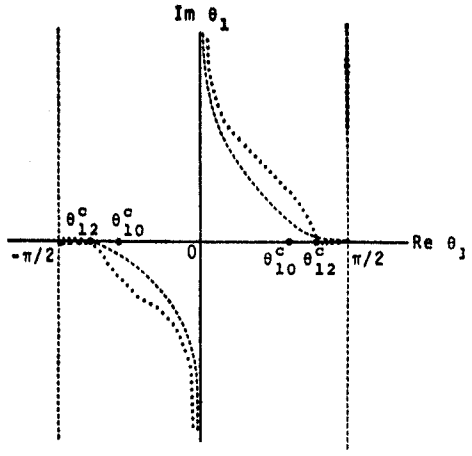

$K_0 = 1$	FREE SPACE
K_1	PERFECT DIELECTRIC
$K_2 < K_1$	PERFECT DIELECTRIC

(c)

FIG. 6. Sketches of complex θ_1-plane showing positions of branch points and pole lines for 3 simple two-layer earth cases; case (a), dielectric slab over a perfect conductor; case (b), dielectric slab over dielectric half-space with $K_2 > K_1$; case (c) dielectric slab over a dielectric half-space with $K_2 < K_1$. The dashed lines are contours where $|R_{10}R_{12}\beta| = 1$; the dotted lines are contours where $|X_{10}X_{12}\beta| = 1$; the branch points are denoted by solid circles.

case (b), no unattenuated mode can exist, since energy is continually flowing out of the slab into the lower half-space. The effect of a finite loss in the slab moves the pole contours up away from the real axis, and all modes have a finite attenuation. These models demonstrate the general position and behavior of the singular points in the complex plane. More detailed studies are given by Wait (1970), Brekhovskikh (1960), and Budden (1961).

The normal mode approach is most useful when the distance from the source is greater than the depth of the boundary d and when the earth has a very low loss. In a lossy dielectric, the complex dielectric constant is $K'(1+i \tan \delta)$, where K' is the real dielectric constant and $\tan \delta$ is the loss tangent; and the attenuation distance in free-space wavelengths for a plane wave is

$$D = \frac{1}{\pi \sqrt{K'} \tan \delta}, \tag{44}$$

when $\tan \delta \ll 1$. When d approaches the attenuation distance, the solutions begin to approach those of a lossy dielectric half-space. An alternate approach to evaluating the fields when the distance from the source is less than d, or when $d \geq D$, is desirable, since the normal mode approach is cumbersome in these cases.

The integrals can be approximately evaluated by the saddle-point method of integration when multiple reflections are not strong. The fields can then be expressed as the half-space solution plus a contribution from the subsurface boundary. By regrouping the coefficients b_0 and c_0 in the form

$$b_0 = R_{01} + b_0^1 \beta, \tag{45}$$

$$c_0 = \frac{1}{2}(\gamma_{01} - 1)\frac{S_{01}T_{01}}{P_0} + c_0^1 \beta, \tag{46}$$

$$b_0^1 = \frac{T_{01}T_{10}R_{12}}{(1 - R_{10}R_{12}\beta)}, \tag{47}$$

and

$$c_0^1 = \frac{1}{2P_0}\left[\frac{(\gamma_{01} - 1)S_{01}T_{01}[T_{10}R_{12} + S_{10}X_{12} + (S_{01} + T_{01} - S_{21}T_{01})X_{12}R_{12}\beta]}{(1 - R_{10}R_{12}\beta)(1 - X_{10}X_{12}\beta)} - \frac{(\gamma_{21} - 1)\xi_{10}S_{10}S_{12}m_{01}T_{01}\gamma_{12}T_{12}}{(1 - R_{10}R_{12}\beta)(1 - X_{10}X_{12}\beta)}\right]. \tag{48}$$

The Hertz vector components can then be written as

$$\Pi_x^0 = L_1 + L_2, \tag{49}$$

and

$$\Pi_z^0 = L_3 + L_4, \tag{50}$$

where L_1 and L_3 are the half-space earth solutions discussed earlier, and L_2 and L_4, given by

$$L_2 = \frac{ik_1}{2W}\int_c \sin \theta_1 m_{10} b_0^1(\theta_1) \cdot e^{ik_0 z \cos \theta_0} \beta H_0^1(k_1 \rho \sin \theta_1) d\theta_1, \tag{51}$$

and

$$L_4 = \cos \phi \frac{ik_1^2}{2W}\int_c \sin^2 \theta_1 m_{10} c_0^1(\theta_1) \cdot e^{ik_0 z \cos \theta_0} \beta H_1^1(k_1 \rho \sin \theta_1) d\theta_1 \tag{52}$$

describe the effect of the subsurface boundary.

L_2 and L_4 can be approximately evaluated by the saddle-point method, which results in the geometric optics solution. Since z is assumed close to zero throughout, the expression

$$\beta H_n^1(k_1 \rho \sin \theta_1) \tag{53}$$

in the integrands may be regrouped using the asymptotic expansion of the Hankel function in the manner discussed in Appendix B. L_2 and L_4 then contain the expression

$$e^{i2k_1 d \cos \theta_1 + ik_1 \rho \sin \theta_1} = e^{ik_1 R_d \cos(\theta_1 - \alpha_d)} \tag{54}$$

in the integrand, where $R_d = (\rho^2 + 4d^2)^{1/2}$ and $\alpha_d = \tan^{-1}(\rho/2d)$. In this form α_d is the saddle point of the integrand and is the geometric optics direction of a ray reflected from the subsurface boundary. The saddle-point solutions of L_2 and L_4, outlined in Appendix B, are

$$L_2 \approx \frac{e^{ik_1R_d}}{WR_d}\left[P(\alpha_d) - \frac{i}{2k_1R_d}\left(P''(\alpha_d) + P'(\alpha_d)\cot\alpha_d\right)\right], \quad (55)$$

and

$$L_4 \approx \cos\phi \sin\alpha_d \frac{e^{ik_1R_d}}{WR_d} \cdot\left[Q(\alpha_d) - \frac{i}{2k_1R_d}\left(Q''(\alpha_d) + 3\cot\alpha_d Q'(\alpha_d) - 2Q(\alpha_d)\right)\right], \quad (56)$$

where

$$P = m_{10}(\alpha_d)b_0^1(\alpha_d)e^{ik_0Z(1-\gamma_{10}\sin^2\alpha_d)^{1/2}}, \quad (57)$$

and

$$Q = m_{10}(\alpha_d)c_0^1(\alpha_d)e^{ik_0Z(1-\gamma_{10}\sin^2\alpha_d)^{1/2}}. \quad (58)$$

Expressions (55) and (56) can be interpreted as having replaced the subsurface boundary by an image source at twice the depth. The image source has a radiation pattern which depends on the reflection and transmission coefficients of the boundaries and the layer thickness.

In obtaining the saddle-point solution, the effect of the poles and branch points has been neglected; such neglect is justified when the boundary is deep and the earth has a significant loss. This is illustrated in Figure 7. To obtain the saddle-point contribution, the integration contour C must be deformed into the saddle-point contour Γ. The position of Γ in the complex θ_1 plane is determined by α_d, which, in turn, is determined by the ratio of the radial distance to the depth of the boundary, $\rho/2d$. In order that a given pole or branch point be crossed when C is deformed to Γ, α_d must exceed a certain value which is determined by equation (B-11), which defines the contour Γ. Since $\rho = 2d \tan\alpha_d$, the radial distance from the source at which the singular point is

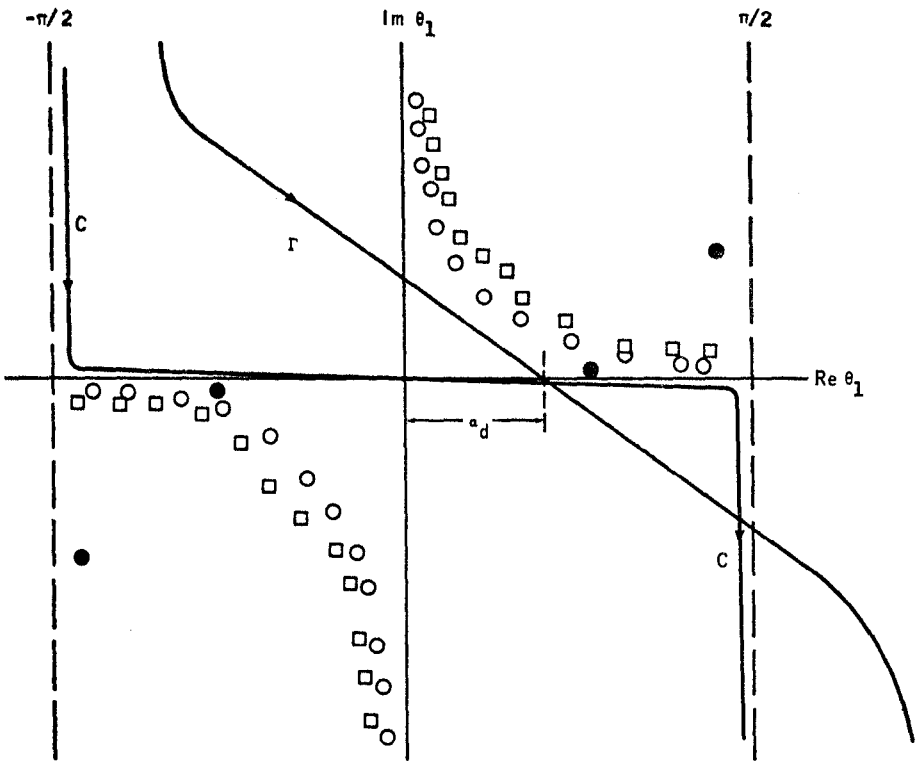

FIG. 7. Complex θ_1-plane showing deformation of contour C to saddle-point contour Γ. Solid circles = branch points' squares = *TE* poles, and open circles = *TM* poles.

crossed in obtaining Γ is defined. When the singular point is a pole, the contribution to the integral after crossing the pole is a residue of a form similar to those in Table 2. When the pole is not on the real θ_1 axis, the residue is exponentially attenuated with increasing radial distance. The value of ρ at which the pole must be considered in determining the integral is also defined, and is usually much greater than the attenuation distance of the mode. As a result, the residue of the pole is extremely small and is negligible compared to the saddle-point contribution. For cases when some poles lie on or near the real θ_1 axis, a fixed radial distance from the source must be exceeded before their effect needs to be considered. Beyond this distance, the normal mode approach is more convenient for expressing the solutions.

The branch-point contributions yield inhomogeneous and lateral waves generated at or reflected from the subsurface boundary. As in the case of the poles, a finite distance from the source must be exceeded before these contributions need to be considered. For the earth models where the saddle-point method is useful, these contributions, which are second-order effects, are negligible. When these second-order waves are significant in the determination of the field strengths at the earth's surface, the normal mode approach is the better method for computing the fields.

The two-layer earth solutions cover a wide range of possible responses. The important results are as follows:

1. When the first layer of the earth is very thin and the second layer is a low-loss medium, the first layer is undetectable. The response of the earth is the same as that of a half-space composed of the second layer of the earth.

2. When the first layer of the earth is on the order of one wavelength thick, the surface fields become extremely complex. The fields exhibit a $\rho^{-1/2}$ fall-off out to the attenuation distance of the least attenuated mode which is strongly excited. Beyond this distance, the contribution of the modes becomes negligible and the second-order lateral and inhomogeneous waves, with no radial exponential attenuation, determine the field strengths which then fall off as ρ^{-2}. When modes with low attenuation are excited, they are generally few in number. Since each propagates radially with a different phase velocity, the fields will show a regular periodic beating as the various modes move in- and out-of-phase.

3. When the first layer of the earth is lossy and several wavelengths deep, the geometric optics solution is more useful than the normal mode approach. The expression for the fields is the half-space solution plus a contribution from the reflecting boundary. This is the type of solution used by El-Said (1956). In El-Said's analysis, the waves propagating along the surface were not correctly expressed, and the modification in directionality of the source due to the air-earth interface was not considered. This form of solution is particularly useful for a quick computation of the strength of reflections from subsurface boundaries and of the effect on surface fields of changes in electrical properties.

4. The saddle-point solution is useful for determining the radial distance from the source at which the various contributions of the singularities of the integrand become important. Since the saddle-point contour is positioned in the complex plane by the ratio $\rho/2d$, a ratio $\rho/2d$ can be defined for each singularity. For normal modes, the radial distance defined by this ratio may be interpreted as the distance from the source required for a given mode to develop. For the branch points, this ratio defines the critical distances from the source, where lateral waves and inhomogeneous waves from the subsurface boundary reach the surface.

DISCUSSION

The radio interferometry technique provides a method of determining electrical properties in situ and of detecting subsurface stratification of the electrical properties in environments which are moderately transparent to electromagnetic waves. The theoretical analysis of the two-layer earth problem defines the behavior of the fields at the earth's surface and provides a basis for understanding experimental results reported by Rossiter et al (1973) in Part II. The various solutions derived here are also useful for computing rough estimates of the interference patterns in the fields at the earth's surface, provided the asymptotic

nature of the expressions is given due respect. Examples of these are given in Part II.

The half-space solutions provide a method of determining the electrical properties for a half-space. Any strong departures from the half-space wave nature (i.e., a regular interference pattern and a ρ^{-2} distance dependence) indicate that reflections from depth are important. When the reflections from depth are due to a horizontal boundary in electrical properties, the behavior of the fields varies considerably. For example, when normal modes are excited, the fields fall off as $\rho^{-1/2}$ with regular beating in the field strengths with distance from the source.

The treatment of a two-layer earth with plane boundaries, homogeneous media, and point sources is a considerable simplification of most real environments. These simple models and the approximate solutions obtained do, however, provide insight into the field behavior in the radio interferometry application. Methods to accurately compute field strengths for these models are currently under investigation. The effect of rough and dipping boundaries on the solutions is extremely important. Also, the presence of scattering by inhomogeneities in the earth can drastically alter the fields at the earth's surface. These problems are virtually impossible to treat in a general manner theoretically. Scale model experiments seem to be the most feasible method of studying these problems. This work is presently in progress.

The free-space wavelength provides the most useful unit of length when discussing and plotting radio interferometry data. Scale model construction is based on keeping all dimensions the same on the wavelength scale and having the same loss tangent. In the analysis of field data, plotting distances on a wavelength scale makes comparison of data taken at different frequencies straightforward. If the electrical properties are not frequency dependent, running the experiment using several different frequencies can effectively vary the depth of a subsurface interface from a fraction of a wavelength to many wavelengths.

APPENDIX A: COEFFICIENTS AND PARAMETERS

The coefficients in the integral expressions for the Hertz vectors for the various dipole sources are obtained by satisfying the boundary conditions at $z=0$ and $z=-d$. Without a consistent notation, the coefficients are extremely complicated expressions, which lose the symmetry of equations (1) through (6) and are difficult to interpret physically. In this section, the solutions for the coefficients are tabulated, and the notation used throughout the body of the text is defined.

In Table A-1, the boundary conditions for the Hertz vectors are listed. In Table A-2, the expressions for the $a_j(\lambda)$, $b_j(\lambda)$, and $c_j(\lambda)$ are listed for each dipole source. Examination of these solutions shows the symmetry between the electric and magnetic dipole sources. Interchanging the roles of K_i and M_i, one can readily obtain the solution for a magnetic dipole source from that of an equivalent electric dipole source, and vice versa

Table A-1. Boundary conditions for Hertz vectors for various dipole sources.

Vertical Magnetic Dipole (VMD)	Magnetic	$M_i\Pi_Z^i = M_{i+1}\Pi_Z^{i+1}$	$\frac{\partial \Pi_Z^i}{\partial Z} = \frac{\partial \Pi_Z^{i+1}}{\partial Z}$
Vertical Electric Dipole (VED)	Electric	$K_i\Pi_Z^i = K_{i+1}\Pi_Z^{i+1}$	$\frac{\partial \Pi_Z^i}{\partial Z} = \frac{\partial \Pi_Z^{i+1}}{\partial Z}$
Horizontal Magnetic Dipole (HMD)	Magnetic	$k_i^2\Pi_X^i = k_{i+1}^2\Pi_X^{i+1}$ $\nabla\cdot\mathbf{\Pi}^i = \nabla\cdot\mathbf{\Pi}^{i+1}$	$M_i\Pi_Z^i = M_{i+1}\Pi_Z^{i+1}$ $M_i\frac{\partial \Pi_X^i}{\partial Z} = M_{i+1}\frac{\partial \Pi_X^{i+1}}{\partial Z}$
Horizontal Electric Dipole (HED)	Electric	$k_i^2\Pi_X^i = k_{i+1}^2\Pi_X^{i+1}$ $\nabla\cdot\mathbf{\Pi}^i = \nabla\cdot\mathbf{\Pi}^{i+1}$	$K_i\Pi_Z^i = K_{i+1}\Pi_Z^{i+1}$ $K_i\frac{\partial \Pi_X^i}{\partial Z} = K_{i+1}\frac{\partial \Pi^{i+1}}{\partial Z}$

Table A-2(a). Coefficients $a_i(\lambda)$, $b_i(\lambda)$, and $c_i(\lambda)$ for vertical dipole source.

		Two-layer earth	Half-space
Vertical Magnetic Dipole	a_0	$\dfrac{R_{01}+R_{12}\beta}{1-R_{10}R_{12}\beta}$	R_{01}
	a_1	$\dfrac{\eta_{01}T_{01}}{1-R_{10}R_{12}\beta}$	$\eta_{01}T_{01}$
	a_2	$\dfrac{\eta_{01}T_{01}R_{12}\beta}{1-R_{10}R_{12}\beta}$	0
	a_3	$\dfrac{\eta_{01}T_{01}\eta_{12}T_{12}}{1-R_{10}R_{12}\beta}$	$\eta_{01}T_{01}$
Vertical Electric Dipole	a_0	$\dfrac{X_{01}+X_{12}\beta}{1-X_{10}X_{12}\beta}$	X_{01}
	a_1	$\dfrac{\xi_{01}S_{01}}{1-X_{10}X_{12}\beta}$	$\xi_{01}S_{01}$
	a_2	$\dfrac{\xi_{01}S_{01}X_{12}\beta}{1-X_{10}X_{12}\beta}$	0
	a_3	$\dfrac{\xi_{01}S_{01}\xi_{12}S_{12}}{1-X_{10}X_{12}\beta}$	$\xi_{01}S_{01}$

The various parameters used in the solutions are listed in Table A-3.

The expressions X_{ij}, S_{ij}, R_{ij}, and T_{ij} are the Fresnel plane-wave reflection and transmission coefficients. The subscript notation ij has the following meaning: subscript i denotes the medium from which the plane wave is incident on the plane boundary between media i and j. For example, the subscripts 01 mean a plane-wave incident from the air on the boundary between the air and the first layer of the earth. The X_{ij} and S_{ij} are the reflection and transmission coefficients respectively for a *TM* plane wave; the R_{ij} and S_{ij} are the reflection and transmission coefficients for a *TE* plane wave.

APPENDIX B: PLANE-WAVE SPECTRUM AND EVALUATION OF INTEGRALS

The physical meaning of the integral expressions for the various Hertz vector solutions is much more apparent when the plane-wave spectrum notation is used. The form of the plane-wave spectrum used throughout is obtained by defining three complex angles, θ_0, θ_1, θ_2, and transforming the integration variable by setting

$$\lambda = k_0 \sin\theta_0 = k_1 \sin\theta_1 = k_2 \sin\theta_2. \quad \text{(B-1)}$$

The angle θ_0 is used in the region $Z \geq 0$, θ_1 in the region $-d \leq Z \leq 0$, and θ_2 in the region $Z \leq -d$. The above transformation is just an expression of Snell's law. A plane-wave incident from the region $Z > 0$ on the earth's surface at an angle θ_0 to the z-axis is refracted into medium 1 at an angle θ_1, and to the z-axis and into medium 2 at an angle θ_2, as illustrated in Figure B-1. The reader is referred to Clemmow (1966) for details.

The expressions for the Hertz vectors in equations (10) through (18) transform as follows, where the Π_Z^0 for a vertical dipole has been chosen as an example:

$$\Pi_Z^0 = \frac{e^{ik_0R}}{WR} + \frac{ik_0}{2W}\int_c \sin\theta_0 a_0(\theta_0) \cdot e^{ik_0\cos\theta_0(Z+h)} H_0^1(k_0\rho\sin\theta_0)\,d\theta_0. \quad \text{(B-2)}$$

The integration contour C runs from $-\pi/2+i\infty$ to $-\pi/2$ along the real θ_0 axis to $\pi/2$ and then to $\pi/2-i\infty$, as illustrated in Figure B-2. For the angles θ_i, the contour C is obtained from equation (B-1). The P_i transform to $-ik_i\cos\theta_i$, where the negative sign is chosen in order to satisfy the radiation condition. Substituting for P_i in the Fresnel coefficients of Table A-3 results in the more familiar form

$$X_{ij} = \frac{\left(\frac{K_j}{K_i}\right)^{1/2}\cos\theta_i - \left(\frac{M_j}{M_i}\right)^{1/2}\cos\theta_j}{\left(\frac{K_j}{K_i}\right)^{1/2}\cos\theta_i + \left(\frac{M_j}{M_i}\right)^{1/2}\cos\theta_j}, \quad \text{(B-3)}$$

where the TM reflection coefficient is shown as an example.

The integral expressions can be approximately evaluated by manipulating the integration contour C in the complex θ plane. The approach is to replace the Hankel function by its asymptotic expansion, which is valid when the argument is considerably greater than unity.

Table A-2(b). Coefficients $a_i(\lambda)$, $b_i(\lambda)$, and $c_i(\lambda)$ for horizontal dipole sources.

		Two-layer earth	Half-space
HMD	b_0	$\dfrac{X_{01}+X_{12}\beta}{1-X_{10}X_{12}\beta}$	X_{01}
	b_1	$\dfrac{\gamma_{01}S_{01}}{1-X_{10}X_{12}\beta}$	$\gamma_{01}S_{01}$
	b_2	$\dfrac{\gamma_{01}S_{01}X_{12}\beta}{1-X_{10}X_{12}\beta}$	0
	b_3	$\dfrac{\gamma_{01}S_{01}\gamma_{12}S_{12}}{1-X_{10}X_{12}\beta}$	$\gamma_{01}S_{01}$
	c_0	$\dfrac{1}{2P_0}\dfrac{(\gamma_{01}-1)T_{01}(1+R_{12}\beta)S_{01}(1+X_{12}\beta)-(\gamma_{21}-1)\eta_{01}T_{10}T_{12}m_{01}\gamma_{01}S_{01}\gamma_{12}S_{12}\beta}{(1-R_{10}R_{12}\beta)(1-X_{10}X_{12}\beta)}$	$\dfrac{1}{2P_0}(\gamma_{01}-1)T_{01}S_{01}$
	c_1	$\dfrac{1}{2P_0}\dfrac{(\gamma_{01}-1)\eta_{01}T_{01}S_{01}(1+X_{12}\beta)-(\gamma_{21}-1)R_{10}T_{12}m_{01}S_{01}\gamma_{12}S_{12}\beta}{(1-R_{10}R_{12}\beta)(1-X_{10}X_{12}\beta)}$	$\dfrac{1}{2P_0}(\gamma_{01}-1)\eta_{01}T_{01}$
	c_2	$\dfrac{1}{2P_0}\dfrac{(\gamma_{01}-1)\eta_{01}T_{01}R_{12}\beta S_{01}(1+\gamma_{12}\beta)-(\gamma_{21}-1)T_{12}m_{01}\gamma_{01}S_{01}\gamma_{12}S_{12}\beta}{(1-R_{10}R_{12}\beta)(1-X_{10}X_{12}\beta)}$	0
	c_3	$\dfrac{1}{2P_0}\dfrac{(\gamma_{01}-1)\eta_{01}T_{01}\eta_{12}T_{12}S_{01}(1+X_{12}\beta)-(\gamma_{21}-1)\eta_{12}T_{12}(1+R_{10}R_{12}\beta)m_{01}\gamma_{01}S_{01}\gamma_{12}S_{12}}{(1-R_{10}R_{12}\beta)(1-X_{10}X_{12}\beta)}$	$\dfrac{1}{2P_0}(\gamma_{01}-1)\eta_{01}T_{01}$
HED	b_0	$\dfrac{R_{01}+R_{12}\beta}{1-R_{10}R_{12}\beta}$	R_{01}
	b_1	$\dfrac{\gamma_{01}T_{01}}{1-R_{10}R_{12}\beta}$	$\gamma_{01}T_{01}$
	b_2	$\dfrac{\gamma_{01}T_{01}R_{12}\beta}{1-R_{10}R_{12}\beta}$	0
	b_3	$\dfrac{\gamma_{01}T_{01}\gamma_{12}T_{12}}{1-R_{10}R_{12}\beta}$	$\gamma_{01}T_{01}$
	c_0	$\dfrac{1}{2P_0}\dfrac{(\gamma_{01}-1)S_{01}(1+X_{12}\beta)T_{01}(1+R_{12}\beta)-(\gamma_{21}-1)\xi_{10}S_{10}S_{12}m_{01}\gamma_{01}T_{01}\gamma_{12}T_{12}\beta}{(1-R_{10}R_{12}\beta)(1-X_{10}X_{12}\beta)}$	$\dfrac{1}{2P_0}(\gamma_{01}-1)S_{01}T_{01}$
	c_1	$\dfrac{1}{2P_0}\dfrac{(\gamma_{01}-1)\xi_{01}S_{01}T_{01}(1+R_{12}\beta)-(\gamma_{21}-1)S_{12}X_{10}m_{01}\gamma_{01}T_{01}\gamma_{12}T_{12}\beta}{(1-R_{10}R_{12}\beta)(1-X_{10}X_{12}\beta)}$	$\dfrac{1}{2P_0}(\gamma_{01}-1)\xi_{01}S_{01}$
	c_2	$\dfrac{1}{2P_0}\dfrac{(\gamma_{01}-1)\xi_{01}S_{01}X_{12}\beta(1+R_{12}\beta)T_{01}-(\gamma_{21}-1)S_{12}m_{01}\gamma_{01}T_{01}\gamma_{12}T_{12}\beta}{(1-R_{10}R_{12}\beta)(1-X_{10}X_{12}\beta)}$	0
	c_3	$\dfrac{1}{2P_0}\dfrac{(\gamma_{01}-1)\xi_{01}S_{01}\xi_{12}S_{12}T_{01}(1+R_{12}\beta)-(\gamma_{21}-1)\xi_{12}S_{12}(1+\gamma_{01}\beta)m_{01}\gamma_{01}T_{01}\gamma_{12}T_{12}}{(1-R_{10}R_{12}\beta)(1-X_{10}X_{12}\beta)}$	$\dfrac{1}{2P_0}(\gamma_{01}-1)\xi_{01}S_{01}$

Table A-3. Parameters used and Fresnel coefficients.

Parameters

$$\gamma_{ij} = \frac{k_i^2}{k_j^2} \qquad \xi_{ij} = \frac{K_i}{K_j}$$

$$m_{ij} = \frac{P_i}{P_j} \qquad \beta = e^{-2P_1 d}$$

$$\eta_{ij} = \frac{M_i}{M_j} \qquad k_i^2 = K_i M_i (2\pi)^2$$

TM Fresnel Coefficients

Reflection: $X_{ij} = \dfrac{K_j P_i - K_i P_j}{K_j P_i + K_i P_j}$

Transmission: $S_{ij} = \dfrac{2K_j P_i}{K_j P_i + K_i P_j}$

Relations: $X_{ij} = -X_{ji} \qquad X_{ij} = S_{ij} - 1$

$X_{ij} = 1 - S_{ji} \qquad S_{ij} = \dfrac{\xi_{ji}}{m_{ji}} S_{ji}$

TE Fresnel Coefficients

Reflection: $R_{ij} = \dfrac{M_j P_i - M_i P_j}{M_j P_i + M_i P_j}$

Transmission: $T_{ij} = \dfrac{2M_j P_i}{M_j P_i + M_i P_j}$

Relations: $R_{ij} = -R_{ji} \qquad R_{ij} = T_{ij} - 1$

$R_{ij} = 1 - T_{ji} \qquad T_{ij} = \dfrac{\eta_{ji}}{m_{ji}} T_{ji}$

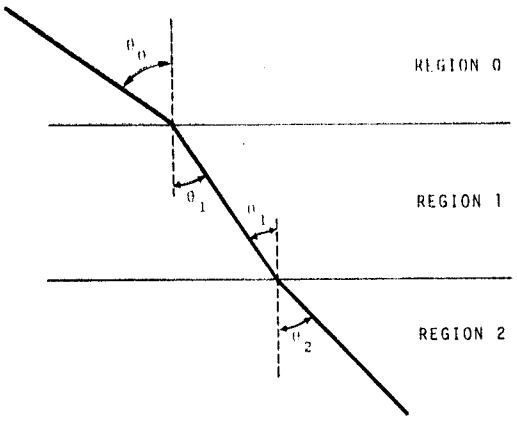

FIG. B-1. Illustration of integration variables θ_0, θ_1, and θ_2 and Snell's law.

$$H_0^1(t) = e^{i(t-(\pi/4))}\left(\frac{2}{\pi t}\right)^{1/2} \cdot \left(1 + \frac{1}{i8t} + \cdots\right), \tag{B-4}$$

and

$$H_1^1(t) = e^{i(t-(3\pi/4))}\left(\frac{2}{\pi t}\right)^{1/2} \cdot \left(1 - \frac{3}{i8t} + \cdots\right). \tag{B-5}$$

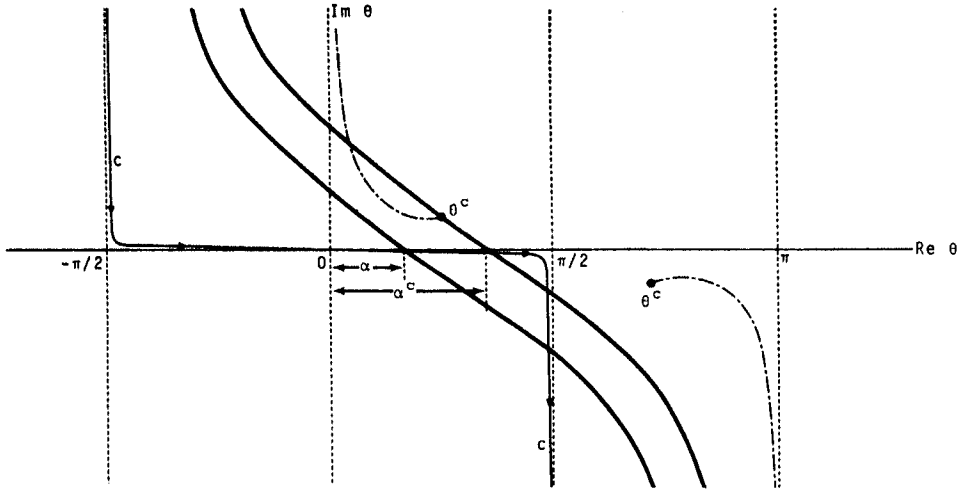

FIG. B-2. Complex θ-plane showing contour C, saddle-point contours Γ and Γ', and the positions of the branch point θ^c and branch cut (chain line).

Substitution into the integrals, such as that in equation (B-2), results in an expression of the form

$$e^{iZk\cos\theta+ik\rho\sin\theta} \tag{B-6}$$

in the integrand, which can be written as

$$e^{ikR\cos(\theta-\alpha)}, \tag{B-7}$$

where $R=(\rho^2+Z^2)^{1/2}$, and R and α are just the length and direction of the geometric-optics ray-path. An integral with exponential of the form (B-7) is amenable to the saddle-point method integration, where $\theta=\alpha$ is the saddle point. By deforming C to the contour of most rapid descent away from the saddle point Γ one obtains an asymptotic series in the parameter $(kR)^{-1}$ for the integral. The leading term in the series is the geometric-optics solution to the problem.

The saddle-point contour Γ is defined from the argument of the exponential in expression (B-7). Along the contour Γ,

$$ikR\cos(\theta-\alpha)=ikR-kRs^2, \tag{B-8}$$

where

$$s^2=-\sin(\theta'-\alpha)\sinh\theta'', \tag{B-9}$$

and

$$\theta=\theta'+i\theta''. \tag{B-10}$$

The contour Γ is then given by the equation

$$\cos(\theta'-\alpha)\sinh\theta''=1 \tag{B-11}$$

and is illustrated in Figure B-2.

An excellent evaluation of the particular types of integrals that appear in the text is given by Brekhovskikh (1960), and the reader is referred to this reference for more detailed discussion. In the rest of the discussion, solutions to the integrals valid to the second order in kR^{-1} are used. This involves using the second-order terms in the Hankel-function expansion and then taking the asymptotic solution to the integrals to the second order. The integrals in the text have two forms:

$$I_1=\frac{ik}{2W}\int_c \sin\theta A(\theta) \cdot e^{ikZ\cos\theta}H_0^1(k\rho\sin\theta)d\theta, \tag{B-12}$$

and

$$I_2=\frac{ik^2}{2W}\int_c \sin^2\theta A(\theta) \cdot e^{ikZ\cos\theta}H_1^1(k\rho\sin\theta)d\theta. \tag{B-13}$$

The solutions to the second order are given by

$$I_1\simeq\frac{e^{ikR}}{WR}\left\{A(\alpha)-\frac{i}{2kR}\cdot\left[A''(\alpha)+A'(\alpha)\cot\alpha\right]\right\}, \tag{B-14}$$

and

$$I_2\simeq -ik\sin\alpha\frac{e^{ikR}}{WR}\left\{A(\alpha)-\frac{i}{2kR}\cdot\left[A''(\alpha)+3\cot\alpha A'(\alpha)-2A(\alpha)\right]\right\}. \tag{B-15}$$

Solutions (B-14) and (B-15) are valid as long as $A(\theta)$ is a slowly varying function of θ near the saddle point α. This assumption is valid provided $A(\theta)$ does not have a singular point near α. In the expressions for the various $A(\theta)$ appearing in the text, branch points and poles of $A(\theta)$ are of the utmost importance in the solutions. The branch points of $A(\theta)$ are the critical angles of the boundaries in the problem. The critical angles enter all the $A(\theta)$ through the relation

$$\cos\theta_j=\pm\left[1-\gamma_{ij}\sin^2\theta_i\right]^{1/2} \tag{B-16}$$

in all the Fresnel coefficients subscripted ij.

The radical splits the complex θ-plane into two Riemann sheets with branch points at

$$\sin\theta_{ij}^{\bullet}=\pm\frac{k_j}{k_i}. \tag{B-17}$$

For the two-layer earth there are two boundaries which give two critical angles and result in a four-sheeted θ-plane. In the half-space earth problem, the complex θ-plane is two-sheeted. The convention followed throughout is that of taking the positive square root. The surface defined in this manner is referred to as the upper Riemann surface. For one to evaluate the integrals, the branch cuts from the branch points must be defined. The convention used here is the same as that of Ott and Brekhovskikh, who define the branch lines as those contours along which the imaginary part of

equation (B-16) is zero. The branch line is the chain line in Figure B-2.

The branch points must be taken into account for saddle-point angles greater than α^c. As illustrated in Figure B-2, for $\alpha > \alpha^c$, in order to deform contour C into Γ, the branch point θ^c must be crossed. A modified integration contour to take θ^c into account is shown in Figure B-3. As long as α and θ^c are well separated, the saddle-point and branch-point contributions can be evaluated separately. The contribution of the branch point is a second-order effect (Ott, 1941) as long as $\alpha \neq \theta^c$ and an approximate evaluation of the branch-point contribution can be obtained using the method of steepest descent. In general, α^c is obtained by substituting $\theta = \theta^c$ in equation (B-11). In the particular case of two perfect dielectric materials, i and j, forming the boundary,

$$\alpha_{ij}^c = \sin^{-1}\left(\frac{k_i}{k_j}\right), \qquad k_i < k_j, \quad \text{(B-18)}$$

and

$$\alpha_{ij}^c = \sin^{-1}\left(\frac{k_j}{k_i}\right), \qquad k_j < k_i. \quad \text{(B-19)}$$

The steepest-descent evaluation of the branch-point contribution is summarized as follows: The branch cut integral has the form

$$I_B = \frac{ik_i^{(n+1)}}{2W} \int_B \sin^{n+1}\theta_i A(\theta_i) \cdot e^{ik_i Z \cos\theta_i} H_n^1(k_i\rho \sin\theta_i) d\theta_i, \quad \text{(B-20)}$$

where the contour B runs from $i\infty$ to θ^c on the left of the branch cut and from θ^c back to $i\infty$ along the right of the branch cut. For approximate evaluation, I_B is rewritten

$$I_B \sim -\frac{ik_i^{n+1}}{2W} e^{-i(2n+1)\pi/4}\left(\frac{2}{\pi k_i\rho}\right)^{1/2} \cdot \int_{B'} \sin^{n+(1/2)}\theta_i \left[A^+(\theta_i) - A^-(\theta_i)\right] \cdot e^{ik_i R\cos(\theta_i - \alpha)} d\theta_i, \quad \text{(B-21)}$$

where the Hankel function has been replaced by the first term of its asymptotic expansion. The superscripts + and − on $A(\theta_i)$ denote the sign of the radical in equation (B-16) taken in $A(\theta_i)$, and the contour B' runs from θ_{ij}^c to $i\infty$. The contour B' is deformed into the steepest-descent contour, B'', away from θ_{ij}^c. The path of steepest descent is defined by

$$\text{Im } ik_i R\cos(\theta_i - \alpha) = \text{constant} \quad \text{(B-22)}$$

and is illustrated by the dotted line in Figure B-3. On the assumption that $k_i R \gg 1$, so that only

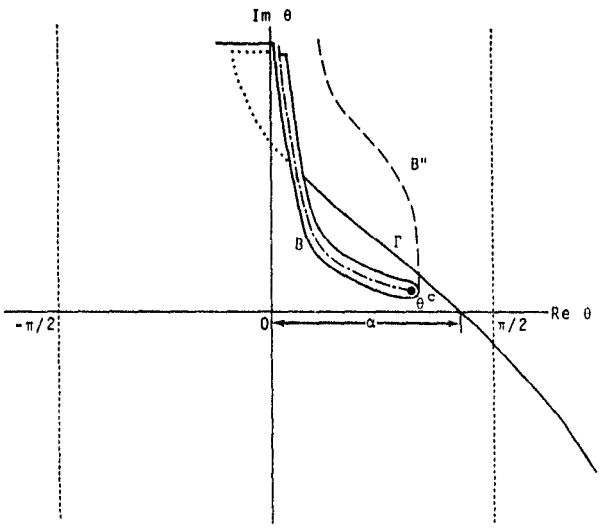

FIG. B-3. Complex θ-plane showing modification of saddle-point contour Γ to contour B in order to account for branch-point contribution, and path of steepest descent (dotted line).

angles very close to θ_{ij}^c contribute significantly to the integral, θ_i can be set equal to θ_{ij}^c in all expressions in the integrand except for the radical. In general,

$$A^+(\theta_i) - A^-(\theta_i) = F(\theta_i)\cos\theta_j, \quad \text{(B-23)}$$

and the integral is approximately

$$I_B = \frac{-ik_i^{n+1}}{2W} e^{-i(2n+1)\pi/4} \cdot \left(\frac{2}{\pi k_i \rho}\right)^{1/2} \sin^{n+(1/2)} \theta_{ij}^c F(\theta_{ij}^c) \quad \text{(B-24)}$$
$$\cdot \int_{B'} \cos\theta_j e^{ik_i R\cos(\theta_i - \alpha)} d\theta_i.$$

For low-loss media, θ_{ij}^c is close to the real axis for $k_j < k_i$ or close to the $\pi/2$ line for $k_i < k_j$ in the complex θ_i plane. The method of solution of the integral in equation (B-24) is slightly different in the two situations, but the results are identical. Here, the θ_{ij}^c will be assumed close to the real axis. The approximate solution is valid for θ_{ij}^c near the $\pi/2$ line.

Along the steepest-descent contour near θ_{ij}^c,

$$\theta_i \approx \theta_{ij}^c + iu, \quad \text{(B-25)}$$

where u is much less than unity. Then,

$$\cos\theta_j \simeq -e^{-i\pi/4}\sqrt{2u}\left(\frac{k_i^2 - k_j^2}{k_j^2}\right)^{1/4}, \quad \text{(B-26)}$$

and

$$ik_i R\cos(\theta_i - \alpha) \simeq ik_i R\cos(\theta_{ij}^c - \alpha) - k_i R\sin(\alpha - \theta_{ij}^c)u. \quad \text{(B-27)}$$

The integral in equation (B-24) becomes

$$-ie^{-i\pi/4}\sqrt{2}\left(\frac{k_i^2 - k_j^2}{k_j^2}\right)^{1/4} e^{ik_i R\cos(\theta_{ij}^c - \alpha)} \cdot \int_{B''} \sqrt{u}\, e^{-k_i R\sin(\alpha - \theta_{ij}^c)u} du. \quad \text{(B-28)}$$

Now, the integral

$$\int_{B''} \sqrt{u}\, e^{-\delta u} du \simeq \int_0^\infty x^2 e^{-\delta x^2} dx = \frac{1}{2}\sqrt{\frac{\pi}{\delta^3}}. \quad \text{(B-29)}$$

Rearranging equations (B-24) and (B-28), one finally obtains

$$I_B = \frac{ik_j^n}{2W\rho^2} \frac{e^{-in(\pi/2)} F(\theta_{ij}^c)}{(k_i^2 - k_j^2)^{1/2}} \cdot (1 - \cot\alpha\tan\theta_{ij}^c)^{-3/2} \cdot e^{ik_j\rho\sin\theta_{ij}^c + ik_i\cos\theta_{ij}^c Z}, \quad \text{(B-30)}$$

which must be added to equations (B-14) and (B-15) when $\alpha > \alpha^c$.

The assumption in the saddle-point and steepest-descent techniques that $kR \gg 1$ is reasonably valid when R is greater than two wavelengths, since $k > 2\pi$ and $kR > 10$ when $R > 2$.

The poles of the integrands are also of importance in the solutions. Discussion of their role in the solutions is given in the text.

ACKNOWLEDGMENTS

The author is grateful to the National Research Council of Canada for a fellowship which supported this work.

This work is the first paper in a series providing the background for the Surface Electrical Properties Experiment planned for the Apollo 17 lunar mission.

REFERENCES

Brekhovskikh, L. M., 1960, Waves in layered media: New York, Academic Press.

Budden, K. G., 1961, The wave-guide mode theory of wave propagation: Englewood Cliffs, Prentice-Hall, Inc.

Clemmow, P. C., 1966, The plane wave spectrum representation of electromagnetic fields: New York, Pergamon Press.

El-Said, M. A. H., 1956, Geophysical prospection of underground water in the desert by means of electromagnetic interference fringes: Proc. I.R.E., v. 44, p. 24–30 and 940.

Evans, S., 1963, Radio techniques for the measurement of ice thickness: The Polar Record, v. 11, p. 406–410 and 795.

Katsube, T. J., and Collett, L. S., 1971, Electrical properties of Apollo 11 and 12 lunar samples, *in* Proceedings of the Second Lunar Science Conference, Houston, Texas, edited by A. A. Levinson: Cambridge, Mass. Inst. Tech. (in press).

Norton, K. A., 1937, The propagation of radio waves over the surface of the earth and in the upper atmo-

sphere, Part I: Proc. I.R.E., v. 24, p. 1367–1387; Part II: Proc. I.R.E., v. 25, p. 1203–1236.
Ott, H., 1941, Reflexion und Brechung von Kugelwellen; Effekte Q. Ordnung: Ann. Physik, v. 41, p. 443–466.
——— 1943, Die Sattelpunktsmethode in der Umgeburg eines Pols mit Anwendungen auf die Wellenoptik und Akustic: Ann. Physik, v. 43, p. 393.
Rossiter, J. R., LaTorraca, G. A., Annan, A. P. Strangway, D. W., and Simmons, G., 1973, Radio interferometry depth sounding: part II—experimental results: Geophysics, this issue.
Saint-Amant, M., and Strangway, David W., 1970, Dielectric properties of dry, geologic materials: Geophysics, v. 35, p. 624–645.
Sommerfeld, A., 1909, Uber die Ausbreitung der Wellen in der Drahtlosen telegraphie: Ann. Physik, v. 28, p. 665–737.
1949, Partial differential equations in physics: New York, Academic Press.
Strangway, D. W., 1969, Moon: Electrical properties of the uppermost layers: Science, v. 165, p. 1012–1013.
Van der Waerden, B. L., 1951, On the method of saddle points: Appl. Sci. Res., B2, p. 33–45.
Wait, J. R., 1951, The magnetic dipole over the horizontally stratified earth: Can. J. Phys., v. 29, p. 577–592.
Wait, J. R., 1970, Electromagnetic waves in stratified media, 2nd edition: New York, The Macmillan Co.
Ward, S. H., and Dey, A., 1971, Lunar surface electromagnetic sounding: A theoretical analysis, I.E.E.E. Trans. GE-9, no. 1, p. 63–71.

GEOPHYSICS, VOL. 38, NO. 3 (JUNE 1973), P. 581-599, 17 FIGS

RADIO INTERFEROMETRY DEPTH SOUNDING: PART II—EXPERIMENTAL RESULTS†

JAMES R. ROSSITER*, GERALD A. LATORRACA‡, A. PETER ANNAN*, DAVID W. STRANGWAY*§, AND GENE SIMMONS‡

In such highly resistive geologic environments as ice sheets, salt layers, and the moon's surface, radio waves penetrate with little attenuation. The field strengths about a transmitting antenna placed on the surface of such an environment exhibit interference maxima and minima which are indicative of the in-situ electrical properties and the presence of subsurface layering.

Experimental results from an analog scale model and from field tests on two glaciers are interpreted on the basis of the theoretical results of Part I. If the upper layer is thick, the pattern is very simple and the dielectric constant of the layer can be easily determined. An upper bound on the loss tangent can be estimated. For thin layers, the depth can be determined if the loss tangent is less than about 0.10, and a crude estimate of scattering can be made.

INTRODUCTION

The attenuation of electromagnetic waves propagating through terrestrial rocks is extremely high due to the moisture content; as a result, EM methods in the radio-frequency range have not found general use in exploring the earth. A few highly resistive geologic environments, such as ice sheets (Evans, 1963, 1965, 1967; Jiracek, 1967) and dry salt layers (Unterberger et al, 1970; Holser et al, 1972), are sufficiently dry to be transparent to radio waves. The uppermost layers of the moon are also very resistive (Strangway, 1969; Saint-Amant and Strangway, 1970), and typical attenuation distances (or skin depths) for lunar material are shown in Figure 1.

In these materials, EM waves propagate with little attenuation and are useful, in theory, for depth sounding. The Surface Electrical Properties Experiment, which was developed for Apollo 17, uses such a method to measure the electrical properties of the moon and to search for layering. The method is based on the interference pattern generated between various radio waves.

Theoretical background to the method and a general introduction to this series of papers is presented in Part I by Annan (1973, p. 557). In preparation for interpretation of lunar data, we have tested the method both in the laboratory with analog scale models using wavelengths in the centimeter range and in the field on glaciers using wavelengths about the same as will be used on the moon. These results are presented here.

INTERFEROMETRY TECHNIQUE

Radio-frequency interferometry (RFI) is described simply as follows: A transmitter and associated antenna on the dielectric surface generate RF waves which are received and amplified at some distance. Several waves reach the receiver —e.g., A, B, and C shown in Figure 2. Because the various waves travel different distances and/or at different velocities, they interfere with each other. The interference pattern can be generated in one of two different ways. Either frequency or distance can be varied, holding the other constant. Frequencies of 500 khz to 50 Mhz and distances

† Presented at the 40th Annual International SEG Meeting, November 9, 1970, New Orleans, Louisiana. Manuscript received by the Editor April 6, 1972; revised manuscript received November 22, 1972.

* University of Toronto, Toronto 181, Ontario, Canada.

‡ Massachusetts Institute of Technology, Cambridge, Massachusetts 02139.

§ Presently on leave to NASA Manned Spacecraft Center, Houston, Texas 77058.

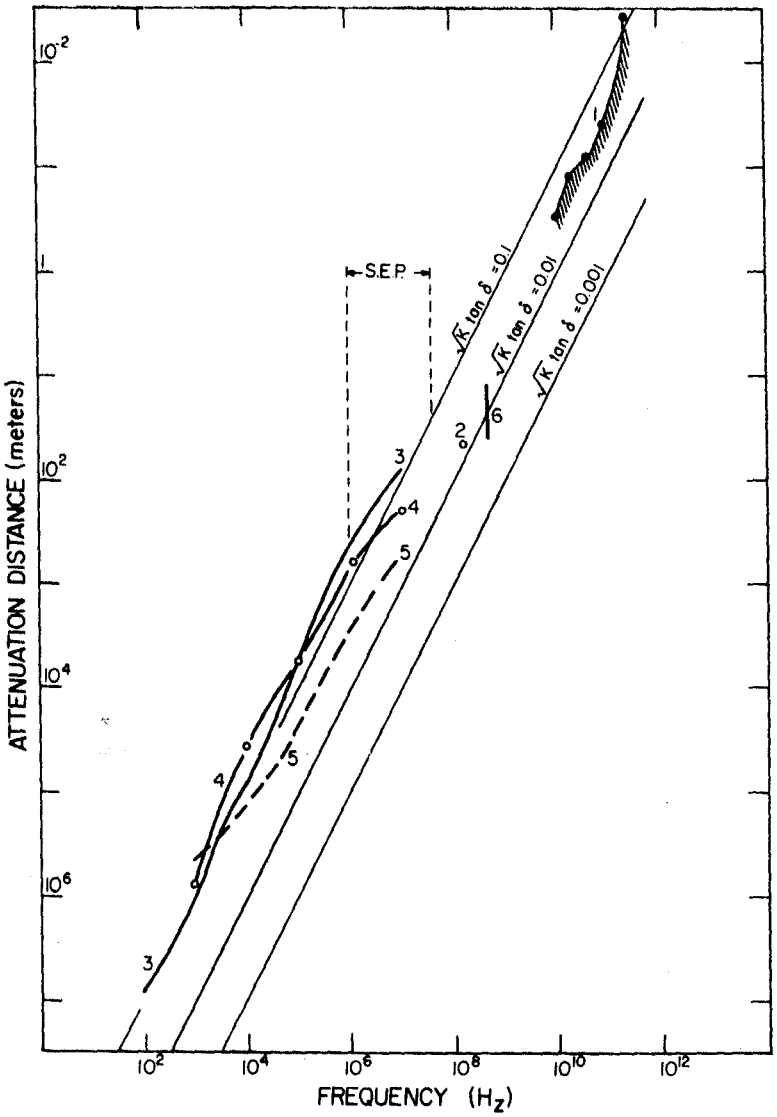

FIG. 1. Attenuation distance in lunar surface material: 1. Weaver (1965)—thermal emission; 2. Tyler (1968)—bistatic radar; 3. Chung et al (1971)—igneous sample 12002,58; 4. Katsube and Collett (1971)—breccia sample 10065; 5. Katsube and Collett (1971)—fines sample 10084; 6. Gold et al (1971)—fines, various densities. The frequency range to be used in the Surface Electrical Properties Experiment on Apollo 17 is marked 'S.E.P.'

of a few meters to a few kilometers are characteristic. However, it is not feasible now to build a tuned sweep-frequency antenna that gives interpretable results over our frequency band of interest; thus, we restrict ourselves to the variation of distance of a few fixed frequencies.

Two criteria must be met for the RFI method to effectively detect and determine depth of a subsurface boundary. First, the dielectric medium must have a loss tangent less than about 0.1, or the amplitude of the waves that travel in the medium will be too low to interfere well with the direct wave—i.e., the medium probed must be transparent at the frequency used. Second, there must exist a contrast in electrical or magnetic properties below the surface in order to reflect energy.

Several waves are generated which are im-

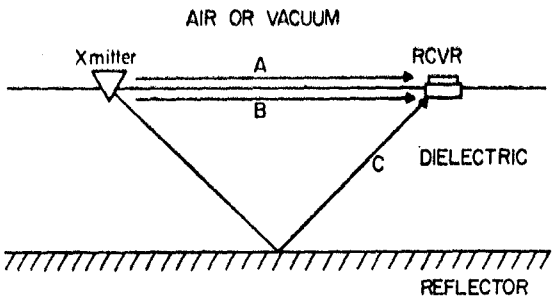

FIG. 2. The basic interferometry concept. The interference of the direct waves A and B and the reflected waves C is measured at the receiver.

portant near the source. Their geometric relations are illustrated in Figure 3. Two spherical waves, A and C, travel directly between the transmitter and the receiver. Wave C travels in the upper medium (air or vacuum), and wave A, in the earth. Since these waves have different velocities, they will interfere with each other. This interference gives a measure of the dielectric constant of the lower medium, since the greater the difference in the velocities of these two waves, the greater will be the interference frequency.

The flank, head, or lateral wave B and the spherical wave A give the transmitting antenna a highly directional radiation pattern. The lateral wave satisfies the boundary conditions imposed by wave C at the interface, since the horizontal phase velocity of B in the earth is the same as that of wave C in the upper medium. To have the same horizontal phase velocity, wave B propagates downward at an angle β as shown in Figure 3. This angle is the angle of total internal reflection between the two media familiar to seismologists, defined by

$$\sin \beta = \sqrt{\frac{\epsilon_0}{\epsilon_1}}, \qquad (1)$$

where the critical angle β is the angle between the negative z-axis and the direction of propagation of wave B, and ϵ_0 and ϵ_1 are the dielectric constants of the upper and lower media, respectively (assuming nonmagnetic media). The amplitudes of A and B are largest in the direction β. This feature is important in RFI depth sounding since energy is preferentially transmitted downward at an angle β.

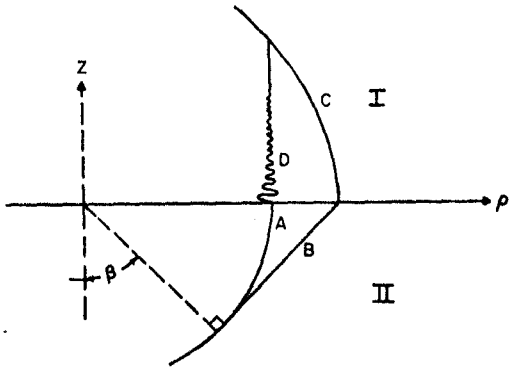

FIG. 3. Wavefronts at the air-dielectric ($z=0$) boundary. ρ is the radial direction from the source. Medium I is air or vacuum (ϵ_0, μ_0), and medium II is a dielectric (ϵ_1, μ_1). A is a spherical wave propagating radially in medium II; B is a head wave propagating downward at the critical angle; C is a spherical wave propagating radially in medium I; and D is an inhomogeneous wave propagating radially in medium I, but attenuating exponentially with height.

The spherical wave A, traveling in the lower medium, also has a complementary wave which matches the boundary conditions. An inhomogeneous wave D is produced at the surface; this wave propagates radially from the source with the velocity of A, but decays exponentially with height above the surface. This wave is significant near the boundary, but its effect decreases as the receiver moves away from the surface.

A "critical distance" r_c is defined as

$$r_c = 2d \tan \beta, \qquad (2)$$

where d is the depth to a plane horizontal reflector. Three general regions exist: the near-field, where the transmitter-receiver distance is much less than r_c; the region near the critical distance, where the bulk of the reflected energy arrives; and the far-field, well beyond r_c. In the near-field

the interaction between the two spherical waves A and C dominates and can be used to measure the dielectric constant of the upper layer. As the transmitter-receiver distance approaches r_c, several different waves with roughly comparable magnitudes arrive and produce a very confusing interference pattern. In the far-field, multiple reflections are important, and only the normal modes of the system propagate with low attenuation.

From data obtained in the three regions, three pieces of information can be determined. The *dielectric constant* is related simply to the spatial frequency in the near-field. The *depth* to an interface can be roughly estimated from the dielectric constant and the critical distance. Third the shape of the curve and the number of far-field peaks are indicative of the *loss tangent* of the upper layer.

Two different configurations of equipment have been used in our tests; namely, horizontal electric dipole sources with magnetic dipole receivers for field work, and a vertical magnetic dipole source with an electric dipole receiver for early analog scale-model studies. Both horizontal electric and vertical magnetic dipoles produce horizontally polarized waves. Since the E-field polarization is then perpendicular to the plane of incidence, the reflection coefficient does not go through the Brewster angle null, which is associated only with waves polarized in the plane of incidence on the assumption of nonmagnetic materials.

The general configuration and notation used are shown in Figure 4 for the electric dipole. The dipole is on the surface, extends along the x-axis, and traverses are run orthogonal to it. For this configuration, approximate theoretical solutions for components H_z (vertical magnetic field), H_ρ (radial magnetic field), and E_ϕ (tangential electric field) have been found. The other components are negligible for the case of infinite horizontal plane boundaries. Nonmagnetic materials have been assumed throughout so that $\mu_0=\mu_1=\mu_2$.

Three cases involving infinite plane horizontal layers have been studied theoretically:

(a) the half-space;

(b) the two-layer earth with a perfect reflector at some depth; i.e., either $\epsilon_2\to\infty$ or $\tan\delta_2\to\infty$ so that the reflection coefficient of the lower boundary is always unity;

(c) the general two-layer earth in which $\epsilon_1\neq\epsilon_2$ and $\tan\delta_1\cong\tan\delta_2$. For the experimental results, the material properties are such that only cases (a) and (b) need to be considered. Theoretical computations are compared with both scale-model and glacier field data. First, however, a brief description of the scale model and the field tests will be given.

ANALOG SCALE MODEL

Scaling of an electromagnetic model is particularly simple when the conductivity is negligible. The wavelength is inversely proportional to the frequency used, and all other relations remain invariant. In our scale model, we used microwave frequencies with free-space wavelengths of 3 to 5 cm. By scaling all data in terms of wavelengths, model, field, and theoretical results can readily be compared.

The first scale model consisted of a klystron source at 10 Ghz feeding a vertical magnetic slot antenna, a small diode receiver, a traversing system, and an automatic recording arrangement. The dielectric used was dry, pure quartz sand (160 mesh), and the reflector was an aluminum plate. The plate and sand were contained in a plywood box with sides that sloped out at about 45 degrees. The box was approximately 30 wavelengths long and 15 wavelengths wide, at the bottom. The setup is shown schematically in Figure

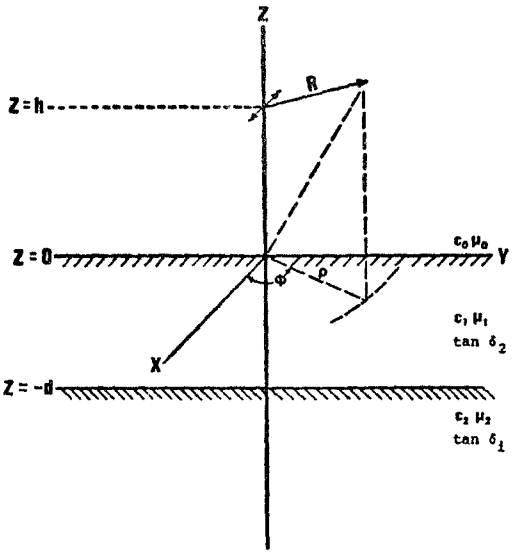

FIG. 4. General configuration of a horizontal electric dipole over a two-layer earth. ϵ_i is the real dielectric constant, μ_i is the permeability, and $\tan\delta_i$ is the loss tangent of the ith layer.

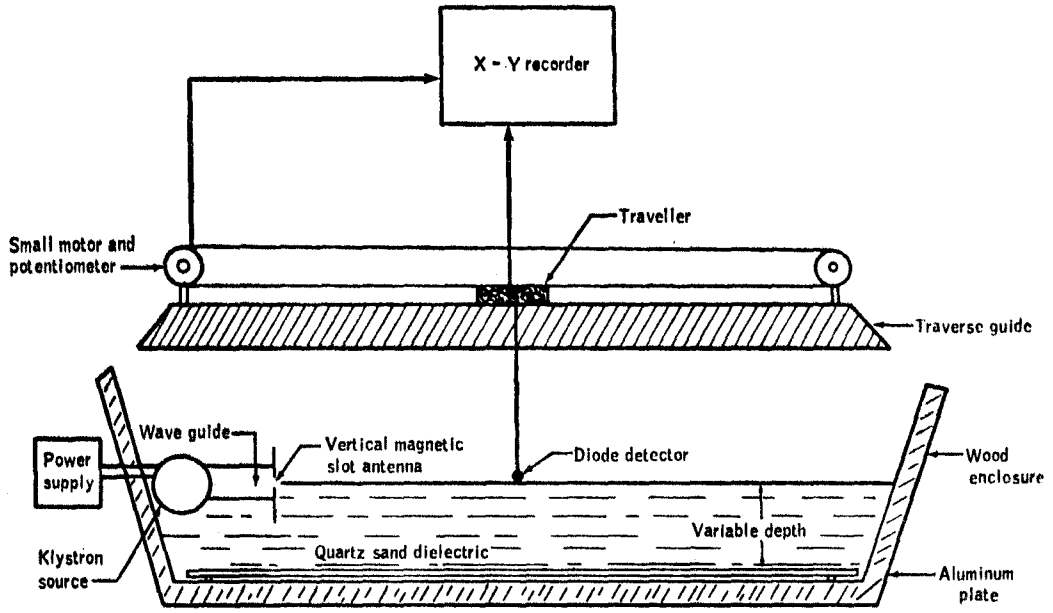

FIG. 5. The analog scale model. The transmitter was composed of a klystron tube radiating at 10 GHz into a rectangular waveguide. A vertical magnetic slot antenna was formed by a slit at the end of the waveguide. The transmitter could be raised or lowered. Signals were received by a small diode which could traverse for about 20 wavelengths at any height. The dielectric used was quartz sand and the reflector was a flat aluminum plate. Received signal strength versus receiver position was recorded directly on an X–Y recorder.

5. A later version of the scale model using transformer oil as a liquid dielectric has also proved very successful. The transmitter and receiver were small electric dipoles, operated at 6 Ghz, and the model was contained in a tank lined with microwave absorbing material.

The validity of our experimental arrangement was initially tested by comparing model results with theoretical predictions for a very simple case. The transmitter and receiver were both placed at height h above the aluminum plate without the sand.

From Part I, the EM radiation from a vertical magnetic dipole at height h over a magnetically uniform half-space is described completely by the vertical magnetic Hertz vector, given by

$$\pi_z = \frac{e^{ik_0R}}{R} + R_{01}\frac{e^{ik_0R'}}{R'}, \qquad z \geq 0, \quad (3)$$

where k_0 is the wavenumber, R_{01} is the reflection coefficient at the boundary ($z=0$), R is the direct distance to the receiver, and R' is the distance traveled by the reflected wave. If the boundary is a perfect reflector, $R_{01}=-1$. For the receiver at height h:

$$R = [r^2 + (z-h)^2]^{\frac{1}{2}} = r, \quad (4)$$

and

$$R' = [r^2 + (z+h)^2]^{\frac{1}{2}} = [r^2 + 4h^2]^{\frac{1}{2}}. \quad (5)$$

The tangential electric field E_ϕ is then

$$\begin{aligned} E_\phi &= -i\omega\mu\frac{\partial \pi_z}{\partial r} \\ &= -i\omega\mu\left[\frac{e^{ik_0r}}{r}\left(ik_0 - \frac{1}{r}\right)\right. \\ &\quad \left. - \frac{e^{ik_0\sqrt{r^2+4h^2}}}{\sqrt{r^2+4h^2}}\left(ik_0 - \frac{1}{\sqrt{r^2+4h^2}}\right)\left(\frac{r}{\sqrt{r^2+4h^2}}\right)\right]. \end{aligned} \quad (6)$$

Then,

$$E(r,h) = A\left[\frac{e^{ik_0r}}{r}\left(i - \frac{1}{r}\right) - \frac{e^{ik_0\sqrt{r^2+4h^2}}}{\sqrt{r^2+4h^2}}\frac{r}{\sqrt{r^2+4h^2}}\left(i - \frac{1}{\sqrt{r^2+4h^2}}\right)\right], \quad (7)$$

where $A = -i\omega\mu(4\pi^2/\lambda^2)$ and is an arbitrary scaling factor for a unit magnetic dipole, r is the transmitter-receiver separation in wavelengths, h is the transmitter-receiver height above the reflecting plate in wavelengths, and λ is the wavelength in free-space.

Typical comparisons between theory and experiment are shown in Figure 6. The agreement in the position of the peaks is very good. Although the amplitudes are on an arbitrary scale and are therefore not directly comparable, the ratio between each theoretical and experimental peak is approximately constant. Experimental deviations from theoretical solutions are not large and are primarily due to reflections between the transmitter and either the receiver or the sides of the box. The good agreement between calculated and measured curves was taken as the main proof that the experimental arrangement was satisfactory to measure interference between various waves.

GLACIER FIELD TESTS

Introduction

Ice is one of the few terrestrial rocks with uniformly high resistivity. Resistivities of 10^6 to 10^7 ohm-m have been measured consistently (e.g., Röthlisberger, 1967; Keller and Frischknecht, 1961). A few glaciers have been carefully mapped and are accessible for field tests. We selected two on which to test the RFI technique.

The dielectric properties of ice and snow have been reviewed by Evans (1965). The dielectric properties of glacial ice and snow have been studied in situ by Watt and Maxwell (1960) and by Walford (1968). Two parameters are important —the dielectric constant and the loss tangent. Ice has a relaxation in the audio-frequency range, but unlike many dielectric materials has none near the radio frequencies. Hence, while the value of its dielectric constant is frequency independent in the radio frequencies, the value of its loss tangent is roughly inversely proportional to frequency and is strongly temperature dependent.

From 1 to 30 Mhz, the value of the dielectric constant is 3.20 ± 0.05 and is fairly independent of frequency, impurities, or temperature. Over the same frequencies, $f \cdot \tan \delta \cong 0.25$ at 0°C, but $f \cdot \tan \delta \cong 0.10$ at -10°C, where f is the frequency in Mhz. Although the effects of impurities, cracks, air bubbles, and free water on the loss tangent are not well understood, the values for losses in gla-

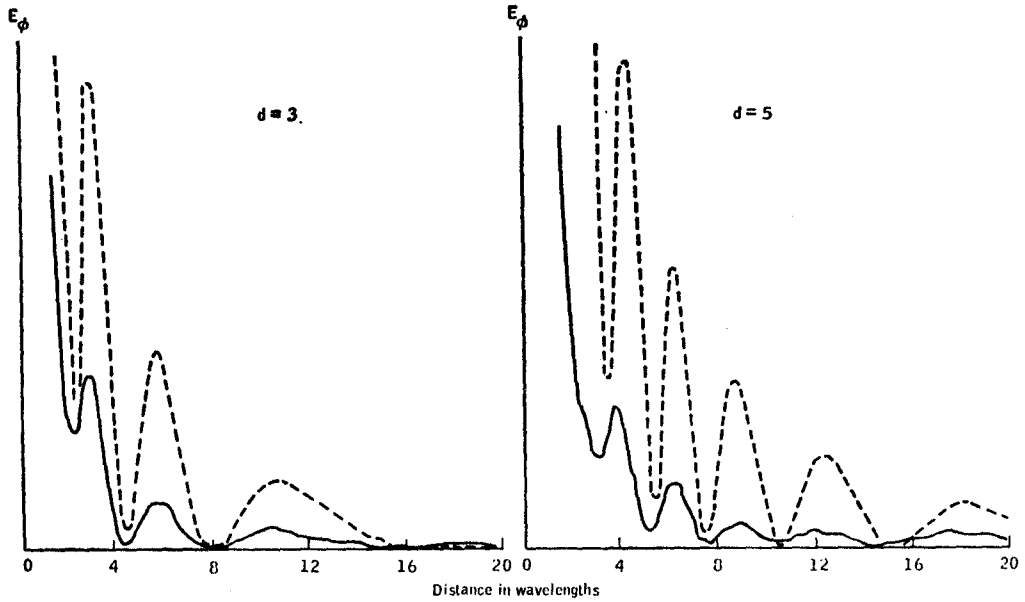

FIG. 6. Typical theoretical and experimental curves for calibration of the scale model. Dashed line is theoretical and solid line is scale model. Curves for a depth of 3 wavelengths are on the left, and for 5 wavelengths, on the right. No dielectric is present. Scaling is different for each of the four curves.

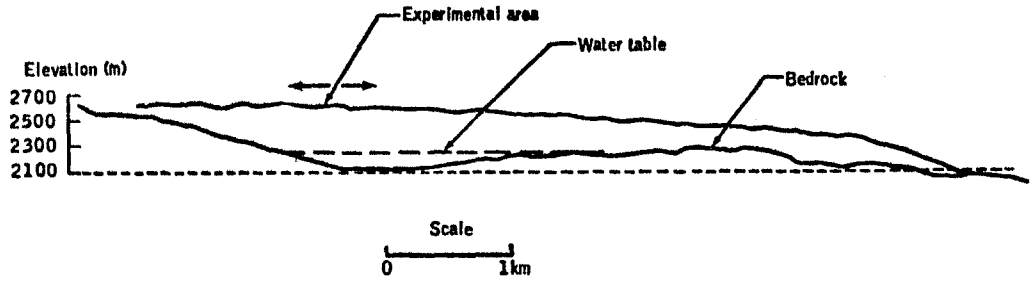

FIG. 7. Cross-section of the Gorner Glacier, from Swiss seismic data.

cier ice are not appreciably different from those in pure ice.

The inverse-frequency dependence of the loss tangent in ice implies that the attenuation of an EM wave in ice is directly proportional to the absolute distance, not to the number of wavelengths that the wave travels. Therefore, the maximum sounding depth in ice free of scattering bodies is virtually independent of the frequency used by any radio or radar technique in the frequency range from 0.1 to nearly 1000 Mhz.

The Gorner Glacier

The Gorner Glacier, located in southern Switzerland, has been extensively drilled and mapped seismically for the Swiss Hydroelectric System, and a longitudinal section of the glacier is shown in Figure 7. It is a deep glacier; the depth in the test area to the postulated water-table is about 400 m and the depth to bedrock is 500 m. It is effectively a half-space for the interferometry technique.

Equipment used on the tests, run in September, 1969, was both simple and portable. The transmitter was a General Radio 1330A bridge oscillator, which fed the transmitting antenna through a ferrite core 1 to 1 balun. Two types of transmitting antennas were used: an untuned horizontal electric dipole and a small ($\lambda/10$ diameter) loop as a vertical magnetic dipole. Output power was less than $\frac{1}{2}$ watt. The receiver was fed by either a 5-m electric dipole or a Singer single-turn 1-m diameter loop, with simple broad-band matching to the 50-ohm input impedance of a Galaxy R530 communications receiver. The receiver output was read from a Hewlett-Packard 427A portable voltmeter and recorded manually.

Field procedure consisted of recording field strength about every $\frac{1}{4}$ wavelength along traverses away from the transmitter. Frequencies of 1, 2 4, 7, and 10 Mhz were used. E_ϕ, H_z, and H_ρ components were measured for both horizontal electric and vertical magnetic transmitting antennas.

The Athabasca Glacier

The Athabasca Glacier, located in Alberta, Canada, has also been studied extensively: a gravity survey has been conducted by Kanasewich (1963), seismic and drilling studies have been made by Paterson and Savage (1963), and EM and resistivity soundings have been run by Keller and Frischknecht (1961). A depth contour map, reconstructed from Paterson and Savage and showing our traverse line, is given in Figure 8. The thickness of the ice along the traverse varies from about 130 m to 280 m.

The Athabasca Glacier tests, run in March, 1970 used a crystal-controlled transmitter that was operated at frequencies of 2, 4, 8, 16, and 24 Mhz. Output power was about one watt. It fed a ribbon-wire tuned horizontal electric dipole antenna through a balun feed network. The antenna consisted of several number-22 wires, each cut to the resonant length for a single frequency, lying beside each other on the ice surface. Each wire was cut to the resonant length of one of the frequencies in free space and connected in parallel to the balun feed. Each wire had to then be cut to between 75 and 90 percent of its length in order to reflect minimum power back to the transmitter.

This antenna was experimental, and several problems may have been associated with its use. The amount of clipping needed to retune the wires after they had been placed on the ice was insufficient to account for the dielectric contrast between ice and air. We feel that each wire was

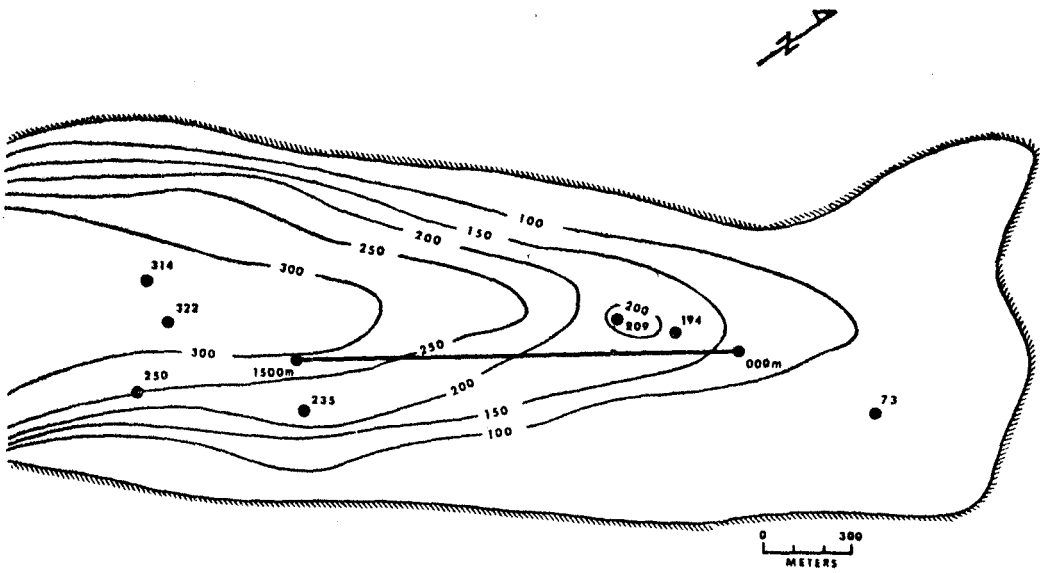

FIG. 8. Contour map of the Athabasca Glacier, drawn from the seismic and drilling data of Paterson and Savage (1963). Boreholes, with depths in meters, are shown. Our interferometry traverse line is marked 000 m to 1500 m.

reactively coupled to the other wires, which then radiated energy. Therefore, the longer wires were effectively long antennas (greater than a half wavelength) for the higher frequencies and could have radiated significantly off the orthogonal direction. The antenna was probably not well coupled either to the subsurface or to the traverse direction, and spurious reflections could have been received from the sides of the glacier.

The receiver and the field procedure were similar to those used on the Gorner Glacier with the following differences: A smaller $\frac{1}{3}$-m-diameter loop was used for 16 and 32 Mhz. Readings were taken every $\frac{1}{6}$ wavelength, to a distance of 20 wavelengths or until the signal was too low to detect. Most traverses were run from NE to SW, although a few were run from SW to NE with the transmitter displaced to the SW end of the traverse line. Both H_z and H_ρ components were taken, as well as one E_ϕ traverse.

RESULTS

The half-space

If the boundary between the first and second layers is not important, the only waves which reach the receiver are the direct waves through the air (or vacuum) and the dielectric. This case is simple to solve theoretically, and suites of curves have been compiled for the E_ϕ, H_ρ, and H_z components (see, for example, Figure 9). There is very good agreement between theory and experimental results from the Gorner Glacier. Figure 10 shows a typical experimental curve and a series of theoretical curves for various dielectric constants. The interference peaks and troughs align best with those calculated for $\epsilon_1 = 3.2$. By comparison with curves like those in Figure 9, we have estimated the loss tangent to be less than 0.07 at 10 Mhz.

One interesting feature of both the theoretical and experimental half-space curves is that results for the H_z and E_ϕ components are identical, but the peaks and troughs of the H_ρ component are shifted $\frac{1}{2}\lambda$ away from the transmitter (see Figure 11). This relation between the interference patterns in H_z, E_ϕ, and H_ρ provides a basis on which to detect departures of the fields from the half-space response which could be due to subsurface reflections or scattering from surface or subsurface irregularities.

Therefore, in a half-space, RFI can easily be used to determine the dielectric constant of the upper layer if we know the positions of the peaks and troughs. Theoretical results indicate that the

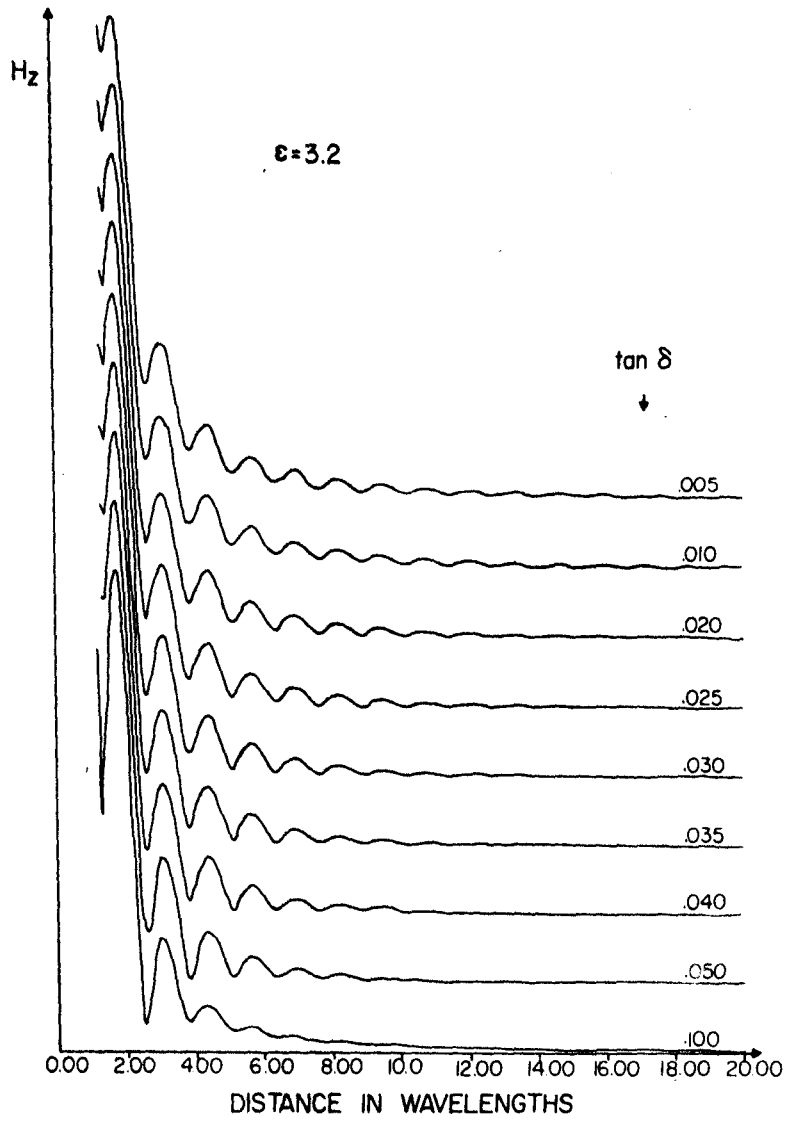

FIG. 9. Theoretical half-space curves for a dielectric constant of 3.2 and various loss tangents. Peaks and nulls, are less distinct for higher loss tangents, but their positions do not change.

loss of the layer does not change the position of the peaks, but as the loss decreases, both the sharpness of the nulls and the number of observable peaks increases. By measuring several components it may be possible to determine if the measurements have been affected by random scattering.

Two-layer earth: Perfect reflector

Calculations for the two-layer model are more complex. Exact theoretical solutions have not been obtained, but after performing the mathematical manipulations discussed in Part I, approximate numerical solutions have been compiled and plotted. Typical suites of curves are shown in Figure 12 to illustrate the effect of changes in dielectric constant, thickness, and loss tangent, of the first layer. Although the effects of these parameters are not fully separable, in general, the frequency of the initial peaks and troughs is indi-

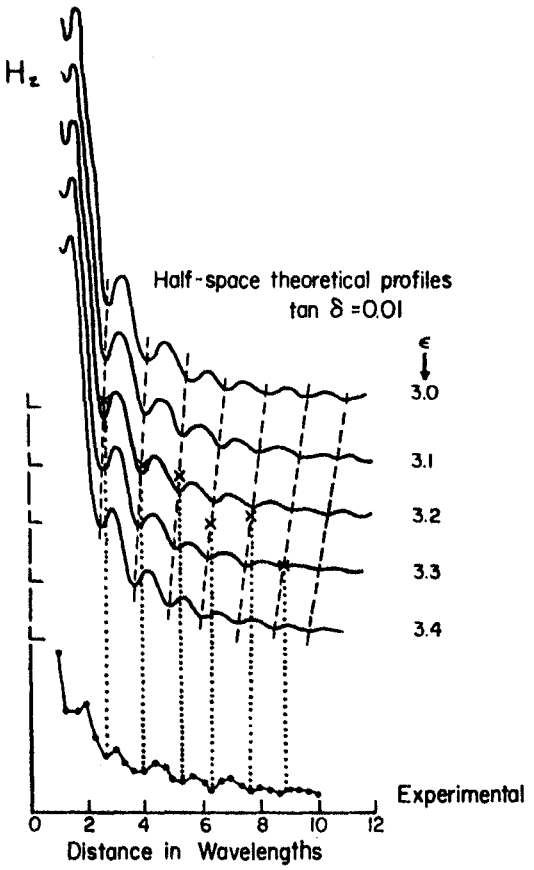

FIG. 10. Several theoretical half-space curves and an experimental curve from the Gorner Glacier at 10 Mhz (H_z component). The experimental curve has peaks and troughs that correspond to the theoretical curve for a dielectric constant of 3.2.

cative of the dielectric constant; the position of the main energy peak is determined by the thickness and the dielectric constant; and the sharpness of the pattern changes with the loss tangent. For this example, the dependence on loss tangent is particularly noticeable for loss tangents in the range .01 to .05.

A suite of analog scale-model patterns and the corresponding theoretical curves are shown in Figure 13. The dielectric oil had a measured dielectric constant of 2.16 and a loss tangent of 0.0022. In general, for thicknesses greater than 2 or 3 wavelengths the agreement in both position and amplitude of the peaks and nulls is good. For thinner layers the agreement is poorer, probably because the theoretical solutions become less accurate (see Part I). Differences between experimental and theoretical results in the near field may also be caused by the theoretical approximations. They might also be caused by spurious reflections in the experimental tank from wires connecting the transmitting antenna to its source. The other major discrepancy between the two solutions is at the critical angle where the approximations made in the theory are most significant. However, the good agreement between theoretical and scale-model results has given us confidence in both.

The results from the Athabasca Glacier are complicated by the fact that the thickness of the glacier increases along the traverse with a slope of approximately 1:10. Since the general theory for this geometry is extremely difficult, and has not been worked out in detail, we used theoretical curves for several thicknesses near the mean traverse thickness for comparison. Such a comparison is not altogether accurate, since the effects of a thickening layer depend on both the thickness and the rate of change of thickness.

Comparisons were made between data measured on the Athabasca Glacier and many suites of theoretical curves. It was found that the family of theoretical curves for the known parameters of the glacier, when compared with the experimental data as a whole, fitted better than any other set, although there was some ambiguity. Several examples are shown in Figure 14. The experimental data were run through a simple 1, 1, 1 running average filter before plotting. This filtering enhanced the main features of the curves by reducing small random variations. The agreement between theoretical and experimental data is far from perfect. However, if it is recognized that because the thickness of the ice is increasing along the traverse, some moveout of the measured peaks is to be expected, and a consistent picture emerges.

Figure 14 shows data obtained at 2, 4, 8, and 24 Mhz on the Athabasca Glacier, along with three theoretical curves with depths bracketing those along the traverse. As the frequency increases, the thickness of the ice, measured in wavelengths, also increases, so that quite different curves are found for each frequency. At 2 Mhz the curves are smooth and regular and the agreement between theory and experiment is quite good. At 4 Mhz the patterns are more complex, and although these are similar features, the the-

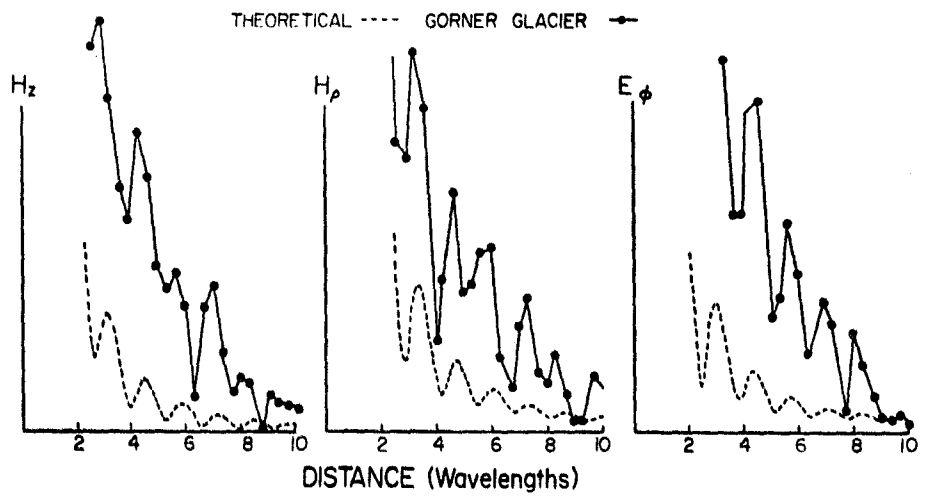

FIG. 11. Theoretical half-space curves and results from the Gorner Glacier. Source is a horizontal electric dipole at 10 Mhz. Theoretical curves are for dielectric constant of 3.2 and a loss tangent of 0.03. Peaks and troughs for the $H\rho$ component are shifted away from the transmitter one-half wavelength.

oretical curves do not correspond exactly to the experimental. At 8 Mhz the curves are complex, but the agreement is better, especially the large peak at about 7 wavelengths distance. At 24 Mhz there are many peaks and troughs in both curves. We feel the lack of correlation between theory and experiment is largely due to many randomly scattered reflections in the experimental curve. At 24 Mhz the wavelength of 12.5 m is the same size as many crevasses and surface roughness features.

In summary, as the thickness of the dielectric layer increases, the interference patterns change from curves with a few well-defined peaks to curves with high spatial frequencies and no large peaks. These features are seen in both theoretical and experimental results. The fact that both H_ρ and H_z components are basically similar, although they differ in their fine structure, increases our confidence in the match between theory and experiment.

INTERPRETATION

Dielectric constant

This parameter is easy to obtain directly from the data, since, as shown above, the direct air and subsurface waves interact near the source to give a pattern dependent only on this parameter. If the air wave has a wavenumber k_0,

$$k_0 = \frac{2\pi}{\lambda_0}, \tag{8}$$

where λ_0 is the free-space wavelength; and if the subsurface wave has wavenumber k_1,

$$k_1 = \frac{2\pi}{\lambda_1} = \frac{2\pi\sqrt{\epsilon_1}}{\lambda_0} = \sqrt{\epsilon_1}\, k_0, \tag{9}$$

then the beat frequency wavenumber k is

$$\Delta k = k_1 - k_0 = \frac{2\pi}{\lambda_0}(\sqrt{\epsilon_1} - 1). \tag{10}$$

The spatial interference wavelength λ_b is then

$$\lambda_b = \frac{2\pi}{\Delta k} = \frac{\lambda_0}{\sqrt{\epsilon_1} - 1}. \tag{11}$$

Therefore,

$$\epsilon_1 = \left(\frac{\lambda_0}{\lambda_b} + 1\right)^2 \tag{12}$$

and can be obtained directly from the data. For ice, $\lambda_b \cong 1.27\lambda_0$.

Loss tangent

The loss tangent can be estimated in a qualitative way from the sharpness of the patterns in the

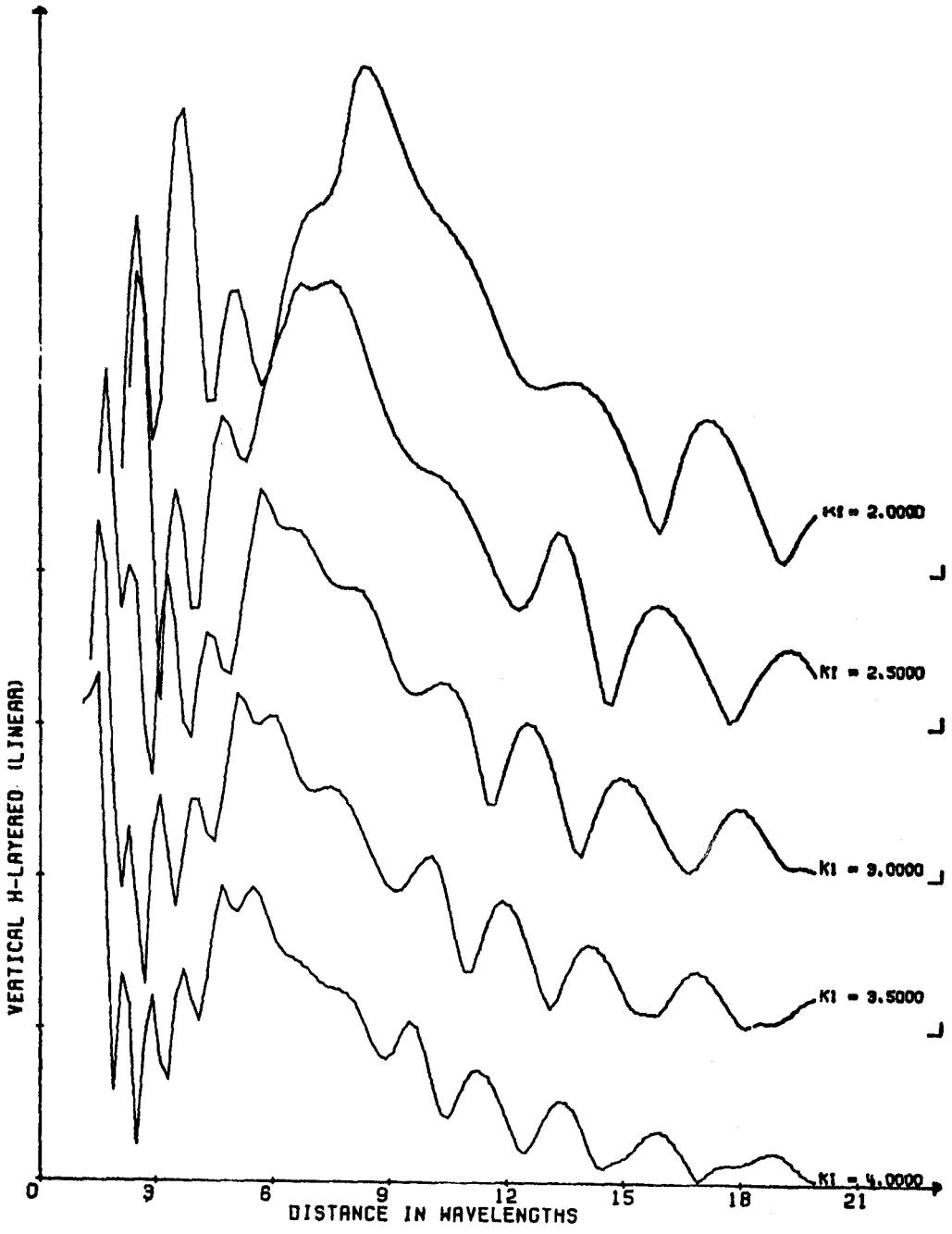

Fig. 12a. Theoretical interference curves for H_z component over a two-layer earth. Dependence on dielectric constant is shown. Depth = 4.000 λ, LT1 = 0.0200, K1 = varying.

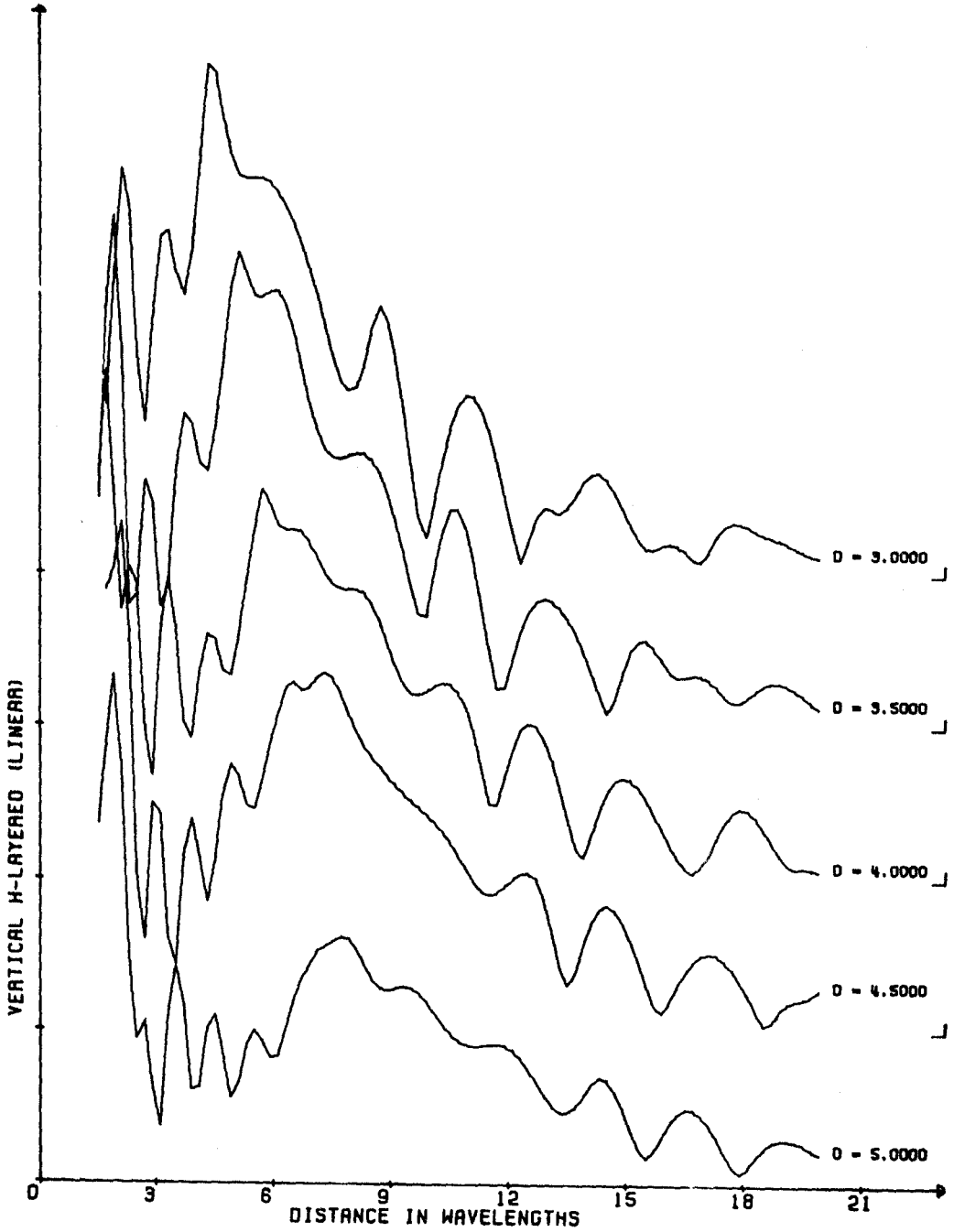

Fig. 12b. Theoretical interference curves for H_z component over a two-layer earth. Dependence on thickness is shown. Depth = varying, LT1 = 0.0200, K1 = 3.000.

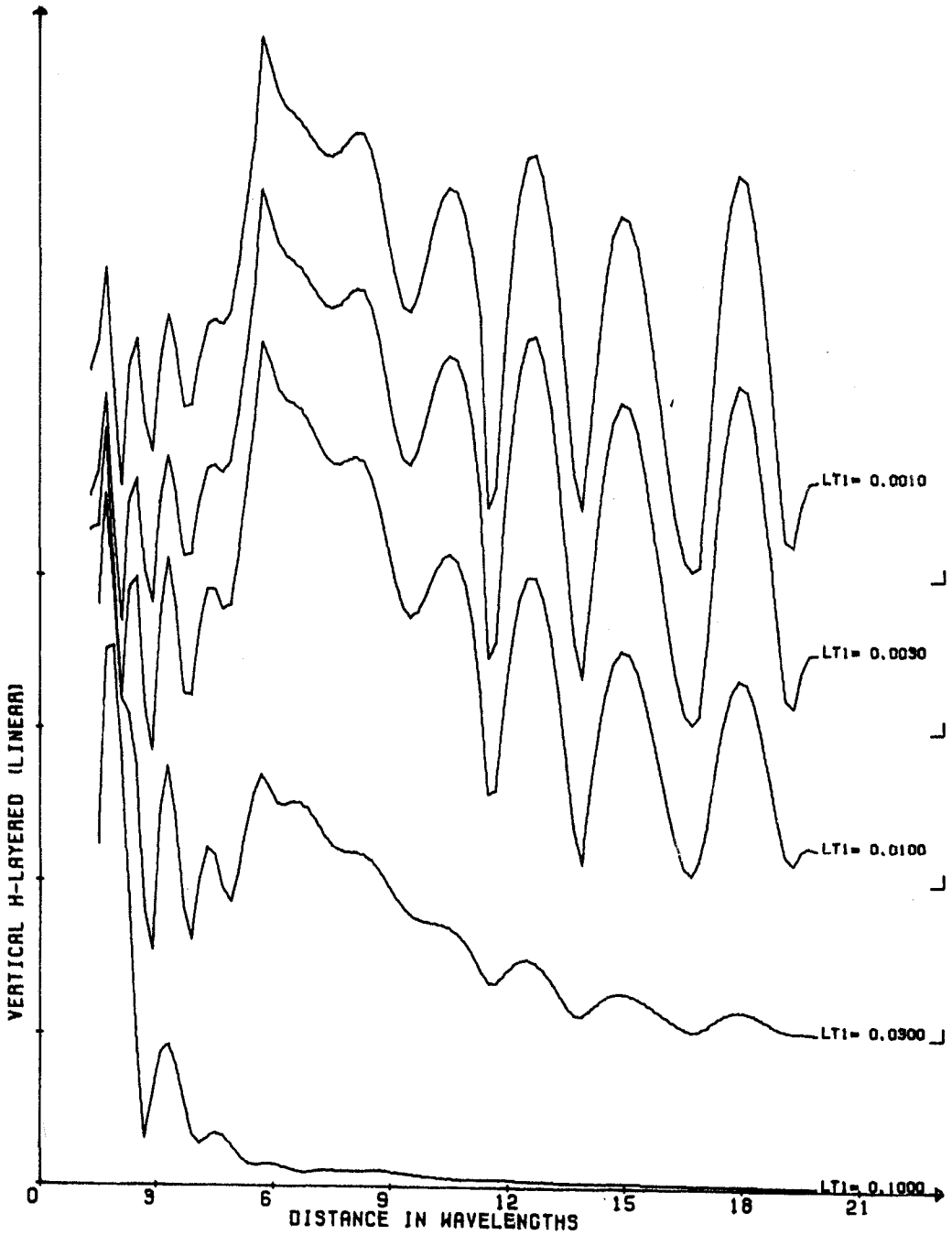

FIG. 12c. Theoretical interference curves for H_z component over a two-layer earth. Dependence on loss tangent is shown. Depth = 4.000λ, LT1 = varying, K1 = 3.000.

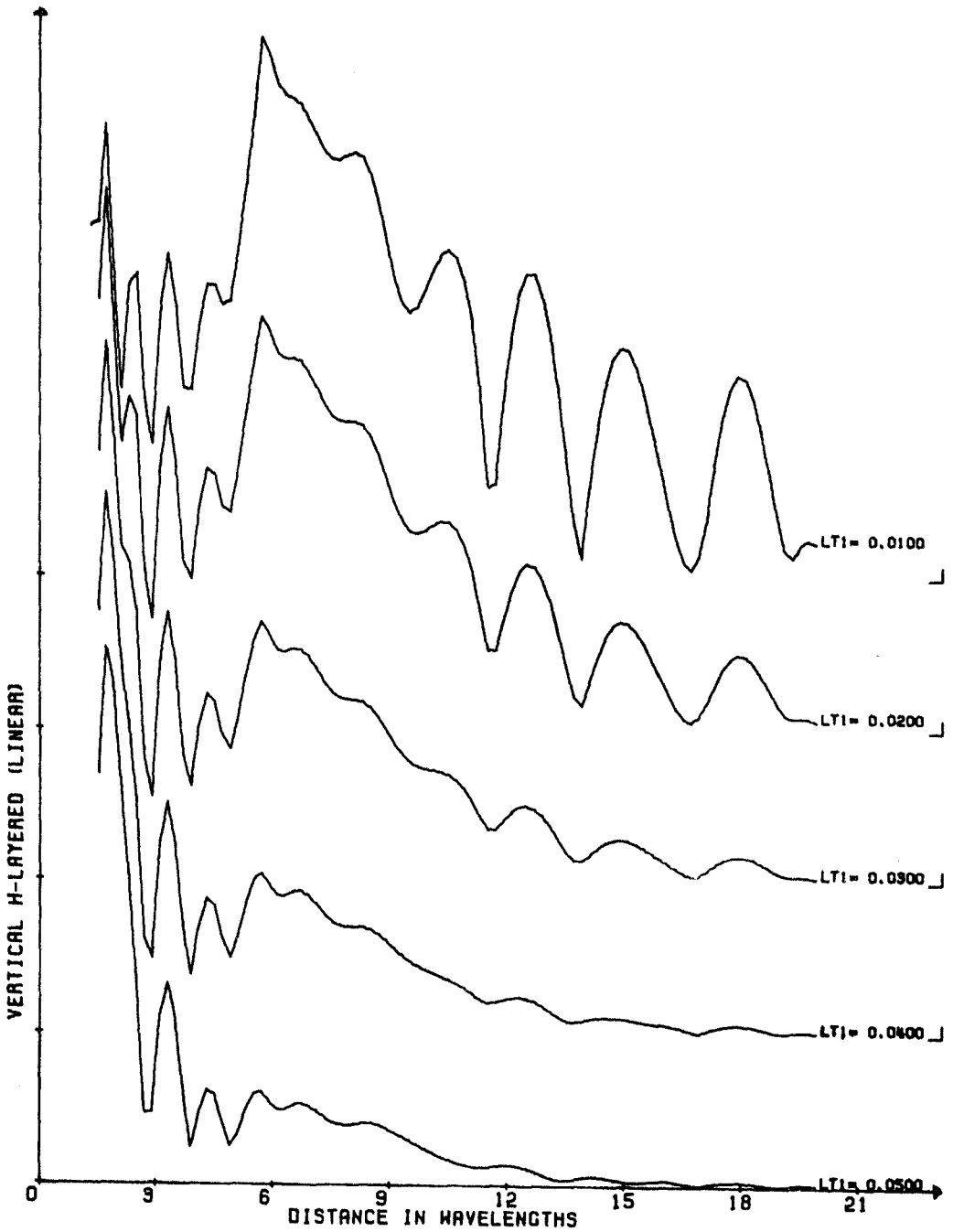

FIG. 12d. Theoretical interference curves for H_z component over a two-layer earth. Dependence on loss tangent is shown. Depth = 4.000 λ, LT1 = varying, K1 = 3.000.

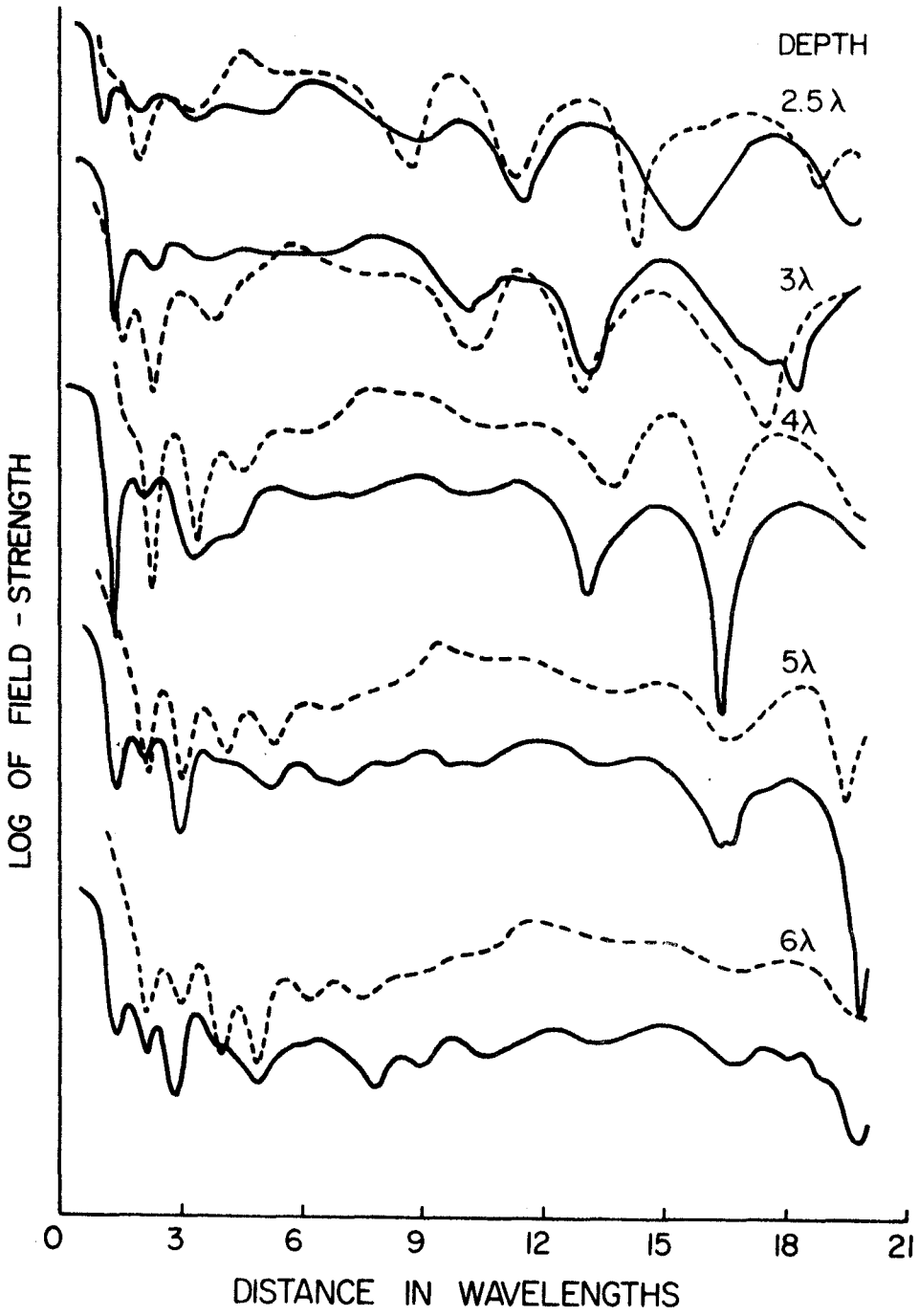

FIG. 13. Analog scale-model curves (solid line, E_θ) and corresponding theoretical curves (dashed line, H_z, $K = 2.16$, $\tan \delta = .0022$) for various thicknesses of the upper layer. E_ϕ and H_z are identical in this configuration. Dielectric constant (K) and loss tangent ($\tan \delta$) were measured independently.

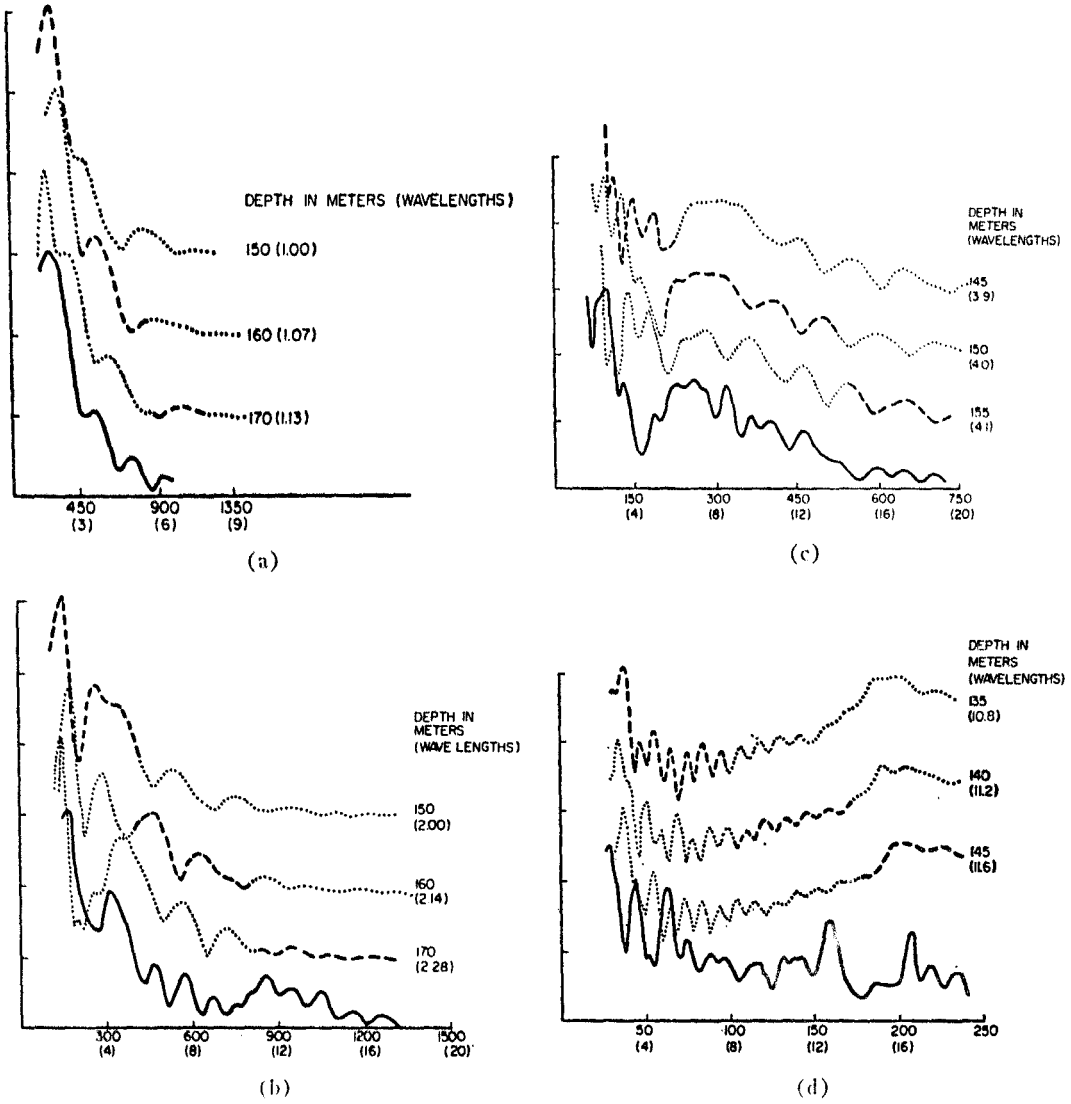

FIG. 14. Theoretical curves and Athabasca Glacier results at (a) 2, (b) 4, (c) 8, and (d) 24 Mhz. (a) dashed/dotted line, theoretical H_z, $K=3.2$, $\tan\delta=0.08$; solid line, experimental Athabasca Glacier, H_z, 2 Mhz. (b) dashed/dotted line, theoretical $H\rho$, $K=3.2$, $\tan\delta=0.04$; solid line, experimental Athabasca Glacier, $H\rho$, 4 Mhz. (c) dashed/dotted line, theoretical $H\rho$, $K=3.2$, $\tan\delta=0.02$; solid line, experimental Athabasca Glacier, $H\rho$, 8 Mhz. (d) dashed/dotted line, theoretical H_z, $K=3.2$, $\tan\delta=0.007$; solid line, experimental Athabasca Glacker, $H\rho$, 24 Mhz. Distance in meters (wavelengths).

near field. In the near field the two direct waves add to form peaks and subtract to form nulls. If the waves are about the same size, the peaks and nulls will be sharp, but if one wave is much larger than the other, there will be little interference.

As the amplitude of the subsurface wave decreases below the amplitude of the air wave, the pattern becomes less sharp. An envelope formed by joining the peaks and by joining the nulls of the interference pattern becomes thinner at a rate determined by the loss tangent of the medium.

In the Gorner Glacier data, the loss tangent was estimated to be less than 0.7/f (Mhz), well

within the published value for ice. In the Athabasca data, reflections appear to disturb the two direct waves too greatly to be able to use this simplified approach.

Depth

An estimate of the dielectric constant and the critical distance from the field data can be used to estimate the depth. However, an assumption about the dip of the reflector must be made. The method fails if either the dielectric constant or the critical distance cannot be estimated accurately.

Scattering

One of the major unknowns in the application of the RFI technique is the effect of irregularities in the medium. It is reasonable to believe that the effects of irregular surfaces, inhomogeneities within the dielectric, and objects near the antennas could all perturb the measured data. One possible way to remove small random effects is to appropriately filter the data, and a simple running-average filter was used to enhance the pertinent features of the Athabasca Glacier data.

An estimate of scattering is important to understand geologic structure. During the Athabasca trials the H_ϕ component, which should theoretically be null for plane horizontal layers, was observed to be significant (though weaker than the other components). Therefore, H_ϕ provided a measurement of the scattering, which was considerable at the higher frequencies. The similarity of all the components measured on the Gorner Glacier on the other hand implied that scattering was not significant up to 10 Mhz.

CONCLUSIONS

1. The RFI technique is a practical method with which to study layering in low-loss dielectrics ($\tan \delta < 0.1$).

2. Three parameters of the upper layer can be estimated from the data: the dielectric constant, the loss tangent, and an estimate of the thickness to a reflector. Measurements of $\epsilon = 3.2$ and $f \cdot \tan \delta = 0.7$ (f in Mhz) for ice are in agreement with known results.

3. The method is an inexpensive way to sound ice sheets less than a few hundred meters thick, and could be used to study low-loss layers on the moon.

4. Further work is required to refine and quantify the interpretational procedure, to extend it to more complex geometries, and to understand better the effects of random scatterers.

ACKNOWLEDGMENTS

We would like to acknowledge the assistance of the following: Mr. E. A. Johnston of MIT's Center for Space Research, who built the transmitter used on the Athabasca Glacier and participated in the expedition; Dr. H. Röthlisberger, Mr. P. Fohn, and Mr. M. Aellen, who provided advice on the logistics of the Gorner Glacier; The Department of National and Historic Parks Branch, Calgary, who gave us permission to work on the Athabasca Glacier, and, along with Brewster Transport Company and the Administration of Jasper National Park, provided much useful support; and Dr. A. K. Sinha, who allowed us to use some of his preliminary theoretical curves. We would also like to thank Mr. L. Tsang and Dr. J. A. Kong for pointing out a sign error in programming the theoretical equations.

Financial support was provided by NASA grant no. NGL 22-009-257 and contract NAS9-11540 at MIT with subcontracts at the University of Toronto; Rossiter thanks The Lunar Science Institute, Houston, Texas for support under contract no. NSR 09-051-001.

This work is the second paper in a series providing the background for the Surface Electrical Properties Experiment, planned for the Apollo 17 lunar mission.

REFERENCES

Annan, A. P., 1973, Radio interferometry depth sounding: Part I—Theoretical discussion: Geophysics, this issue.

Chung, D. H., Westphal, W. B., and Simmons, G., 1971, Dielectric behavior of lunar samples: Electromagnetic probing of the lunar interior, *in* Proceedings of the Second Lunar Science Conference: MIT Press, Cambridge, v. 3, p. 2381–2390.

Evans, S., 1963, Radio techniques for the measurement of ice thickness: The Polar Record, v. 11, p. 406–410 and 795.

——— 1965, Dielectric properties of ice and snow—a review: J. Glaciol., v. 5, p. 773–792.

——— 1967, Progress report on echo sounding: The Polar Record, v. 13, p. 413–420.

Gold, T., O'Leary, B. T., and Campbell, M., 1971, Some physical properties of Apollo 12 lunar samples, *in* Proceedings of the Second Lunar Science Conference: MIT Press, Cambridge, v. 3, p. 2173–2181.

Holser, W. T., Brown, R. J. S., Roberts, F. A., Fredriksson, O. A., and Unterberger, R. R., 1972, Radar logging of a salt dome: Geophysics, v. 37, p. 889–906.

Jiracek, G. R., 1967, Radio sounding of Antarctic ice: Res. Rep. No. 67-1, Geophys. and Polar Res. Center, University of Wisconsin.

Kanasewich, E. R., 1963, Gravity measurements on the

Athabasca Glacier, Alberta, Canada: J. Glaciol., v. 4, p. 617–631.
Katsube, T. J., and Collett, L. S., 1971, Electrical properties of Apollo 11 and 12 lunar samples, *in* Proceedings of the Second Lunar Science Conference: MIT Press, Cambridge, v. 3, p. 2367–2379.
Keller, G. V., and Frischknecht, F. C., 1961, Induction and galvanic resistivity studies on the Athabasca Glacier, Alberta, Canada, *in* Geology of the Arctic (International Symposium): edited by G. O. Raasch, Toronto, University of Toronto, v. 2, p. 809–832.
Paterson, W. S. B., and Savage, J. C., 1963, Geometry and movement of the Athabasca glacier: J. Geophys. Res., v. 68, p. 4513–4520.
Röthlisberger, Hans, 1967, Electrical resistivity measurements and soundings on glaciers: Introductory remarks: J. Glaciol., v. 6, p. 599–606.
Saint-Amant, M., and Strangway, David W., 1970, Dielectric properties of dry, geologic materials: Geophysics, v. 35, p. 624–645.
Strangway, D. W., 1969, Moon: electrical properties of the uppermost layers: Sci., v. 165, p. 1012–1013.
Tyler, G. L., 1968, Oblique scattering radar reflectivity of the lunar surface: Preliminary results from Explorer 35: J. Geophys. Res., v. 73, p. 7609–7620.
Unterberger, R. R., Holser, W. T., and Brown, R. J. S., 1970, Radio frequency propagation in salt domes 1. Theory, laboratory and field measurements of attenuation: Presented at SEG 40th Annual International Meeting, New Orleans.
Walford, M. E. R., 1968, Field measurements of dielectric absorption in Antarctic ice and snow at very high frequencies: J. Glaciol., v. 7, p. 89–94.
Watt, A. D., and Maxwell, E. L., 1960, Measured electrical properties of snow and glacial ice: J. Res. U. S. Nat. Bur. Stan., v. 64D, p. 357–363.
Weaver, Harold, 1965, The interpretation of thermal emissivity from the moon, *in* Solar system radio astronomy: edited by J. Aarons, New York, Plenum Press, p. 295–354.

VOL. 78, NO. 17 JOURNAL OF GEOPHYSICAL RESEARCH JUNE 10, 1973

Interference Patterns of a Horizontal Electric Dipole over Layered Dielectric Media

L. TSANG AND J. A. KONG

Department of Electrical Engineering, Massachusetts Institute of Technology Cambridge, Massachusetts 02139

GENE SIMMONS

Department of Earth and Planetary Sciences, Massachusetts Institute of Technology Cambridge, Massachusetts 02139

Interference patterns for em fields due to a subsurface reflector below a layered lossy dielectric are calculated with the geometrical optics approximation for use in interpreting data to be collected on the moon by Apollo 17 as well as data currently being obtained on terrestrial glaciers. The radiating antenna lies on the surface. All six field components are calculated and studied. For the endfire solutions the peak of the first reflected wave is found to be different from that of the broadside ones. To facilitate a physical discussion, we plotted the radiation patterns due to the antenna on the surface. We find that, although the maximum broadside power goes into the first medium at the critical angle, the maximum endfire power enters the first medium at the angle $\sin^{-1}\ [2n^2/(1 + n^2)]^{1/2}$, where $1/n$ is the index of refraction of the first medium.

The surface electrical properties experiment will be used on Apollo 17 to detect subsurface layering and to measure both dielectric constant and loss tangent of the lunar subsurface [*Simmons et al.*, 1972]. In this lunar experiment a horizontal electric dipole that transmits at discrete radio frequencies is laid on the lunar surface, and the electromagnetic field amplitudes are measured continuously, as a function of distance, with a receiver and tape recorder mounted on the astronaut's lunar roving vehicle. Ideally they will travel along the direction of the antenna and also perpendicular to the direction of the antenna. In actual practice a pair of crossed orthogonal dipoles radiate sequentially at frequencies of 1, 2.1, 4, 8.1, 16, and 32.1 MHz. The time window during which energy at any given frequency is radiated from either of the antennas is sufficiently long (several thousand cycles minimum), so that the experiment is essentially that of continuous wave interferometry experiment. The presence of various waves produces an interference pattern. The peaks and troughs of the pattern contain information about the subsurface properties of the moon. To interpret such data, we present here the results of theoretical studies. Additional details of the lunar experiment are given by *Simmons et al.* [1972] and *Rossiter et al.* [1972]. Applications of the technique to the study of terrestrial glaciers are described by *Strangway et al.* [1972].

We take as our model stratified media. Antenna radiation in the presence of stratified media has been studied for many decades [*Baños*, 1966; *Brekhovskikh*, 1960; *Sommerfeld*, 1949]. Some theoretical investigations specifically related to this experiment have been undertaken already. *Annan* [1970] applied the saddle point method and used the geometrical optics approximation to solve for the vertical component of the magnetic field on the surface of a half-space dielectric and also a two-layer medium. *Kong* [1972] abandoned the conventional use of potential functions and obtained closed-form expressions for the reflection coefficients that embody all information about the stratified medium. The symmetry of the reflection coefficients makes the evaluation of the integrals comparatively easy. In this paper we employ his formulation to determine all six field components. Specifically, the problem considered

here is that of a two-layer medium. We describe in some detail the steepest descent path based on the saddle point method.

SOLUTIONS IN INTEGRAL REPRESENTATION

Consider an electric dipole transmitting antenna lying on the surface of a stratified medium. We use cylindrical coordinates (ρ, ϕ, z) with the z axis perpendicular to the boundaries of stratification. The dipole points in the direction of $\phi = 0$. The total electromagnetic fields are decomposed into TM and TE components. Above the stratified medium the solutions are [*Kong*, 1972]

$$\mathbf{E}^{TM} = \int_{-\infty}^{\infty} dk_\rho \left(i \frac{Il}{8\pi\omega\epsilon}\right) \begin{bmatrix} ik_z k_\rho (1 - R^{TM}) e^{ik_z z} H_1^{(1)\prime}(k_\rho \rho) \cos\varphi \\ -i(k_z/\rho)(1 - R^{TM}) e^{ik_z z} H_1^{(1)}(k_\rho \rho) \sin\varphi \\ k_\rho^2 (1 - R^{TM}) e^{ik_z z} H_1^{(1)}(k_\rho \rho) \cos\varphi \end{bmatrix} \tag{1a}$$

$$\mathbf{H}^{TM} = \int_{-\infty}^{\infty} dk_\rho \left(\frac{Il}{8\pi}\right) \begin{bmatrix} -(1/\rho)(1 - R^{TM}) e^{ik_z z} H_1^{(1)}(k_\rho \rho) \sin\varphi \\ -k_\rho (1 - R^{TM}) e^{ik_z z} H_1^{(1)\prime}(k_\rho \rho) \cos\varphi \\ 0 \end{bmatrix} \tag{1b}$$

$$\mathbf{E}^{TE} = \int_{-\infty}^{\infty} dk_\rho \left(\frac{Il\omega\mu}{8\pi}\right) \begin{bmatrix} -(1/k_z \rho)(1 + R^{TE}) e^{ik_z z} H_1^{(1)}(k_\rho \rho) \cos\varphi \\ (k_\rho/k_z)(1 + R^{TE}) e^{ik_z z} H_1^{(1)\prime}(k_\rho \rho) \sin\varphi \\ 0 \end{bmatrix} \tag{2a}$$

$$\mathbf{H}^{TE} = \int_{-\infty}^{\infty} dk_\rho \left(i \frac{Il}{8\pi}\right) \begin{bmatrix} ik_\rho (1 + R^{TE}) e^{ik_z z} H_1^{(1)\prime}(k_\rho \rho) \sin\varphi \\ (i/\rho)(1 + R^{TE}) e^{ik_z z} H_1^{(1)}(k_\rho \rho) \cos\varphi \\ (k_\rho^2/k_z)(1 + R^{TE}) e^{ik_z z} H_1^{(1)}(k_\rho \rho) \sin\varphi \end{bmatrix} \tag{2b}$$

where k_ρ and k_z are, respectively, the ρ component and the z component of the wave vector $\mathbf{k}$, $H_1^{(1)}$ is the first-order Hankel function of first kind, ω is the angular frequency, Il is the source strength, μ is the permeability, and ϵ is the permittivity. Both the permeability and the permittivity can be complex. In (1), R^{TM} is the reflection coefficient for TM waves, and in (2), R^{TE} is the reflection coefficient for TE waves. For the two-layer case with the interface located at $z = -d$, the reflection coefficients, calculated from (31) and (32) of *Kong* [1972], are

$$R^{TE} = \frac{1}{R_{01}} \left[1 - \frac{1/R_{01} - R_{01}}{1/R_{01} + R_{12} \exp(i2k_{1z}d)}\right] \tag{3}$$

$$R^{TM} = \frac{1}{S_{01}} \left[1 - \frac{1/S_{01} - S_{01}}{1/S_{01} + S_{12} \exp(i2k_{1z}d)}\right] \tag{4}$$

where

$$R_{ij} = \frac{\mu_j k_{iz} - \mu_i k_{jz}}{\mu_j k_{iz} + \mu_i k_{jz}} \tag{5}$$

$$S_{ij} = \frac{\epsilon_j k_{iz} - \epsilon_i k_{jz}}{\epsilon_j k_{iz} + \epsilon_i k_{jz}} \tag{6}$$

where ϵ_i and μ_i are the permittivity and the permeability of the ith medium, respectively, and k_{iz} denotes the z component of the wave vector $\mathbf{k}_i$ in region i.

Because $1 - R^{TM}$ and $1 + R^{TE}$ appear in the integrands of (1) and (2), we write

$$1 + R^{TE} = \frac{1 + R_{12} \exp(i2k_{1z}d)}{1 + R_{01}R_{12} \exp(i2k_{1z}d)} X_{01} \tag{7}$$

$$1 - R^{TM} = \frac{1 - S_{12} \exp(i2k_{1z}d)}{1 + S_{01}S_{12} \exp(i2k_{1z}d)} Y_{10} \tag{8}$$

where

$$X_{ij} = 1 + R_{ij} = \frac{2\mu_j k_{iz}}{\mu_j k_{iz} + \mu_i k_{jz}} \tag{9}$$

$$Y_{ij} = 1 + S_{ij} = \frac{2\epsilon_j k_{iz}}{\epsilon_j k_{iz} + \epsilon_i k_{jz}} \tag{10}$$

At this point we have obtained mathemati-

cally the solution to our problem. However, in order to apply the solution to a model with numerical values assigned to the various physical properties, we must evaluate the various expressions. In the next section we study the asymptotic solutions of the above integrals by using the saddle point method under the geometrical optics approximations. And then in the following section we illustrate the solutions with plots of the interference patterns for a set of possible values of physical properties of the moon.

ASYMPTOTIC EVALUATION OF INTEGRALS

In the geometrical optics approximation the interference pattern is determined by three waves: (1) the direct wave from the antenna, (2) the lateral wave excited by the antenna along the surface, and (3) the wave reflected in the subsurface following ray optics paths (Figure 1). We first expand the denominators in (7) and (8) in power series:

$$1 + R^{TE} = X_{01}\left[1 + \sum_{m=1}^{\infty} X_{10}R_{10}^{m-1}R_{12}^{m} \cdot \exp(i2k_{1z}md)\right] \quad (11)$$

$$1 - R^{TM} = Y_{10}\left[1 - \sum_{m=1}^{\infty} Y_{01}S_{10}^{m-1}S_{12}^{m} \cdot \exp(i2k_{1z}md)\right] \quad (12)$$

The convergence of the series is assured because along the original path of integration the denominators of (7) and (8) are $1 + A$, where A is a complex number with magnitude less than 1 for all k_ρ.

The first term in the power series expansion gives rise to the half-space solution, which consists of the first two kinds of waves. Mathematically, the direct wave corresponds to the saddle point contribution, and the lateral wave corresponds to the branch point contribution due to k_{1z}. The summation term gives rise to all reflections from the subsurface. At each observation point the number of reflections from the bottom layer can be determined by exercising ray optics. Each optical path can be traced back to an image source.

Now we consider the solution to the half-space problem. The contribution due to a saddle point at θ for a typical integral takes the following form:

$$I_s = \int_{-\infty}^{\infty} F(k_\rho)\frac{k_\rho}{k_z}e^{ik_z z}H_0^{(1)}(k_\rho\rho)\,dk_\rho \quad (13)$$

$$I_s = (2/i)(e^{ikr}/r)[F(\theta) + (1/i2kr)(F''(\theta) + F'(\theta)\cot\theta)] \quad (14)$$

where we have used the transformations $k_\rho = k\sin\theta$ and $k_z = k\cos\theta$. Here θ and r are referred to the spherical coordinate system with the origin at the antenna; θ is the angle between the radius vector and z axis and corresponds to the observation angle. Note that near

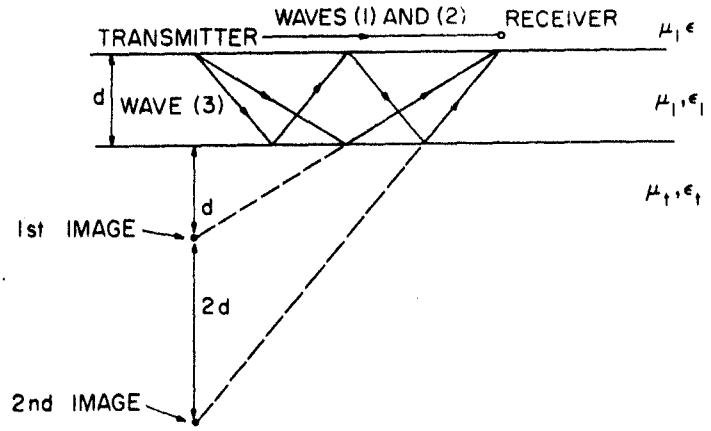

Fig. 1. Geometrical configuration of the problem. The three waves under geometrical approximation are also illustrated.

the surface $\theta \simeq \pi/2$. All field components are calculated up to second order in $r^{-\frac{1}{2}}$ according to (1) and (2) by using (14). The results are listed in Appendix 1. For $\theta = \pi/2$ the dominant terms are all of the order $r^{-\frac{1}{2}}$.

Near the surface the contribution due to the branch point at k_{1z} is also of order $r^{-\frac{1}{2}}$ and cannot be neglected. The integration around the branch point gives rise to the lateral wave. Assume a general form for $F(k_\rho)$ in (13) to be

$$F(k_\rho) = (k_\rho{}^m k_z{}^n k_{1z}{}^p)/(k_z + bk_{1z}) \quad (15)$$

$$m, n, p \geq 0$$

The branch point contribution I_b of the integral is

$$I_b = -i2b \frac{k_1{}^{m+1}}{\rho^{\frac{1}{2}}} \frac{i^{n-2}}{a^{\frac{1}{2}-n}} \cdot \frac{e^{-az+ik_1\rho}}{(1 + i \sec\theta_c \cot\theta)^{3/2}} \quad (16)$$

$$p = 0$$

$$I_b = i2 \frac{k_1{}^{m+1}}{\rho^{\frac{1}{2}}} \frac{i^{n-1}}{a^{\frac{1}{2}-n}} \cdot \frac{e^{-az+ik_1\rho}}{(1 + i \sec\theta_c \cot\theta)^{3/2}} \quad (17)$$

$$p = 1$$

where $a = (k_1{}^2 - k^2)^{1/2}$. For $p > 1$ the contribution is of order higher than $\rho^{-\frac{1}{2}}$ and is safely neglected.

As was stated in the beginning, only the waves that follow geometrical optics paths are considered. The solutions are of the order of $1/r$. The integrals to be evaluated are

$$I_c = \sum_{m=1}^{\infty} \int_{-\infty}^{\infty} dk_\rho \frac{k_\rho}{k_{1z}} H_0{}^{(1)}(k_\rho\rho) e^{i2k_{1z}md} D(k_\rho) \cdot \frac{k_{1z}}{k_\rho} X_{01} X_{10} R_{10}{}^{m-1} e^{ik_{1z}z} R_{12}{}^m \quad (18)$$

The integral is now in the form of (13), where $2md$ plays the same role as z before. We again apply (14) to (18), and the solution is

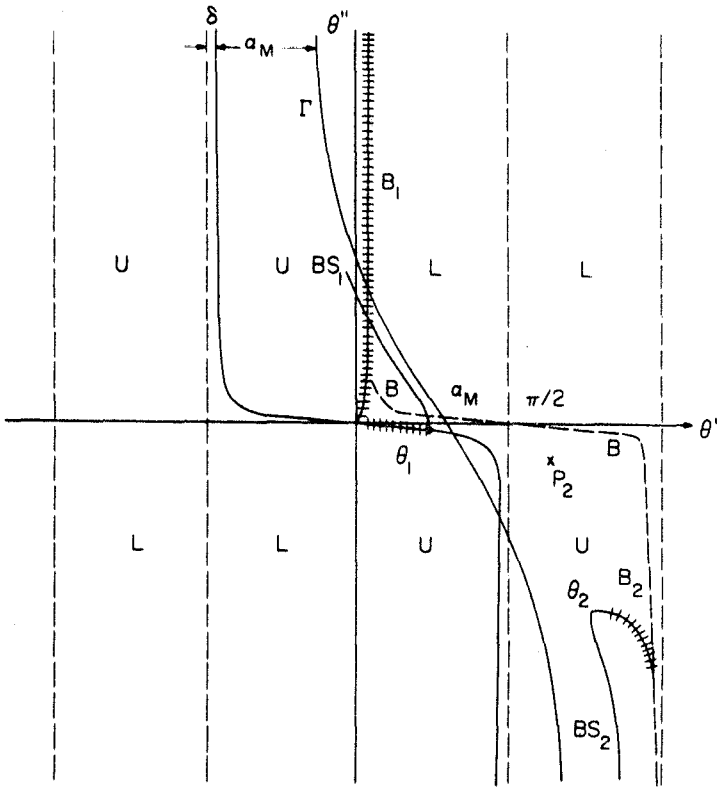

Fig. 2. The complex plane illustrating singularities and contours for the case of conducting subsurface.

$$I_v = \sum_{m=1}^{\infty} \left[\frac{2}{i} \frac{e^{ik_1 R_m}}{R_m} D(k_\rho) \cdot \frac{k_{1z}}{k_\rho} X_{01} X_{10} R_{10}^{m-1} R_{12}^{m} e^{ik_{2z}z} \right]$$

$$k_\rho = k_1 \sin \alpha_m$$

where $R_m = [\rho^2 + (2md)^2]^{1/2}$ and $\alpha_m = \tan^{-1}(\rho/2md)$. These results hold for $k_1 d \gg 1$ and $d \gg z$. All field components are evaluated to the order of $1/r$ in Appendix 1.

When the observation angle of the mth image source $\alpha_m = \tan^{-1}(\rho/2md)$ exceeds the critical angle, branch cut contributions need to be included. The branch cut is evaluated by deforming to a steepest path through the branch point. In geometrical optics approximation contributions due to the branch points are usually neglected. In deforming the branch cuts to the steepest descent path through the branch point and before deciding that the final contribution due to the latter is negligible, we must show that the deformation is valid. If the deformation is invalid, two alternative approaches can be taken. One alternative is to choose another path, and the other is to choose a different branch cut. When α_m is used in the integrals or, rather, in the coefficients before the exponential in the integrals, we must remember that in those coefficients two terms (k_z and k_{2z}) are double valued, and the proper one of those two values must be taken.

TWO-LAYER INTERFERENCE PATTERN

We now consider the interference patterns. Our formulation includes different medium constituents for all layers. We shall illustrate here two cases in which the first layer is slightly conductive and the second layer is (1) a good conductor and (2) a good dielectric. Other cases can be treated in a similar way. Details of the complex plane are shown in Figures 2 and 3. Plots of numerical results for all six field components are shown in Figures 4–6. In these figures the H components have been normalized by the relation

$$H = (Il/4\pi\lambda^2) H_{\text{norm}}$$

whereas the E components have been normalized by the relation

$$E = i(Il\omega\mu/4\pi\lambda) E_{\text{norm}}$$

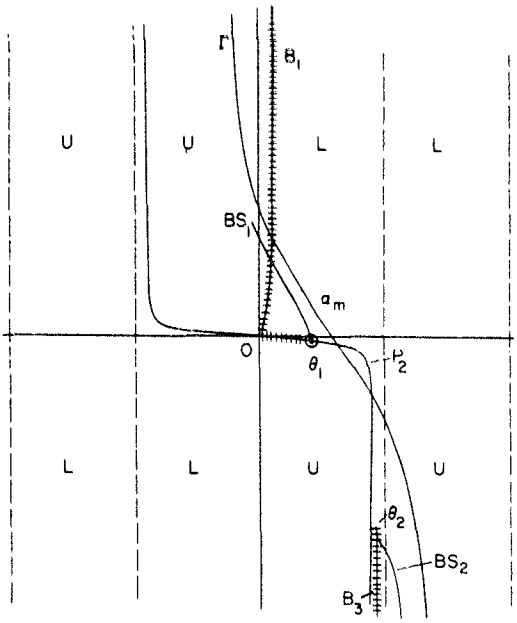

Fig. 3. The complex plane illustrating singularities and contours for the case of a dielectric subsurface.

Case 1: Second layer is good conductor. Various singularities and contours are shown in Figure 2. The task is to determine reflections from the bottom layer, which combines with the well-known half-space solution to form the interference pattern. We note the following points. (1) The transformation $k_\rho = k_1 \sin\theta$ is used. On the branch cuts the imaginary parts of k_z and k_{2z} are equal to zero. They are shown as B_1 and B_2 in the diagram. Notice that B, the branch cut of k_{1z}, has been stretched. (2) Here C is the original path of integration $k_\rho'' = 0$; Γ is the steepest descent path passing through the saddle point α_m. Here BS_1 is the steepest descent path passing through the branch point $\theta_1 = \sin^{-1}(k/k_1)$ corresponding to that of k_z; BS_2 is the steepest descent passing through the branch point $\theta_2 = \sin^{-1}(k_2/k_1)$ corresponding to that of k_{2z}. (3) On the diagram the regions marked U are those regions in which $Im\ k_{1z} > 0$, and those marked L are the regions for $Im\ k_{1z} < 0$. (4) In the U regions the integrand $e^{ik\rho + 2ik_1 z md}$ vanishes at infinity. Any deformation that requires the path at infinity to be in the U regions is valid. Therefore the path B_1 can be detoured to BS_1, and B_2 to BS_2. (5) The contributions due to BS_1 and BS_2 are smaller than that due to Γ and are

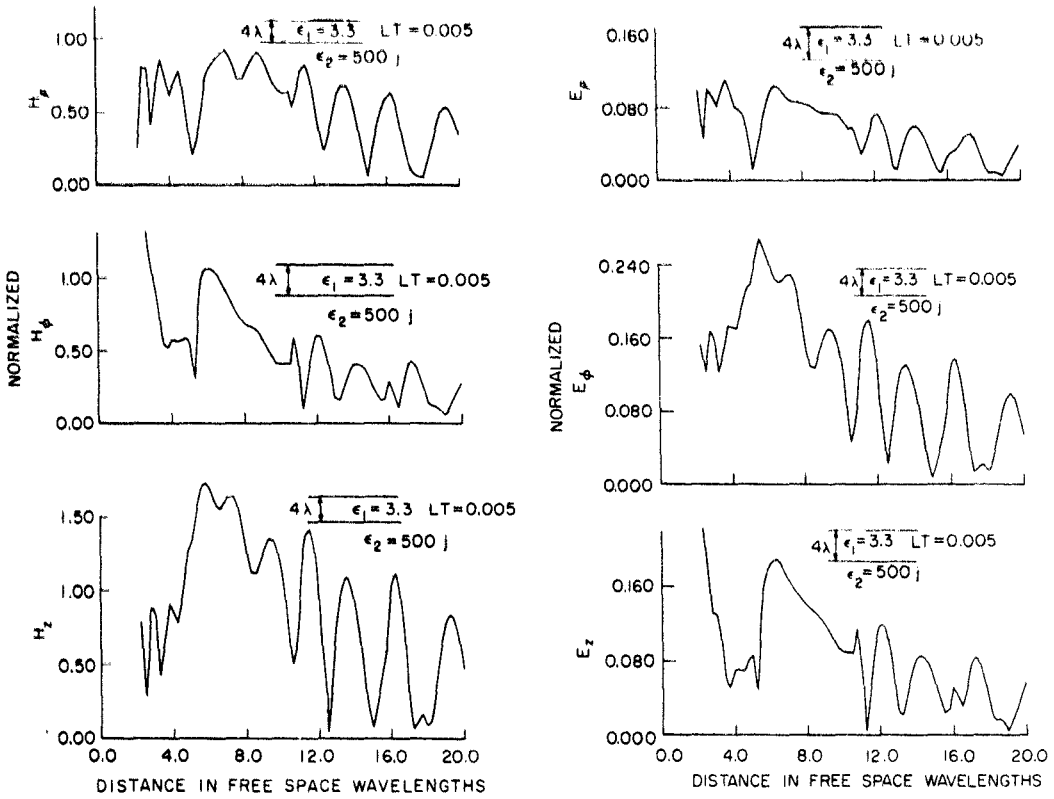

Fig. 4. Interference pattern for $\epsilon_1 = 3.3$, $LT = 0.005$, $\epsilon_2 = 500\ i$.

neglected in the geometrical optics approximation. (6) For $\alpha_m < \theta_1'$, α_m occurs on the lower sheet of k_z, but for $\alpha_m > \theta_1'$, α_m occurs on the upper sheet of k_z. Therefore, when passing through the saddle point, the double-valued functions k_z and k_{2z} are chosen in the following way. For $\alpha_m < \theta_1'$, $Im\ k_z < 0$ and $Im\ k_{2z} > 0$, and for $\alpha_m > \theta_1'$, $Im\ k_z > 0$ and $Im\ k_{2z} > 0$. (7) In evaluating $\theta_1 = \sin^{-1}(k/k_1) = \theta_1' + i\theta_1''$ and $\theta_2 = \sin^{-1}(k_2/k_1) = \theta_2' + i\theta_2''$, both θ_1'' and θ_2'' are negative. If the media are nonmagnetic, these two Sommerfeld poles occur at

$$\sin \theta_{p_1} = k/(k^2 + k_1^2)^{1/2}$$

$$\sin \theta_{p_2} = k_2/(k_1^2 + k_2^2)^{1/2}$$

Point P_2 is marked on the diagram. Its effect can be neglected if α_m is not near $\pi/2$. A sufficient condition is that $d \geq 2.5\lambda$. In the practical situation, $\rho \leq 20\lambda$, and so $\alpha_m \leq 77°$. (9) The effect of the pole P_1 can be neglected. When $\alpha_m \leq \theta_1'$, α_m lies on the lower sheet, whereas θ_{p_1} lies on the upper sheet. When $\alpha_m > \theta_1'$, the analysis is slightly more complicated. When we detour the original path C to the saddle point path Γ, we need to consider two other contributions, one being due to the branch cut B_1 and the other being the residue of the pole P_1. In evaluating B_1 we detour it to BS_1, and, on the detour, P_1 is again passed, and its contribution is exactly the negative of the previous residue. The net effect is that we only have the contribution due to BS_1 left, and it is neglected in the geometrical optics approximation.

Case 2: Subsurface is good dielectric. The various singularities and contours are shown in Figure 3. We note the following. (1) This case contrasts with the previous one in that θ_2 is at a different location. (2) The branch cut $Im\ k_{2z} = 0$ cannot be detoured to BS_2 because the detour involves passing through the L regions at infinity. We thus choose another branch cut such that $Re\ k_{2z} = 0$ (B_3). The upper sheet that we choose is such that $Im\ k_z > 0$ and $Re\ k_{2z} > 0$. (3) Now B_3 can be de-

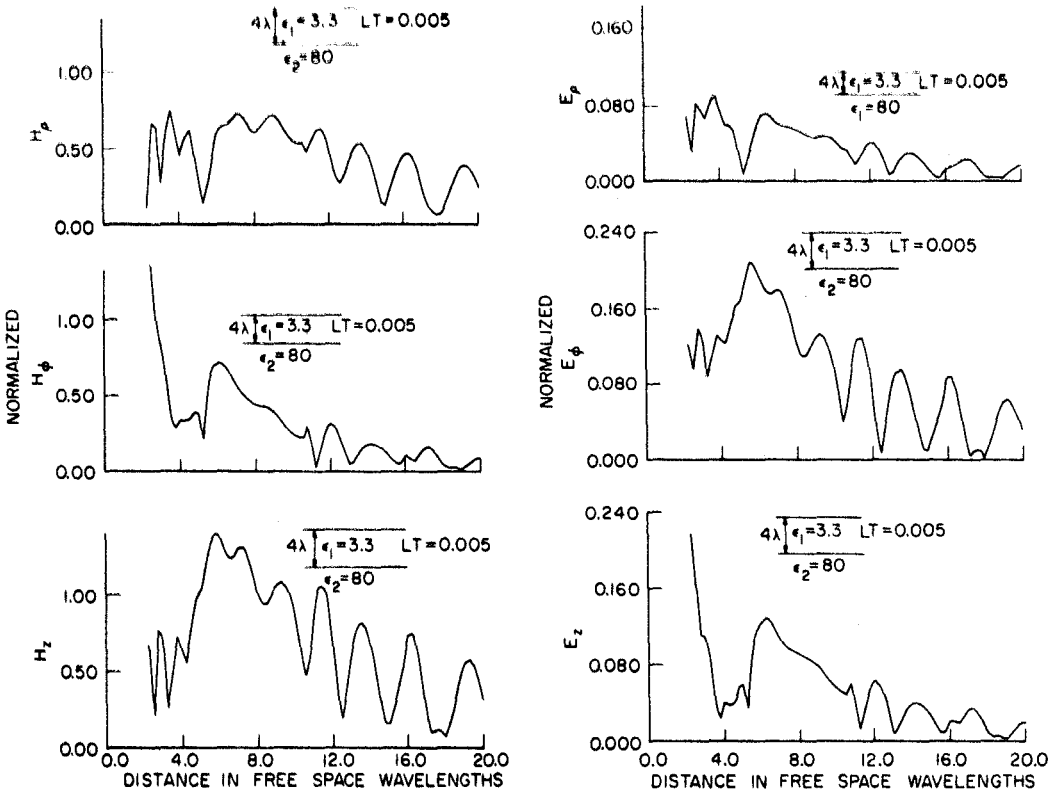

Fig. 5. Interference pattern for $\epsilon_1 = 3.3$, $LT = 0.005$, $\epsilon_2 = 80$.

toured to BS_2, and BS_2 is neglected in the geometrical optics approximation. The pole P_2 is a virtual pole in the upper sheet. The pole P_1 is treated in the same way as in the conductive case. (4) Finally, the choice of the double-valued functions is as follows. For $\alpha_m < \theta_1'$, $Im\ k_z < 0$ and $Re\ k_{2z} > 0$, for $\alpha_m > \theta_1'$, $Im\ k_z > 0$ and $Re\ k_{2z} > 0$.

The two-layer interference patterns obtained with the above prescriptions are plotted in Figure 4 for the conducting case and in Figure 5 for the dielectric case. For the first layer we choose $\epsilon' = 3.3\epsilon_0$ and loss tangents 0.005. These values are possible for the moon [*Simmons et al.*, 1972]. They are also typical of terrestrial glaciers [*Strangway et al.*, 1972]. The interface between the two layers is taken to be four free-space wavelengths below the surface.

Discussion

The interference patterns may be best understood by separating the contributions of the various waves. Thus we depict in Figures 7–8 two typical field components H_z and E_z separated into the half-space solutions and the waves reflected from the first boundary. We note that H_z, H_ρ, and E_ϕ are the field components measured broadside (i.e., $\phi = \pi/2$), whereas E_z, E_ρ, and H_ϕ are those measured endfire (i.e., $\phi = 0$). The maximums of the first reflected waves for H_z and E_z occur at different locations.

To explain this difference, we consider the radiation pattern due to the dipole lying on the lunar surface. Under the geometrical optics approximation the maximum of the wave reflected from the subsurface corresponds to the angle of the Poynting power that is radiated into the first layer. The power radiation pattern of the horizontal electrical dipole at the interface is shown in Figures 9–10, both broadside and endfire [*LaTorraca*, 1972]. For $\phi = \pi/2$ the maximum power occurs at the critical angle $\sin^{-1}(k/k_1)$, and k_1 is assumed to be real. But, for $\phi = 0$, we find that the maximum occurs at an angle $\sin^{-1}[2n^2/(1 + n^2)]^{1/2}$, where $n = k/k_1$.

We note the following. (1) If k_1 contains an

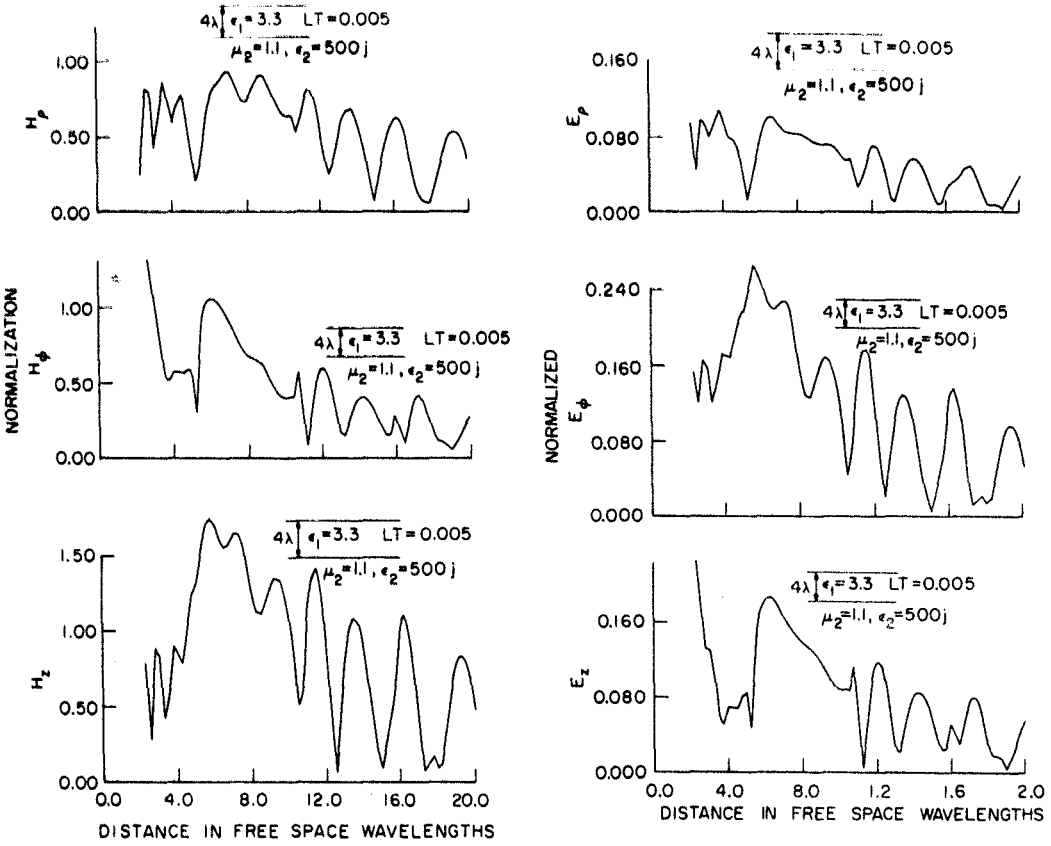

Fig. 6. Interference pattern for $\epsilon_1 = 3.3$, $LT = 0.005$, $\mu_2 = 1.1$, $\epsilon_2 = 500\ i$.

imaginary part, however small, the radiation is null in the lower half space because, by definition, the radiation pattern is measured at infinite distances, and the $Im\ k_1$ gives rise to an exponential attenuation with distance, and the power vanishes at infinity. (2) At the interface of free space and a dielectric medium with permittivity $3\epsilon_0$, the amount of power that radiates into the free space is calculated to be approximately 12% of the total power radiated by the antenna. (3) In the direction of maximum power not all field components have to be maximum. (4) Figure 10 shows that the null of the endfire radiation pattern occurs precisely at the critical angle. (5) A change of permeability from μ_0 to $\mu > \mu_0$ merely changes the magnitude of k_2. If μ becomes complex, the positions of the various singularities change, and the integrals must be reevaluated on the new complex plane. (6) A small loss tangent has small effect on the position of peaks and troughs but changes the amplitudes of the field components drastically. (7) The results obtained by choosing a different branch cut with $Re\ k_z = 0$ agree with those due to the branch cut $Im\ k_z = 0$. This is shown in Appendix 3.

The validity of our calculations can also be verified by carrying out exact solutions of the integrals. *Tsang* [1971] obtained such solutions by numerical integration with a computer. The computation is extremely time consuming, and we show a single comparison. In Figure 11 the exact solution may be compared with the asymptotic solution under the geometrical optics approximation. The calculation is done at a receiver elevation 6 meters above the surface in order to ensure fast convergence. It can be seen that the geometrical approximation is not good near peaks in the interference curves. Mathematically, the peaks are those regions where the saddle point α_m approaches the branch point θ_1. The saddle point method

crumbles. Using Watson's lemma (Appendix 2), the criterion for the validity of the saddle point method is found to be

$$\frac{k_1 R_m(\sin\theta_1 - \sin\alpha_m)^2}{n-1} \gg 1$$

This condition can be achieved either by making k_1 more conductive so that θ_1 has a bigger imaginary part or by making R_m bigger. But both of these procedures will lead to a decay of the curves and thus decrease the interference effects; they are largely undesirable.

One final point requires discussion. In the geometrical optics approximation BS_1 and BS_2, the branch point steepest descent path contributions, have been neglected. These contributions correspond physically to the reflections of the lateral waves from the bottom layer. Thus we have implicitly assumed that the energy arriving at the upper surface of layer 1 due to the reflected lateral waves is small. For a better approximation, these effects should be included.

APPENDIX 1

In the vicinity of the surface (i.e., $z \ll d, \rho$) the six electromagnetic field components are as follows.

$$H_z^{TE} = -\frac{Il}{4\pi}\frac{e^{ikr}}{r}\left[\sin\theta\left(ik - \frac{1}{r}\right)X_{01}(\theta) + \frac{3}{2r}\cos\theta X_{01}'(\theta) + \frac{\sin\theta}{2r}X_{01}''(\theta)\right]\sin\phi$$

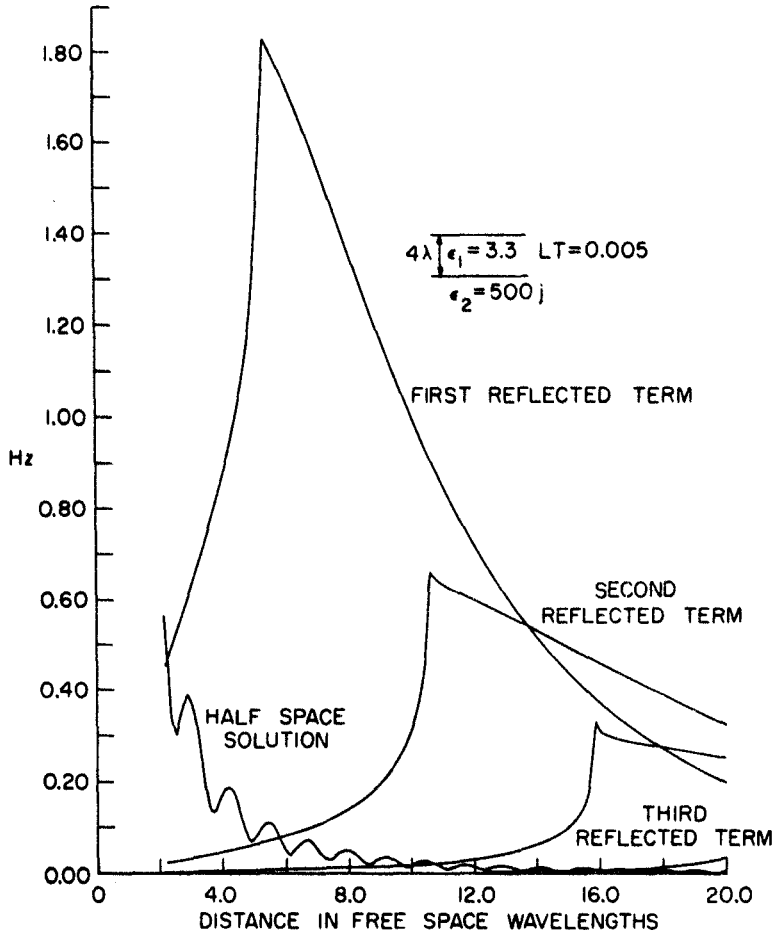

Fig. 7. The reflected H_z compared with the half-space solution, conducting case.

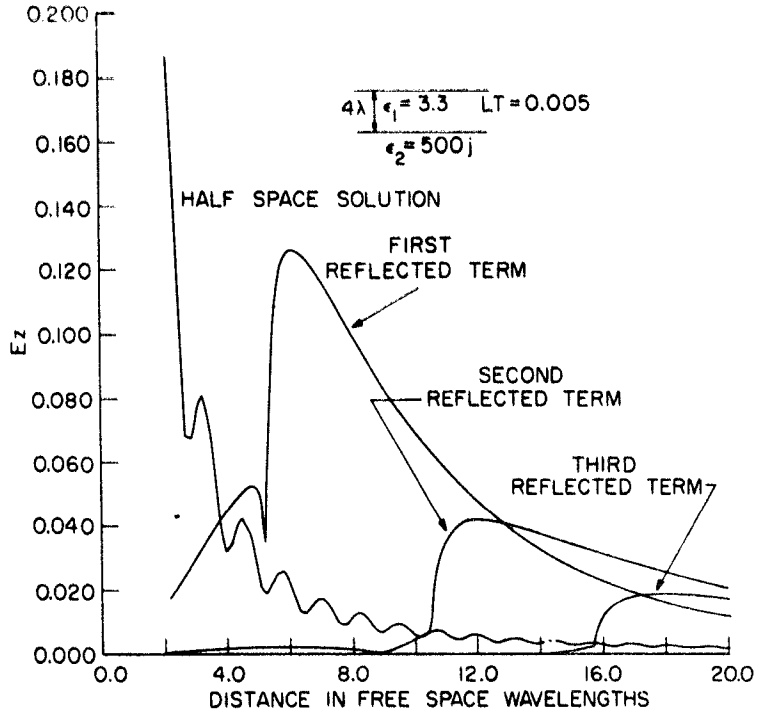

Fig. 8. The reflected E_z compared with the half-space solution, conducting case.

$$- \frac{Il}{4\pi}\frac{\mu}{\mu_1}\frac{2k_1^2}{\rho^2 a^2}\frac{e^{-as+ik_1\rho}}{(1+i\sin\theta_c\cot\theta)^{3/2}}\sin\phi$$

$$- \frac{Il}{4\pi}\frac{\mu_1}{\mu}\sum_{m=1}^{\infty}(X_{10}^2 R_{10}^{m-1}R_{12}^m ik_1\sin\alpha_m e^{ik_{1z}})\frac{e^{ik_1R_m}}{R_m}\sin\phi \qquad k_\rho = k_1\sin\alpha_m$$

$$E_\phi^{TE} = \frac{Il\omega\mu}{4\pi i}\frac{e^{ikr}}{r}\left\{X_{01}(\theta)+\frac{1}{2ikr}\left[\cot\theta X_{01}'(\theta)+X_{01}''(\theta)\right]\right\}\sin\phi$$

$$- \frac{Il\omega\mu}{4\pi}\frac{2k_1}{\rho^2 a^2}\frac{e^{-as+ik_1\rho}}{(1+i\sec\theta_c\cot\theta)^{3/2}}\frac{\mu}{\mu_1}\sin\phi$$

$$+ \frac{Il\omega\mu}{4\pi i}\frac{\mu_1}{\mu}\sum_{m=1}^{\infty}(X_{10}^2 R_{10}^{m-1}R_{12}^m e^{ik_{1z}})\frac{e^{ik_1R_m}}{R_m}\sin\phi$$

$$H_\rho^{TE} = -\frac{Il}{4\pi i}\frac{e^{ikr}}{r}\left\{P(\theta)+\frac{1}{2ikr}[\cot P'(\theta)+P''(\theta)]\right\}\sin\phi$$

$$- \frac{Il}{4\pi}\frac{\mu}{\mu_1}\frac{2ik_1}{\rho^2 a}\frac{e^{-as+ik_1\rho}}{(1+i\sec\theta_c\cot\theta)^{3/2}}\sin\phi$$

$$- \frac{Il}{4\pi i}\sum_{m=1}^{\infty}[k_{1z}X_{01}X_{10}R_{10}^{m-1}R_{12}^m e^{ik_{1z}}]\frac{e^{ik_1R_m}}{R_m}\sin\phi \qquad k_\rho = k_1\sin\alpha_m$$

$$E_z^{TM} = -\frac{Il}{4\pi\omega\epsilon}\frac{e^{ikr}}{r}\left[\left(ik-\frac{1}{r}\right)\sin\theta Q(\theta)+\frac{3\cos\theta}{2r}Q'(\theta)+\frac{1}{2r}\sin\theta Q''(\theta)\right]\cos\phi$$

$$+ \frac{Il}{4\pi\omega\epsilon}\frac{\epsilon}{\epsilon_1}\frac{2ik_1^2}{\rho^2 a}\frac{e^{-as+ik_1\rho}}{(1+i\sec\theta_c\cot\theta)^{3/2}}\cos\phi$$

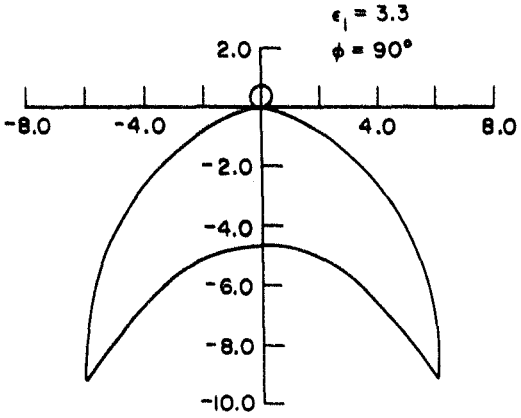

Fig. 9. Radiation pattern at $\phi = \pi/2$.

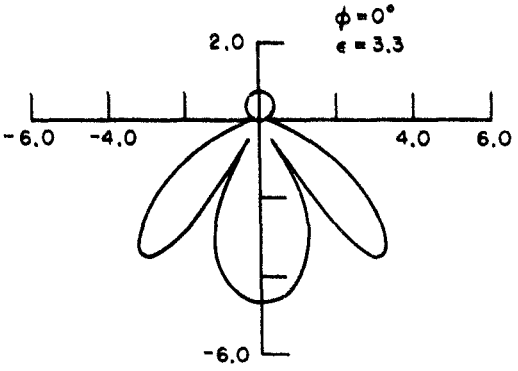

Fig. 10. Radiation pattern at $\phi = 0$.

$$+ \frac{Il}{4\pi\omega\epsilon} \sum_{m=1}^{\infty} (k_{1s} Y_{10} Y_{01} S_{12}{}^{m} S_{10}{}^{m-1} e^{ik_{zs}s}) ik_1 \sin \alpha_m \frac{e^{ik_1 R_m}}{R_m} \cos \phi \qquad k_\rho = k_1 \sin \alpha_m$$

$$E_\rho{}^{TM} = - \frac{Il}{4\pi i\omega\epsilon} \frac{e^{ikr}}{r} \left\{ Q_1(\theta) + \frac{1}{2ikr} [\cot \theta Q_1'(\theta) + Q_1''(\theta)] \right\} \cos \phi$$

$$+ \frac{Il}{4\pi\omega\epsilon} \frac{\epsilon}{\epsilon_1} \frac{2k_1}{\rho^2} \frac{e^{-as + ik_1 \rho}}{(1 + i \sec \theta_c \cot \theta)^{3/2}} \cos \phi$$

$$+ \frac{Il}{4\pi\omega\epsilon i} \sum_{m=1}^{\infty} (k_{1s} Y_{10} Y_{01} S_{12}{}^{m} S_{10}{}^{m-1} e^{ik_{zs}s}) \frac{e^{ik_1 R_m}}{R_m} \cos \phi \qquad k_\rho = k_1 \sin \alpha_m$$

$$H_\phi{}^{TM} = - \frac{Il}{4\pi i} \frac{e^{ikr}}{r} \left\{ Q(\theta) + \frac{1}{2ikr} [\cot \theta Q'(\theta) + Q''(\theta)] \right\} \cos \phi$$

$$- \frac{Il}{4\pi} \frac{2ik_1}{\rho^2 a} \frac{e^{-as + ik_1 \rho}}{(1 + i \sec \theta_c \cot \theta)^{3/2}} \frac{\epsilon}{\epsilon_1} \cos \phi$$

$$+ \frac{Il}{4\pi i} \sum_{m=1}^{\infty} [k_{1s} Y_{10} Y_{01} S_{10}{}^{m-1} S_{12}{}^{m} e^{ik_{zs}s}] \frac{e^{ik_1 R_m}}{R_m} \cos \phi \qquad k_\rho = k_1 \sin \alpha_m$$

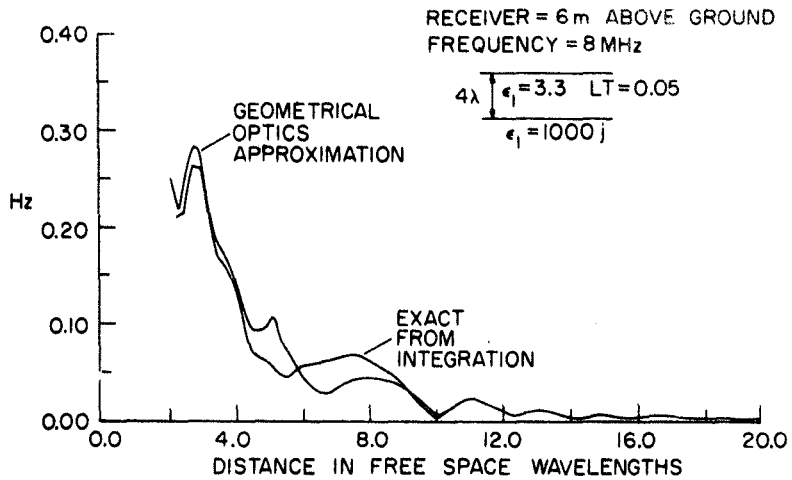

Fig. 11. Comparison of the geometrical optics approximation with the exact solution for H_s.

where $P(\theta) = k \cos \theta X_{01}(\theta)$, $Q(\theta) = k \cos \theta Y_{10}(\theta)$, and $Q_1(\theta) = k^2 \cos^2 \theta Y_{10}(\theta)$. At $z \ll \rho$, the terms $X_{01}(\theta)$ and $Q(\theta)$ are much smaller than their derivatives, $X_{01}'(\theta)$, $X_{01}''(\theta)$, $Q'(\theta)$, and $Q''(\theta)$.

APPENDIX 2

Watson's lemma states that for an integral

$$I = \int_{-\infty}^{\infty} \Phi(x) e^{-x^2/2} \, dx$$

$$\Phi(x) = \sum_{m=0}^{\infty} A_{2m} x^{2m} \qquad |x| < \lambda^{1/2}$$

Namely, $\Phi(x)$ is analytic with radius of convergence equal to $\lambda^{1/2}$. Assume further that

$$|\Phi(x)| < A x^{2p} e^{\eta x^2/2}$$

where $A > 0$, $p = 0, 1, 2, \ldots$, and $0 \leq \eta < 1$ wherever x is real and $x \geq \lambda^{1/2}$, namely, outside the domain of convergence. Then

$$I = \left(\frac{\pi}{2}\right)^{1/2} \left\{ \sum_{m=0}^{n-1} \frac{(2m)!}{2^m m!} A_{2m} + O[(1-\eta)\lambda]^{-M} \right\}$$

Thus the asymptotic expansion

$$I \sim (\pi/2)^{1/2} \sum_{m=0}^{\infty} \frac{(2m)!}{2^m m!} A_{2m}$$

is useful only if $\eta \ll 1$ and $\lambda \gg 1$. Our integral

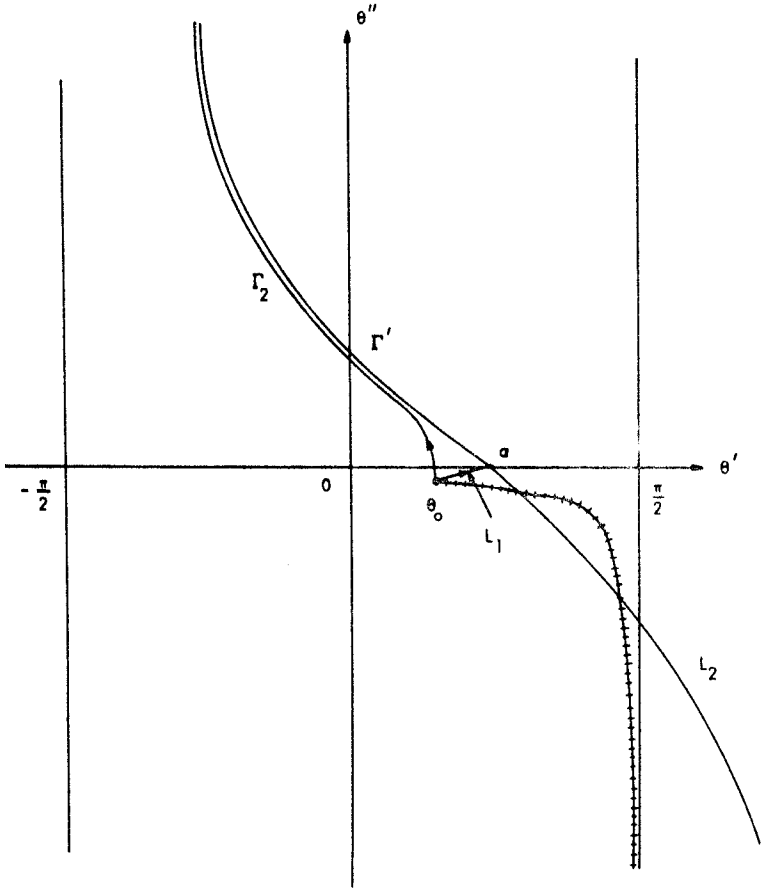

Fig. 12. The choice of the branch cut $Re\ k_z = 0$ yields results identical to choosing the branch cut $Im\ k_z = 0$. Here Γ is the saddle point steepest descent contour, and Γ_2 is the branch point steepest descent contour. L_1 connects θ_0 and α. Γ' starts from $\theta'' \to \infty$ to $\theta = \alpha$. L_2 starts from $\theta = \alpha$ to $\theta'' \to -\infty$. Thus $L_1 = \Gamma_2 + \Gamma'$, and $\Gamma = \Gamma' + L_2$.

is of the form

$$I_m = \int F(\theta) \cdot e^{ik_1 R_m(\theta - \alpha_m)}\, d\theta$$

where m signifies the mth image source and for the mth source α_m is the saddle point. In the coefficient $F(\theta)$ there is a branch point singularity at $\theta = \theta_1$, and $\sin\theta = n$. We know intuitively that, when the saddle point α_m is close to the branch point θ_1, the saddle point method crumbles. To calculate the mathematical expression for the criteria, the integral I_m is turned into a form to which Watson's lemma is applicable.

Let

$$x^2/2 = ik_1 R_m(1 - \cos\theta') \qquad \theta' = \theta - \alpha_m$$

Branch point is due to $(n^2 - \sin^2\theta)^{1/2}$. Therefore radius of convergence $\lambda^{1/2}$ is at $x = x_0$, which, under the transformation, corresponds to $n^2 - \sin^2\theta = 0$.

$$I_m = e^{ik_1 R_m} \int_0^\infty F(\theta)\, \frac{d\theta}{dx}\, dx e^{-x^2/2}$$

$$\sin\theta = \sin(\theta' + \alpha_m)$$

$$[\sin^2\theta_1 = n^2$$

implies

$$n^2 - 2n\left(1 - \frac{x_0^2}{2ik_1R_m}\right)\sin\alpha_m + \left(1 - \frac{x_0^4}{(2k_1R_m)^2} - \frac{x_0^2}{ik_1R_m}\right)\sin^2\alpha_m = \left(\frac{x_0^4}{(2k_1R_m)^2} + \frac{x_0^2}{ik_1R_m}\right)\cos^2\alpha_m$$

For α_m close to θ_1, this can be simplified to

$$|x_0|^2 = k_1R_m(n - \sin\alpha_m)^2/(n - 1)$$

Therefore, by Watson's lemma, for the saddle point method to hold, we require that

$$k_1R_m(n - \sin\alpha_m)^2/(n - 1) \gg 1$$

APPENDIX 3

Discussion of branch cut. Suppose that the branch cut $Re\ k_z = 0$ is chosen, and consider a typical integral

$$I = \int_{-\infty}^{\infty} \frac{k_\rho}{k_{1z}} A(k_\rho) e^{ik_{1z}d} H_0^{(1)}(k_\rho\rho)\, dk_\rho$$

where $A(k_\rho) = k_{1z}/(k_{1z} + k_z)$. After the transformation $k_\rho = k_1 \sin\theta$, we find the saddle point is located at $\alpha = \tan^{-1}(\rho/d)$. For $\alpha < \theta_0'$ we have

$$k_z = (k^2 - k_1^2\sin^2\alpha)^{1/2} \qquad k_{1z} = k_1\cos\alpha$$

$$I = \frac{2}{i}\frac{e^{ik_1R}}{R}\left\{A(\alpha) + \frac{1}{2ik_1R}\cdot[A''(\alpha) + \cot\alpha\, A'(\alpha)]\right\}$$

where

$$A(\alpha) = \frac{k_1\cos\alpha}{k_1\cos\alpha + (k^2 - k_1^2\sin^2\alpha)^{1/2}}$$

$$R = (\rho^2 + d^2)^{1/2} \qquad Re\ k_z > 0$$

Therefore the answer checks with the case with branch cut $Im\ k_z = 0$.

In case $\alpha > \theta_0'$, there are two contributions, one due to the saddle point and the other to the branch point θ_0. The branch cut contribution is, contrary to the case of $Im\ k_z = 0$, of first-order effect.

Set $I = I_1 + I_2$, where I_1 is the saddle point contribution and I_2 is the branch cut contribution. Then

$$I_1 = \frac{2}{i}\frac{e^{ik_1R}}{R}\left\{A(\alpha) + \frac{1}{2ik_1R}\cdot[A''(\alpha) + \cot\alpha A'(\alpha)]\right\}$$

$$Re\ k_z > 0 \qquad Im\ k_z < 0$$

Notice that the saddle point contribution is not the same as it would be for the case $Im\ k_z = 0$.

$$I_2 = \left(\frac{2k_1}{\pi\rho}\right)^{1/2} e^{-i\pi/4} \int_{\substack{\text{down } B- \\ \text{up } B+}} \sin^{1/2}\theta A(\theta) \cdot e^{ik_1R\cos(\theta-\alpha)}\left(1 + \frac{1}{8ik_1\rho\sin\theta}\right)d\theta$$

$$= \left(\frac{2k_1}{\pi\rho}\right)^{1/2} e^{-i\pi/4} \int_{\text{up } B-} \sin^{1/2}\theta k_1\cos\theta \cdot e^{ik_1R\cos(\theta-\alpha)} \cdot \frac{2(k^2 - k_1^2\sin^2\theta)^{1/2}}{k_1^2\cos^2\theta - k^2 + k_1^2\sin^2\theta} \cdot\left(1 + \frac{1}{8ik_1\rho\sin\theta}\right)d\theta$$

where B_+ is the side of branch cut with $Im\ k_z > 0$ and B_- is the side of branch cut with $Im\ k_z < 0$.

To evaluate the integral, the path B_- is detoured to a path that consists of two parts. The first part L_1 is from the branch point to the saddle point, and the second part L_2 is from the saddle point to infinity down the steepest descent path (Figure 12).

By Cauchy's theorem

$$L_1 = \Gamma_2 + \Gamma'$$

Therefore $L_1 + L_2 = \Gamma_2 + \Gamma'$ and the contribution

$$I_{\Gamma_2} = \frac{2}{\rho^2}\frac{k}{a^3}\frac{e^{-iaz+ik\rho}}{(1 - \cot\alpha \tan\theta_0)^{3/2}}$$

is of second-order effect. The contribution of Γ', evaluated by the saddle point method, is

$$\frac{2}{i}\frac{e^{ik_1R}}{R}\left\{D(\alpha) + \frac{1}{2ik_1R} \cdot [D''(\alpha) + \cot\alpha D'(\alpha)]\right\}$$

where

$$D(\alpha) = \frac{2(k^2 - k_1^2\sin^2\alpha)^{1/2}k_1\cos\alpha}{k_1^2\cos^2\alpha - k^2 + k_1^2\sin^2\alpha}$$

$$Re\ k_z > 0 \qquad Im\ k_z < 0$$

Combining these expressions, one has

$$I = I_1 + I_2 = \frac{2}{i}\frac{e^{ik_1R}}{R} \cdot\left\{G(\alpha) + \frac{1}{2ik_1R}[G''(\alpha) + G'(\alpha)\cot\alpha]\right\} + \frac{2}{\rho^2}\frac{k}{a^2}\frac{e^{-iaz+ik\rho}}{(1 - \cot\alpha\tan\theta_0)^{3/2}}$$

where $G(\alpha) = A(\alpha) + D(\alpha)$, which is equal to $A(\alpha)$ of the case of branch cut $Im\ k_z = 0$. Therefore the answers are identical whether we choose the branch cut $Re\ k_z = 0$ or $Im\ k_z = 0$.

Acknowledgments. The numerical computation was carried out at the M.I.T. Computing Center. Thanks are also due W. Y. Kong for preparing the manuscript and C. Navedonsky for the graphical work.

This work was supported in part by NASA contract NAS 9-11540.

REFERENCES

Annan, A. P., Radio interferometry depth sounding, M.S. thesis, 239 pp., Univ. of Toronto, Toronto, Ont., Canada, 1970.

Baños, Jr., A., *Dipole Radiation in the Presence of a Conducting Half Space,* 246 pp., Pergamon, New York, 1966.

Brekhovskikh, L. M., *Waves in Layered Media,* 561 pp., Academic, New York, 1960.

Kong, J. A., Electromagnetic fields due to dipole antennas over stratified anisotropic media, *Geophysics, 37,* 985–996, 1972.

LaTorraca, G. A., Half-wave-length dipole antennas over stratified media, M.S. thesis, 147 pp., Mass. Inst. of Technol., Cambridge, 1972.

Rossiter, J. R., G. A. LaTorraca, A. P. Annan, D. W. Strangway, and G. Simmons, Radio interferometry depth sounding, 2, Experimental results, *Geophysics,* in press, 1972.

Simmons, G., D. W. Strangway, L. Bannister, D. Cubley, and G. LaTorraca, The surface electrical properties experiment, *Geochim. Cosmochim. Acta, 36, Suppl. 3,* 258–270, 1972.

Sommerfeld, A., *Partial Differential Equations,* 335 pp., Academic, New York, 1949.

Strangway, D. W., G. Simmons, R. Watts, G. LaTorraca, L. Bannister, R. Baker, J. E. Redman, and J. R. Rossiter, Radio frequency interferometry—A new technique for studying glaciers, *J. Glaciol.,* in press, 1972.

Tsang, L., Electromagnetic near fields of horizontal dipole on stratified lunar surface, B.S. thesis, 40 pp., Mass. Inst. of Technol., Cambridge, 1971.

(Received October 17, 1972;
revised January 30, 1973.)

Presented 23 Aug. 73 URSI/IEEE Boulder, Colo. by Gene Simmons for the SEP team.

ELECTROMAGNETIC PROBING OF THE MOON

INTRODUCTION

Last December on the Moon, two astronauts set out equipment for a very simple EM experiment: a transmitter with a half-wave electric dipole antenna. They attached to the Rover a receiver with a loop antenna and a magnetic tape recorder. They then proceeded to measure field strength as a function of distance from the transmitter. From those data, we expected to learn something interesting about the electrical properties of the Moon. Today, I would like to tell you about this experiment--about the theoretical work that we have done so that we could interpret the interference patterns, about the results of field testing both the experiment and equipment on earth before the Apollo 17 mission, and finally, about our present interpretation of the lunar data.

THE CONCEPT

Slide 1

The experiment is extremely simple in concept. This FIRST SLIDE shows the essentials. A horizontal electric half-wave resonant dipole is laid directly on the surface and radiates continuously. The amplitude of the radiation field is measured with a small loop and a calibrated receiver. The data are recorded on magnetic tape. We analyze the data in terms of continuous radiation but actually use switched CW at the frequencies shown on the slide. NEXT SLIDE please.

2

A very simple conceptual picture of the wave propagation is shown in this slide. One wave travels above the surface, a second wave travels below. In the vicinity of the interface, these two waves interfere and produce a distinctive interference pattern. The characteristics of the pattern depend uniquely on the frequency and the electrical properties of the medium. A third wave may exist. If a reflector is present in the subsurface, then a reflected wave, labeled "C" in this slide, interferes with the other two waves and complicates the pattern. The NEXT SLIDE shows two theoretical interference patterns for a layer over a half space. The usual features of such patterns are these: a rather rapidly decreasing function of distance with superimposed peaks and troughs. The exact details of the peaks and troughs and the rate of decrease with distance depends on the properties of the materials, as well as the presence, number, and depths of reflecting horizons.

3

These two curves illustrate nicely the effect of loss tangent of the material. The upper curve is for a loss tangent of 0.01, the lower curve for 0.05. Note that the vertical scale is in Db. So there really is quite a large difference between the pattern for different values of the loss tangent for a given geometry. The NEXT SLIDE shows additional features that are typical of such interference patterns. Note on this slide that I have used linear scales.

4

The high-spatial-frequency wiggles in the early part of the pattern are related to the permittivity of the upper layer. In fact, from the spatial beat frequency, we can calculate the dielectric constant of the upper layer. The prominent peak at about five λ is caused by the reflected wave. The later parts of the pattern are not simple functions of the dielectric constant and depth to reflectors. However, they are very sensitive to small variations in depths and properties. For simple geometries, the origin of the peaks and troughs can be readily identified. So let's look briefly at the theoretical basis of the experiment.

THEORY

The calculation of the field produced by a dipole on the interface between semi-infinite media of differing properties is truly a classic problem in electromagnetic theory. Many in the audience have contributed significantly to the development of the present day solutions. I am sure that most of you have examined the solutions in various farms. If not recently, then at least in your classroom days. The history of solutions to this problem goes back to a 1909 paper by A. Sommerfeld and is replete with mistakes. Indeed, because of the mistakes made by so many prominent scientists and engineers in solving the simple half-space problem, it has been with some considerable trepidation that we have extended solutions to our particular problem.

To put the solution in integral form is reasonably straight forward. NEXT SLIDE, please. We use cylindrical coordinates. 5
The transmitting antenna is located at the origin and we calculate the three components of the field at any point (ρ, ϕ, z). I show here the integral for one component only as illustration.

$k\rho$ - transverse wave propagation vector

Il - moment of the antenna

k_z - a-component of wave vector

R^{TE} - reflection coefficient

$H_1^{(1)}$ - Hankel function of the 1st kind

The reflection coefficient is a function of the properties of various layers and their depths. The exponential term $\exp(ik_z z)$ accounts for the receiver height. In integral form, the solution is elegant and almost certainly free of errors, however, I find it difficult to compare this integral diectly with data. Of course, it's in the evaluation of the integral that one is likely to make mistakes. I have always suspected that's why theoreticians lose interest in problems when they get the solution in integral form. So we have used several different schemes to solve the integrals for our particular problem. First, we have solved the integrals numerically

with Simpson's Rule which unfortunatley used rather large amounts of computer time. This direct method has provided a very good standard by which to compare other solutions. A second approach to solving the integrals used the geometrical optics approximation (GOA). In the GOA, we can readily identify the origin of the contributions to the total field. In this NEXT SLIDE, I have plotted the relative 6
amplitudes of the individual contributions to the solution for the H_z field for a particular case. The half-space solution which shows the many characteristic wiggles is identical to the solution that was produced by Sommerfeld in his correct 1926 version, and has been reproduced by many other authors. An excellent discussion of the half-space case is given in the monograph by Baños. NOte especially the relative amplitudes of the first reflection, second reflection, third reflection, and so on. It is from such plots as this that we can understand the failure of the radiation fields to decrease monotonically with distance. The contributions from second and third reflections have increased significantly the amplitude of the field. In adding these various reflections, one includes of course, the phase of the signal.

Perhaps now is the appropriate time to emphasize that in the SEP experiment we use only amplitude. We would have liked to use phase also but the practical difficulties of detecting, measuring, and recording both amplitude and phase seemed too great--at least within the constraints of a flight experiment.

The NEXT SLIDE lets us compare the geometrical optics approxi- 7
mation with the exact solution obtained with Simpson's Rule. We think that the "fit" is quite good.

A third way to evaluate the integrals is that of mode theory. We identify the poles of the integrals on the comples plane and use the theory of residues to evaluate the integrals. The NEXT SLIDE 8
shows a comparison of the result of GOA and mode analysis. We have also included data from a glacier traverse and I will discuss the glacier data later. For this model, at least,both GOA and the mode formulation give comparable results. In actual fact, there is considerable overlap in model conditions for which this occurs. However, for very thin layers, one must use the mode approach. For thick layers, the computation time for the mode approach is prohibitive and the GOA gives adequate solutions. So that we find in working with "real" data that we generally make a choice between the two methods on the basis of practicality when the layers are optically thick, but for thin layers use the mode formulation.

And finally a fourth method that we have just begun using is based on the Fast Fourier Transform (FFT) algorithm. With suitable manipulations of the integral, we can get it in a form to use the FFT to solve the integral. In order to keep credits straight, let me mention that Ray Brown and Leang Tsang were mainly responsible for the FFT method. The results obtained with FFT are identical with those obtained with our other methods. Let me show some slides for comparison. In the NEXT SLIDE, we show FFT, Mode, and GOA for 8-1

a two layer model. Then, quickly, the NEXT SLIDE shows FFT and Simpson's Rule for a three layer model. And then in the NEXT SLIDE we compare FFT and Simpson's Rule for a six layer model. The FFT is especially useful for models with many layers. It has the disadvantage though that the source of individual contributions to the solution is not identifiable. 8-2 8-3a 8-3b

Given that the concept of the experiment might work, and given that we have a mathematical formulation that appears to give reasonable looking results, we had to convince ourselves that (1) the experiment really would work, and (2) we had a correct formulation of theory before going to the Moon. After all, one would be rather fool-hardy to go to the Moon to test an experiment only to discover that he had chosen the wrong sign for a square root!

TESTING THE EXPERIMENT

We field-tested both the experiment concept and the mathematical formulations on several glaciers. Why choose glaciers? In order for the subsurface waves to propagate sufficiently far to obtain interference patterns, we needed a geologic material in which the attenuation was low. Everyone knows that ordinary rocks at the surface of the earth are much too conductive because they contain water. We knew of two such geologic materials that occurred in sufficient quantity to provide useful tests--glacial ice and salt. Both have quite low conductivity. The geometry of glaciers seemed better for our purposes and so, early on, we decided to use glaciers. We have tried the SEP technique on the Gornier Glacier in Switzerland, the Athabasca Glacier in Alberta, Canada, and several glaciers and icefields near Juneau, Alaska. But let me describe the results for the Athabasca Glacier only.

We chose the Athabasca for several reasons. It is easy to get there. One can drive to the foot of the glacier. One can even drive tracked vehicles out onto the glacier. In addition, several other workiers had previously determined rather well the geometry of Athabasca Glacier by several independent techniques including gravity, DC electrical sounding, some EM sounding, seismic work, and the most definitive of all, actual drilling. Shown in the NEXT SLIDE is a contour map of the Athabasca Glacier. On this slide, the dots indicate the location of drill holes. The heavy line indicates the location of a SEP profile. Along this profile we were able to match the depths to about 5 meters. The NEXT SLIDE is an example of the data obtained on the Athabasca and the quality of the "fits" obtained. Quite frankly, not all field data could be matched equally well with our theoretical curves. Perhaps Dave Strangway will show you some of the misfits. In addition to the gross features shown in this slide--and often matched well--there were also quite a few other features in the glacier data probably caused by scattering of the EM waves off such features as crevasses, holes in the ice, boulders, and bottom topography. Even though we had not identified the cause of such features before the Apollo 17 flight, we were very comforted to find that we could indeed match actual field data with our experiment with the theoretical curves. 9

Incidentally, I should add that an unstated reason for choosing the Athabasca Glacier is the excellent working conditions shown in this NEXT SLIDE. Also our field assistants, shown in the NEXT SLIDE 11
resting up, rather liked the Athabasca.

A second method of testing our mathematical formulation was that of model tanks. We scaled wave lengths and used three centimeter radar equipment, modified somewhat, to obtain interference patterns with various dielectric oils and aluminum plates for reflectors. Shown in thes NEXT SLIDE are the results for one exper- 13
iment. I show this slide for two purposes--to illustrate tank results and to indicate that for very thin layers the GOA is inadequate. Notice that we match extremely well the experimental data with the mode results. Note that we use the E-Field, rather than H. In scale models, at least as we construct them, we were unable to make electrically small loops in order to measure the magnetic field and have contented ourselves with measuring the electric field at the receiver. One of the distinct advantages of using tank models for this kind of work is that one can vary the thickness of individual layers over a large range and can see experimentally the conditions under which the various solutions are satisfactory.

Thus, we had essentially three different techniques for verifying that the mathematical formulations for our theory of layered media were essentially correct. One, we could compare with the exact calculations obtained with Simpson's Rule; two, we could match experimentally-observed data on glaciers and could calculate thickness quite accurately; and three, we could match experimentally-observed data from scaled models. From these tests, we were quite sure that our experiment could provide useful data from the Moon.

LUNAR EQUIPMENT

Let's discuss briefly the equipment that was used in the exper- 14
iment on the Moon. In the NEXT SLIDE, we show the transmitter as it was deployed on the surface of the Moon. Note the solar cell panels, the sole power source for the transmitter. At 1 MHz, we used a power input to the antenna of 4 watts. At the other frequencies, 2, 4, 8, 16, and 32 MHz, the power input to the antenna was 2 watts. The transmitter box was about 1 foot on each side. The transmitting antennas were carried on reels to the Moon and then deployed by the astronauts. The antennas were electric wires with traps placed at the appropriate distances to provide tuned half-wave dipoles at each frequency. Total length of the transmitter antenna, tip to tip, was 70 meters. In the NEXT SLIDE, we see the antenna laid out 15
on the surface. The Rover track was used as a reference for laying the antenna. The NEXT SLIDE shows the receiver and receiving antenna 16
mounted on the Lunar Rover. We were always concerned about parasitic resonances in the Rover and the various tools nearby. As you can see, the SEP receiving antennas were uncomfortably close to various potentially disturbing materials. Apparently, and I use the word with careful consideration, apparently the parasitic resonances did not develop, at least with respect to the horizontal loop. To date, we have mainly analyzed the H_z component.

The NEXT SLIDE shows the reciever in an opened condition and the tape recorder being removed. Note the optical surface reflectors used for cooling the receiver and the thermometer used to monitor the temperature of the receiver. The whole tape recorder was returned to earth by the astronauts. Let's now look briefly at what we've learned from the data. 17

THE LUNAR DATA

First, the location of the lunar experiment. NEXT SLIDE, please. The location of the Apollo 17 landing site is here. Previous missions were here, here and so on. The Apollo 17 landing site is in the mountains adjacent to the sourtheast corner of Mare Serenatatis. 18
The NEXT SLIDE shows an artist's sketch of the general region and 19
the NEXT SLIDE shows the immediate vicinity of the landing site, 20
including the valley, the prominent cliff that is 80 meters high, 20A
and the majestic mountains. The planned and actual touchdown spot is shown here. Note the route of the traverses. The location of the SEP transmitter was just south of the LM, about here. We obtained data along the traverse from the SEP site towards Station 2. We also obtained, but have not yet reduced, data from Station 4, back towards the LM. We had planned to obtain data from the SEP site towards Station 6 and beyond. However, a combination of events prevented us. On reaching Station 6, the astronauts found that the switch on the receiver was in the "Standby" position. Subsequently, we were unable to obtain data because of overheating of the receiver. We finally removed the tape recorder about halfway along this traverse in order to prevent the loss of data that had already been recorded. So the data that we have from the Moon consists of the profile from the SEP site towards Station 2, plus some data from Station 4, towards the SEP, which have not yet been reduced. Let's now examine some of the data, and our interpretation of them, from the SEP site towards Station 2.

In the lunar equipment, we used two transmitter antenna orientations, six frequencies, three othogonal receiving antennas. So, 2 X 6 X 3 is 36 individual profiles for each traverse. In this NEXT SLIDE, I show you one such profile, namely the H_Z com- 21
ponent for the north-south antenna and for the 16 MHz frequency. For comparison, I show the theoretical profile calculated for a half space with dielectric constant of 3.2. Note how well we match the locations of the peaks and troughs and the falloff with distance. Thus, we are confident that we have the correct values for dielectric constant and for loss tangent. We match equally well the data for the other frequencies. In this NEXT SLIDE, I show 22
the match for the 1 MHz H_Z data. With a simple half-space model, we match the data quite well with values of permittivity given in the NEXT SLIDE. Note that the model used for each frequency is a half- 23
space. Because the skin depth varies with frequency, we inferred that these data implied a continuous variation of permittivity with depth. So we drew a model with smoothly varying ε with depth and proceeded to calculate the interference pattern. NEXT SLIDE, please. 24
We used a 20 layer model and the FFT program.

Much to our surprise the pattern showed no peaks and troughs. It varied smoothly with distance. We therefore reject the model of a smoothly varying ε with depth.

Our current approach is to restrict the models to a few layers and to include finite discontinuities in ε. We use the "half-space" values of ε as a function of frequency as a guide. We have calculated 2 dozen models with this approach. None fits perfectly. I think, though, that several features have emerged: First, the loss tangent is quite low--at least as low as 0.003 and perhaps as low as 0.001. Second, ε near the surface is about 3.2, attains a maximum within 100 to 200 m of the surface and then decreases slightly. Third, discrete layers are present. Fourth, ε does not change significantly from 5.6 over the next 2 - 2 1/2 km. Fifth, free water is not present in the outer 2 1/2 km of the Moon, at least at the Apollo 17 site.

In this NEXT SLIDE, I show our present best model. As you can see, the match is not perfect and we clearly have not yet wrung out all the information in even the H_z data. 25

Let me summarize the status of the SEP experiment. We have developed and fully tested the concepts that the field strength of the radiation from a dipole antenna can be used to estimate the electrical properties of subsurface materials and to determine the geologic structure. We have applied this technique to the study of the Moon and several glaciers. We suggest that the same technique with some modifications may very well be useful for prospecting for subsurface water in arid regions and for the study of salt domes and salt deposits. In connection with the lunar experiment, our analysis is still in progress but we have found a "best" model that fits the gross features. In closing, let me say that we had great confidence that our equipment would work properly on the Moon. On the other hand, we did have backup equipment in case of failure, shown in the NEXT SLIDE. For some reason, Jack Schmitt insisted on wearing a disguise whenever he practiced. 26 27

SLIDES

Freqs: 1, 2, 4, 8, 16, 32. MHz

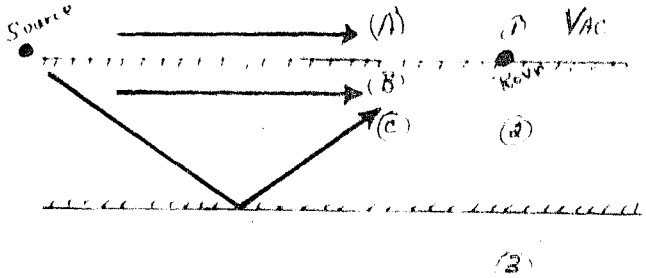

1

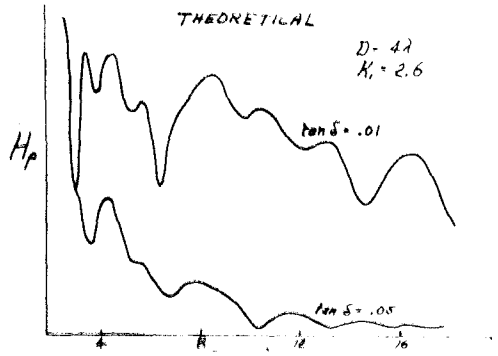

2

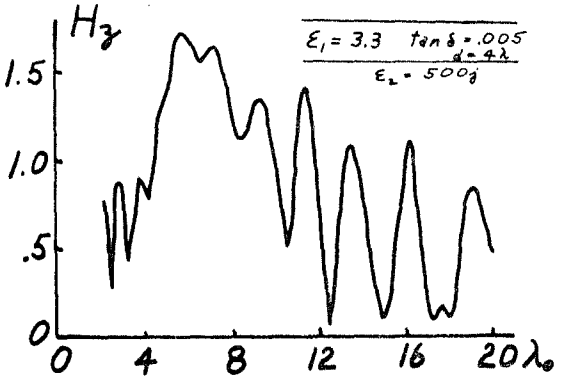

3

4

5

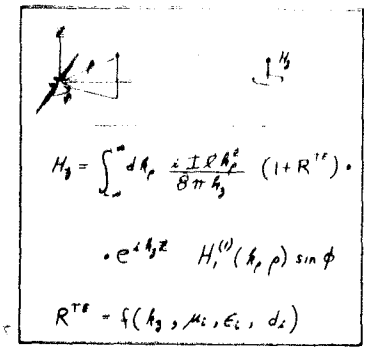

6

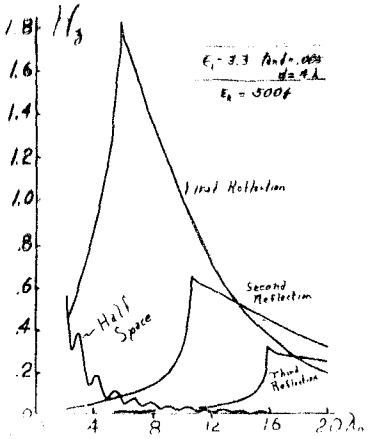

9/18/78 GS

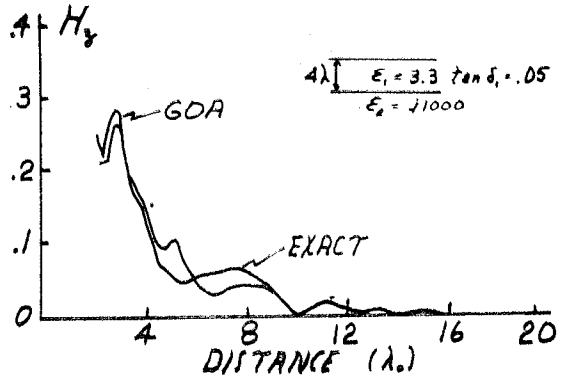

7

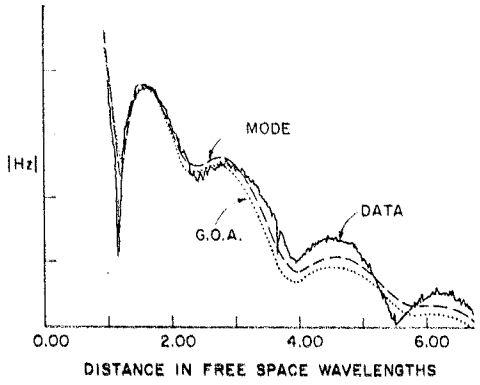

8

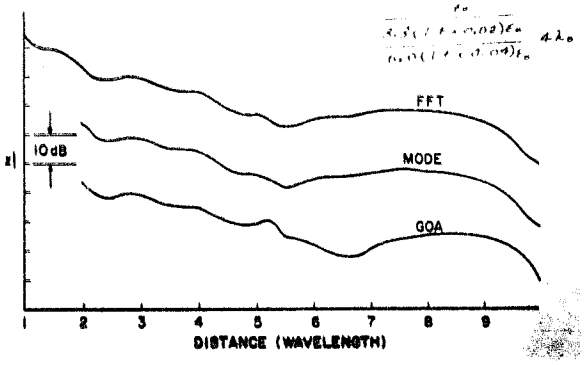

8-1

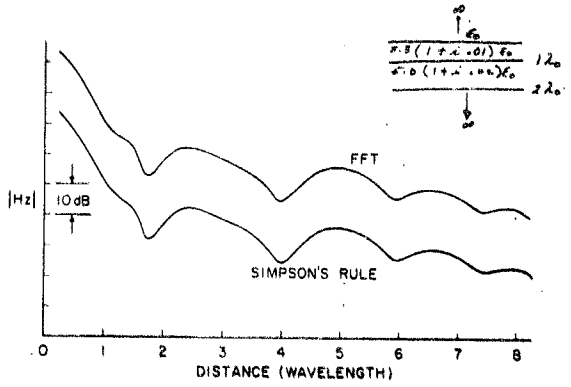

8-2

SIX LAYER MODEL
FOR FFT TEST

$\varepsilon_i/\varepsilon_0$	$d_i(\lambda_0)$
$2(1+i.01)$	0.5
$3(1+i.02)$	1
$4(1+i.03)$	2
$5(1+i.04)$	3
$6(1+i.05)$	4
$8(1+i.06)$	∞

8-3a

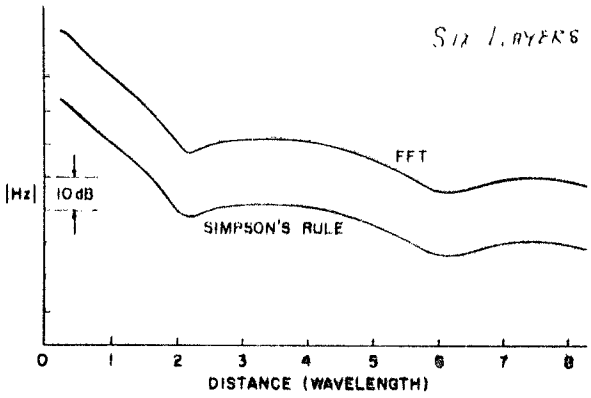

8-3b

ATHABASCA

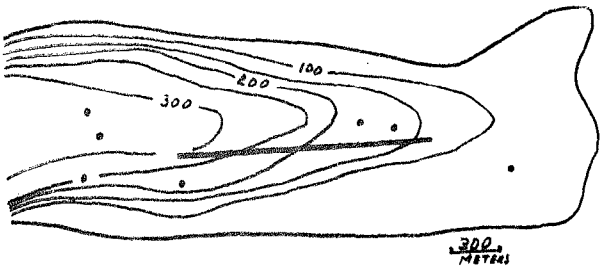

9

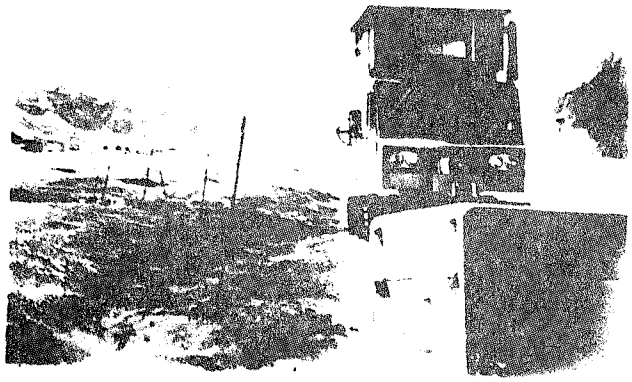

11

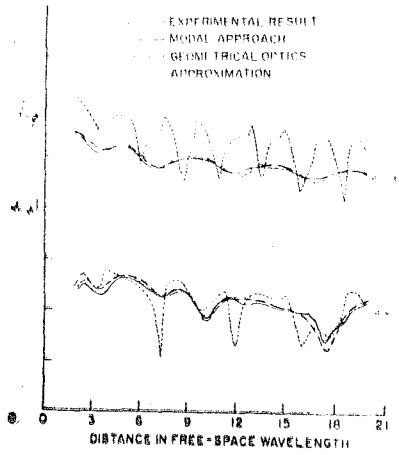

13

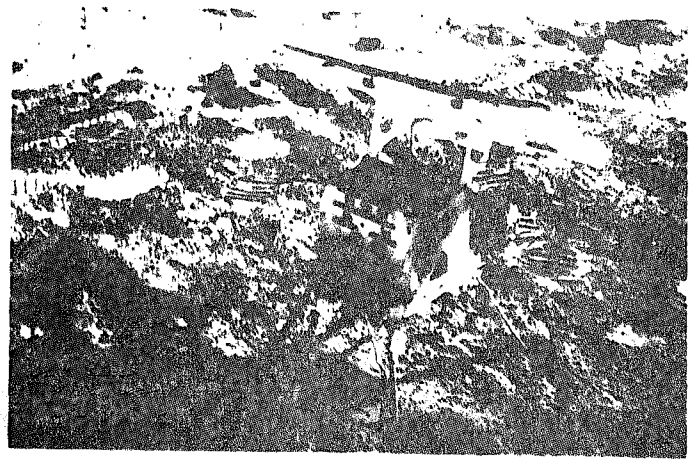

14

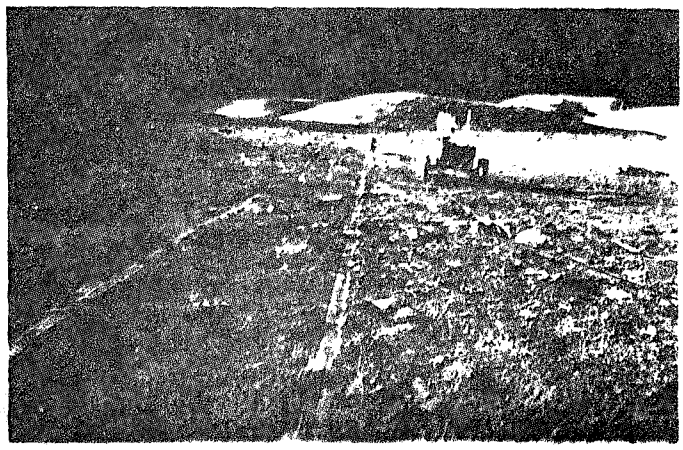

15

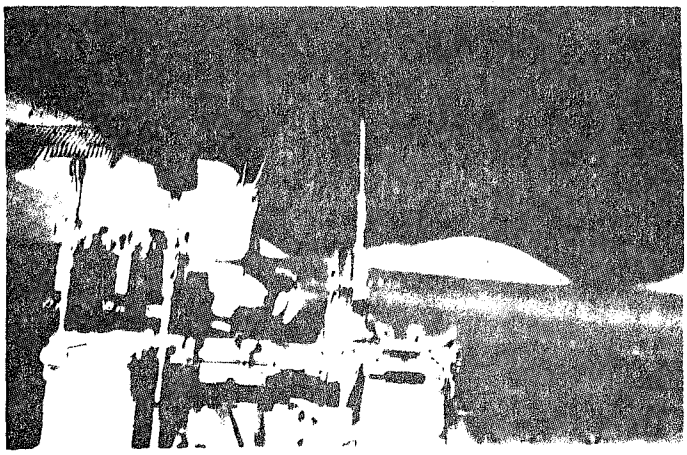

16
(Note image is reversed in this slide)

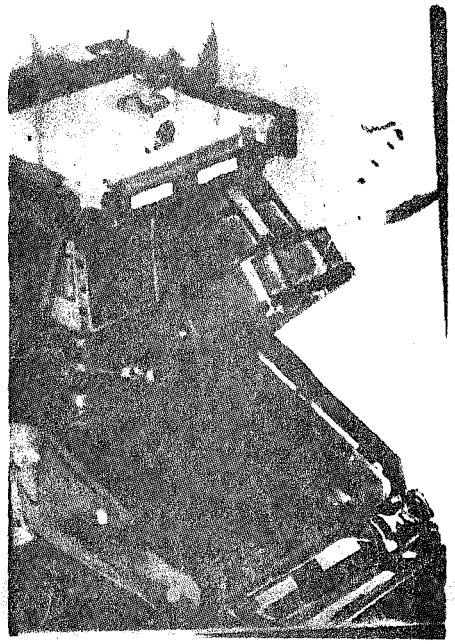

17

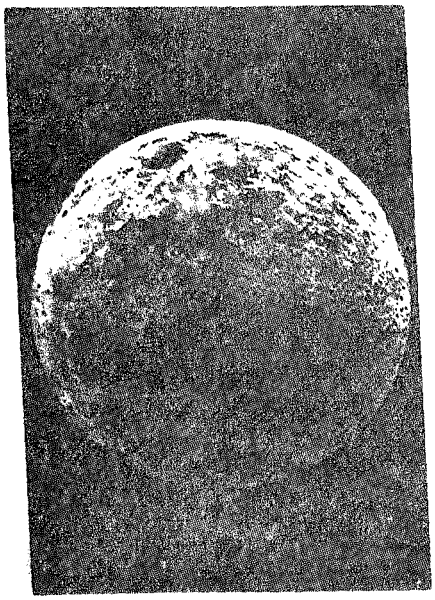

18

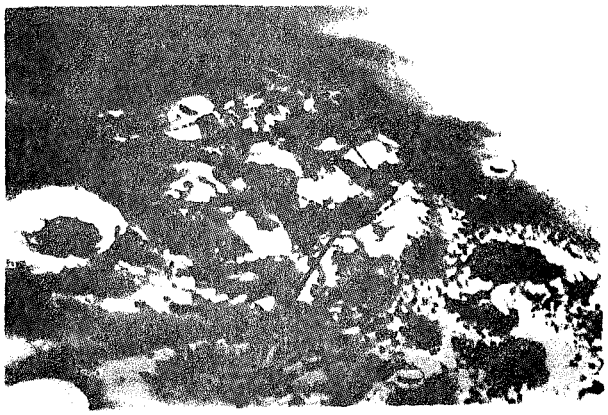

19

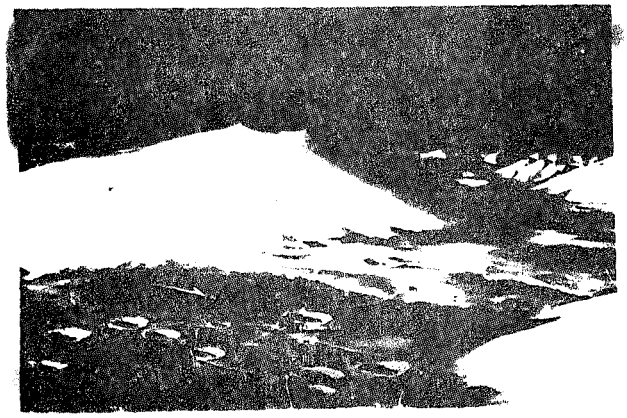

20

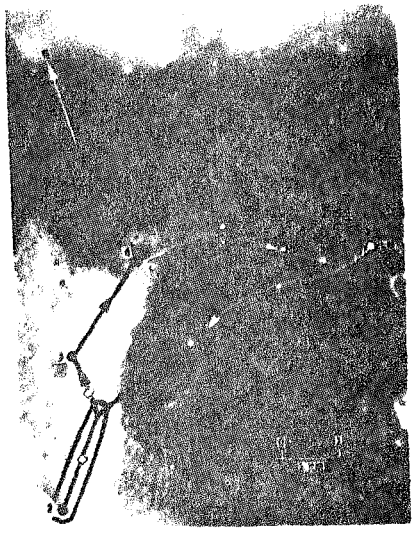

20A

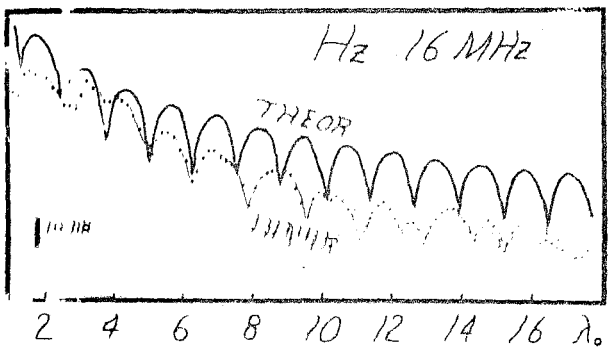

21

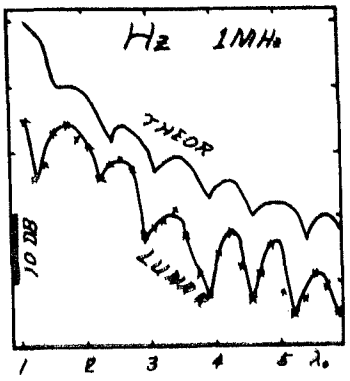

22

SEP RESULTS

H_z N-S ANTENNA

f (MHz)	ϵ/ϵ_0
1	5.4
2	6.2
4	4.2/4.8
8	3.2
16	3.2
32	3.2

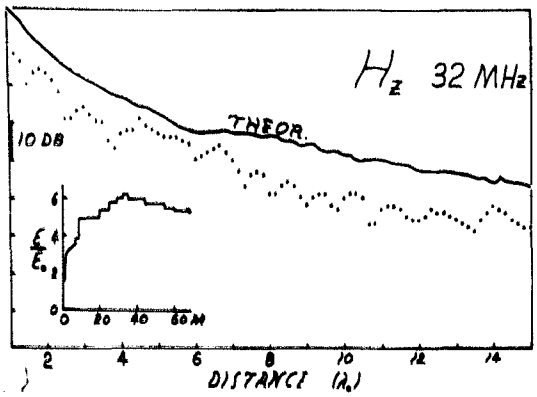

24

23

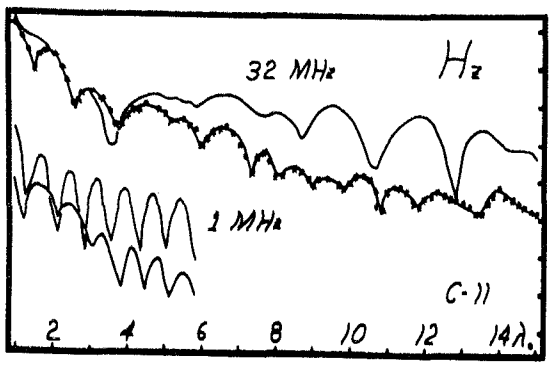

25

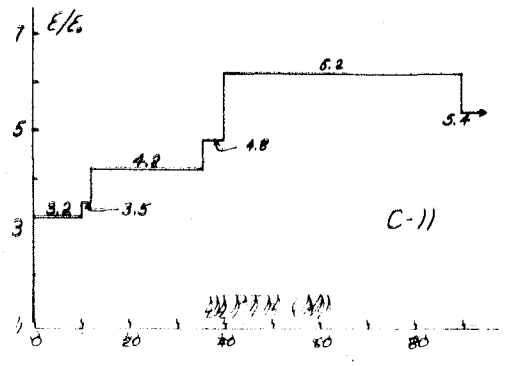

26

27

GEOPHYSICAL SUBSURFACE PROBING WITH RADIO-FREQUENCY INTERFEROMETRY*

by

J. A. Kong+, L. Tsang+, and Gene Simmons++

Abstract: The radio-frequency interferometry method can be used to probe interiors of celestial bodies and terrestrial areas with low conductivity. Several glaciers have been studied with this technique. An experiment based on this method was designed for Apollo 17 to examine the lunar subsurface. In order to interpret the interference patterns, we have studied theoretically the electromagnetic fields due to a dipole antenna on the surface of a horizontally stratified n-layered medium. Three approaches are used to calculate the interference patterns: 1) direct numerical integration 2) asymptotic evaluation by the saddle point method 3) residue series approach. The asymptotic approach leads to the geometrical optics interpretation. The residue approach leads to modal analysis. Validity of the formulation is checked by comparisons with analogue model tank experiments and actual field data obtained from glaciers.

---

* This work was supported in part by NASA Contract No. NAS9-11540 and in part by the Joint Services Electronics Program (Contract DAAB07-71-C-0300). The paper was originally presented at the URSI Symposium held at Williamsburg, Virginia, December 15, 1972.

+ Department of Electrical Engineering and Research Laboratory of Electronics, Massachusetts Institute of Technology.

++ Department of Earth and Planetary Sciences, Massachusetts Institute of Technology.

1. INTRODUCTION

The subsurface of planetary bodies, including the earth and its moon, can be examined with electromagnetic waves. In 1955, radio-frequency interference fringes were used for geophysical prospection of underground water in the Egyptian desert[1-2]. Recently the technique was developed for use during the Apollo 17 mission to measure the subsurface electromagnetic properties of the moon[3]. In the experiment, a transmitting antenna consisting of a pair of orthogonal dipoles is laid directly on the lunar surface. The antenna radiates sequentially at frequencies of 1, 2.1, 4, 8.1, 16 and 32.1 MHz in a time window of 100 millisecond for each frequency. The time window is sufficiently long that the experiment is effectively a continuous wave experiment. A receiving antenna consisting of three orthogonal loops is mounted on the lunar roving vehicle. As the vehicle traverses the lunar surface, the strengths of the magnetic field components are measured as a function of distance from the transmitting antenna. The data are recorded on magnetic tape and returned to earth for analysis. The interference patterns of the field-distance plot contain information about the electromagnetic properties of the lunar subsurface. To test both equipment and theory, experiments have been performed on glaciers[4-5] in Switzerland, Canada, and Alaska and on a scale model tank in the laboratory.

In this paper, we present the theoretical basis of the experiment and compare the various methods of attack. The mathematical model is a stratified n-layer medium. Each layer is bounded by plane boundaries and possesses different electric permittivity, magnetic permeability, and thickness. Although dipole rediation in the presence of stratified media has been studied extensively[6-16], a proper account for the interference fringes method is still lacking. The geometrical optics approximation was the first approach used in calculating intereference patterns[1,15-16]. With the use of the reflection coefficient formulation[14], all field components can be expressed in integral forms with a single variable of integration. In order to obtain explicit expressions for the six field components, the following three different approaches are used to evaluate the integrals: 1) geometrical optics approximation, 2) modal approach, and 3) direct numerical integration. The direct numerical integration can be made to yield accurate results and is useful in calculating near field solutions. The geometrical optics approximation consumes very little computer time and permits a very simple interpretation in terms of ray optics. In the modal approach, the solutions are expressed in terms of summations over normal modes pertaining to the structure of the stratified medium.

II. THEORY

1. General Formulation

Consider a stratified medium of n layers. Each layer is homogeneous, isotropic, and horizontal. The electric permittivity and the magnetic permeability of the ith layer are ϵ_i and μ_i, respectively. The zeroth layer is free space. Both layer 0 and t are semi-infinite half-spaces. An infinitesimal dipole lies on the interface between regions 0 and 1. We use cylindrical coordinates ρ, ϕ and z. The origin of the coordinate system is at the dipole. The z-axis is vertical and perpendicular to the interfaces. The angle ϕ is measured with respect to the dipole and ρ is the distance transverse to the z-axis. The electromagnetic fields produced by a horizontal electric dipole, located at the origin of coordinates and oriented in the x-coordinate direction in free space, can be written in terms of their transverse electric (TE) and transverse magnetic (TM) wave fields in the form of integrals. The TE and TM solutions of the fields are:

$$\bar{E}^{TE} = \int_{-\infty}^{\infty} dk_\rho \left(\frac{\omega\mu I\ell}{8\pi}\right)(1+R^{TE})e^{ik_z z} \begin{bmatrix} -\frac{1}{k_z\rho} H_1^{(1)}(k_\rho\rho)\cos\phi \\ \frac{k_\rho}{k_z} H_1^{(1)\prime}(k_\rho\rho)\sin\phi \\ 0 \end{bmatrix} \tag{1}$$

$$\bar{H}^{TE} = \int_{-\infty}^{\infty} dk_\rho \left(i\frac{I\ell}{8\pi}\right)(1+R^{TE})e^{ik_z z} \begin{bmatrix} ik_\rho H_1^{(1)\prime}(k_\rho\rho)\sin\phi \\ \frac{i}{\rho} H_1^{(1)}(k_\rho\rho)\cos\phi \\ \frac{k_\rho^2}{k_z} H_1^{(1)}(k_\rho\rho)\sin\phi \end{bmatrix} \tag{2}$$

$$\underline{E}^{TM} = \int_{-\infty}^{\infty} dk_\rho \; i\frac{I\ell}{8\pi\omega\varepsilon}\,(1-R^{TM})e^{ik_z z}\begin{pmatrix} ik_z\, k_\rho\, H_1^{(1)'}(k_\rho\rho)\cos\phi \\ -i\,\frac{k_z}{\rho}\,H_1^{(1)}(k_\rho\rho)\sin\phi \\ k_\rho^2\, H_1^{(1)}(k_\rho\rho)\cos\phi \end{pmatrix} \quad (3)$$

$$\underline{H}^{TM} = \int_{-\infty}^{\infty} dk_\rho \;\left(\frac{I\ell}{8\pi}\right)\,(1-R^{TM})\,e^{ik_z z}\begin{pmatrix} -\frac{1}{\rho}\,H_1^{(1)}(k_\rho\rho)\sin\phi \\ -k_\rho\, H_1^{(1)'}(k_\rho\rho)\cos\phi \\ 0 \end{pmatrix} \quad (4)$$

In Eqs. (1) and (2), $I\ell$ is the antenna strength, ω is the angular frequency, k_ρ and k_z are the ρ- and z-components of the wave vector. $H_1^{(1)}(k_\rho\rho)$ is the first order Hankel function of the first kind, the prime on the Hankel function denotes differentation with respect to its argument. In the column matrices, the first element denotes the ρ-component, the second element the ϕ-component, and the third element the z-component. The reflection coefficients R^{TE} and R^{TM} include all contributions due to the stratified medium. They can be obtained by means of propagation matrices[12] which relate wave amplitudes in different layers.

In this paper, we illustrate the solutions of the above formulation with the two layer case, where the reflection coefficients are deduced from (3) and given by:

$$R^{TM} = \frac{1}{R_{01}^{TM}}\left[\,1 - \frac{1-(R_{01}^{TM})^2}{1 + R_{01}^{TM}\,R_{12}^{TM}\exp\,(i2k_{1z}d)}\right] \quad (5)$$

$$R^{TE} = \frac{1}{R_{01}^{TE}}\left[\,1 - \frac{1-(R_{01}^{TE})^2}{1 + R_{01}^{TE}\,R_{12}^{TE}\exp\,(i2k_{1z}d)}\right] \quad (6)$$

For simplicity, we use d to denote the depth of the subsurface reflector. Note that the ten integrals in Eqs. (1) through (4) all contain either $1 - R^{TM}$ or $1 + R^{TE}$ in the integrand. We solve the integrals by the following three approaches.

2. Geometrical Optics Approximation

In the geometrical optics approximation, we expand $1 - R^{TM}$ and $1 + R^{TE}$ in a series.

$$1 - R^{TM} = (1 + R_{10}^{TM})\left[1 + (1 + R_{10}^{TM}) \sum_{m=1}^{\infty} (R_{10}^{TM})^{m-1} (R_{12}^{TM})^{m} \, e^{i2k_{iz}md}\right] \quad (7a)$$

$$1 + R^{TE} = (1 + R_{01}^{TE})\left[1 + (1 + R_{10}^{TE}) \sum_{m=1}^{\infty} (R_{10}^{TE})^{m-1} (R_{12}^{TE})^{m} \, e^{i2k_{iz}md}\right] \quad (7b)$$

Each term in the series can be evaluated by the saddle point method and attributed to a particular image source[15]. The wave that arrives at the receiver after one reflection from the subsurface can be traced back to the first image and is identified with the first term in the summation series in Eq. (7). Similarly, the plane wave that arrives at the receiver after n reflections from the subsurface is represented by the nth image and corresponds to the nth term in the summation series.

The wave that reaches the receiver without reflection from the subsurface corresponds to the first term in both expressions. Thus, the first term is the classic half space solution. If there is no subsurface reflector the spatial wavelength of the interference pattern λ_{int} is related to the refraction index n_t of the half-space medium by

$$n_t = 1 + \lambda_0/\lambda_{int} \quad (8)$$

where λ_0 is the free space wavelength corresponding to the transmitting antenna frequency. From measurements of λ_{int} we can estimate the value of the index of refraction of the half-space medium.

When there is a subsurface reflector, the energy per unit angle launched from the transmitting antenna into the first layer in the broadside direction, is a maximum at the critical angle

$$\theta_c = \sin^{-1}(1/n_t) \qquad (9a)$$

If the peak due to the first reflection occurs at a distance ρ_c, then the thickness of the layer, d , is given by

$$d = \rho_c/2\tan\theta_c = \frac{\rho_c}{2}\sqrt{n_t^2 - 1} \qquad (9b)$$

In the endfire direction, the energy per unit angle launched from the transmitting antenna into layer '1 is a maximum at the angle

$$\theta_d = \sin^{-1}\sqrt{2/(1 + n_t^2)} \qquad (10a)$$

If the peak due to the first reflection occurs at the distance ρ_d, then the layer thickness is given by

$$d = \rho_d / 2\tan\theta_d = \frac{\rho_d}{2}\sqrt{\frac{n_t^2 - 1}{2}} \qquad (10b)$$

The complete interference pattern is obtained by summing all the wave components with due regard given to both amplitude and phase. It is sometimes suggested that Eqs. (9b) and (10b) be used to predict the depth of the subsurface reflector. In practice, the peak positions due to the first reflections in the actual experimental data are difficult to identify.

3. Mode Analysis

In the mode analysis, we first find all the poles of $1 + R^{TE}$ and $1 - R^{TM}$ in the complex plane of k_ρ. The original path of integration from $-\infty$ to $+\infty$ is then deformed to the steepest path passing through the saddle point. In the case of a receiver near the surface the saddle point occurs at $k_\rho = k$. The value of the integral is then equal to the sum of the residues of each pole lying between the original path and the steepest descent path plus the saddle point contribution and any branch cut contributions. The poles of $1 + R^{TE}$ and $1 - R^{TM}$ are determined from

$$R_{10}^{TE} R_{12}^{TE} \exp(i2k_{1z}d) = \exp(i2\ell\pi) \tag{11}$$

$$R_{10}^{TM} R_{12}^{TM} \exp(i2k_{1z}d) = \exp(i2\ell\pi) \tag{12}$$

Setting $\ell = 0, 1, 2, \ldots$ yields positions of the poles. Each pole corresponds to a wave mode[11]. The modes with wave vector components $k < \mathrm{Re}(k_\rho) < k_1$, $\mathrm{Im}(k_\rho) \geq 0$, $\mathrm{Re}(k_z) < 0$ and $\mathrm{Im}(k_z) > 0$ are surface wave modes. They correspond to waves that reach the receiver from the surface and decrease in magnitude exponentially as they leave. There are only a finite number of surface wave modes being excited and they are the significant ones when distance is large from the transmitter.

The other group of modes are the leaky wave modes. The wave vector vomponents $\mathrm{Re}(k_\rho) < k$, $\mathrm{Im}(k_\rho) > 0$, $\mathrm{Re}(k_z) > 0$ and $\mathrm{Im}(k_z) < 0$. They correspond to waves that reach the receiver from beneath the surface and increase in magnitude exponentially as they leave the surface. There are an infinite

number of leaky wave modes being excited and they decay very rapidly with distance from the transmitting antenna. They are important only in the near and intermediate ranges.

In evaluating the integrals, the original path of integrantion is deformed to the steepest descent path possing the saddle point. For the poles that lie between the original and the new path of integration, the corresponding modes are excited. For the poles that lie close to the saddle point, their effect on the saddle point contribution must be taken into account by using the modified saddle point method. The saddle point contribution corresponds to the direct wave from the transmitter to the receiver.

The number of excited modes depends on the thickness of the slab. When the slab is thicker, there will be more surface wave modes existing between the old and the new path of integration. If the slab is sufficiently thin, no surface mode will be generated.

In addition to the saddle point and the pole contributions, there are two branch points at $k_\rho = k_1$ and $k_\rho = k_2$. Since the integrand is an even function of k_{1z}, the branch point at k_1 does not contribute to the integral. The contribution due to the branch point k_2 corresponds to an inhomogeneous wave decaying away from the bottom surface with $\exp\left(-2\sqrt{k_2^2 - k_1^2}\, d\right)$. Thus the inhomogeneous wave is important only when the slab is sufficiently thin.

4. Numerical Evaluation

The integrals in Eqs. (1) through (4) can be readily evaluated numerically provided they are well defined and properly convergent. In the actual computation procedures, we change the Hankel functions to Bessel functions and integrate from 0 to ∞ instead of $-\infty$ to $+\infty$. Although the Hankel function has a singularity at $k_\rho = 0$, the integrand as a whole is regular at that point. For the integrands to be well defined, we must avoid the branch point $k_\rho = k$. When $\mathrm{Im}(k) \neq 0$, the branch point does not lie on the path of integration. If $\mathrm{Im}(k) = 0$, we choose the Sommerfeld path for the integration.

Simpson's rule is used in carrying out the numerical integration. The amount of computer time needed to obtain a given accuracy is reduced in two ways. First, because of the presence of the factor $\exp(ik_z z)$ in the integrand, we choose $z \neq 0$; the larger the value of z, the faster is the rate of convergence. Physically, this choice corresponds to having the receiving point above the surface. In the lunar experiment, the receiving antenna is about 2 meters above ground when mounted on the Lunar Roving Vehicle. Secondly, we vary the integration increments Δk_ρ as a function of distance from the transmitter. The magnitude of Δk_ρ depends mainly on the rate of oscillation of the Bessel function which for large value of the argument $k_\rho \rho$ is proportional to $\cos(k_\rho \rho)$.

For comparison with other techniques, we have evaluated numerically the H_z-component of a two layer model with a perfect reflector. The frequency is 8MHz which corresponds to a free-space wavelength of $\lambda_0 = 37.5$ meters. The layer has

dielectric constant $3.3\varepsilon_0$, loss tangent 0.01, and a layer thickness of $4\lambda_0$. The results are shown in Fig. 6. The receiving antenna has a height of 3 meters. We used $\Delta k_\rho \rho$ as small as 0.5 to determine the increment Δk_ρ. With a distance of $\rho \leq 14\lambda_0$, $\Delta k_\rho = 0.5/14\lambda_0 \simeq 0.004$. The computation is stopped when the absolute magnitude of the integrand becomes smaller than 0.002 of the accumulative area. About 5000 increments are used typical typically for computation. Computation time on the IBM 360-65 was about 2 minutes per point as shown in Figure 1.

The numerical method has both advantages and disadvantages. If the technique is properly applied, the results can be made quite accurate. But the computation time is large and it provides no physical insight. However, as opposed to other asymptotic methods, which are valid only when the distance is far from the transmitter, the numerical method is valid for all distances. Thus the numerical method provides a useful check for other techniques of computation. Most useful of all, it supplements the asymptotic methods for near field calculations. Because the magnitude of the increment Δk_ρ is inversely proportional to ρ, the computation time per point for small values of ρ is also considerably less than that for large values of ρ.

5. Comparison of Theoretical Solutions

In Figure 1, we show H_z as a function of distance calculated on the basis of the three different approaches for a single model. The model consists of a single layer, 4λ in thickness, with $\varepsilon = 3.3\varepsilon_0$ and $\tan\delta = 0.01$, between free space above and a perfect conductor below. The fields are calculated for a

receiver at a height of 3 meters above surface at 8 MHz. Inspection of the figure shows that the results from the mode analysis agree well with those obtained from numerical integration. Note in particular that the positions of the first peaks in the geometrical optics approximation and in the mode analysis occur at different locations. In the following sections, the theoretical calculations are compared with the various experimental results.

III. EXPERIMENTAL CONFIRMATION

Both the concept of this experiment and the equipment have been tested extensively on glaciers and with laboratory-sized scale models. Because of the variability of natural materials, we used several different glaciers--the Gorner Glacier in Switzerland, the Athabasca Glacier in Alberta,Canada, and several glaciers that drain the Juneau, Alaska icefields. Each of these glaciers had been studied previously. Because the shape, depth, and physical properties of each glacier were known already[17-20], the data obtained on the glaciers can be used to check our theoretical expressions. Although we have collected data on several profiles on the Gorner, about 50 profiles on the Athabasca and about 120 profiles with lengths of 1 to $1\frac{1}{2}$ km on the Juneau glaciers, we shall cite results for only two profiles. These results are typical of the other profiles.

1. The Gorner Glacier

The Gorner glacier, located in southern Switzerland, has been studied for more than a century. The rather extensive set of data includes the results of gravity, seismic, and (D.C.)

electrical resistivity surveys. The thickness and shape of the glacier were well-determined. Our field gear was quite simple and included a General Radio 1330A bridge oscillator for the transmitter, a Galaxy R530 communications receiver, and homemade antennas. The glacier was quite thick in our test area. In Fig. 1 we show the interference pattern of the vertival magnetic component for the broadside transmitting antenna at 10 MHz. The observed peaks and troughs match very well the corresponding features in the theoretical curve calculated for a one layer medium with dielectric constant $3.2\varepsilon_0(1 + i0.03)$. For one layer media, the summation terms in Eq. (7) do not contribute.

2. The Athabasca Glacier

The Athabasca glacier, located about 75 miles south of Jasper, Alberta, Canada, has been thoroughly studied[19-20] also by such other methods as seismology, gravity, electrical resistivity measurements, and drill holes. The ice thicknesses measured by seismic reflections and by direct measurement in boreholes agree quite well and we use the profiles reported by Paterson and Savage as standards with which to compare the thicknesses determined from our electrical sounding technique. In figure 3, we show typical results, the interference pattern of the vertical magnetic component at 2 MHz. Note the excellent match between the experimental curve and the theoretical curves obtained with both the geometrical optics approximation and the mode analysis. Our interferometry data indicate a depth of 180 meters which is in good agreement with the results of drilling, seismic and gravity surveys.

3. The Scaled Model Tank Experiment

A scaled model tank, operating at 6 GHz, was used to obtain interference patterns for a dielectric layer with dielectric constant $2.16\varepsilon_o(1 + i0.0022)$ over an aluminum reflector. The General features of the model tank were described by Rossiter et al[5]. With the mode analysis, we are able to match the experimental curves from the model tank experiment. To show which modes are excited, we transform to a complex $\theta = \theta' + i\theta''$ plane such that $k_\rho = k \sin\theta$, and $k_z = k \cos\theta$. In Fig. 4, we illustrate on the θ-plane the solution of the H_z-component by the modal approach. There are two double-valued functions k_{1z} and k_{2z}. We choose the two branch cuts to be $\mathrm{Re}(k_{1z}) = 0$ and $\mathrm{Re}(k_{2z}) = 0$. Of the four Riemann sheets, we are interested in the poles on the sheet with $\mathrm{Re}(k_{1z}) > 0$ and $\mathrm{Re}(k_{2z}) > 0$. The excited modes marked with circles are surface wave modes. The excited modes marked with crosses are the leaky wave modes. All unexcited modes are denoted by triangular signs. In Fig. 5, we compare the experimental results for layer thicknesses of 1λ, 2.5λ, and 5λ. Note specifically that for shallower depths the geometrical optics approximation fails to account for even the gross features whereas the mode approach fits the experimental data excellently.

IV. CONCLUSIONS

The radiation fields due to a horizontal electric dipole laid on the surface of a stratified medium have been calculated with three different approaches and compared with the various experimental results. The solutions are obtained from the reflection coefficient formulation and written in integral forms. In the near field of the transmitting antenna, analytical methods involving asymptotic expansion are not applicable. Direct numerical integration of the integrals by a computer is the simplest and the most useful. The numerical method for near field calculations also yields accurate results and uses less computer time than far field calculations. When the receiver is far away from the transmitting antenna, the integrals can be evaluated asymptotically by the method of steepest decents. For lossy media and large layer thickness, the geometrical optics approach gives rather accurate results. The interference patterns calculated from this approach can be easily interpreted in terms of ray optics. When losses are small and layers are thin, the mode approach is most attractive. The results can be interpreted in terms of normal modes of the layered medium. Although the calculations and illustrations presented in this paper were done for the one layer and the two layer cases, the calculations can be readily generalized to handle more layers.

Acknowledgements

We are indebted to Peter Annan, Gerry LaTorraca, Larry Bannister, James Rossiter, Richard Baker, Frank Miller, Raymon Watts, and David Redman for help in collecting the field data; to David Strangway for supplying the tank model data; to Hans Rothlisberger for his assistance on the Groner Glacier; to James Meyer for discussions and to Wen Kong for preparing the manuscript.

FIGURE CAPTIONS

Fig. 1. Comparison of theoretical results. These interference patterns are calculated for a dielectric layer with dielectric constant $3.3\varepsilon_o(1 + i0.01)$ overlying a perfect conductor. The receiver has a height of 0.08 wavelength. The amplitude is normalized with the factor $I\ell/4\pi\lambda^2$.

Fig. 2. Comparison of Gorner glacier data with theoretical results for the vertical magnetic field component H_z at 10 MHz. The theoretical curve is calculated for a one-layer medium with dielectric constant $3.2\varepsilon_o(1 + i0.03)$ with the amplitude normalized with the factor $I\ell/4\pi\lambda^2$. The experimental curve is shifted upward to show the match.

Fig. 3. A set of Athabasca data taken at 2 MHz, site 3 compared with the theoretical results obtained with mode approach and geometircal optics approach. The theoretical results are calculated for a layer of ice with dielectric constant $3.3\varepsilon_o(1 + i0.15)$ and depth 1.2λ = 180meters. The scale is 8 db/division.

Fig. 4. The comple θ-plane for mode analysis. The calculation is made for a layer of thickness 1 free-space wavelength and dielectric constant $2.16\varepsilon_o(1 + i0.0022)$ lying on a perfect reflector. The transformation is $k_\rho = k_\rho \sin\theta$, $k_z = k_\rho \cos\theta$. The excited surface wave modes and the leaky modes lying between the original path of integration and the path of the steepest decent are shown by circles and crosses, respectively.

Fig. 5. Scaled model tank experimental data compared with theoretical results obtained with the mode approach and the geometrical optics approximation. The model consists of a layer of oil with dielectric constant $\varepsilon = 2.16\varepsilon_o (1 + i0.0022)$. The subsurface reflector is an aluminum plate.

REFERENCES

1. M. A. H. El-Said, "Geophysical Prospection of Underground Water in the Desert by Means of Electromagnetic Interference Fringes," Proc. IRE, Vol. 44, pp. 24-30, Jan. 1956.
2. M. A. H. El-Said, "A New Method for the Measurement of the Average Dielectric Constant of the Underground Medium of Site," IEEE PGAP, Vol. AP-4, pp. 601-604, Oct. 1956.
3. G. Simmons, D. W. Strangway, L. Bannister, R. Baker, D. Cubley, and G. LaTorraca and R. Watts, "The Surface Electric Properties Experiment," Proc. Conf. Lunar Geophys., Houston, Texas pp. 258-270.
4. D. W. Strangway, G. Simmons, R. Watts, G. LaTorraca, L. Bannister, R. Baker, J. D. Redman, and J. R. Rossiter, "Radio Frequency Interferometry - A New Technique for Studying Claciers," in press, J. Glaciology, 1974.
5. J. R. Rossiter, G. A. LaTorraca, A. P. Annan, D. W. Strangway, and Gene Simmons, "Radio Interferometry Depth Sounding, Part II - Experimental Results," Geophysics, June, 1973, Vol. 38, No. 3, pp. 581-589.
6. A. Sommerfeld, Partial Differential Equations, Academic Press, 1949.
7. K. M. Brekhovskikh, Waves in Layered Media, Academic Press, 1960.
8. A. Baños, Dipole Radiation in the Presence of a Conducting Half-Space, Pergamon Press, 1962.

9. P. Gudmandsen, Electromagnetic Probing of Ice: in Electromagnetic Probing in Geophysics (J. R. Wait, ed.), The Golem Press, 1972

10. J. R. Wait, Electromagnetic Waves in Stratified Media, Pergamon Press, 1970

11. L. B. Felsen and N. Marcuvitz, Radiation and Scattering of Waves, Prentice Hall, 1973

12. J. R. Wait, "Influence of a Sub-Surface Insulating Layer on Electromagnetic Ground Wave Propagation," IEEE Trans. on Ant. and Prop., Vol. AP-14, pp. 755-759, 1966.

13. J. R. Wait, "Asymptotic Theory for Dipole Radiation in the Presence of a Lossy Slab Lying on a Conducting Half-Space," IEEE Trans. on Ant. and Prop., Vol. AP-15, pp. 645-648, 1967

14. J. A. Kong, "Electromagnetic Fields due to Dipole Antennas over Stratified Anisotropic Media," Geophysics, V.37, No.6, pp.985-996, Dec. 1972

15. L. Tsang, J. A. Kong, and Gene Simmons, "Interference Patterns of a Horizontal Electric Dipole over Layered Dielectric Media", J. Geophysical Research, Vol. 78, No. 17, pp. 3287-3300, June, 1973.

16. A. P. Annan, "Radio Interferometry Depth Sounding, Part I - Theoretical Discussion," Geophysics, Vol. 38, No. 3, pp. 557-580, June, 1973.

17. S. Evans, "Dielectric Properties of Ice and Snow - a Review," J. Glaciology, v.5, pp.773-792, 1965

18. D. C. Pearce and J. W. Walker, "An Empirical Determination of the Relative Dielectric Constant of the Greenland Ice Cap," J. Geophysical Research, v.72, No.22, pp.5743-5747, 1967

19. J. C. Savage and W. S. B. Paterson, "Borehole Measurements in the Athabasca Glacier," J. Geophysical Research, V.68, No. 15, pp.4521-4536, 1963

20. E. T. Kanasewich, "Gravity Measurements of the Athabasca Glacier, Alberta, Canada," J. Glaciology, V.4, pp.617-631, 1963

Figure 1.

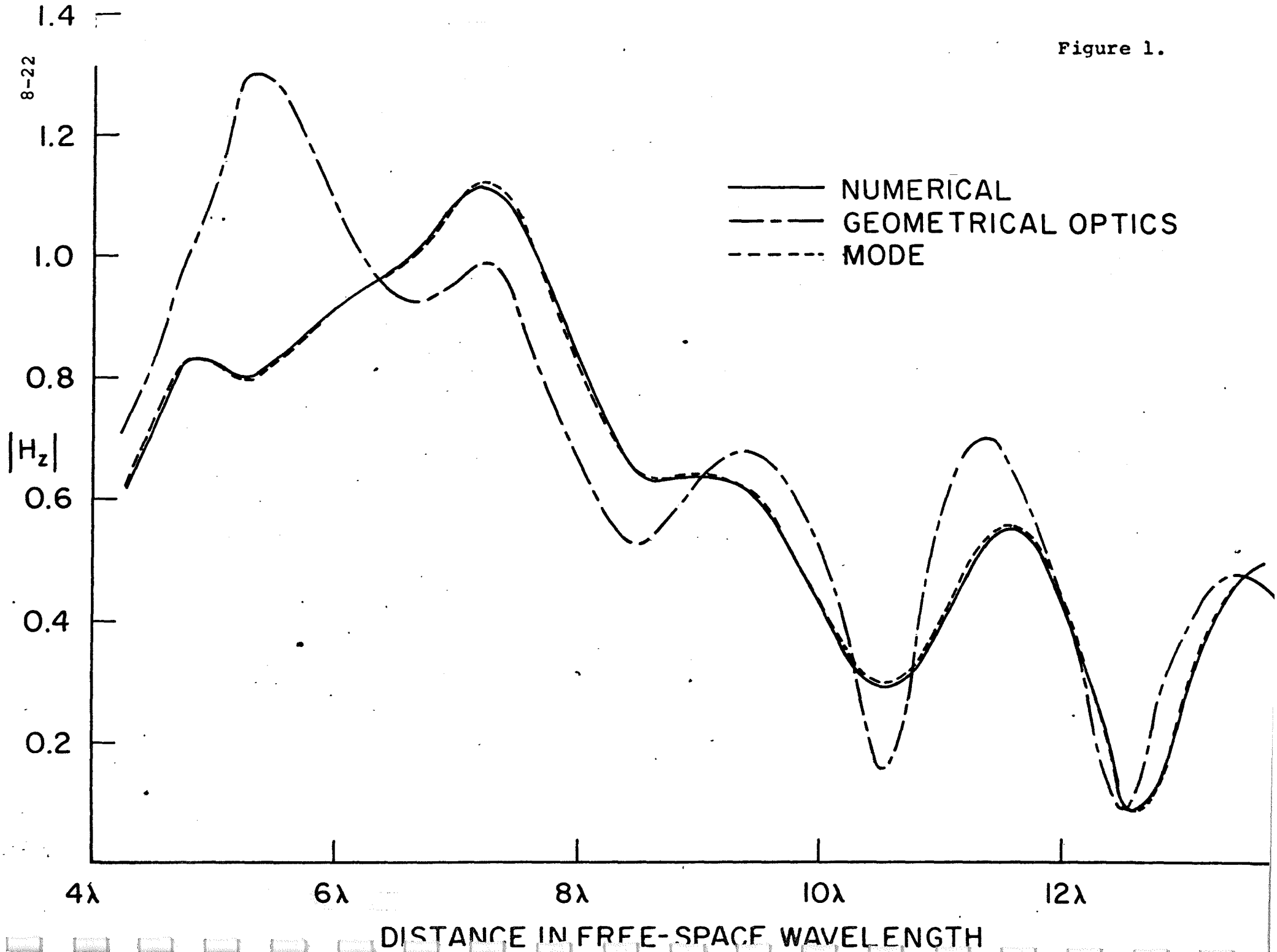
1.4
1.2
1.0
0.8
0.6
0.4
0.2
$|H_z|$
NUMERICAL
GEOMETRICAL OPTICS
MODE
4λ
6λ
8λ
10λ
12λ
DISTANCE IN FREE-SPACE WAVELENGTH

Figure 2.

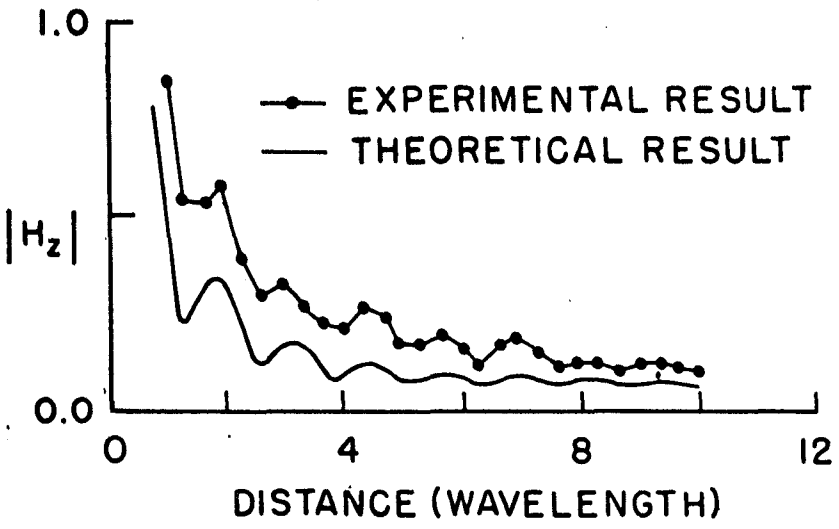
1.0
0.0
$|H_z|$
EXPERIMENTAL RESULT
THEORETICAL RESULT
0
4
8
12
DISTANCE (WAVELENGTH)

Figure 3.

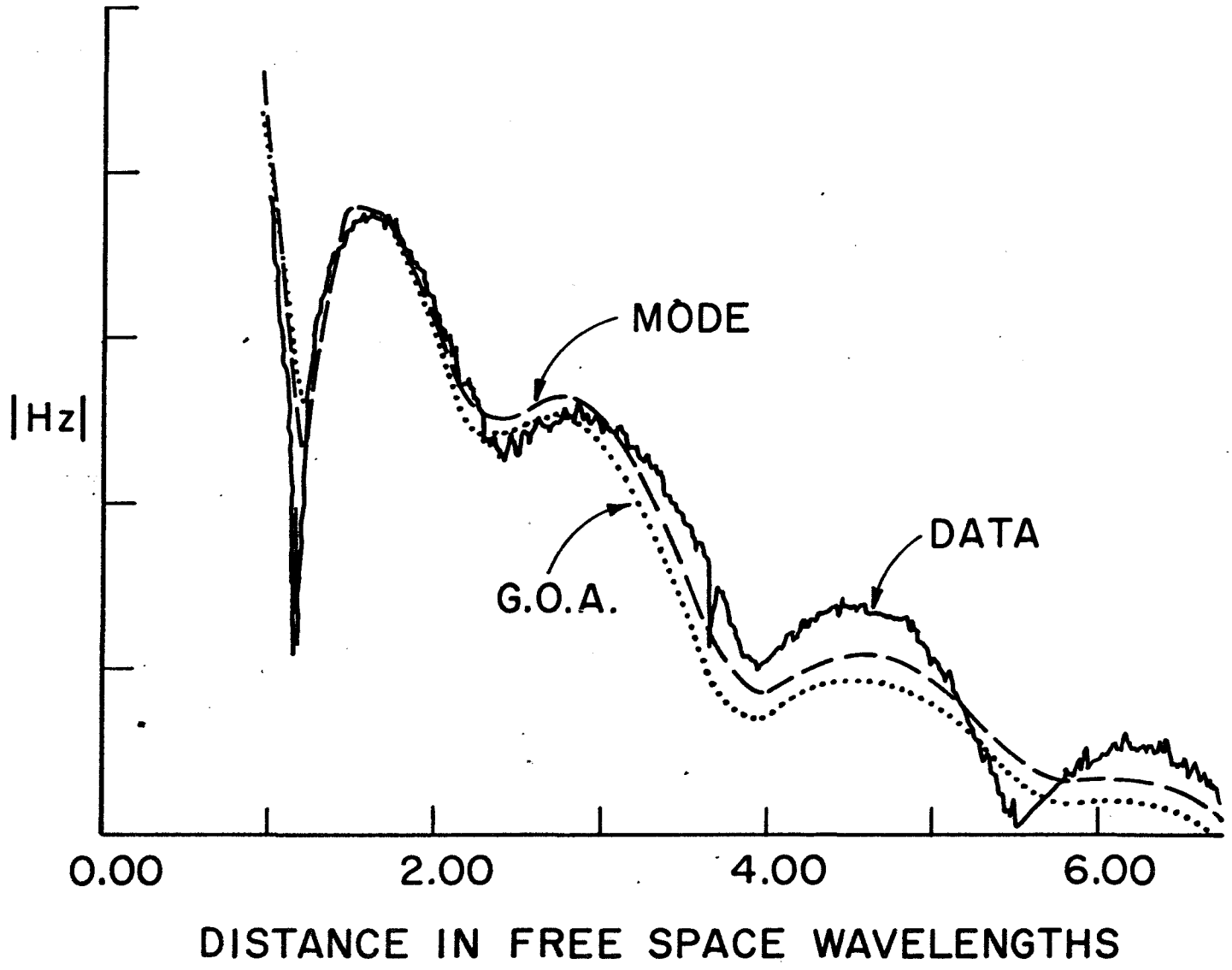
|Hz|
MODE
G.O.A.
DATA
0.00
2.00
4.00
6.00
DISTANCE IN FREE SPACE WAVELENGTHS

Figure 4.

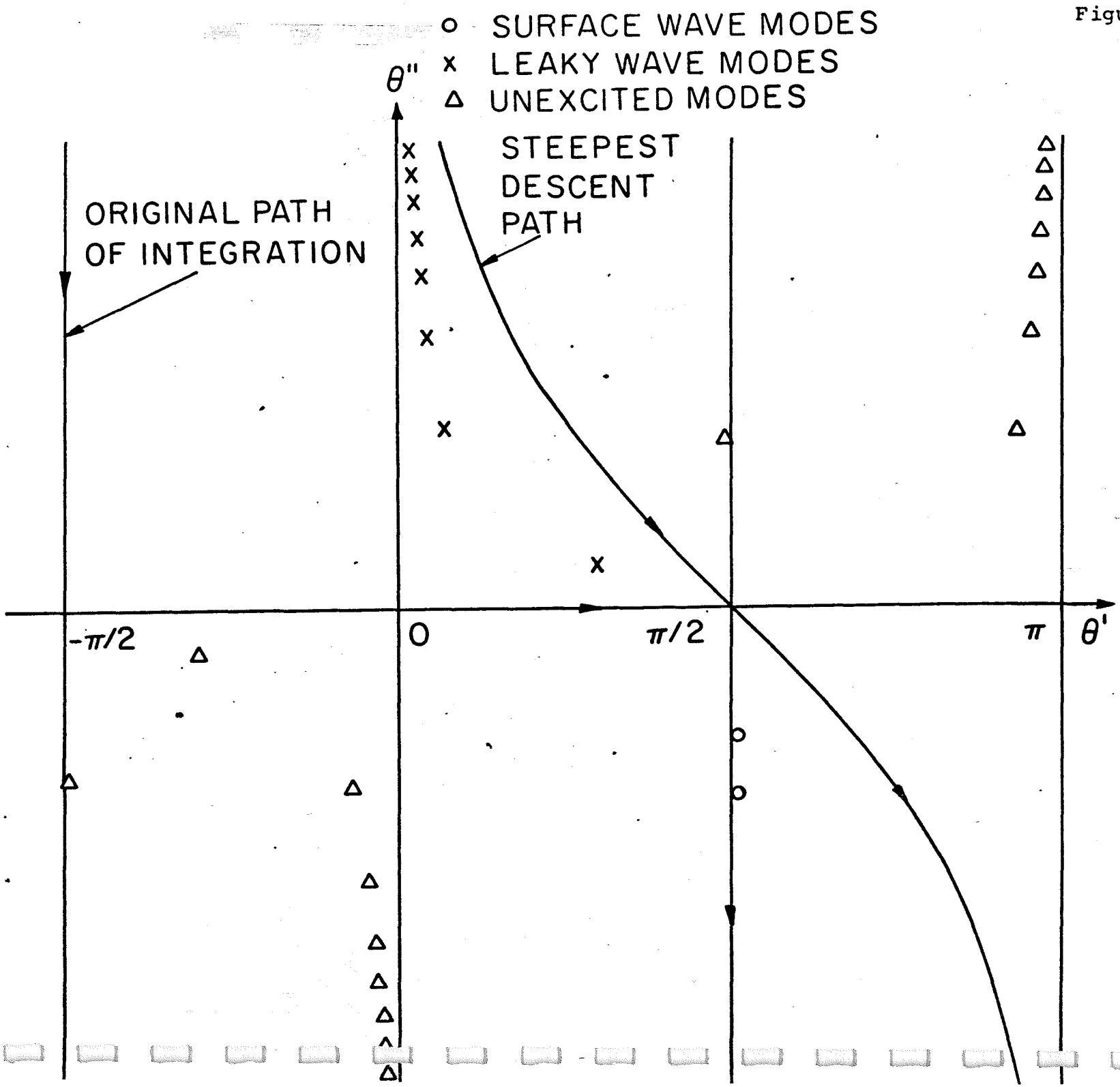
SURFACE WAVE MODES
LEAKY WAVE MODES
UNEXCITED MODES
θ''
STEEPEST DESCENT PATH
ORIGINAL PATH OF INTEGRATION
-π/2
0
π/2
π
θ'

Figure 5.

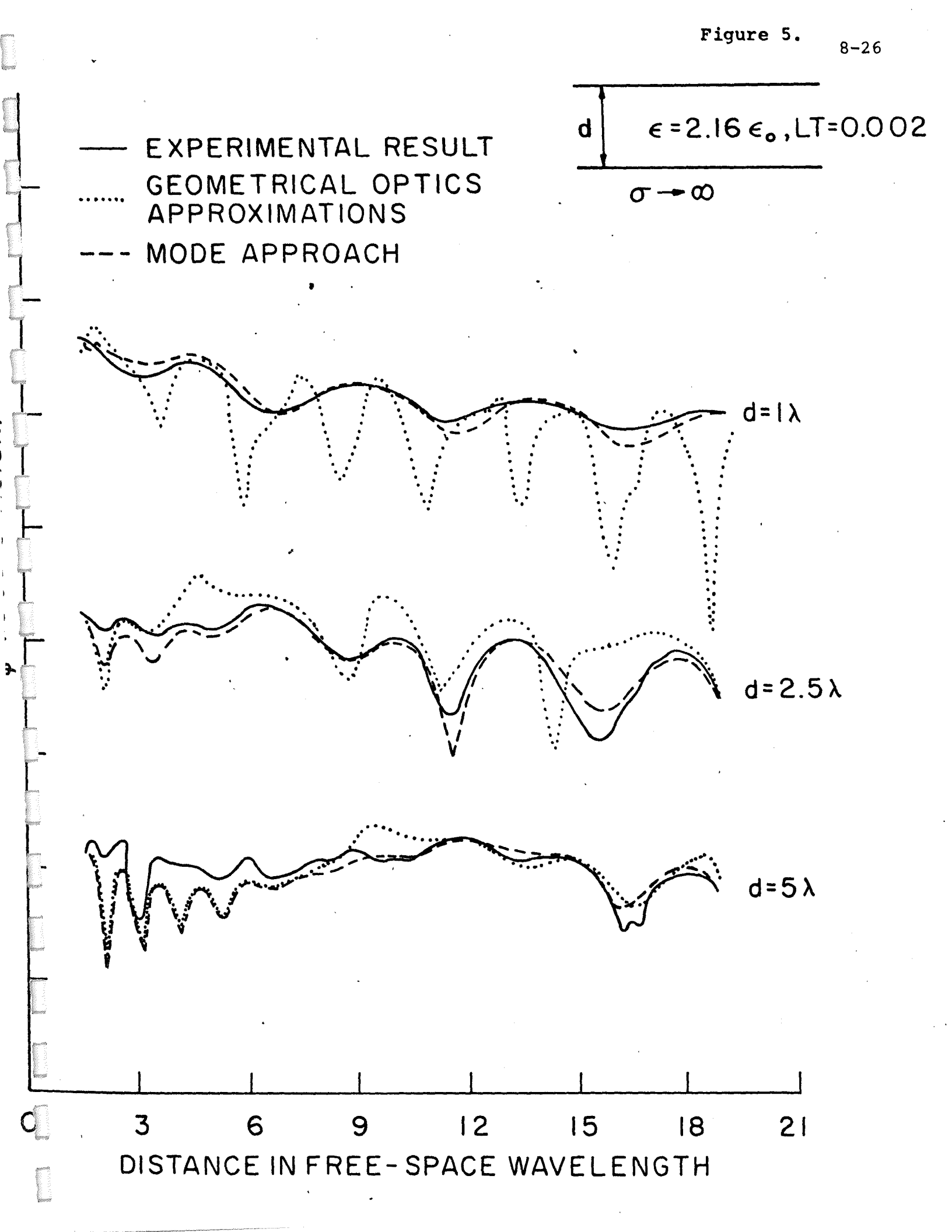
d
$\epsilon = 2.16\,\epsilon_o$, LT=0.002
$\sigma \to \infty$
EXPERIMENTAL RESULT
GEOMETRICAL OPTICS APPROXIMATIONS
MODE APPROACH
d=1λ
d=2.5λ
d=5λ
0
3
6
9
12
15
18
21
DISTANCE IN FREE-SPACE WAVELENGTH

Numerical Evaluation of Electromagnetic Field Due to Dipole Antennas in the Presence of Stratified Media

L. Tsang
Department of Electrical Engineering
Massachusetts Institute of Technology
Cambridge, Massachusetts 02139

Raymon Brown
Department of Earth and Planetary Sciences
Massachusetts Institute of Technology
Cambridge, Massachusetts 02139

J. A. Kong
Department of Electrical Engineering
Massachusetts Institute of Technology
Cambridge, Massachusetts 02139

and

Gene Simmons
Department of Earth and Planetary Sciences
Massachusetts Institute of Technology
Cambridge, Massachusetts 02139

Submitted to the Journal of Geophysical Research 20 March 1973
Revised 31 January 1974

Abstract

Two numerical methods are used to evaluate the integrals which express the EM fields due to dipole antennas radiating in the presence of a stratified medium. The first method is a direct integration by means of Simpson's rule. The second method is indirect and approximates the kernel of the integral by means of the Fast Fourier Transform (FFT). In contrast to previous analytical methods which applied only to two layer cases, the numerical methods can be used for any arbitrary number of layers with general properties.

I. Introduction

In the Radio Frequency Interferometry technique described by Rossiter et al. (1973), propagating electromagnetic waves are used to explore various geological features. This technique was the basis of an Apollo 17 flight experiment to probe the subsurface features of the moon (Simmons et al., 1972, 1974). It has been used also to study several terrestrial glaciers (Strangway et al., 1974).

The theoretical basis of the technique has been described by Annan (1973) and by Tsang et al. (1973). Briefly, the electromagnetic fields due to dipole antennas radiating in the presence of layered media are formulated in terms of reflection coefficients (Kong, 1972) and the results written in integral form for all field components. The chief practical difficulties arise in the evaluation of the integrals. For some techniques, the computation time on a large digital computer is prohibitive. For others, the region of validity does not include any region of interest. These matters are discussed in detail by Tsang et al. (1973) and Kong et al. (1974) who described both analytical and numerical methods for evaluating the integrals. Due to the complication introduced by the reflection coefficients, the analytical methods apply only to a few simple cases. Regions of validity of such analytical methods are also limited. The geometrical optics approximation, mode analysis, and Simpson's rule have been used to solve our problem for the case of a single layer overlying a half space. In this paper, the Simpson's rule has been extended to multilayer cases. In addition, we formulate

the expressions, so that the FFT can be used to calculate the integrals. The case of many layers and the case of continuous variation with depth of the electrical properties can then be readily handled.

II. Formulation of the Problem

Consider the case of a transmitting dipole antenna which is laid on the free surface of a horizontally stratified medium with n layers. For notation, we use a cartesion coordinate system with the dipole coincident with the x-axis. The ith layer is characterized by permeability μ_i, permittivity ε_i, and position of the boundaries $z= -d_{i-1}$ and $z= -d_i$. The zeroth-layer is free space and the layer, denoted by i = t, extends to infinity in the Z-direction. Distance is always scaled to the free space wavelength λ_o. The integral expressions for the electromagnetic fields due to the radiation from such an antenna have been obtained by Kong (1972). In the region above the stratified medium, all six components of the electric and the magnetic field vectors take the form of an integral which involves Hankel functions of the first kind, reflection coefficients that contain all the information necessary to characterize the medium, and an exponent $\exp(ik_z z)$, where z is the distance above the free surface and k_z is the wave vector component along the z-axis. We shall develop the details for a single field component as typical of the whole set, the vertical component of magnetic field vector H_z. We now use a cylindrical coordinate system with the transmitting antenna located at the origin; ρ denotes distance and ϕ denotes the angle made with the direction of the horizontal dipole. Then

$$H_z = \int_{-\infty}^{\infty} dk_\rho \frac{iI\ell k^2}{8\pi k_z \rho}(1 + R^{TE}) e^{ik_z z} H_1^{(1)}(k_\rho \rho)\sin\phi \qquad (1)$$

where

k_ρ is the ρ-component of the propagation vector k

$I\ell$ is the current moment of the antenna

R^{TE} is the reflection coefficient

$H_1^{(1)}(u)$ is the Hankel function of the first kind with argument u,

the reflection coefficient R^{TE} contains all of the information on the physical properties of the medium that pertain to Transverse Electric (TE) fields and is given by Kong (1972)

$$R^{TE} = \exp(i2k_z d_0)\,\frac{\mu(+)_0^1}{\mu(-)_0^1}\left(1 - \frac{\mu(+)_0^1/\mu(-)_0^1 - \mu(-)_0^1/\mu(+)_0^1}{\mu(+)_0^1/\mu(-)_0^1}\right. \tag{2}$$

$$+ \exp(i2k_{1z}(d_1 - d_0))\,\frac{\mu(+)_1^2}{\mu(-)_1^2}\left(1 - \frac{\mu(+)_1^2/\mu(-)_1^2 - \mu(-)_1^2/\mu(+)_1^2}{\mu(+)_1^2/\mu(-)_1^2}\right.$$

$$+ \ldots + \exp(i2k_{nz}(d_n - d_{n-1}))\,\frac{\mu(-)_n^t}{\mu(+)_n^t}\ldots.)).$$

where

$$\mu(\pm)_i^{i+1} = \frac{\mu_{i+1}}{\mu_i} \pm \frac{k_{(i+1)z}}{k_{iz}} \tag{2a}$$

k_{iz} is the z-component of the wave vector in the $i^{\underline{th}}$ layer,

n is the number of layers, and t denotes the last region which is semi-infinite. The properties of the ith layer are completely general and are given as the complex permittivity ε_i and the complex permeability μ_i.

In the following sections we use the Fast Fourier Transform (FFT) to evaluate the integral for typical models. We then compare the results obtained by means of the FFT with the results based on Simpson's rule, the geometrical optics approximation and mode analysis. First though, we note a few preliminary observations with regard to the integral: (a) The singularity at $k_\rho = 0$ in the Hankel function is a removable singularity. (b) The reflection coefficient is an even function of k_ρ. The Hankel function can be changed into a Bessel function and the range of integration can also be changed to $0 - \infty$. The integral becomes

$$H_z = \int_0^\infty dk_\rho \; i\frac{I\ell}{4\pi} \frac{k_\rho^2}{k_z} (1 + R^{TE}) e^{ik_z z} J_1(k_\rho \rho) \sin\phi \qquad (3)$$

(c) As $k_\rho \to \infty$, $R^{TE} \to 0$ and $\exp(ik_z z)$ also tends to 0.

(d) The Bessel function oscillates rapidly for large arguments. The integrand will converge rapidly if we choose $z \neq 0$. Physically, this choice corresponds to the observation point being above the free surface of the stratified medium. (e) The integrand may possess branch points, poles, and other singularities along the axis of integration. One can eliminate the mathematical difficulties caused by these singularities by either of two devices--move these singularities away from the real axis by setting loss tangents of the media not equal to zero or deform the path of integration a small distance away from the real axis on the complex k_ρ-plane.

III. Integration by Fast Fourier Transform Method

Separate the integral (1) into two parts I_1 and I_2. The first part corresponds to solutions in the absence of any stratified medium, and the result is given by the identity

$$I_1 = \frac{\partial}{\partial \rho}\left(\frac{e^{ikr}}{r}\right) = \frac{-i}{2}\int_{-\infty}^{\infty} \frac{k_\rho^2}{k_z} e^{ik_z z} H_1^{(1)}(k_\rho \rho)\, dk_\rho \qquad (4)$$

where $r = \sqrt{\rho^2 + z^2}$

The second part includes all effects due to the reflection coefficient R^{TE} and after changing to Bessel functions,

$$I_2 = \int_0^{\infty} dk_\rho \frac{iI\ell k_\rho^2}{4\pi k_z} R^{TE} e^{ik_z z} J_1(k_\rho \rho)\sin\phi \qquad (5)$$

which is the integral that we want to solve with the FFT.

In applying the FFT, we use the formula (Gradsheteyn and Ryzhik, 1965)

$$\int_0^{\infty} e^{-\nu k\rho} J_1(k_\rho \rho)\, dk_\rho = \frac{1}{\rho}\left(1 - \frac{\nu}{\sqrt{\nu^2 + \rho^2}}\right) \qquad (6)$$

$$\nu = \nu_R + i\nu_I, \quad \mathrm{Re}\{\nu + i\rho\} > 0$$

The integral is written in the following form

$$I_2 = \int_0^{\infty} dk_\rho\, g(k_\rho) e^{-\nu_R k\rho} J_1(k_\rho \rho)\, dk_\rho \qquad (7)$$

where

$$g(k_\rho) = i \frac{I\ell}{4\pi} \frac{k_\rho^2}{k_z} R^{TE} e^{ik_z z + \nu_R k_\rho} \quad (8)$$

We can write (Cooley, 1967) for $\Delta k_\rho \simeq 1/2F$ where F is the Nyquist frequency

$$g(k_\rho) = \frac{1}{N\Delta k_\rho} \sum_{n=-\frac{N}{2}}^{\frac{N}{2}-1} a(f) \; e^{i2\pi f k_\rho} \text{ for } 0 < k_\rho < (\tfrac{N}{2} - 1)\Delta k_\rho \quad (9)$$

where

$$a(f) = \int_{-\infty}^{\infty} g(k_\rho) e^{-2\pi i f k_\rho} \, dk_\rho$$

$$f = n/N\Delta k_\rho$$

The proper choice of N, the number of samples, is essential for the best performance of the FFT and should be some integral power of two (i.e. 2^1, 2^2, 2^3, etc.).

The factor $-2\pi f$ corresponds to ν_I in Equation (6). The right hand side of (9) is periodic and does not tend to zero at ∞. We can multiply (9) by $\exp(-\nu_R k_\rho)$ so that the right hand side of (9) is sufficiently small for the range of k_ρ between $(\frac{N}{2} - 1)\Delta k_\rho$ and ∞. Then the final solution becomes, in view of the identity (6)

$$I_2 = \frac{1}{N\Delta k_\rho} \sum_{n=-N/2}^{\frac{N}{2}-1} a\left(\frac{n}{N\Delta k_\rho}\right) \frac{1}{\rho} \left[1 - \left(\nu_R - \frac{i2\pi n}{N\Delta k_\rho}\right) \Big/ \sqrt{\left(\nu_R - i2\pi n/N\Delta k_\rho\right)^2 + \rho^2}\right] \tag{10}$$

In choosing the increment Δk_ρ, we recall the two alternatives suggested in Section II. If we make the upper half space slightly conductive, which corresponds to Im $k \neq 0$, then we choose Δk_ρ to be smaller than the distance of the branch point from the real axis on the complex k_ρ-plane. If we insist on a real k, then we choose Δk_ρ such that one of the data points coincides with the branch point and such that Δk_ρ is smaller than the distance of the pole or branch point closest to the real axis on the complex k_ρ-plane.

To calculate the expansion coefficient a in Equation (9) we use the FFT algorithm in a subroutine which, for a given set of data d_k, returns the result

$$T_j = \sum_{n=0}^{N-1} d_k e^{-i\frac{2\pi jn}{N}} \qquad j = 0, 1, \ldots N-1 \tag{11}$$

We first alias the function $g(k_\rho)$ with period $N\Delta k_\rho$ and denote the aliased version by $g_p(k_\rho)$. The subroutine requires data points of $g_p(k_\rho\rho)$ between 0 and $(N-1)\Delta k_\rho$. Note that the function $g_p(k_\rho\rho)$ is equal to $g(k_\rho)$ between 0 and $(N/2-1)\Delta k_\rho$ but $g_p(k_\rho)$ between $(\frac{N}{2}-1)\Delta k_\rho$ and $(N-1)\Delta k_\rho$ is equal to $g(k_\rho)$ between $-(N/2)\Delta k_\rho$ and $-\Delta k_\rho$. In the subroutine we calculate

$$a_p\left(\frac{n}{N\Delta k_\rho}\right) = \Delta k_\rho \sum_{\ell=0}^{N-1} g_p(\ell\Delta k_\rho) e^{-i2\pi\ell n/N} \qquad n = 0, 1, \ldots N-1 \tag{12}$$

and return the aliased version of $a(n/N\Delta k_\rho)$, $a_p(n/N\Delta k_\rho)$. We must be careful in translating from $a_p(n/N\Delta k_\rho)$ to $a(n/N\Delta k_\rho)$ within the limits $-\frac{1}{2\Delta k_\rho}$ to $\frac{1}{2\Delta k_\rho}$ in order to use the result (10).

We must choose $N\Delta k_\rho$ such that the function $g(k_\rho)$ is sufficiently near zero outside the limits $-N\Delta k_\rho/2$ to $N\Delta k_\rho/2$. Although mathematically, we could choose z to be large, its value is predetermined by the experimental arrangement. ν_R must not be too small. Note that ν_R must be greater than zero but cannot be larger than z or the exponent in (8) will cause $g(k_\rho)$ to diverge. We choose $\nu_R = z/2$.

In Figures 1 and 2, we show the interference patterns for H_z calculated with FFT on the IBM 360/65 computer for a three layer and a six layer case, respectively. The height of the observation point was taken to be 2 meters, the height used in the lunar experiment. The computation time was about 2.5 minutes for each case. These results are to be compared with the results obtained with Simpson's rule and shown also in Figures 1 and 2.

IV. Integration by Simpson's Rule

Evaluation of the integral (1) by Simpson's rule was discussed by Kong, Tsang, and Simmons (1974). In applying the Simpson's rule for integration, the integration intervals are divided into small increments Δk_ρ. The criterion for the choice of the increment depends on the rate of oscillation of the Bessel function. We choose $\Delta k_\rho \rho$ as small as 0.1 radian. Thus when $\rho = 20\lambda_0$ and the frequency is 32 MHz, we have $\Delta k_\rho \simeq 0.0005$. We stop computation when the absolute amplitudes of the integrand become less than 0.2 % of the accumulative value for the integral.

Note that the error term in Simpson's rule is given by $n(\Delta k_\rho)^5/90$ times the fourth derivative of the integrand. The presence of the branch point due to k_z at $k_\rho = k$ will invalidate the integration even in the simple case of $R^{TE} = 0$, if one integrates along the real axis. We choose to keep k real and to deform the path to the Sommerfeld path of integration. Subroutines for Bessel functions of complex arguments are constructed. For small arguments, we use a power series representation, and for large arguments, we use asymptotic expansions for the Bessel functions. The subroutines have been checked against tables of Bessel functions.

The computation is very time consuming. However, the convergence of the integrand will be very fast if the observation point is far above ground, i.e., for a large positive value of z. Note also that the magnitude of Δk_ρ is inversely proportional to ρ. Thus the computation takes

less time for regions near the transmitting dipole, where, in fact, most computational methods that use asymptotic expansion are invalid.

V. Discussion

The magnitude of H_z for the three layer case and for the six layer case, calculated by FFT and by Simpsons rule are shown in Figures 1 and 2 for comparison. We conclude that both techniques yield identical results. Computation times are very different though - Simpsons rule used 32 minutes for the three layer case and about 40 minutes for the six layer case on an IBM 360/65 computer which is to be compared with 2.5 minutes for each FFT calculation. Another possible consideration for some applications may be the fact that the FFT consumes large amounts of storage space in the computer when the Nyquist frequency and the number of sampling points are large. Also, the comparisons have been made for ranges that are unfavorable to Simpson's rule.

Further substantiation that our FFT formulation is correct can be obtained by comparison of FFT-results for a two layer model with results obtained with both the geometrical optics approximation and mode analysis. See Figure 3. Note that the curves have been displaced 20db so they can be seen more easily. Because the features of the FFT-results are also present in the results of both mode and geometric optics approximation (within the range of validity), we conclude that the FFT formulation is correct. We note briefly though that other factors are sometimes important in the choice of a computational technique. The analytical methods consume very little

time, but they are applicable only in certain regions because of the approximations involved. The geometrical optics result applies when the distance is far from the transmitting antenna (ideally, greater than about 5-10 λ_o) and when the layer is thick and lossy. The mode method can be applied to general cases, and is extremely useful for thin layers. Tsang et al. (1973) discussed the geometrical optics approximation in greater detail. See Kong et al. (1974) for a complete discussion of mode analysis applied to electromagnetic wave propagation in layered media.

Acknowledgement

This work was supported by NASA Contract No. NAS9-11540 through the Center for Space Research, Massachusetts Institute of Technology. We would like to thank Norman Brenner for the use of his FFT subroutine algorithm.

References

Annan, A.P., Radio Interferometry depth sounding: Part I - Theoretical discussion, Geophysics, vol. 38, 557, 1973.

Cooley, J.W., P.A.W. Lewis, and P.D. Welch, Application of the Fast Fourier Transform to computation of Fourier integrals, Fourier series, and convolution integrals, IEEE Trans. on Audio and Electroacoustics, AU-15, 79, 1967.

Gradsheteyn, I.S., and I.W. Ryshik, Tables of Integrals Series and Products, p. 707, Academic Press, New York, 1965.

Kong, J.A., Electromagnetic fields due to dipole antennas over stratified anisotropic media, Geophysics, 37, 985, 1972.

Kong, J.A., L. Tsang, and G. Simmons, Lunar subsurface probing with radio frequency interferometry, IEEE Trans. on Ant. and Prop., in Press, 1974.

Rossiter, J.R., G.A. LaTorraca, A.P. Annan, D.W. Strangway, and G. Simmons, Radio interferometry depth sounding: Part II - Experimental results, Geophysics, v. 38, 581, 1973.

Simmons, G., D.W. Strangway, L. Bannister, R. Baker, D. Cubley, G. LaTorraca, and R. Watts, The Surface Electrical Properties Experiment, Lunar Geophysics, Z. Kopal and D. Strangway (eds) D. Reidel Publishing Co., 258, 1972.

Simmons, G., D. Strangway, P. Annan, R. Baker, L. Bannister, R. Brown, W. Cooper, D. Cubley, J. deBettencourt, A.W. England, J. Groener, J.A. Kong, G. LaTorraca, J. Meyer, V. Nanda, D. Redman, J. Rossiter, L. Tsang, J. Urner, and R. Watts, Apollo 17 Preliminary Science Report, NASA, in Press, 1974.

Strangway, D.W., G. Simmons, R. Watts, G. LaTorraca, L. Bannister, R. Baker, J.E. Redman, and J.R. Rossiter, Radio frequency interferometry-- A new technique for studying glaciers, in Press, J. Glaciology, v. 13, N. 67, April 1974.

Tsang, L., J.A. Kong, and G. Simmons, Interference patterns of a horizontal electric dipole over layered dielectric media, J. Geophys. Res., V. 78, N. 17, 3287, 1973.

FIGURE CAPTIONS

Figure 1. Comparison of the direct and FFT methods for a three layer model in which

$\varepsilon_1 = (3.3)(1 + i0.01)\varepsilon_0$ $\quad d_1 = 1\lambda_o$

$\varepsilon_2 = (5.0)(1 + i0.02)\varepsilon_0$ $\quad d_2 = 2\lambda_o$

$\varepsilon_3 = (8.0)(1 + i0.04)\varepsilon_0$

Vertical scale is 10 db per division. The curves have been displaced vertically 20 db for ease of comparison.

Figure 2. Comparison of the direct and FFT methods for a six layer model in which

$\varepsilon_1 = (2.0)(1 + i0.01)\varepsilon_0$ $\quad d_1 = 0.5\lambda_o$

$\varepsilon_2 = (3.0)(1 + i0.02)\varepsilon_0$ $\quad d_2 = 1\lambda_o$

$\varepsilon_3 = (4.0)(1 + i0.03)\varepsilon_0$ $\quad d_3 = 2\lambda_o$

$\varepsilon_4 = (5.0)(1 + i0.04)\varepsilon_0$ $\quad d_4 = 3\lambda_o$

$\varepsilon_5 = (6.0)(1 + i0.05)\varepsilon_0$ $\quad d_5 = 4\lambda_o$

$\varepsilon_t = (8.0)(1 + i0.06)\varepsilon_0$

Vertical scale is 10 db per division. The curves have been displaced vertically 20 db for ease of comparison.

Figure 3. Comparison of the FFT, Geometrical Optics (GOA), and Mode Theory (MODE) for a two layer model in which

$\varepsilon_1 = 3.3(1 + i0.02)\varepsilon_0$ $\quad d_1 = 4\lambda_o$

$\varepsilon_t = 6.0(1 + i0.04)\varepsilon_0$

Vertical scale is 10 db per division. The curves have been displaced vertically 20 db for ease of comparison.

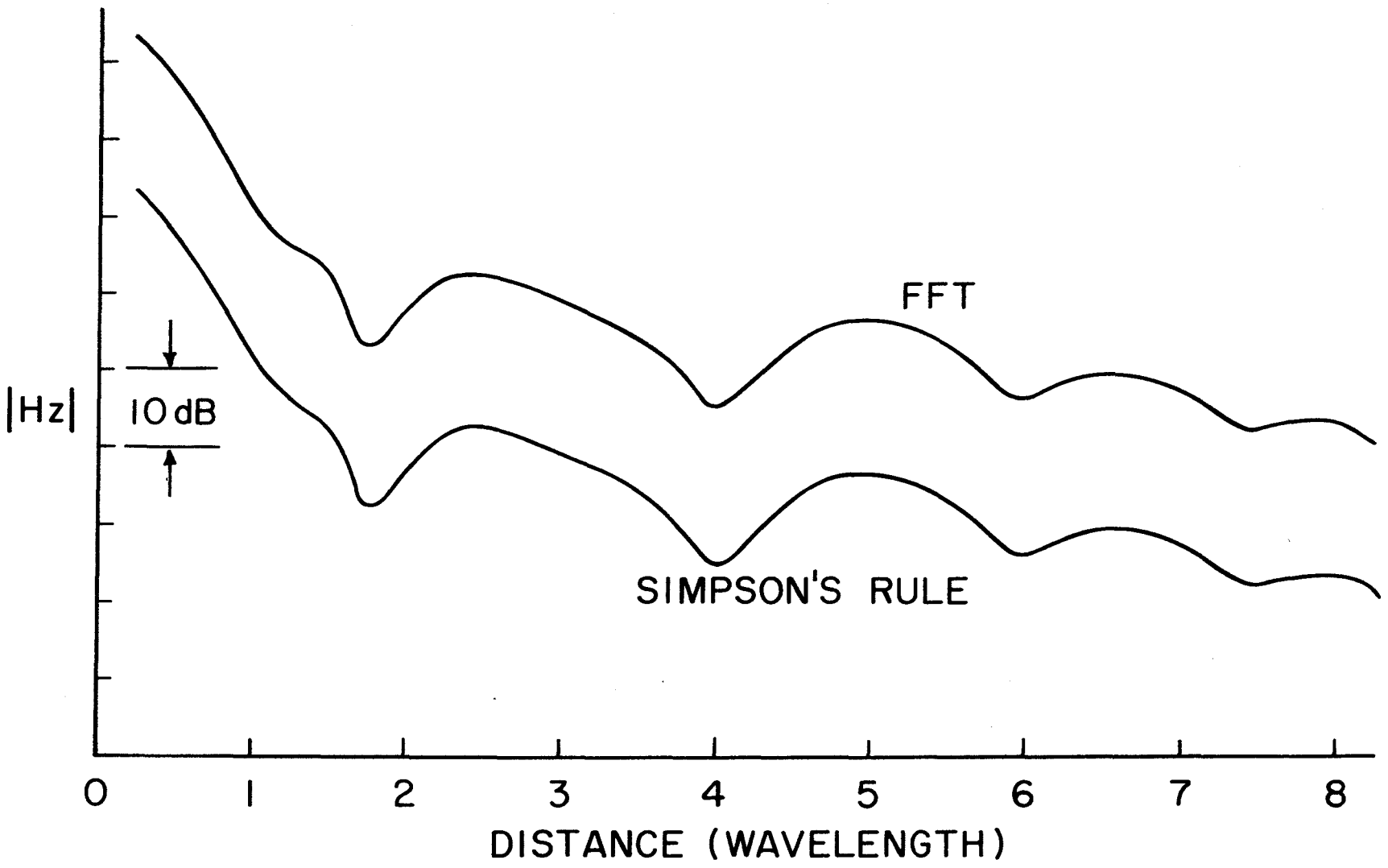
FFT
|Hz|
10 dB
SIMPSON'S RULE
0
1
2
3
4
5
6
7
8
DISTANCE (WAVELENGTH)

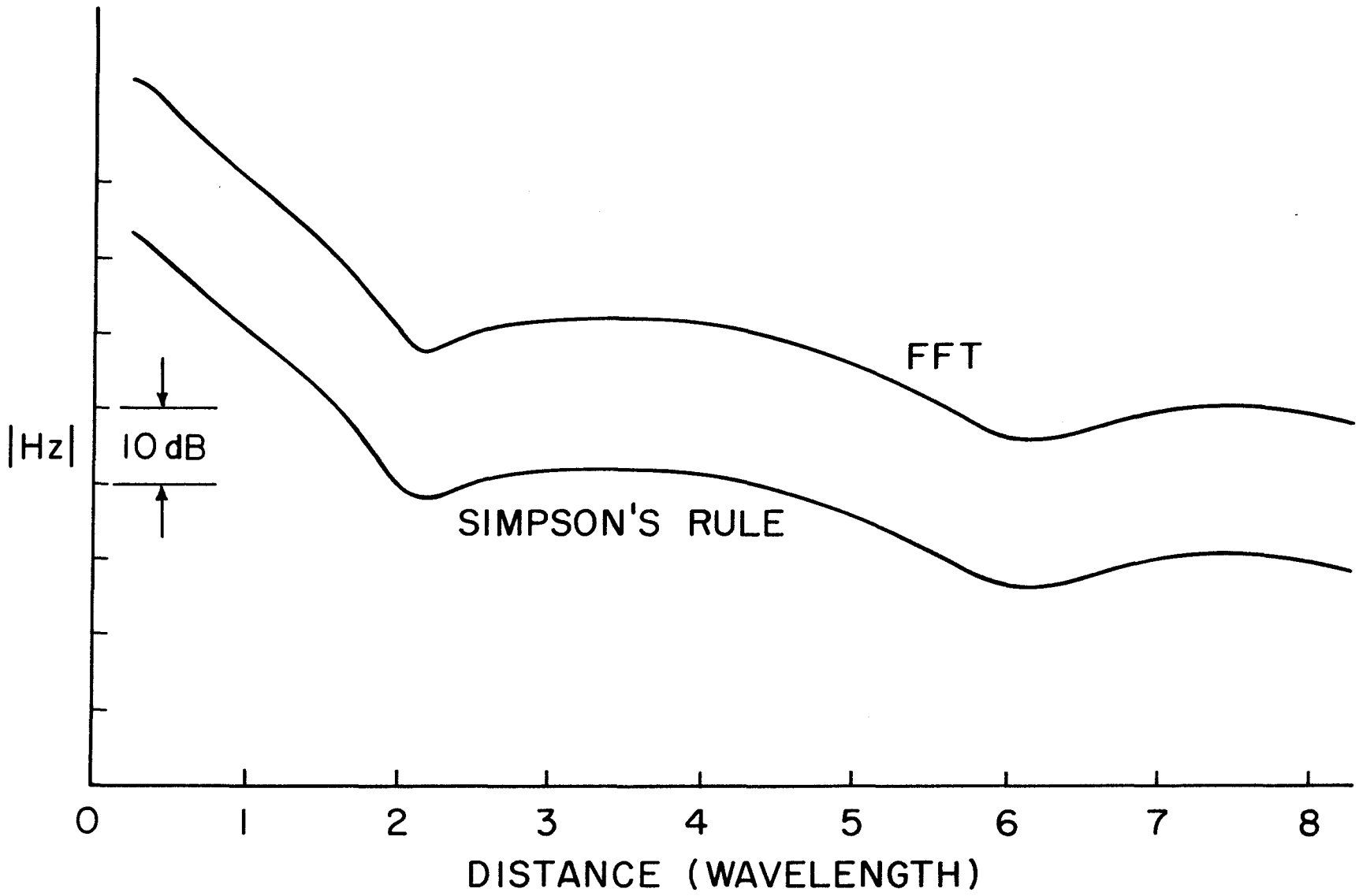
|Hz|
10 dB
FFT
SIMPSON'S RULE
0
1
2
3
4
5
6
7
8
DISTANCE (WAVELENGTH)

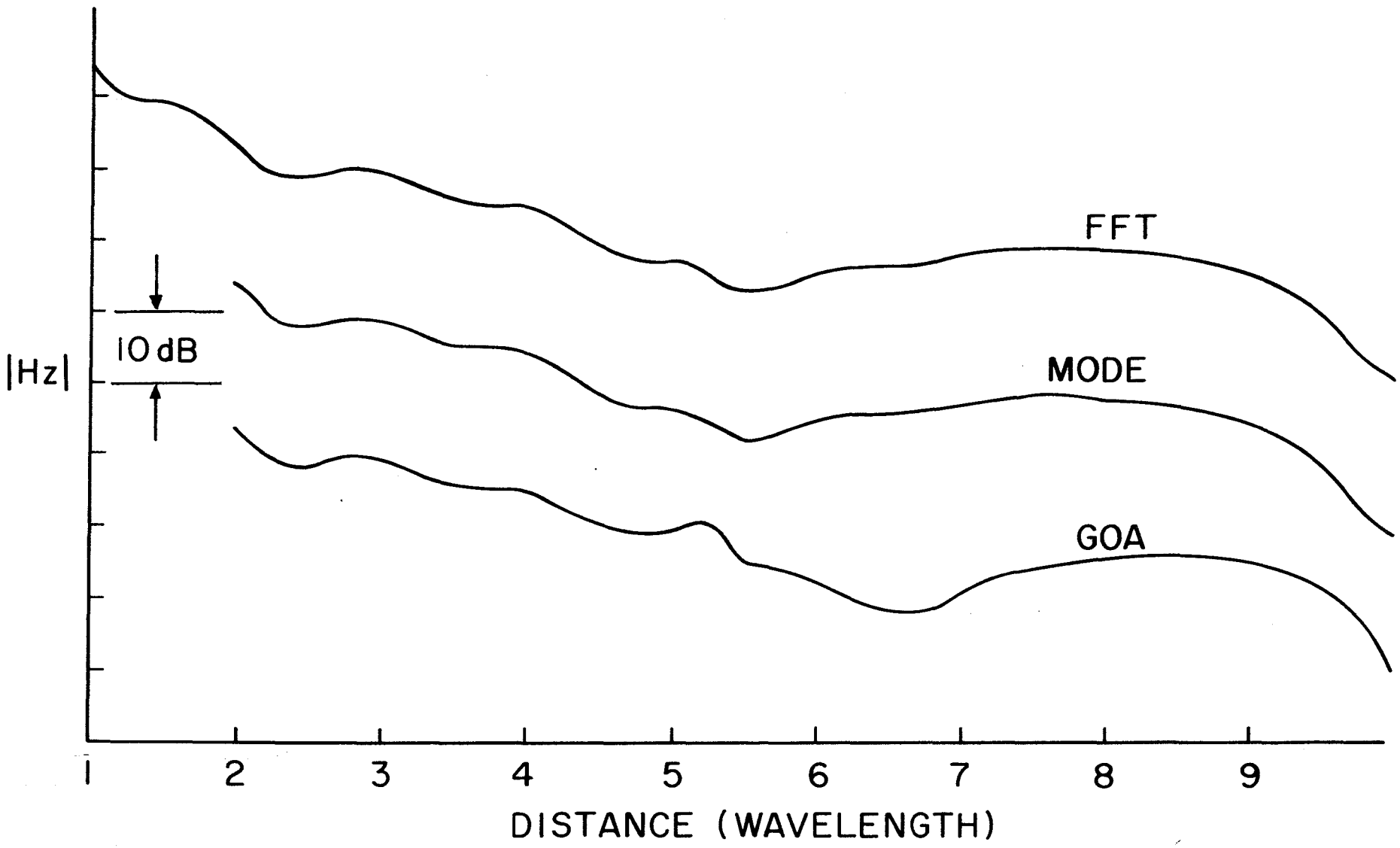
FFT
MODE
GOA
10 dB
|Hz|
1
2
3
4
5
6
7
8
9
DISTANCE (WAVELENGTH)

The Electromagnetic Response of a Low-loss, 2 Layer, Dielectric Earth for Horizontal Electric Dipole Excitation.

A.P. Annan[1], W.M. Waller[2], D.W. Strangway[3], J.R. Rossiter[1], J.D. Redman[3].

1. Department of Physics
   University of Toronto
   Toronto, Ontario
   Canada

2. Lockheed Electronics Company
   NASA - JSC, Houston
   Texas, U.S.A.

3. Department of Geology
   University of Toronto
   Toronto, Ontario
   Canada

Abstract

This paper presents the results of a concentrated theoretical and experimental study into the electromagnetic response of a 2-layer dielectric earth. The side by side analysis of the theoretical response and the results of a scale model experiment demonstrates the fundamental features of electromagnetic wave propagation in such an environment. For layers thick on a wavelength scale the response is readily interpreted from a geometrical optics analysis. For thin layers, the response is best analysed from the normal mode viewpoint. The responses for both depth extremes as well as intermediate depths are presented and interpretations of the observations given. The onset of mode propagation in the model data is very distinctive.

Introduction

The radio interferometry method, previously summarized by Annan (1973) and Rossiter et al (1973), is a useful geophysical method in geologic regions exhibiting extremely high electrical resistivities. In this context, high resistivity implies that displacement currents in the media must be considerably greater than the conduction currents. In terrestrial materials, this situation is encountered in ice-covered regions (glaciers, polar ice caps) for radio frequencies of the order of 1Mhz. and higher. Lunar materials

also behave as low-loss dielectric materials in the Mhz. frequency range (Olhoeft et al (1973), Katsube and Collett(1971)).

The original papers, mentioned above, presented much of the preliminary work conducted to study the feasibility of the radio interferometry method. Subsequent to this work, a lunar experiment was designed, constructed and carried on Apollo 17 (Simmons et al (1972)). In order to be able to make a coherent interpretation of data from glaciers and the Moon, a much more detailed understanding of the basic features of the radio interferometry method was required. An in-depth computational analysis of the theoretical response of idealized models was made and these responses were simulated with a scale model experiment to check their validity. In addition, full scale experiments were conducted on glaciers in Alberta (Strangway et al (1974) and in Alaska (Rossiter et al see companion paper).

In this paper, a subset of the theoretical and scale model studies are analysed. The purpose is to present a detailed, documented study of the response of a 2-layer, low-loss dielectric earth for excitation by an electric dipole antenna laid on the surface. Some preliminary results of the scale model and theoretical analysis are given by Rossiter et al (1973). In the course of this study, the theoretical and experimental work were carried out together in order that each could be used to confirm the other. The end product was an in-depth understanding of the intuitively simple, but complex in detail, physical phenomena involved.

Idealized 2-Layer Earth

The idealized model studied is shown in Fig. 1. The 2-layer earth is characterized by the dielectric constants K_i and the loss tangents $\tan \delta_i$. The cartesian coordinates (x_1, x_2, x_3), the associated unit vectors $(\hat{e}_1, \hat{e}_2, \hat{e}_3)$ and the cylindrical coordinates (ρ, φ, z) are shown in the diagram. For the computational analysis, the earth is excited by a point electric dipole located at the origin of the coordinate system with its moment aligned with the $\hat{e}_1$ axis. In actual experiments, the source is a half wavelength electric dipole antenna. The time variation of the dipole moment is of the form $e^{-j\omega t}$ and in all subsequent mathematical expressions the time dependence is suppressed.

The radio interferometry method measures the field strength about the transmitter primarily along profiles which run radially outward from the dipole. The profiles commonly used are denoted the broadside (B) and the endfire (E) profiles. The B profile is run radially out from the dipole normal to the direction of the dipole moment. The E profile runs radially away from the dipole along the direction of the dipole moment. In Fig. 1, the B profile is along the $\hat{e}_2$ axis while the E profile is along the $\hat{e}_1$ axis. The field strength along these profiles exhibits maxima and minima at various spatial positions due to interference of waves propagating

with different horizontal phase velocities. The position of these maxima and minima and the rate of decay of the fields with distance are indicators which can be used to infer the electrical properties of the earth and the layer thickness.

In the following discussions, all spatial dimensions are normalized in terms of the free space wavelength w. All propagation constants and wavenumbers are normalized in terms of the free space propagation constant $k_o = 2\pi/w$.

Mathematical Formalism

The mathematical formulation of the electromagnetic response of a plane layered earth is well known since it is a standard boundary value problem (Wait (1970), Brekhovskikh (1960)). The difficult part of the analysis occurs when actual numerical computations of the response are required. The fields are expressed as Hankel transforms (or 2 dimensional Fourier transforms) which cannot be evaluated analytically. In all but the simplest case of a whole-space, approximate methods of integration must be used to extract useable results. The most straight forward method of obtaining numerical results is to numerically integrate the Hankel transforms. Other methods involve limiting material properties to special values and reducing the integrand to a sufficiently simple form that an analytical evaluation can be made. The other alternative is to look at the physical nature of the response by

approximate solutions which can be obtained by manipulation of the integration contour in the complex plane. Two solutions in this class are known as the geometrical optics and the normal mode solutions.

The details of the applications of these techniques to low-loss dielectric earth models is discussed by Annan (1970, 1973), Tsang et al (1973) for various dipolar excitations. In the following discussions, the geometrical optics and the normal mode solutions are used. The reason for this is that sufficiently accurate results can be obtained in a very economical manner. The computation cost of numerical integration rules out this method for all but very particular cases under consideration. Of the two solutions obtained by contour integration, the normal mode solution is the more correct solution. The only approximations involved here are in the analysis of the branch line contributions which yield lateral and inhomogeneous waves associated with the boundaries. The actual "normal mode" part of the solution is exact within the computational error of evaluating its contribution. The geometrical optics solution involves asymptotic expansions for each multiple reflection and has built in approximations from the first step of analysis. The main advantage of the geometrical optics solution is that the response has a simple physical interpretation and is economically computed. As pointed out by Annan (1973), this solution can only be used when spatial dimensions are on the order of the wavelengths or attenuation lengths in the media involved.

The electric and magnetic fields at the surface of the 2 layer earth shown in Fig. 1 are summarized in Table 1. The complex radial wavenumber plane and integration contours are shown in Fig. 2. For the expressions in Table 1, the geometrical optics solution is obtained by expanding the expression in the denominators

$$\frac{1}{1 - R_+R_-\beta} = \sum_{n=0}^{\infty} R_+^n R_-^n \beta^n \qquad (1)$$

whereas the mode solution is obtained by solving the transcendental equation

$$R_+R_-\beta = 1 \qquad (2)$$

which yields the TE and TM normal mode wavenumbers of the layered earth. The contour of integration is deformed into a steepest descent contour through a saddle point for each term in the geometrical optics expansion. For the normal mode analysis, the contour is deformed to yield a sum over the normal modes of the system plus integrals along the branch lines.

Scale Model Description

For electromagnetic systems to be similar, the spatial dimensions in free space wavelengths and the loss tangents must be the same. In order to simulate the radio interferometry method in a reasonably sized laboratory, wavelengths

in the centimeter range are necessary; this corresponds to radio frequencies in the GHz range. The 2 layer earth model and associated electronics are shown in Fig. 3 and 4.

The transmitting (TX) and receiving (RX) antennas are tuned half-wavelength electric dipoles. The excitation frequency is 5.9 GHz. which corresponds to a free space wavelength w = 5.08 cm. The 2 layer earth is simulated by a tank of dielectric oil with a plane reflector suspended at a depth d in the oil. The effects of the finite size of the tank (30w long x 15w wide x 15w deep at 5.9 GHz) are minimized by lining the inside with a microwave absorbing materials (Eccosorb). This reduces undesired spurious reflections from the walls of the tank. The Tx and Rx antennas are mounted on a track suspended over the tank; the Rx antenna is mounted on a mechanized carriage so that profiles of field strength versus Tx-Rx separation can be made automatically. The track and associated supports are also covered with microwave absorbing material.

Three sets of electrical properties of the 2-layer models were used in the model. The first set was an oil with dielectric constant $K_1 = 2.16$ and $\tan \delta_1 = 0.0022$, and an aluminum sheet, $\tan \delta_2 = \infty$, acting as a perfectly reflecting substratum. A second set of electrical properties were obtained by doping the oil with benzonitrile to increase its loss tangent. The third layered consisted of oil

(undoped) underlain by a dielectric slab $K_2 = 6.75$ and tan $\delta_2 = 0.11$. The slab was 2 w thick and had a sufficiently high loss that it eliminated the possibility of spurious reflections from the bottom of the slab returning to the surface. The thickness of the oil layer was varied from 0.2w up to 10w and profiles of $\log_{10} | E_\phi |$ versus Tx-Rx separation along the B profile were measured in most instances.

The automatic traverse equipment and associated recording apparatus are sketched in Fig. 4 (Waller (1973)). The field strength versus distance is displayed on an X-Y recorder and at the same can be recorded on a two channel analog tape recorder. The recorded data was later digitized in order that data enhancement and automatic interpretation schemes could be tested.

Theoretical and Experimental Results

(a) Half Space Earth: Radiation Pattern Directionality

Before discussing the 2 layer earth in detail the half-space response is briefly reviewed. The interaction of the dipole source with the air-earth interface drastically modifies the directionality of the antenna. This result is important when analysing 2 layer models with the geometrical optics solution. This effect has been discussed by Tsang et al (1973), Annan (1970, 1973), Cooper (1971). The pattern

for E_ϕ in the X_2X_3 plane is sketched in Fig. 5; (a) shows E_ϕ for the dipole in a whole-space while (b) shows the response of the dipole when placed on a perfectly dielectric half-space. E_ϕ in the X_2-X_3 plane for the whole-space is simply given by

$$E_\phi = j\,\omega\,\mu_o\ \mathrm{Idl}\ \frac{e^{j2\pi R}}{4\pi RW} \tag{3}$$

while for the half space, as $R \rightarrow \infty$,

$$E_\phi = T_{10}\left(\frac{|Z|}{R}\right)\ j\omega\mu_o\ \mathrm{Idl}\ \frac{e^{j2\pi R}}{4\ RW} \qquad Z > 0$$

$$E_\phi = T_{01}\left(\frac{|Z|}{R}\right)\ j\omega\mu_o\ \mathrm{Idl}\ \frac{e^{j2\pi\sqrt{K_1^*}\,R}}{4\ RW} \qquad Z < 0 \tag{4}$$

where

$$R = \left(\sum_{i=1}^{3}(\ x_i\ )^2\right)^{1/2}$$

Idl = electric dipole moment

μ_o = free-space permeability

$n_{ij} = (K_i/K_j)^{1/2}$

$T(\alpha)$ = TE Fresnel transmission coefficient from region i to region j.

$$= \frac{2\ \alpha}{\alpha + n_{ji}\left(1-n_{ij}^{\ 2}(1-\alpha^2)\right)^{1/2}}.$$

The modified pattern is highly directional with a strong peak into the earth at the critical angle of the interface. Similar analyses can be carried out for other field components; all show highly directional patterns.

Experimental measurements of the radiation pattern obtained with the scale model with no subsurface reflector confirm the directionality of the source in the presence of an interface. The results of measurements of $|E_\phi|$ are shown in Fig. 6. The pattern for E_ϕ was measured at distances of 3 w, 4.5 w, and 6 w from the source. The "theoretical" pattern for the air-oil-dipole configuration computed by Cooper (1971) is shown with the experimental results. It should be noted that the experimental results are not normalized and that the shape of the patterns, not the magnitudes, should be considered.

The discrepancy between the theoretical response and observed response are primarily explained by the fact that the experimental measurements were made at a finite distance from the source. The theoretical pattern shown is valid only infinitely far from the source by definition. As the Tx-Rx separation is increased, the experimental pattern changes shape and becomes more like the theoretically predicted pattern.

The preceding solution for the theoretical response is obtained from the first term in an asymptotic expansion for the field. At finite source-receiver distances higher order terms in the expansion must become important. At the peak of the pattern, however, alternate solutions must be used since the higher terms of the asymptotic expansion are infinite. Brekhovskikh(1960) has studied the fields in the region of the peak of the pattern in detail and obtained a modified expansion with the first correction term decreasing as $(1/r)^{5/4}$. A rough calculation shows that this term is significant out to distances of tens of wavelengths.

The physical rationale for the lobate pattern is quite simple. The explanation can be seen most easily if the waves radiated by the antenna are examined from the ray theory point of view. In a whole space the source radiates uniformly in all directions. The presence of the half-space modifies this, since rays which propagate horizontally are continually refracted downward at the critical angle of the interface. Combining the whole-space pattern of the antenna with the directional selectivity of the interface yields a complex radiation pattern with high directionality.

To first order, the fields along the interface are zero. If higher terms of the asymptotic expansions are retained, the fields fall off as $(1/r)^2$. There are two components in this second order effect; one which propagates with the phase velocity of the earth and one which travels with the phase velocity of the air. As a result the fields at the surface of the half-space exhibit a regular beating as a function of spatial distance from the antenna. This is discussed by Annan (1970, 1973).

(b) 2 Layer Earth: Perfectly Reflecting Substratum

The 2 layer earth can exhibit a wide variety of responses depending upon the range of electrical properties and layer thickness. In early analysis, the case of a perfectly reflecting substratum was considered as a starting point. In order to demonstrate the general character of the 2 layer earth, a suite of responses for various values of d and a perfectly reflecting substratum obtained with the scale model and computed theoretically using both the normal mode and geometrical optics solution are shown in Fig. 7. The layer thickness ranges from 0.5w to 7. The E_ϕ field strengths in decibels are plotted versus transmitter receiver separation in free-space wavelengths along the B profile. The scale model response is shown along with the mode and geometrical optics solution. The geometrical optics curve is shifted upward from the

experimental curve while the mode solution is shifted downward. This offset of the curves is used to minimize the overlap of the various responses which tends to confuse the visual presentation of the data.

The results in Fig. 7 span most of the important depth ranges and demonstrate most of the features of the 2 layer response. For the shallow depths of 0.5w, 1.0w, and 1.5w, the fields are expressible in terms of one, two, or three guided modes plus the lateral and inhomogeneous waves given by branch line contributions (see Appendix). The fields decay with distance as $(1/r)^{1/2}$ and exhibit a regular beating as the modes move in and out of phase. For d = 0.5w, only one mode is guided and the only interference occurs near the source where the branchline and modal contributions are comparable in magnitude. The remainder of the infinite sequence of modes are either not excited or are leaky modes which decay exponentially with distance from the transmitter. As the depth increases more and more modes move into the guided regime and the field strength versus distance becomes more complicated as the various modes move in and out of phase.

Examination of the theoretical responses show that the geometrical optics solution and the model response are in good agreement for layer thicknesses greater than 3.0w. For shallower depths, the experimental and theoretical

responses diverge from one another. The breakdown in the geometrical optics solution is to be expected from its asymptotic nature. The normal mode solution, however, shows excellent agreement at the shallow depths and becomes the same as the geometrical optics solution at the larger depths.

(c) Thin Layers and Critical Depths

The preceding discussion of the 2-layer earth with a perfectly reflecting substratum illustrates the general nature of the response. At very shallow depths and at various critical depths, the response changes quite drastically with layer thickness. A suite of curves for depths $d < 0.2w$ to $d > 0.8w$ at various depth increments in wavelengths show this behaviour clearly. The critical depths for the electrical properties model are given by $d_c = 0.23\,(2n + 1)\,\lambda$ (TE modes) and $d_c = 0.46n\,\lambda$ (TM modes), $n = 0, 1, 2 \ldots$ (see Appendix). For $d < 0.23$, (E_ϕ is composed of TE modes only on B profile), no normal modes are excited since the layer is too thin. As a result, the fields versus distance are described totally by the branchline integrals and fall off as $(1/r)^2$. As d increases past 0.23 the first normal mode moves into the guided regime and the field strength versus distance falls off as $(1/r)^{1/2}$. The field strength versus distance varies only slightly with depth changes until $d \rightarrow 0.69$.

As $d \to 0.69$, the field strength versus distance begins to show a weak beating. For d just greater than 0.69 , the fields show very deep interference nulls at regular spacing. Two guided modes (TE) are now propagating in the layer for $0.69 < d < 1.16$, the profiles exhibit the regular beating; however, the maxima and minima locations are very sensitive to the layer thickness. As $d \to 1.16$, the same behaviour as $d \to 0.69$ is seen and a third normal mode moves from the leaky to the guided regime. (see Appendix.)

The theoretical reponses computed by the normal mode method are shown along with experimental results. The mode solutions match the experiment results very well except at the critical depths. At the critical depths, two poles and a branch point merge together in the mathematical solution. The branchline contribution is evaluated approximately by steepest descent integration; the approximate solution fails at the critical depths. The results of evaluating the branchline contribution by numerical integration are also shown on the profiles. The agreement between experiment and theory is much better at the critical depths with this improvement.

(d) 2 Layer Earth; Dielectric Substratum

The response of a dielecric substratum is not greatly different from the previous responses for a perfectly reflecting substratum. The major difference is that there

are no longer any unattended guided modes; all the modes are leaky since energy can always leak out of the layer into the substratum. As a result, the field shows the same basic behaviour but all responses have a strong attenuation with distance from the Tx.

The data collected with the scale model experiment are shown in Fig. 9. The experimental results are presented along with the theoretically (normal mode) computed responses. The results compare extremely well. (It should be noted that when the experimental field strength falls below the Rx sensitivity the field strength levels off at a constant value. This is noticeable at large distances from the Tx in all the dielectric bottom responses.) The normal modes no longer have a sharp onset as they do for a perfectly reflecting substratum. The modes now move from a very leaky regime to a much less leaky regime with no sharp dividing line present. This improves the accuracy of the theoretical solution since there are no true critical depths and the mathematical approximations in evaluating branchline contributions are greatly improved.

Summary and Conclusions

The results of theoretical and experimental work have led to a clear understanding of the physical mechanisms of wave propagation in a 2 layered dielectric earth. This detailed

understanding of the waves propagations in such a system is necessary for the interpretation of radio interferometry data from geologic environments which can be simulated by a 2 layer model.

The practical aspects and limitations of constructing scale model experiments at GHz. frequencies are well understood and the reliability of the model makes it an ideal method of examining problems which are not tractable from a theoretical point of view. With such excellent agreement between theory and experiments, the model can be applied analysing more complex problems with confidence.

The scale model has proved to be invaluable in checking out the computer programs which generate the theoretical responses. The mathematical formalism is very complex and its translation into a computational format is difficult; particularly when approximations are made in certain parts of the analysis.

The normal mode approach to analysing moderately to very thin layers has greatly improved the ability to interpret layered structures. The initial analysis of responses was made using the geometrical optics solutions which is invalid for thin layers. The model study confirming the mode analysis has already le to successful interpretation of radio interferometry data obtained in thin layer environments (Rossiter et al. ( ) see accompanying paper).

Appendix

TE and TM Mode Critical Depths for a 2-Layer Earth

The radial wave numbers of the normal modes of a plane stratified 2 layer earth are obtained by solving the transcendental equations

$$\text{TE Mode} \quad 1 - R_+^{TE} \; R_-^{TE} \; e^{j2\pi d\gamma_1} = 0 \qquad \text{A-1}$$

$$\text{TM Mode} \quad 1 - R_+^{TM} \; R_-^{TM} \; e^{j2\pi d\gamma_1} = 0 \qquad \text{A-2}$$

The $R_\pm$ are the Fresnel reflection coefficients indicated in Fig. A(a) and $\gamma_1 = (K_1-\lambda^2)^{1/2}$ is the vertical component of the wave vector in the layer. For the dielectric media discussed here

$$R_\pm^{TE} = \frac{\gamma_1 - \gamma_{1\pm1}}{\gamma_1 + \gamma_{1\pm1}} \qquad R_\pm^{TM} = \frac{\frac{K_1}{\gamma_1} - \frac{K_{1\pm1}}{\gamma_{1\pm1}}}{\frac{K_1}{\gamma_1} + \frac{K_{1\pm1}}{\gamma_{1\pm1}}} \qquad \text{A-3}$$

In general the λ_p^{TE} and λ_p^{TM} are complex and A-1 and A-2 have no pure real solutions. Only totally real λ_p^{TE} yield modes which are unattenuated radially.

True guided modes exist only when $|R+| = |R-| = 1$ which physically occurs only when the media are lossfree and region 1 is a low velocity region (i.e. $K_1 > K_0$ and K_2) and d is greater than a minimum critical thickness. Analysis of equations A-1 and A-2 in the complex λ plane show that the λ_p^{TE} must lie along a line which intertwines the various Riemann

surfaces defined by the branchlines of the $(K_i^* - \lambda^2)^{1/2}$ functions. The case of a perfectly dielectric slab ($\tan \delta_1 \equiv 0$) overlying a perfectly reflecting ($\tan \delta_2 = \infty$) substratum is sketched in Fig. A(b). The roots of the transcendental equation lie on the line indicated in A(b). The solid circles denote roots on the upper Riemann surface ($+ (K_i^* - \lambda^2)^{1/2}$ for branchlines shown) which are excited modes and the open circles indicate roots on the lower Riemann surfaces (any combination of signs for $(K_i^* - \lambda)^{1/2}$ other than +). The poles on the real axis between $\sqrt{K_0^*}$ and $\sqrt{K_1^*}$ are guided unattenuated modes while the poles $\lambda_p < \sqrt{K_0^*}$ are leaky modes and have a positive imaginary component.

The behaviour of the λ_p^{TE} λ_p^{TM} with variations in d is twofold; the poles λ_p^{TE} λ_p^{TM} move down the contours and are more closely packed as d increases and the contour, on which the poles lie, swings towards the imaginary axis. As the depth varies, a pair of the poles coincide with the $\sqrt{K_0^*}$ branchpoint at regular depth spacings. These depths are the critical depths for the modes and mark the depth where a mode moves from the leaky to the unattenuated or guided regime.

The critical depths for the case of the perfectly reflecting substratum are obtained by noting that

$$R_-^{TE} = R_-^{TM} = -1 \qquad \text{A-4}$$

and that for $\lambda = \sqrt{K_0}$,

$$R_+^{TE} = 1 \qquad R_+^{TM} = -1 \qquad \text{A-5}$$

Substituting into A-1 and 2 yields.

$$ {}^{TE}d_c^n = \frac{2n+1}{4(K_0-1)^{1/2}} W \qquad n = 0, 1, 2, \cdots\cdots \qquad \text{A-6} $$

$$ {}^{TM}d_c^n = \frac{n}{4(K_1-1)^{1/2}} W $$

For finite loss tangents, and a dielectric bottom, the contours on which λ_p lie still pass through $\sqrt{K_1}$ but are displaced away from the real λ axis between $\sqrt{K_0}$ and $\sqrt{K_1}$ so that all modes have a finite imaginary component which corresponds to attenuation with distance.

Acknowledgements

This research has been supported by NASA grant no. NAS 9-11540 for model construction and collection of model data and by the Canadian Department of Energy, Mines and Resources grant no. 1135- D 13-4-16/73 for analysis and preparation of this manuscript. We wish to thank Mr. J. Proctor for his able assistance in the computational aspects of this work.

Bibliography

Annan, A.P., 1973, Radio Interferometry Depth Sounding: Part I - Theoretical Discussion, Geophysics, v. 30, no. 3, p. 557-580.

Annan, A.P., 1970, Radio Interferometry Depth Sounding, M.Sc. Thesis, University of Toronto, Toronto, Ontario, Canada.

Brekhovskikh, L.M., 1960, Waves in Layered Media: New York, Academic Press.

Cooper, W.W., 1971, Patterns of Dipole Antenna on Stratified Medium, Technical Report TR71-3, MIT Centre for Space Research.

Katsube, T.J., and Collett, L.S., 1971, Electrical properties of Apollo 11 and 12 lunar samples, in Proceedings of the Second Lunar Science Conference, Houston, Texas, edited by A.A. Levinson: Cambridge, Mass. Inst. Tech.

Olhoeft, G.R., Strangway, D.W., and Frisillo, A.L. , 1973, Lunar Sample Electrical Properties, Proc. Fourth Lunar Sci. Conf., (Suppl. 4, Geochim. Cosmochim. Acta), v. 3, p. 3133-3149.

Rossiter, S.R., LaTorraca, G.A., Annan, A.P., Strangway, D.W., and Simmons, G., 1973, Radio Interferometry Depth Sounding, Part II - Experimental Results, Geophysics, v. 38, no. 3, p. 581-599.

Rossiter, J.R., Strangway, D.W., Annan, A.P., Watts, R.D., and Redman, J.D., Detection of Thin Layers by Radio Interferometry, submitted to Geophysics, 1974.

Simmons, G., Strangway, D.W., Bannister, L., Baker, R., Cubley, D., LaTorraca, G., and Watts, R., 1972, The Surface Electrical Properties Experiment, in Kopal, Z. and Strangway, D., eds., Lunar Geophysics, Proceedings of a Conference at the Lunar Science Institute, Houston, Texas, 18-21, October, 1971, D. Reidel, Dor drecht, p. 258-271.

Strangway, D.W., Simmons, G., LaTorraca, G.A., Watts, R.D., Bannister, L., Baker, R., Redman, J.D., Rossiter, J.R., 1974, Radio-Frequency Interferometry - A New Technique for Studying Glaciers, J. of Glaciology, in press.

Tsang, L., Kong, J.A., and Simmons, G., Interference Patterns of a Horizontal Electric Dipole over Layered Dielectric Media, J. Geophys. Res., v. 78, pp. 3287-3300, 1973.

Wait, J.R., 1970, Electromagnetic Waves in Stratified Media, 2nd Edition: New York, The Macmillan Co.

Waller, W.M., 1973, Surface Electrical Properties of Simulation Model, Lockheed Electronics Co. Final Report. LEC/PESD 634-TR-139 for contract NAS 9-122200, NASA-JSC, Houston, 1973.

Figure Captions

Fig. 1. Sketch of 2-layer earth geometry and the associated cartesian and cylindrical coordinate systems.

Fig. 2 Complex radial wavenumber plane illustrating integration contours and location of singular points;

◆ branch points
o TE pole, lower Riemann surface
● TE pole, upper Riemann Surface
△ TM pole, lower Riemann surface
▲ TM pole, upper Riemann surface

Fig. 3 Schematic drawing of scale model 2-layer earth.

Fig. 4 Schematic diagram of scale model electronics, display and recording system.

Fig. 5 (a) sketch of radiation pattern for $|E_\phi|$ in X_2-X_3 plane in a whole-space,
(b) sketch of radiation pattern for $|E_\phi|$ in X_2-X_3 plane for dipole on surface of a half-space.

Fig. 6 Scale model experimental measurements of (E_ϕ) pattern in X_2-X_3 plane compared with the theoretical pattern computed by Cooper (1971).

Fig. 7 Suite of 2-layer earth responses where the substratum is a perfect reflector; —scale model response, ------normal mode theoretical response, ····· geometrical optics theoretical response.

Fig. 8 Suite of 2-layer earth responses for a perfectly reflecting substratum and shallow reflector depths. —— scale model response ----- normal mode theoretical response.

Fig. 9 Suite of 2-layer earth responses for a dielectric substratum.

Fig. A (a) Sketch of multiple reflections in thin layer.
(b) Illustration of pole positions in complex λ plane as a function of d.

Table Captions

Table 1: Cylindrical components of the E and H fields about a Horizontal Electric Dipole (HED) on the surface of a 2-layer earth in Hankel transform notation.

Table 1

(a)

$$E_\rho = \int_0^\infty \left\{ E_\rho^{TM} J_1'(\lambda\rho) + E_\rho^{TE} J_1(\lambda\rho) \right\} d\lambda$$

$$E_\varphi = \int_0^\infty \left\{ E_\varphi^{TM} J_1'(\lambda\rho) + E_\varphi^{TE} J_1'(\lambda\rho) \right\} d\lambda$$

$$E_z = \int_0^\infty E_z^{TM} J_1(\lambda\rho)\, d\lambda$$

$$H_\rho = \int_0^\infty \left\{ H_\rho^{TM} J_1(\lambda\rho) + H_\rho^{TE} J_1'(\lambda\rho) \right\} d\lambda$$

$$H_\varphi = \int_0^\infty \left\{ H_\varphi^{TM} J_1'(\lambda\rho) + H_\varphi^{TE} J_1(\lambda\rho) \right\} d\lambda$$

$$H_z = \int_0^\infty H_z^{TE} J_1(\lambda\rho)\, d\lambda$$

$$J_1'(z) = \frac{\partial J_1(z)}{\partial z}$$

(b)

	TE	TM
E_ρ	$-j\frac{\omega\mu_0 I\,dl}{4\pi}\frac{\cos\varphi}{j\gamma_0\rho}\left[e^{\pm j\gamma_0(z-h)} + R^{TE}e^{j\gamma_0(z+h)}\right]$	$j\frac{\omega\mu_0 I\,dl}{4\pi k_0^2}\cos\varphi\, j\gamma_0\lambda\left[e^{\pm j\gamma_0(z-h)} - R^{TM}e^{j\gamma_0(z+h)}\right]$
E_φ	$j\frac{\omega\mu_0 I\,dl}{4\pi}\frac{\sin\varphi\,\lambda}{j\gamma_0}\left[e^{\pm j\gamma_0(z-h)} + R^{TE}e^{j\gamma_0(z+h)}\right]$	$j\frac{\omega\mu_0 I\,dl}{4\pi k_0^2}\sin\varphi\left(-\frac{\gamma_0}{\rho\omega}\right)\left[e^{\pm j\gamma_0(z-h)} - R^{TM}e^{j\gamma_0(z+h)}\right]$
E_z	0	$j\frac{\omega\mu_0 I\,dl}{4\pi k_0^2}\cos\varphi\;\lambda^2\left[\pm e^{\pm j\gamma_0(z-h)} - R^{TM}e^{j\gamma_0(z+h)}\right]$
H_ρ	$-\frac{I\,dl}{4\pi\omega^2}\sin\varphi\,\lambda\left[\pm e^{\pm j\gamma_0(z-h)} + R^{TE}e^{j\gamma_0(z+h)}\right]$	$-\frac{I\,dl}{4\pi\omega^2}\frac{\sin\varphi}{\rho}\left[\pm e^{\pm j\gamma_0(z-h)} - R^{TM}e^{j\gamma_0(z+h)}\right]$
H_φ	$-\frac{I\,dl}{4\pi}\frac{\cos\varphi}{\rho\omega^2}\left[\pm e^{\pm j\gamma_0(z-h)} + R^{TE}e^{j\gamma_0(z+h)}\right]$	$-\frac{I\,dl}{4\pi\omega^2}\cos\varphi\,\lambda\left[\pm e^{\pm j\gamma_0(z-h)} - R^{TM}e^{j\gamma_0(z+h)}\right]$
H_z	$-\frac{I\,dl\sin\varphi}{4\pi\omega^2}\frac{\lambda^2}{j\gamma_0}\left[e^{\pm j\gamma_0(z-h)} + R^{TE}e^{j\gamma_0(z+h)}\right]$	0

$$\pm = \text{sign}(z-h)$$

(c) Parameters

λ Radial wavenumber

γ_i Vertical wavenumber in region i $= (K_i^* - \lambda^2)^{1/2}$ 2π

$K_i^* = K_i (1 + j \tan\delta_i)$ complex dielectric constant

$k_i = 2\pi (K_i^*)^{1/2} \simeq (K_i)^{1/2} (1 + j \frac{\tan\delta_i}{2})$ normalized propagation constant in region i

w = free space wavelength

h = elevation of dipole above surface in wavelengths

(d) TE and TM Reflection and Transmission Coefficients at Plane Boundaries

$$R_{ij}^{TE} = \frac{\gamma_i - \gamma_j}{\gamma_i + \gamma_j} \qquad R_{ij}^{TM} = \frac{K_i^* \gamma_j - K_j^* \gamma_i}{K_i^* \gamma_j + K_j^* \gamma_i}$$

$$T_{ij}^{TE} = 1 + R_{ij}^{TE} \qquad T_{ij}^{TM} = 1 + R_{ij}^{TM}$$

(e) 2 layer Earth Reflection Coefficient

$$R^{TE}_{TM} = R^{TE}_{TM\,01} + \frac{T^{TE}_{TM\,01}\, T^{TE}_{TM\,10}\, R^{TE}_{TM\,12}\, \beta}{1 - R^{TE}_{TM\,10}\, R^{TE}_{TM\,12}\, \beta}$$

$\beta = e^{j\gamma_1 d}$ 2 way phase shift in layer

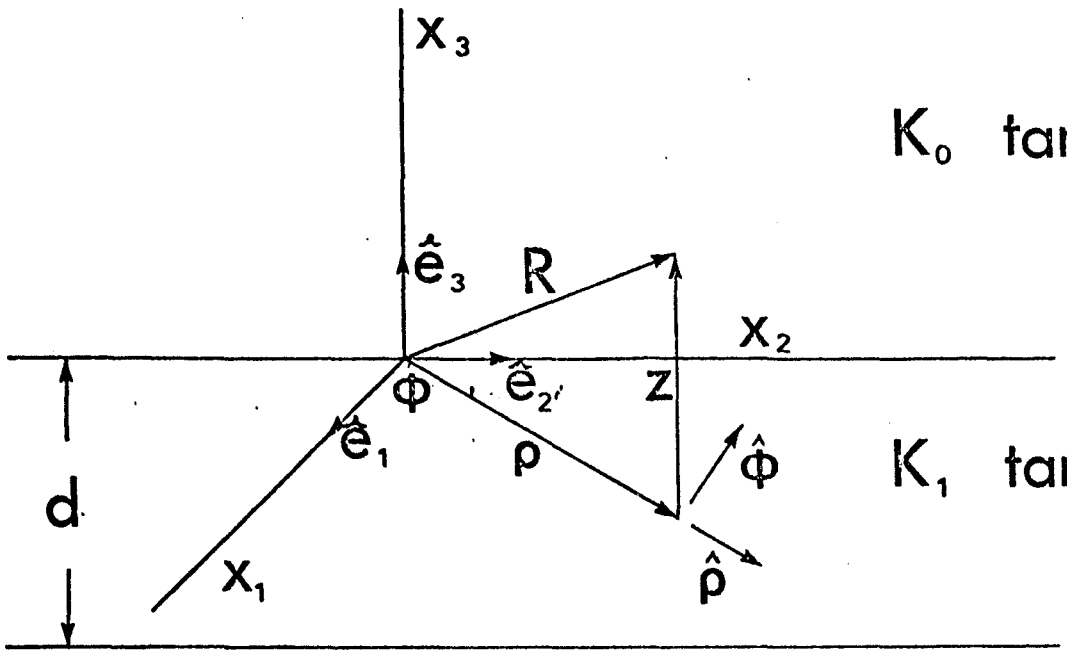

$K_0 \tan \delta_0$

$K_1 \tan \delta_1$

$K_2 \tan \delta_2$

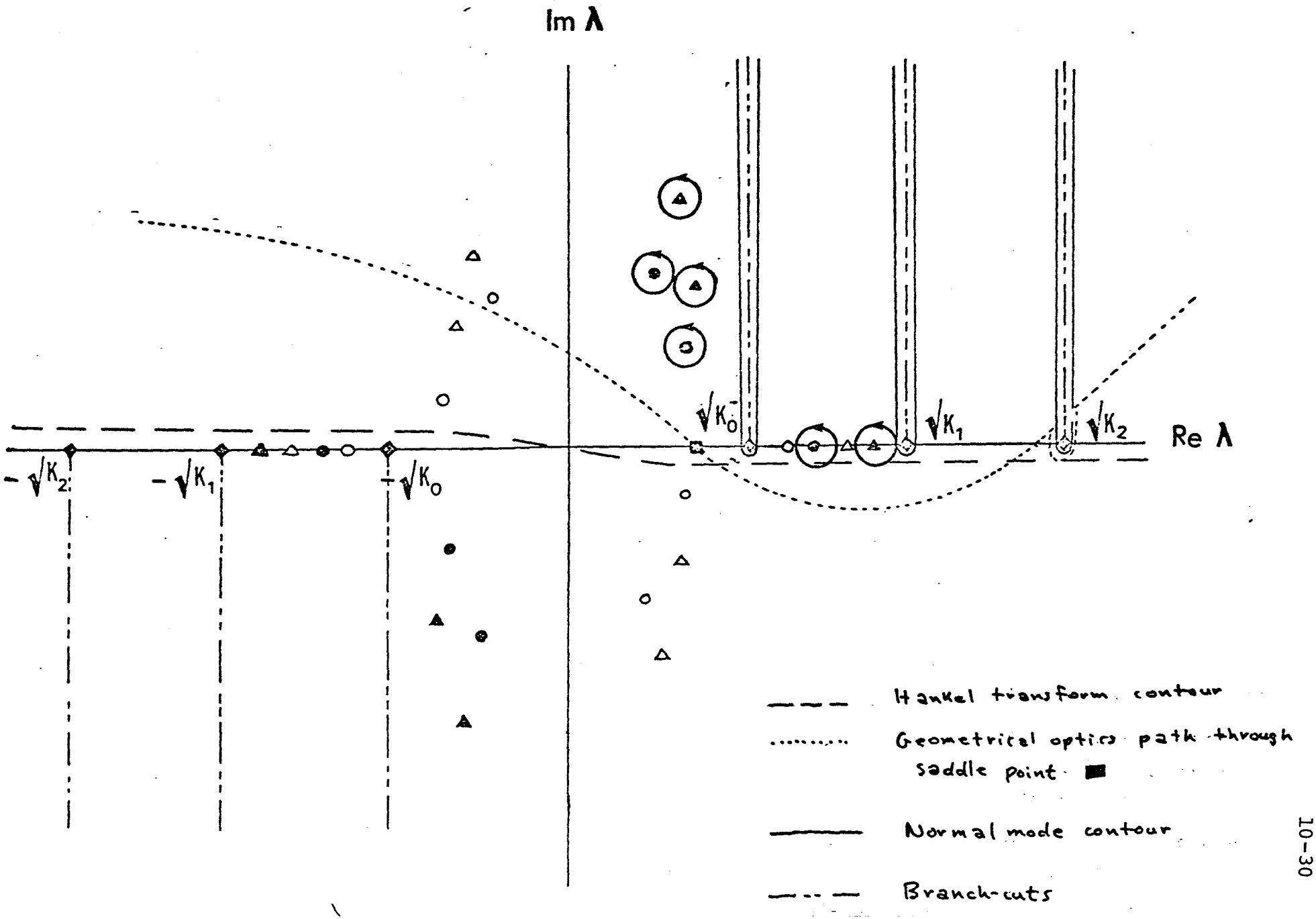
Im λ
Re λ
$\sqrt{K_0}$
$\sqrt{K_1}$
$\sqrt{K_2}$
$-\sqrt{K_2}$
$-\sqrt{K_1}$
$-\sqrt{K_0}$
Hankel transform contour
Geometrical optics path through saddle point
Normal mode contour
Branch-cuts

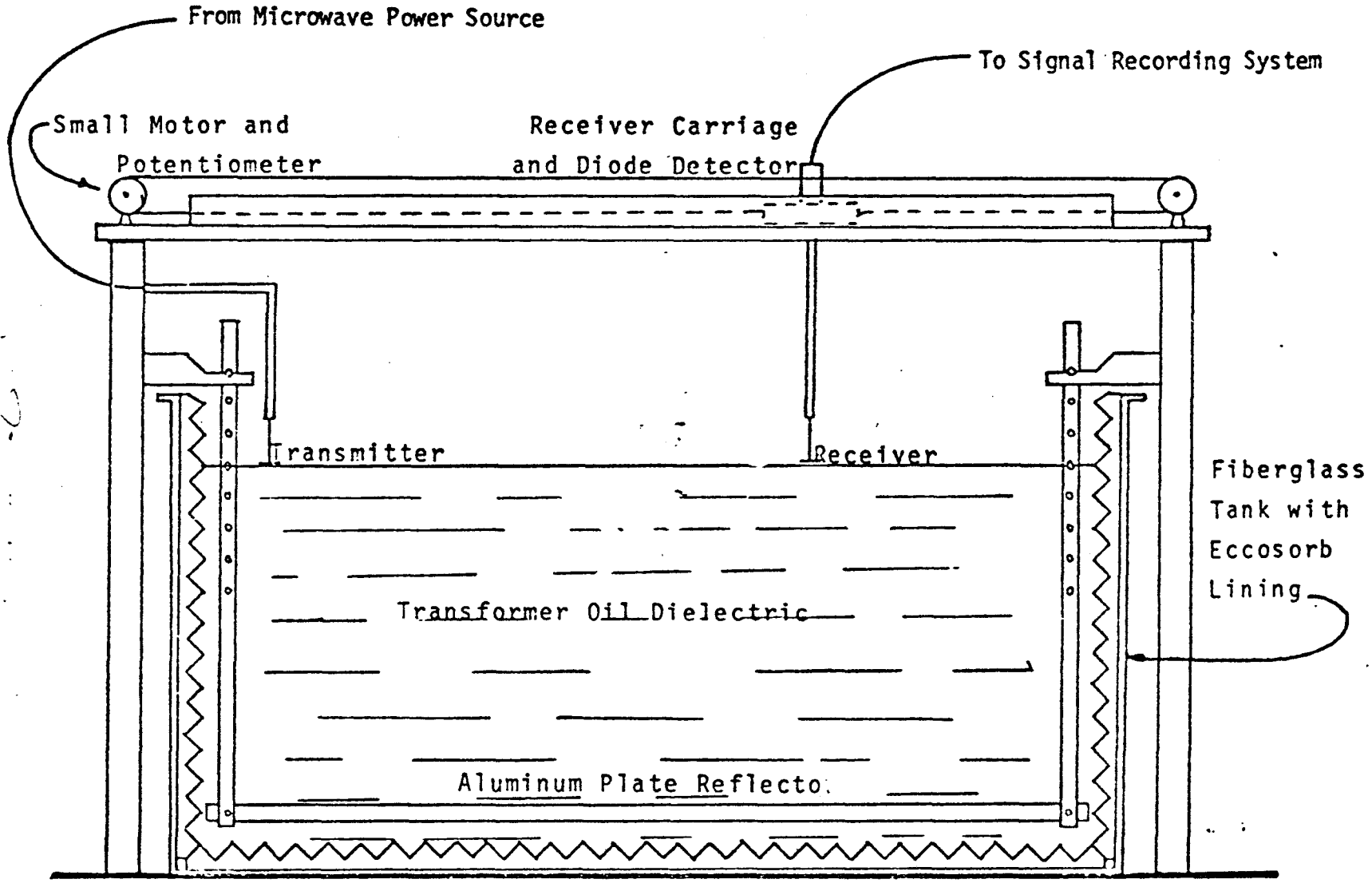
From Microwave Power Source
To Signal Recording System
Small Motor and
Potentiometer
Receiver Carriage
and Diode Detector
Transmitter
Receiver
Fiberglass
Tank with
Eccosorb
Lining
Transformer Oil Dielectric
Aluminum Plate Reflecto

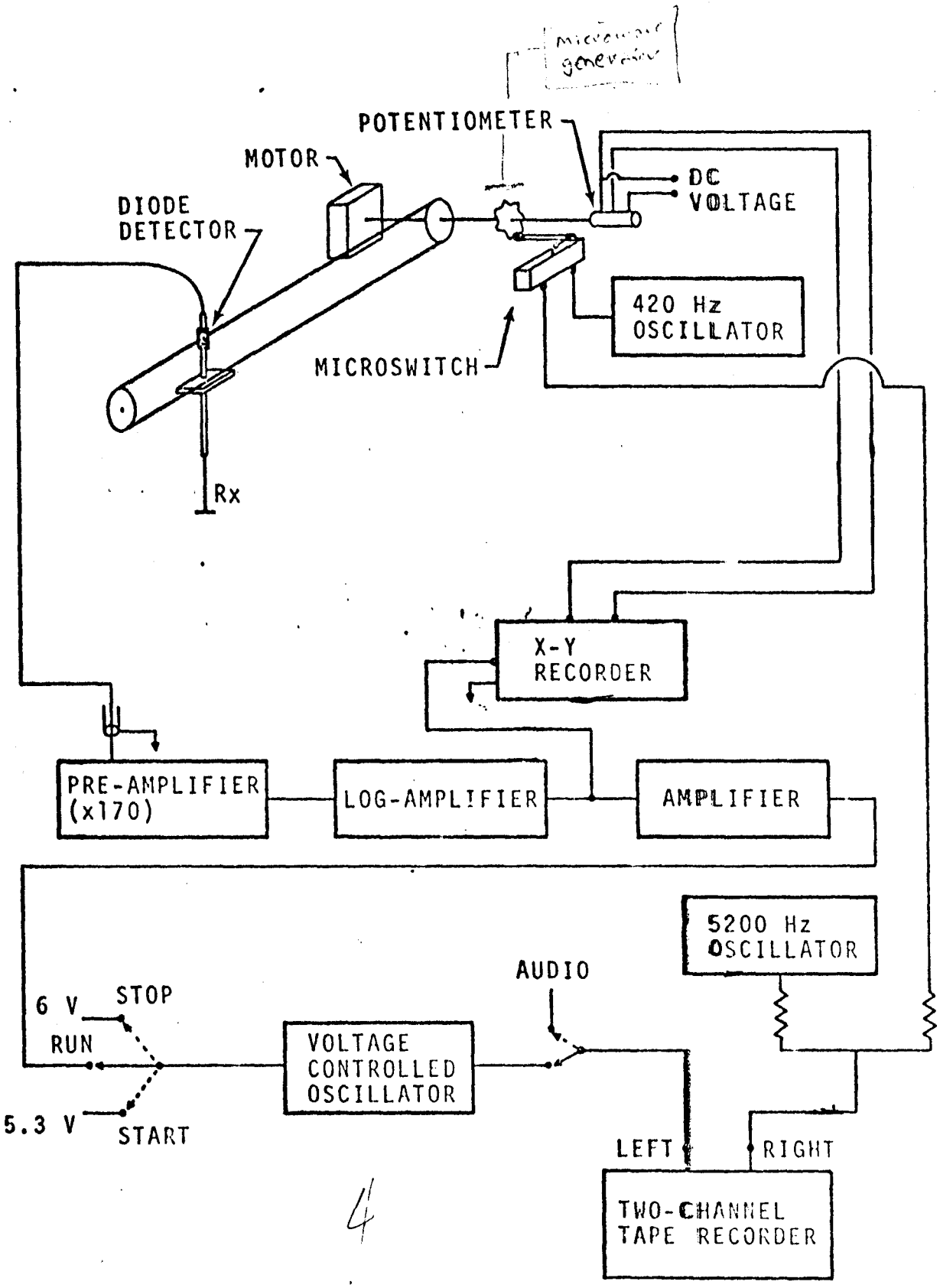
POTENTIOMETER
MOTOR
DIODE DETECTOR
DC VOLTAGE
420 Hz OSCILLATOR
MICROSWITCH
Rx
X-Y RECORDER
PRE-AMPLIFIER (x170)
LOG-AMPLIFIER
AMPLIFIER
5200 Hz OSCILLATOR
AUDIO
6 V
STOP
RUN
5.3 V
START
VOLTAGE CONTROLLED OSCILLATOR
LEFT
RIGHT
TWO-CHANNEL TAPE RECORDER

4

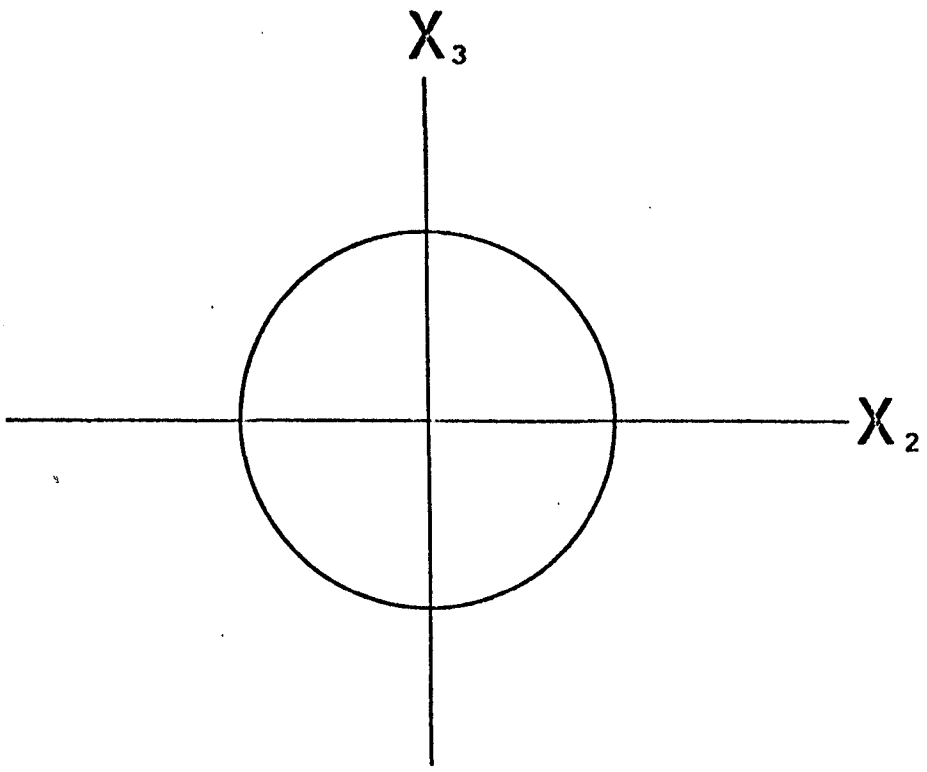

(a)

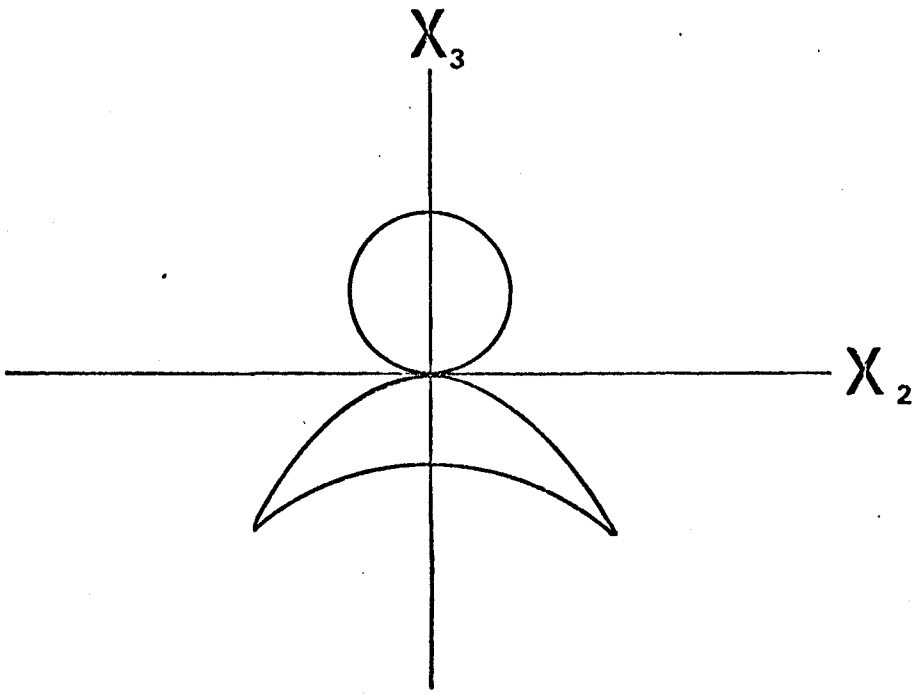

(b)

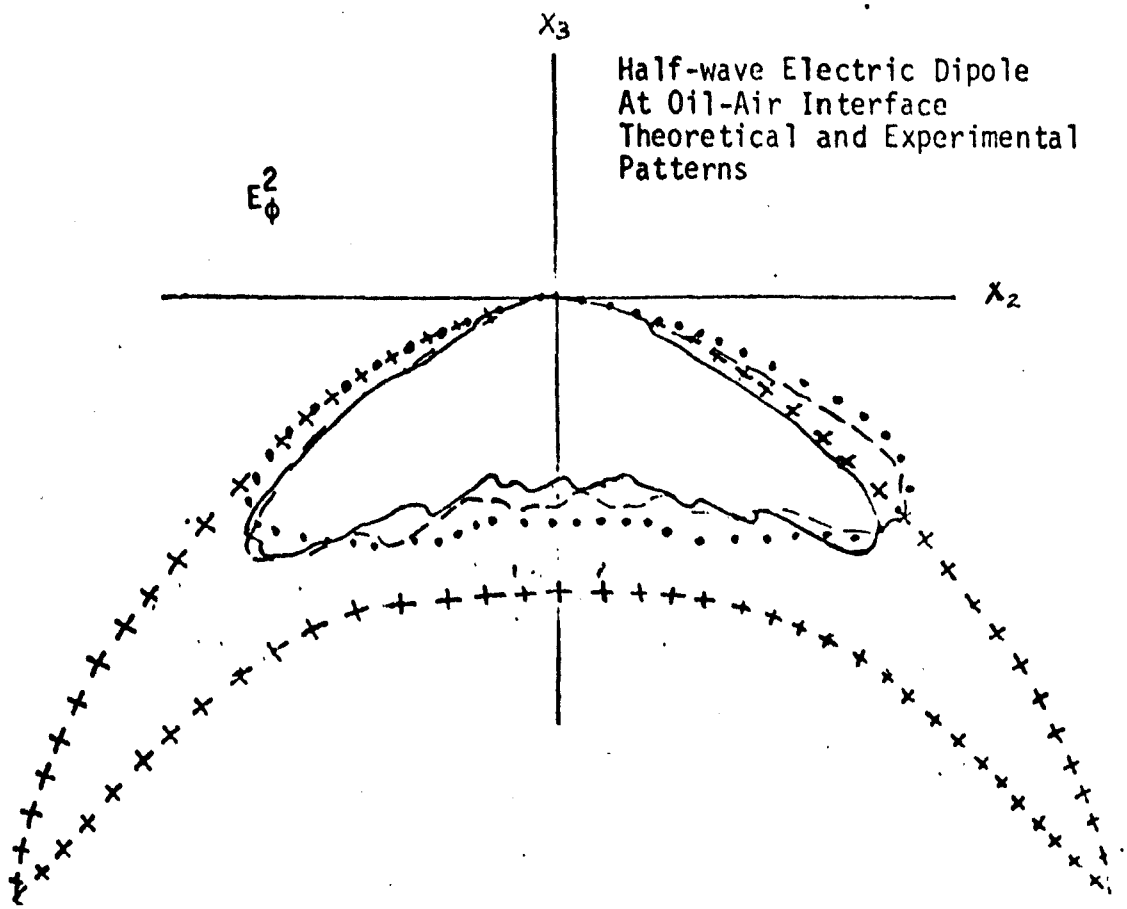

+++ Cooper--K'=2.16..... 43°

Experimental
—— 6λ radius.....~52°
--- 4.5λ radius.....~54°
••• 3λ radius.....~57°

Figure 6 — Antenna pattern at various radii.

THEORETICAL SOLUTIONS AND SCALE - MODEL RESULTS

PLANE LAYERED GEOMETRY, VARIOUS DEPTHS TO REFLECTOR

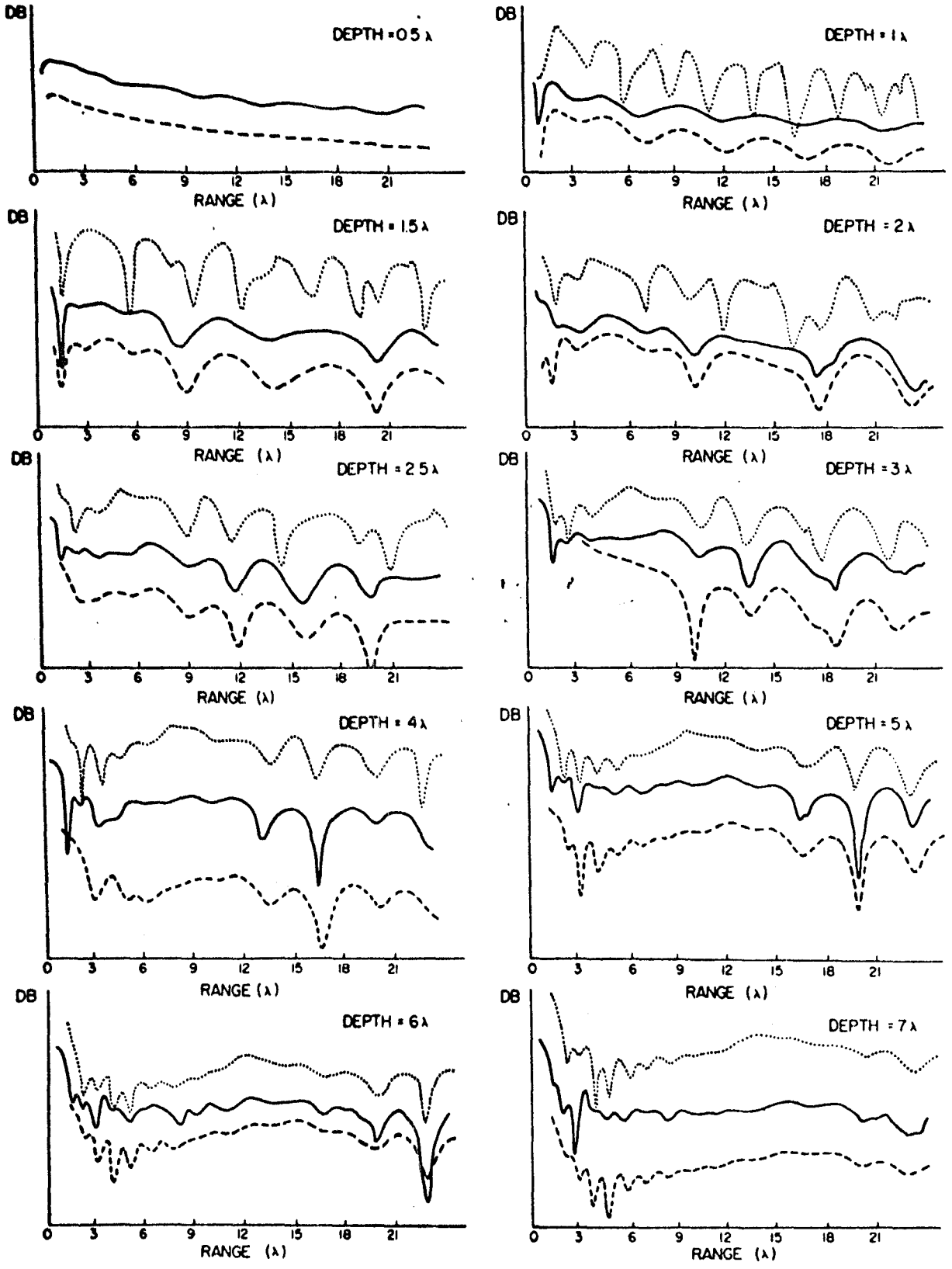

Fig. 7

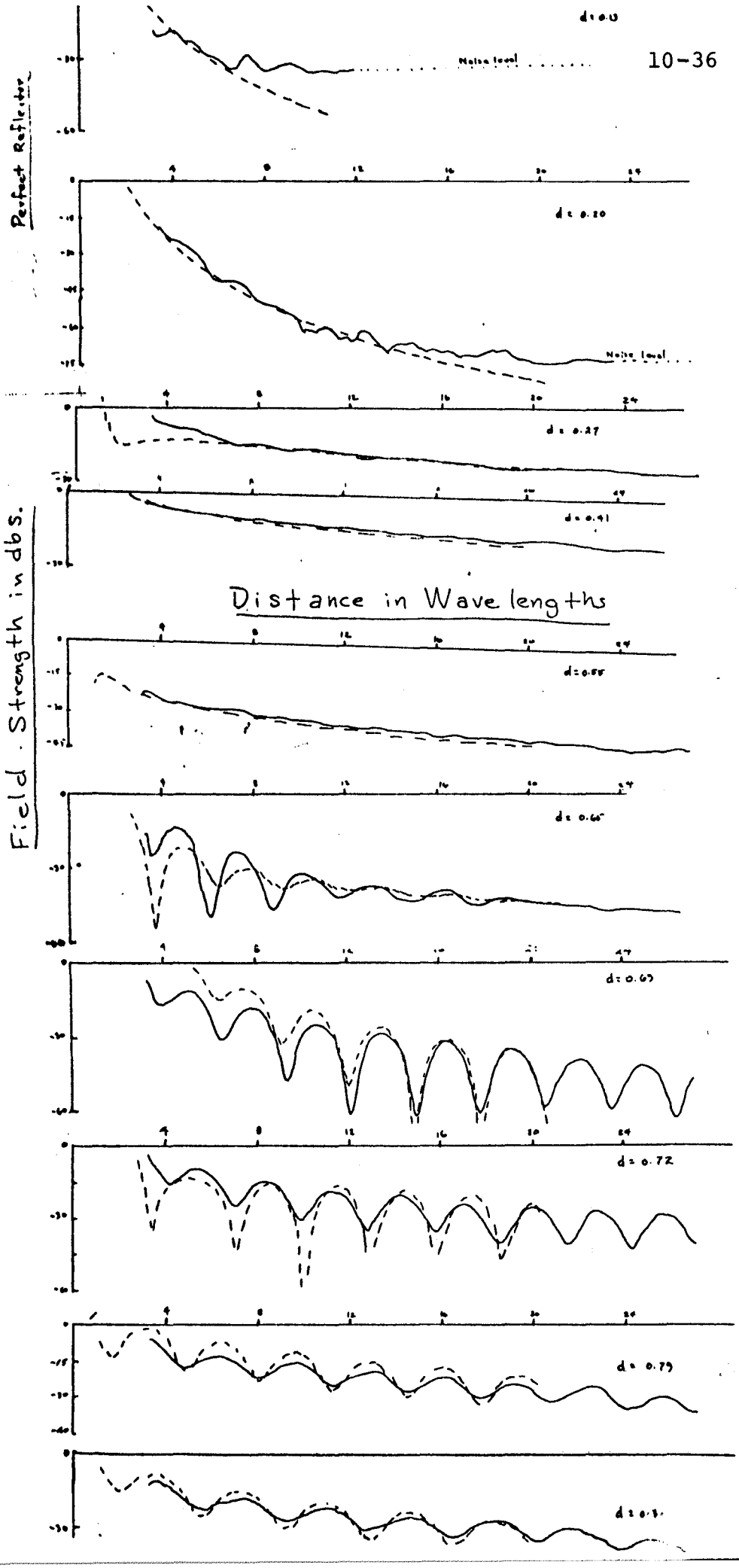
Perfect Reflector
Field Strength in dbs.
Distance in Wave lengths
Noise level
d = 0.20
d = 0.27
d = 0.41
d = 0.55
d = 0.67
d = 0.72
d = 0.79

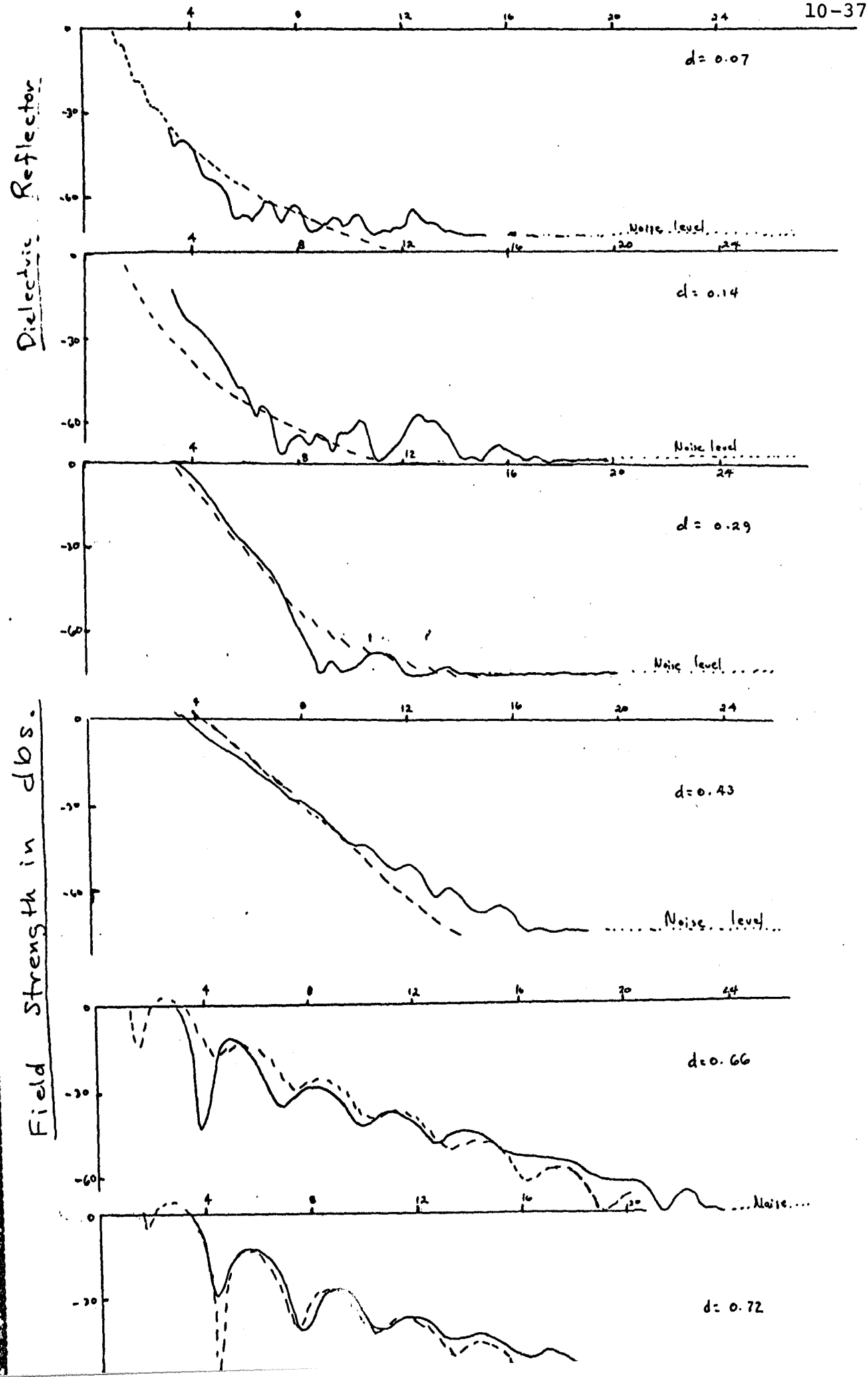
Dielectric Reflector
Field Strength in dbs.
d = 0.07
Noise level
d = 0.14
Noise level
d = 0.29
Noise level
d = 0.43
Noise level
d = 0.66
Noise
d = 0.72

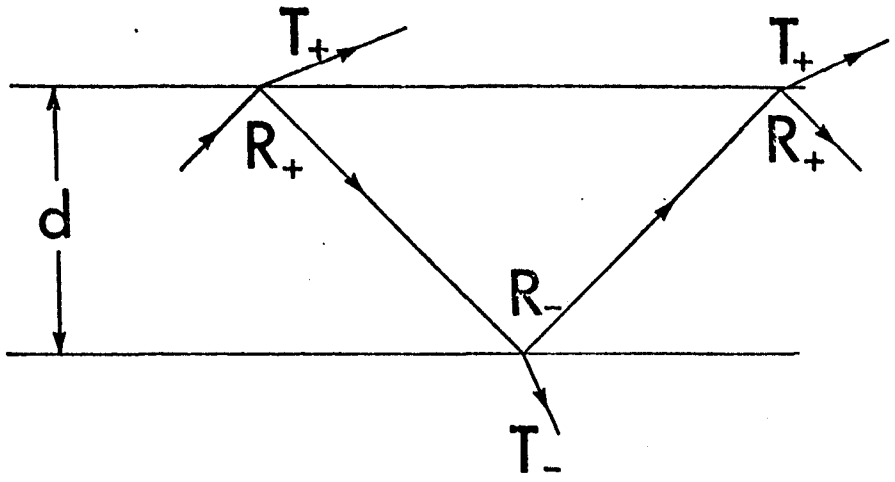
T+
T+
R+
R+
d
R-
T-

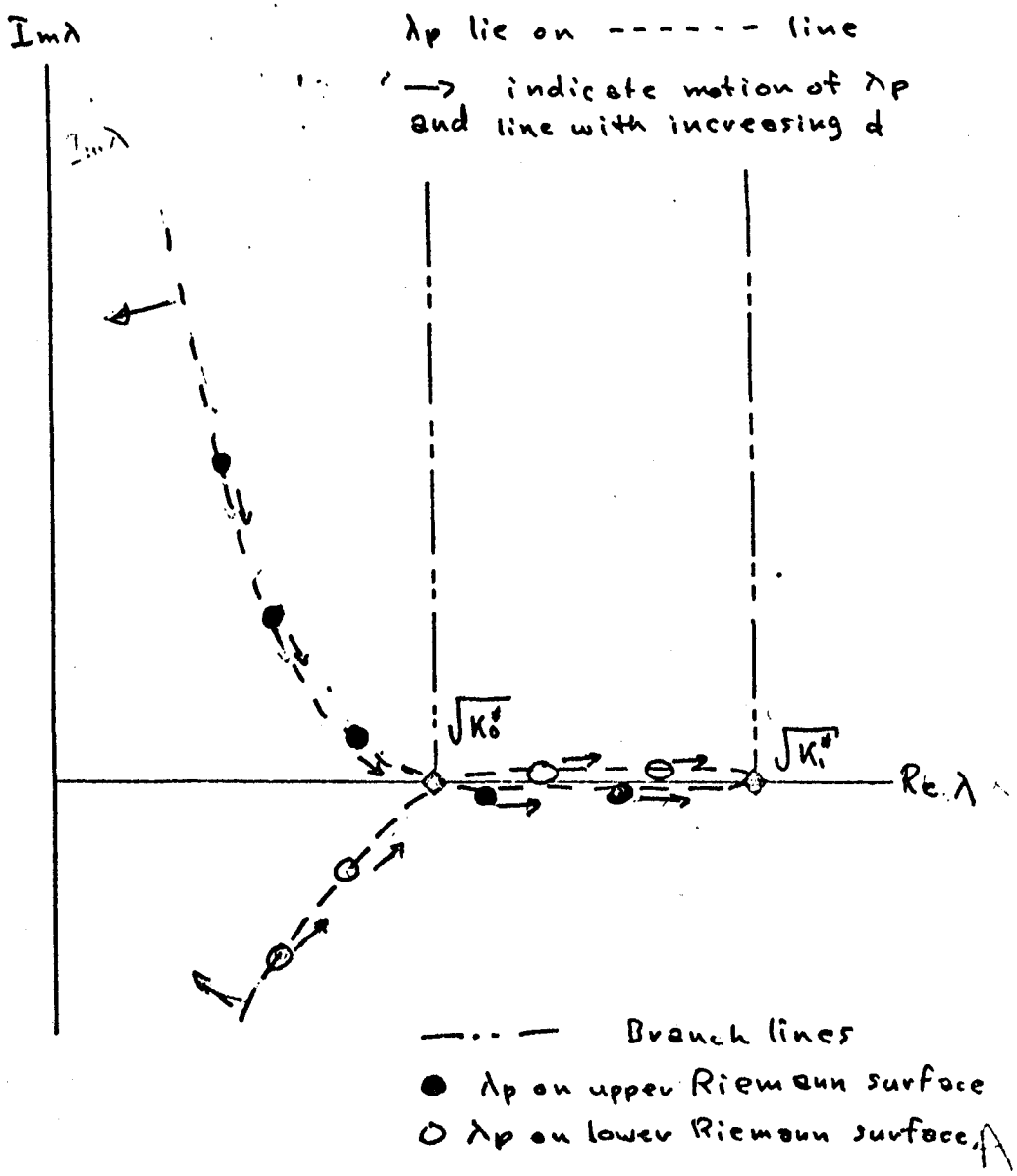
Im λ
λp lie on ------ line
→ indicate motion of λp and line with increasing d
√K0'
√K1''
Re λ
—·· — Branch lines
● λp on upper Riemann surface
○ λp on lower Riemann surface

DETECTION OF THIN LAYERS BY RADIO INTERFEROMETRY

J.R.Rossiter[1], D.W.Strangway[2], A.P.Annan[1]
R.D.Watts,[3] and J.D.Redman[2].

1. Department of Physics
University of Toronto
Toronto, M5S 1A7
Canada

2. Department of Geology,
University of Toronto,
Toronto, M5S 1A1
Canada

3. Presently at U.S.G.S.
Denver, Colorado, U.S.A.

February 22, 1974

ABSTRACT

Recent theoretical work on the radio interferometry technique for dielectric layers of less than one free space wavelength thick, has indicated that there is a thickness for which no interference is observed. This thickness is about 0.2 wavelengths for ice, and it lies between the thickness that allows one single mode to propagate in the layer ($\gtrsim 0.2$) and a thickness ($\lesssim 0.2$) that is essentially transparent to the wavelength being used.

Field work was done on the Juneau Icefield using frequencies from 1 to 32 MHz. At 1 and 2 MHz, an interference pattern typical of a half space of ice (dielectric constant of 3.3) is observed, while at 4 MHz essentially no interference is seen. At higher frequencies, the interference observed is typical of that of a layer overlying a half space. These results can be interpreted to be the result of a dielectric layer of depth 15 to 20 m (0.2 wavelengths at 4 MHz) with a dielectric constant of 2.4. The layer of snow overlies a half space of ice. The technique is therefore of potential interest in interpreting the nature of a snow layer overlying a glacier.

INTRODUCTION

Radio frequency interferometry depth sounding was originally developed to measure the dielectric properties and structure of highly resistive geological regions (Annan, 1970, 1973). It has been used successfully for sounding glaciers (Rossiter et al., 1973; Strangway et al., 1974), and on the moon (Simmons et al., 1972; SEP Team, 1974). The technique consists of setting a radio transmitter on the surface to be sounded, and measuring the field strength as a function of distance from the transmitter. Several waves propagate from the transmitter to the receiver, generating an interference pattern that is indicative of both the dielectric properties and the structure of the medium.

Theoretical studies have determined the fields to be expected over dielectric layers (Annan, 1973; Kong, 1972, Tsang et al.,1973). Early work used geometrical optics approximations in order to evaluate the integral expressions, but it can be shown that the method is highly inaccurate for layers less than about 2 free space wavelengths (abbreviated "wl" throughout) thick. In more recent work, a normal model approximation has been used that is particularly suitable for calculating the fields in the presence of a thin layer. In a companion paper (Annan et al.,1974), theoretical and experimental data from an analogue scale model are compared. In the present paper, we will examine the particular case of a thin dielectric layer (0 to 1 wl thick) overlying a thick dielectric layer (see Fig.1), using mode theory and field data collected on the Juneau Icefields, Alaska.

THEORY OF THIN LAYERS

Radio interferometry data show three distinct types of behaviour as the upper layer increases from being very thin and transparent, through a critical thickness, to being thick enough to allow propagating modes. We will examine each of these three cases.

(a) Very thin transparent upper layer

When the upper layer is very thin (less than about 0.2 wl thick), it is essentially transparent. Therefore, the observed interference pattern is independent of the properties of the upper layer, and looks like that of a half space with the properties of the lower layer (see Figures 2 and 3).

(b) Transition thickness - decoupled layer

As the upper layer becomes approximately 0.2 wl thick (depending on its dielectric constant), it effectively decouples any signal from the lower layer. However, if it is still too thin to allow free propagation within itself, the observed patterns will show no interference at all (see Figure 4). Since this transition band is very narrow (and may be non-existent for very low losses), it is extremely diagnostic of upper layer thickness.

(c) Modal propagation in the upper layer

As the upper layer becomes thick enough to support freely propagating modes, the interference patterns again show clear beating (see Figures 5 and 6). Since the interference is generated by modes propagating along the thin layer guide, the spatial frequency of the

beats is relatively low, and dependent on the properties of the upper layer (although occasionally a higher spatial frequency ripple, due to the lower layer, can be seen).

JUNEAU ICEFIELD DATA

During the summer of 1972, measurements were made at various locations on the Juneau Icefields (see Figure 7). We will examine two runs - Run 36 made from Site 6 on the Taku Glacier, and Run 92 made from Site 25, in the accumulation zone of the Matthes Glacier. At Site 6, the thickness of ice has been determined seismically to be approximately 350 m. (Miller, 1950). The thickness of the ice at Site 25 is uncertain, but it is probably about 200 m.

Measurements were made at six frequencies - 1, 2, 4, 8, 16, and 32 MHz, so that the free space wavelength varied from 300 m to about 10 m. Six components of the magnetic field were measured - three from each of two transmitting antenna orientations. Of these components, we presently have theoretical solutions for two of them - the vertical (Hz) and radial (H_ρ) magnetic fields from a broadside transmitting antenna. These two components were compared to suites of theoretical curves and a best fit that gave consistent results for all frequencies was found.

For both runs, the data at 32 MHz were so scattered that interpretation was not possible. The scattering is seen slightly at 16 and 8 MHz, and seems typical of glacier data (Strangway et al., 1974). We attribute this scattering to random reflections from crevasses and other irregularities in the ice with typical sizes of about 10 m.

The parameters deduced from each frequency for the two runs are listed in Table 1, and the best fit is illustrated in Figures 8 and 9.

In each case, the two components gave similar results. From the 1 and 2 MHz data, the dielectric constant and loss tangent of the lower layer can be estimated. From the 4 MHz curves, very tight limits can be put on the thickness of the upper layer. From 8 and (to some extent) 16 MHz data, the properties of the upper layer can be determined.

Runs 36 and 92 differ in two basic respects. For Run 36, the loss tangents are typical for ice - 0.2/f, where f is frequency in MHz (Evans, 1965). The values obtained for the thickness of the upper layer are very consistent from frequency to frequency. For Run 92, it was not possible to obtain a consistent thickness without letting the loss tangent drop to at least 0.1/f. Even then, the depths obtained for the lower frequencies (especially 4 MHz) were less than 15 m while for 8 and 16 MHz a depth of about 20 m was required.

DISCUSSION

We interpret the thin upper layer at both sites as being snow about 15 to 20 m thick, with a dielectric constant of 2.4, overlying thick glacial ice, with a dielectric constant of 3.3. The loss tangent at Site 6 (Run 36) is about 0.2/f, while at Site 25 (Run 92), it is 0.1/f.

These dielectric properties are typical for ice and snow (Evans, 1965). Since snow is a mixture of air and ice, its dielectric constant is somewhat lower than that of ice, although its loss tangent is not greatly different. We attribute the lower loss tangent at Site 25 to the lower temperature of the ice and snow at the higher site. It is interesting that although the measurements were made in summer with

runoff water abundant on the surface, the losses were not very high. Presumably, the water is too thin or too well disseminated to be noticeable at the frequencies used.

The inconsistency of the depth determinations between frequencies at Site 25 could possibly be due to a grading of the snow-ice boundary at that altitude. Since Site 25 is in the accumulation zone of the glacier, snow may be compacting in that area.

CONCLUSION

Using radio-frequency interferometry, a thin layer can be detected and estimates of the thickness of the layer to within a few meters can be made. By using a range of frequencies, the dielectric parameters of both the upper and the lower layer can be obtained.

Acknowledgements

Field work, data collection and reduction was done under NASA Contract No. NAS 9-11540 to MIT and a subcontract to the University of Toronto for the Apollo Surface Electrical Properties Experiment. We thank Messrs. G. LaTorraca, R. Baker, and L. Bannister, and Dr. G. Simmons.

Support for the analysis and interpretation of the data from the Department of Energy, Mines and Resources, under Research Agreement 1135-D13-4-16/73, is gratefully acknowledged.

References

Annan, A.P., "Radio Interferometry Depth Sounding", M.Sc. thesis, Department of Physics, University of Toronto, 1970.

Annan, A.P., "Radio Interferometry Depth Sounding: Part I - theoretical discussion", Geophysics, v. 38, pp. 557-580, 1973.

Annan, A.P., Waller, W.M., Strangway, D.W., Rossiter, J.R., and Redman, J.D., "The electromagnetic response of a low-loss two-layer dielectric earth for horizontal electric dipole excitation", submitted to Geophysics, 1974.

Evans, S., "Electrical properties of ice and snow - a review", J. Glaciology, v. 5, pp. 773-792, 1965.

Kong, J.A., "Electromagnetic fields due to dipole antennas over stratified anisotropic media", Geophysics, v 37, pp.985-996, 1972.

Miller, M.M., "Preliminary Report of field operations, Juneau Icefield Resarch Project, 1949", J.I.R.P., no.2, American Geographical Society, New York, 1950.

Rossiter, J.R., LaTorraca, G.A., Annan, A.P., Strangway, D.W., and Simmons, G., "Radio interferometry depth sounding: Part II - experimental results", Geophysics, v. 38, pp. 581-599, 1973.

Simmons, G., Strangway, D.W., Bannister, L., Baker, R., Cubley, D., LaTorraca, G., and Watts, R., "The Surface Electrical Properties Experiment", Lunar Geophysics, Proceedings of a conference at the Lunar Science Institute, Houston, Texas, 18-21 October, 1971, D. Reidel, Dordrecht, pp. 258-271, 1972.

Strangway, D.W., Simmons, G., LaTorraca, G., Watts, R., Bannister, L., Baker, R., Redman, D., and Rossiter, J., "Radio-frequency interferometry - a new technique for studying glaciers", J. Glaciology, in press, 1974.

Surface Electrical Properties Team, "The Surface Electrical Properties Experiment", Apollo 17 Preliminary Science Report, in press, 1974.

Tsang, L., Kong, J.A., and Simmons, G., "Interference patterns of a horizontal electric dipole over layered dielectric media", J. Geophys. Res. v. 78, pp. 3287-3300, 1973.

TABLE 1: INTERPRETATION OF JUNEAU RUNS 36 AND 92 BY COMPARISON TO THEORY

RUN 36

Frequency (MHz)	d_1 wl (m.)	k_1	$\tan\delta_1$	k_2	$\tan\delta_2$
1	$\lesssim$0.075($\lesssim$23)	-	-	3.3 $\pm$ 0.1	0.20 $\pm$ 0.10
2	.100-.150(15-23)	-	-	3.3 $\pm$ 0.1	0.10 $\pm$ 0.05
4	0.2-0.3 (15-22)	-	-	-	0.05 $\pm$ 0.03
8	0.45-0.60 (17-22)	2.4$\pm$0.1	.02$\pm$01	-	-
16 (1)	0.9 -1.2 (17-22)	2.4$\pm$0.2	0.010$\pm$0.005	-	-
Interpretation:	19 $\pm$ 4 m.	2.4$\pm$0.1	0.2$\pm$0.1/f[2]	3.3 $\pm$ 0.1	0.2 $\pm$ 0.1/f[2]

RUN 92

1	$\lesssim$ 0.1 ($\lesssim$30)	-	-	3.3 $\pm$ 0.1	0.10 ?
2	$\lesssim$ 0.125 ($\lesssim$20)	-	-	3.3 $\pm$ 0.1	0.05-0.10
4	.100-.175(7-13) .125-.200(9-15)	@ 2.4	-	-	@ .05 @ .02
8	0.5 - 0.7(19-26)	2.4$\pm$0.1	.02$\pm$.01	-	-
16(1)	1.2 $\pm$ 0.1(22$\pm$2)?	2.4$\pm$0.2	$\lesssim$.02	-	-
Interpretation:	18 $\pm$ 8 m.	2.4$\pm$0.2	0.10/f?[2]	3.3 $\pm$ 0.1	0.10$\pm$0.05/f[2]

1. 16 MHz data are fairly scattered (see text).

2. f in MHz. Because of its dielectric mechanism, the loss tangent of ice essentially behaves as $f \cdot \tan\delta =$ constant. (Evans, 1965).

FIGURE CAPTIONS

Fig. 1. Configuration of a thin dielectric layer overlying an infinite dielectric half space. By varying the frequency, the thickness of the upper layer in wavelengths can be changed.

Fig. 2 Theoretical curves for a very thin upper layer, with the dielectric constant of the lower layer varying. The spatial frequency of the pattern increases with increasing k_2. (a) H_ρ broadside component; (b) H_z broadside component.

Fig. 3 Theoretical curves for a very thin upper layer with the loss tangent of the lower layer varying. The sharpness of the interference drops off with increasing $\tan\delta_2$. (a) H_ρ broadside component, (b) H_z broadside component.

Fig. 4 Theoretical curves for the region of no interference showing the transition from a transparent upper layer to an upper layer that propagates freely. (a) H_ρ broadside component, (b) H_z broadside component.

Fig. 5 Theoretical curves for a propagating upper layer, with the dielectric constant of the upper layer varying. (a) H_ρ broadside component, (b) H_z broadside component.

Fig. 6 Theoretical curves for a propagating upper layer, with the loss tangent of the upper layer varying. (a) H_ρ broadside component, (b) H_z broadside component.

Fig. 7 Map of the Juneau Icefield near Camp 10. Radio interferometry was conducted at "R.F.I.Sites". Seismic depths are indicated where known. Run 36 was made at Site 6. Run 92 was made high on the Matthes Glacier (not on the map) near Camp 18.

Fig. 8 Radio interferometry data, H_ρ and H_z broadside components, 1 to 16 MHz for Run 36, Site 6 (Solid lines). The best fit theoretical curves are also shown (dashed lines).

Fig. 9 Radio interferometry data, H_ρ and H_z broadside compoents, 1 to 16 MHz, for Run 92, Site 25 (solid lines). The best fit theoretical curves are also shown (dashed lines).

	Air	$k_1 = 1$	$\tan \delta_o = 0$	
d_1	Thin layer	k_1	$0 < \tan \delta_1 < .2$	$0 < d_1 < 1$ wl
	Thick layer	$k_2 > k_1$	$\tan \delta_2 \approx \tan \delta_1$	$d_2 \to \infty$
d_2				

Fig. 1: Configuration of a thin dielectric layer overlying an infinite dielectric half-space.

D: 0.05
LT1: 0.02 LT2: 0.05
K1: 2.4 K2: VARYING.

(a)

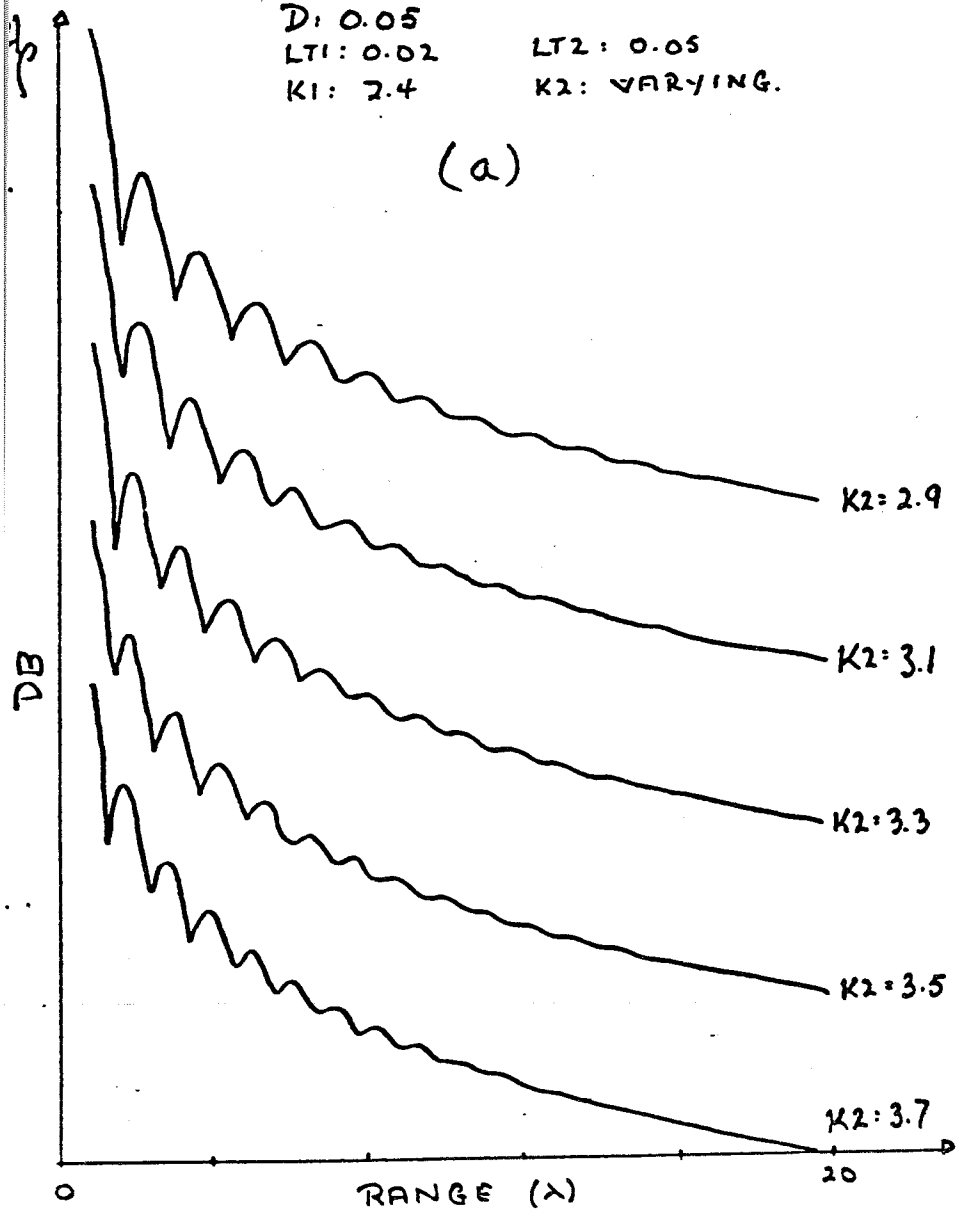

D: 0.05
LT1: 0.02 LT2: 0.05
K1: 2.4 K2: VARYING

(b)

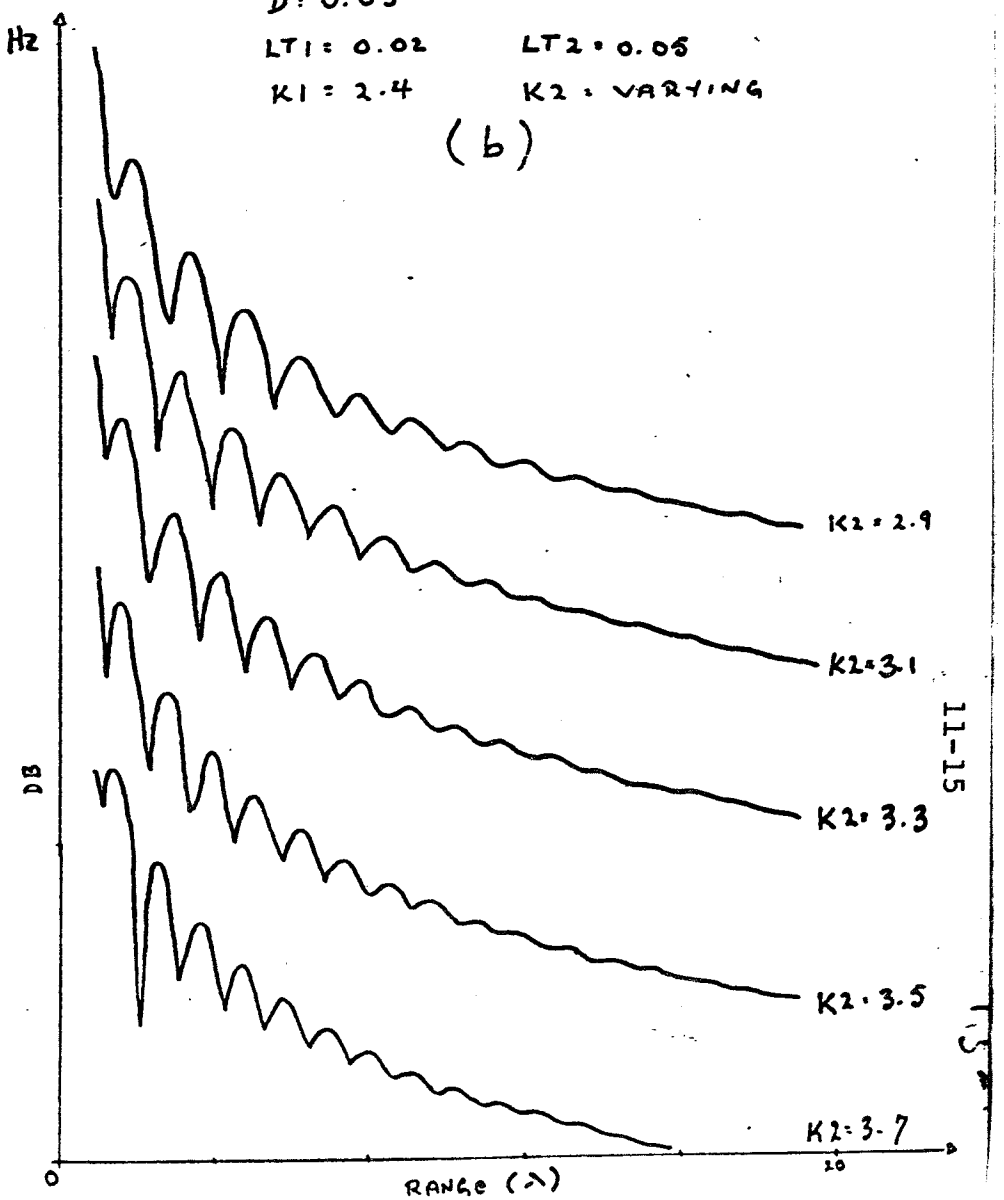

D: 0.05
LT1: 0.02 LT2: VARYING
K1: 2.4 K2: 3.3

(a)

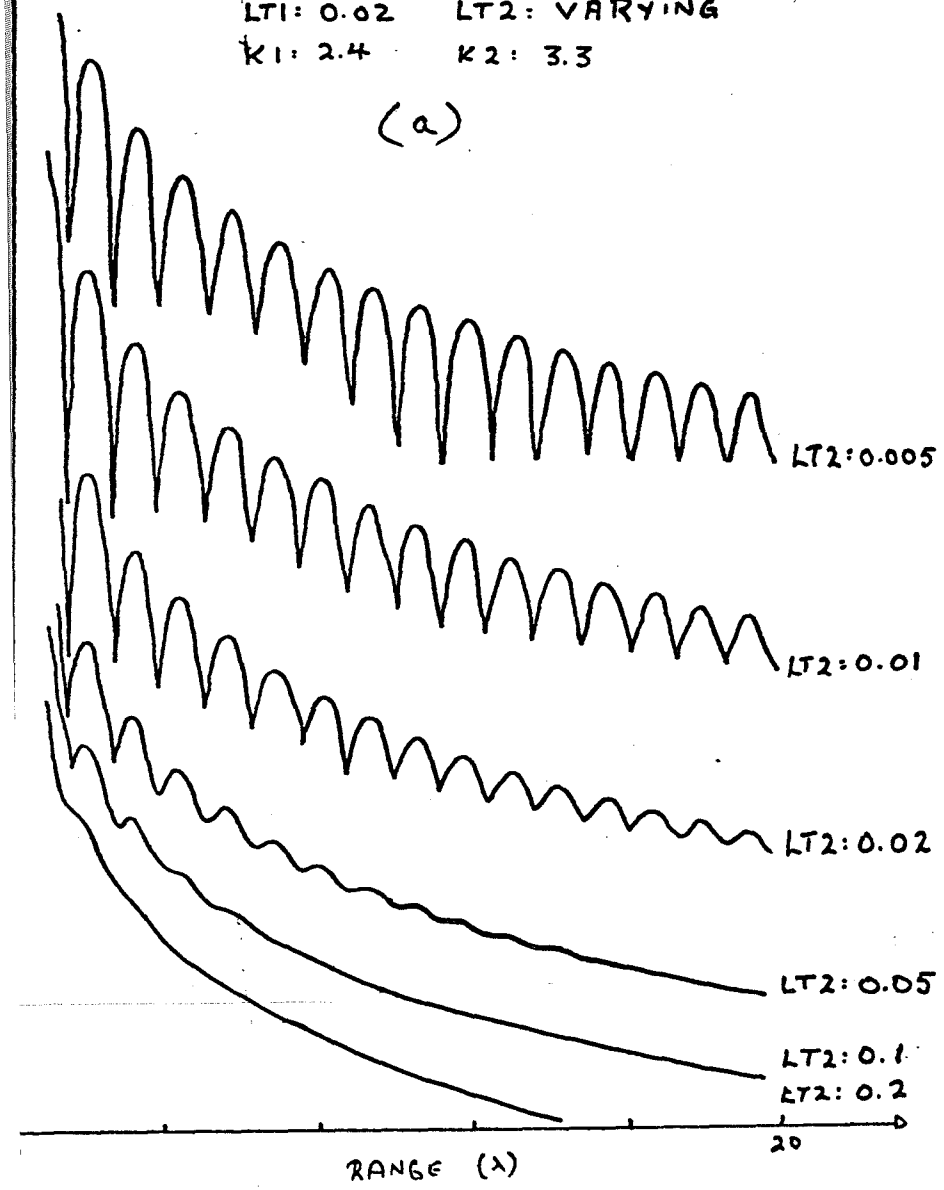

D: 0.05
LT1: 0.02 LT2: VARYING
K1: 2.4 K2: 3.3

(b)

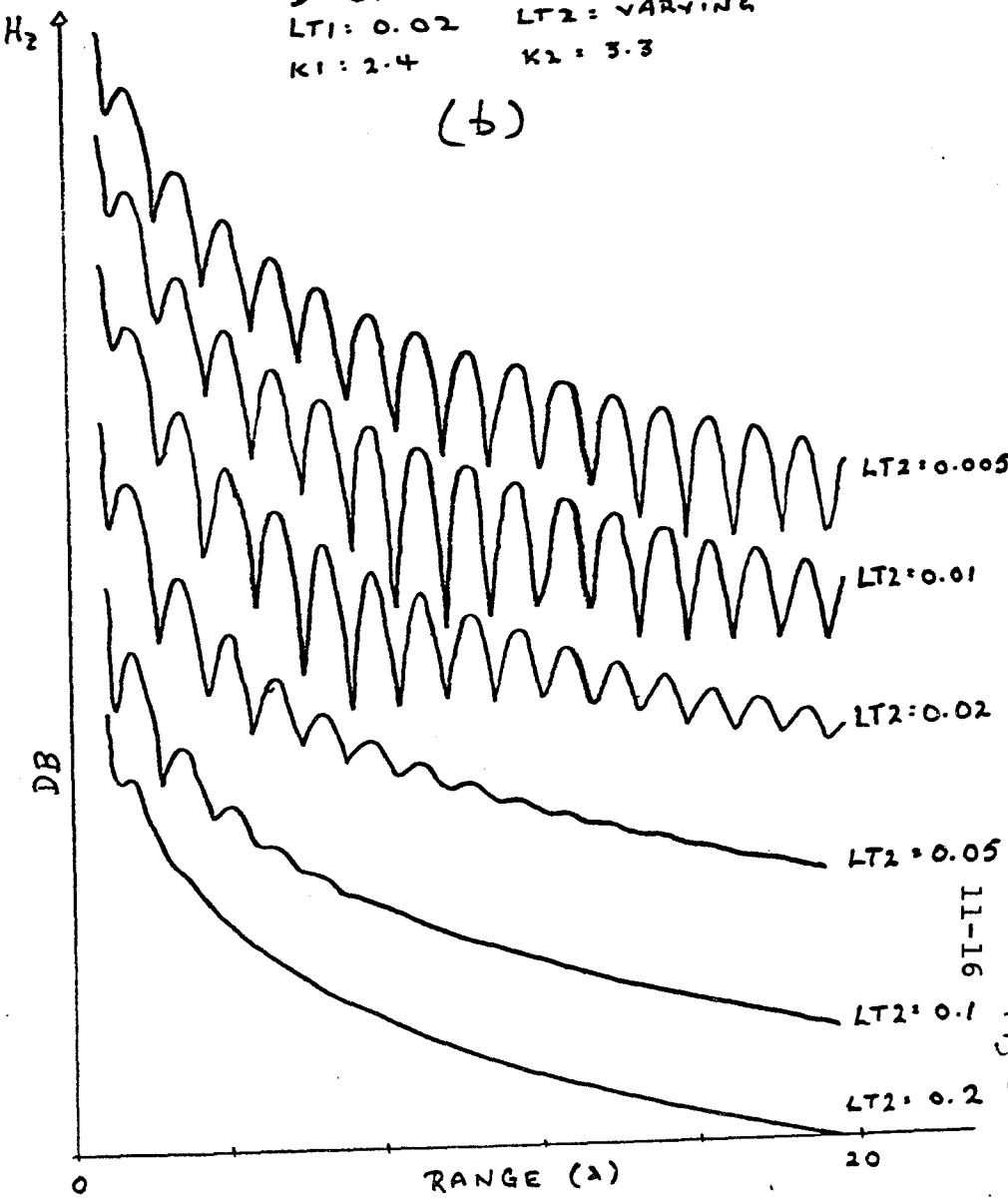

Fig 4.

(a)

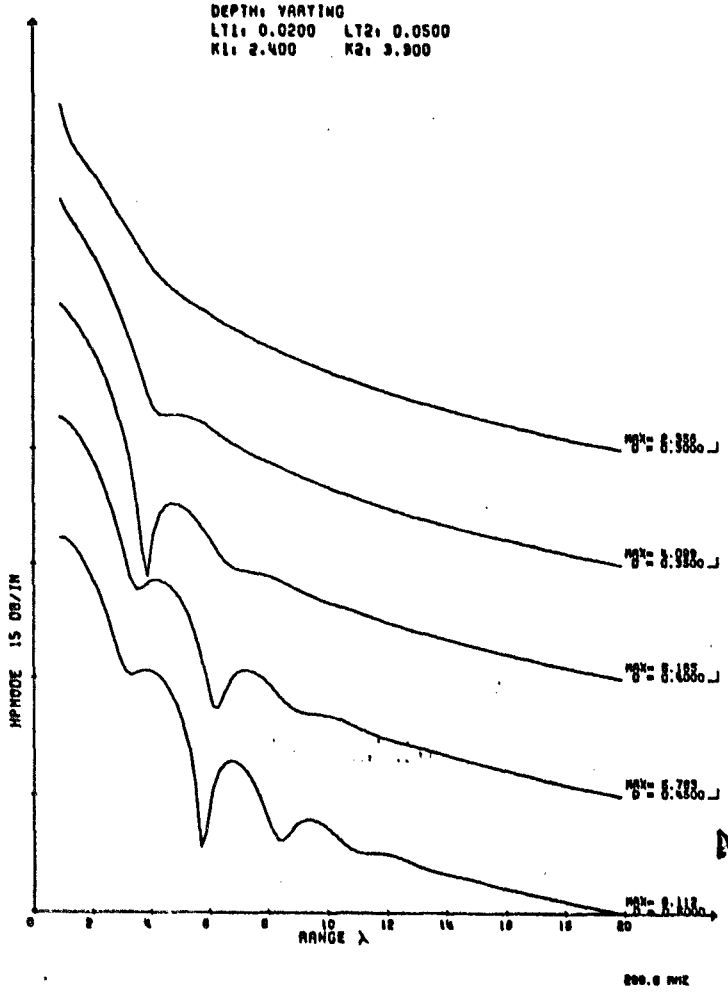
DEPTH: VARYING
LT1: 0.0200 LT2: 0.0500
K1: 2.400 K2: 3.900
HPMODE 15 DB/IN
RANGE λ
200.0 MHZ

(b)

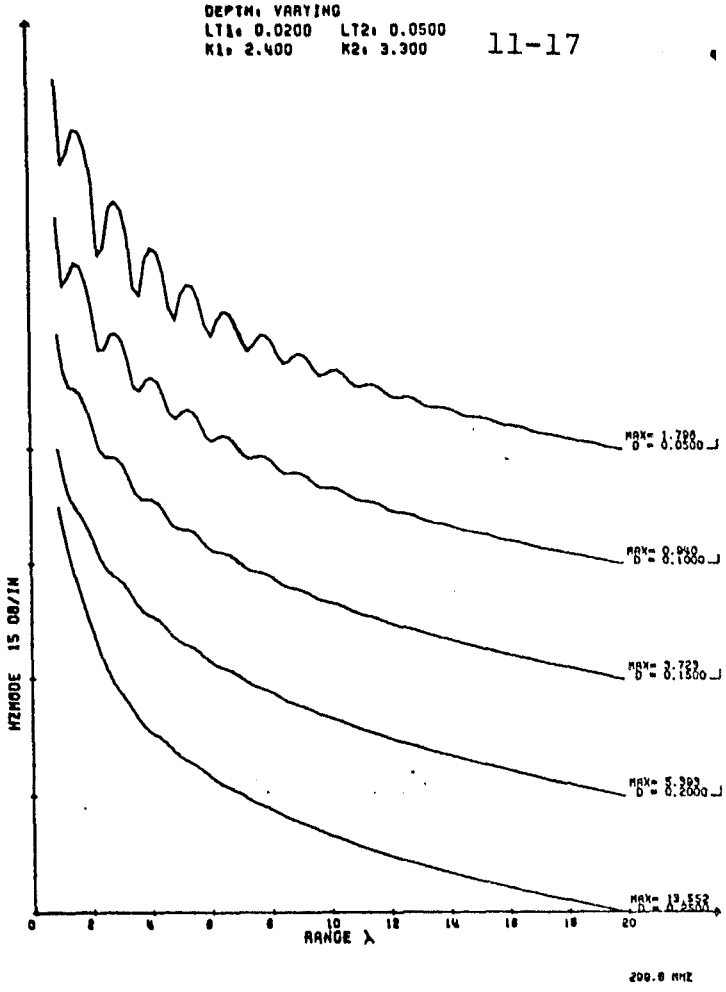
DEPTH: VARYING
LT1: 0.0200 LT2: 0.0500
K1: 2.400 K2: 3.300
HZMODE 15 DB/IN
RANGE λ
200.0 MHZ

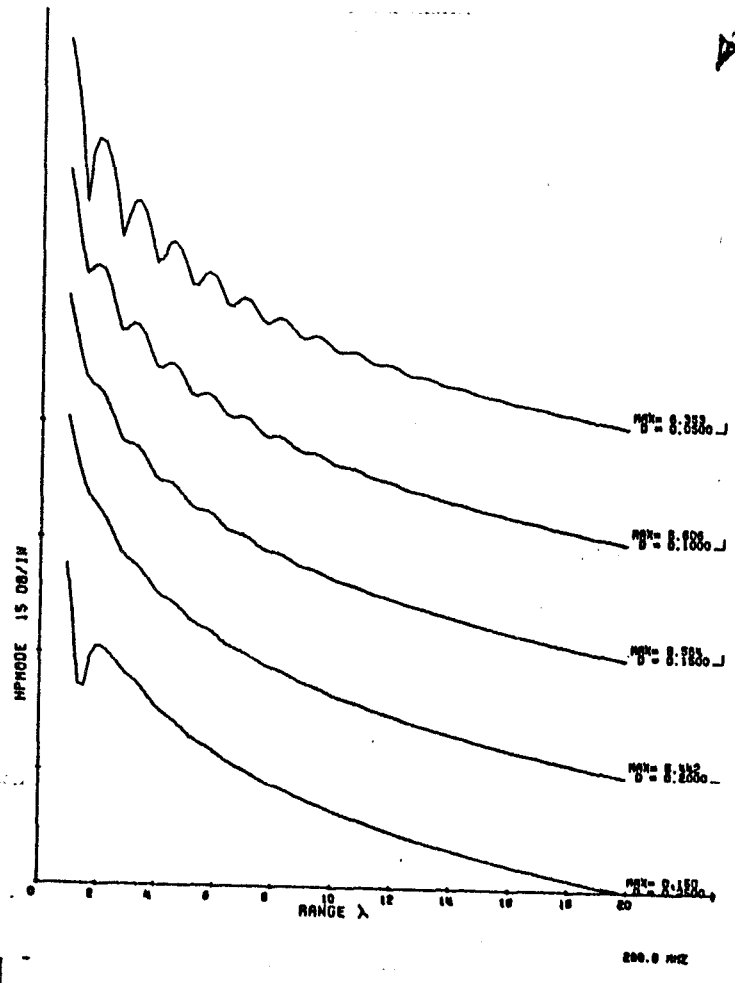
HPMODE 15 DB/IN
RANGE λ
200.0 MHZ

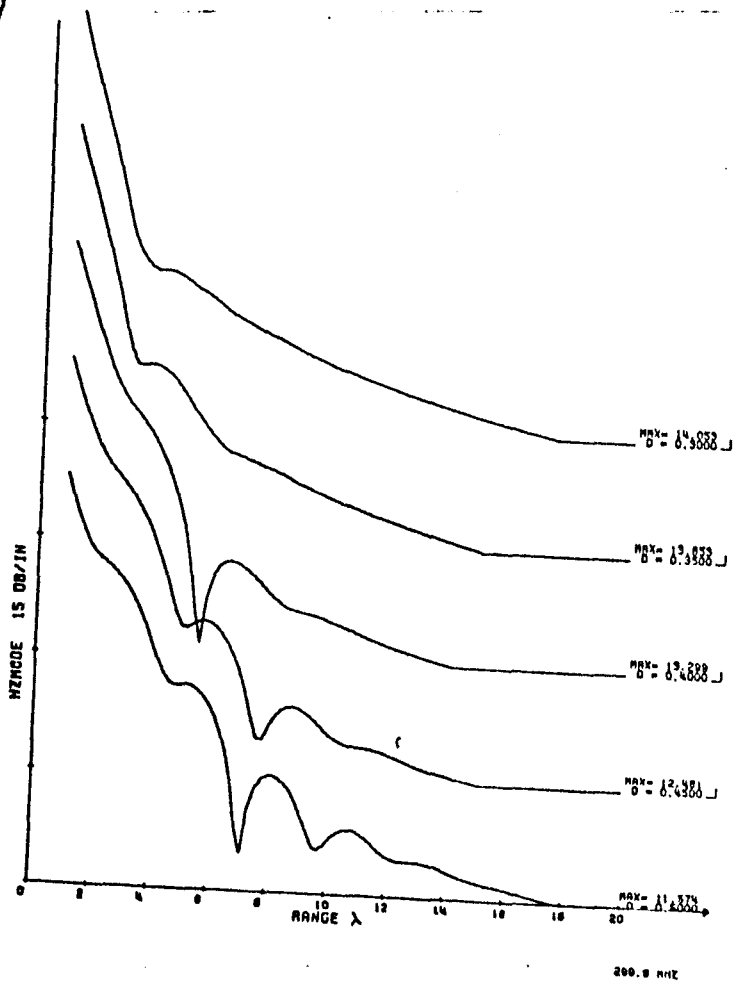
HZMODE 15 DB/IN
RANGE λ
200.0 MHZ

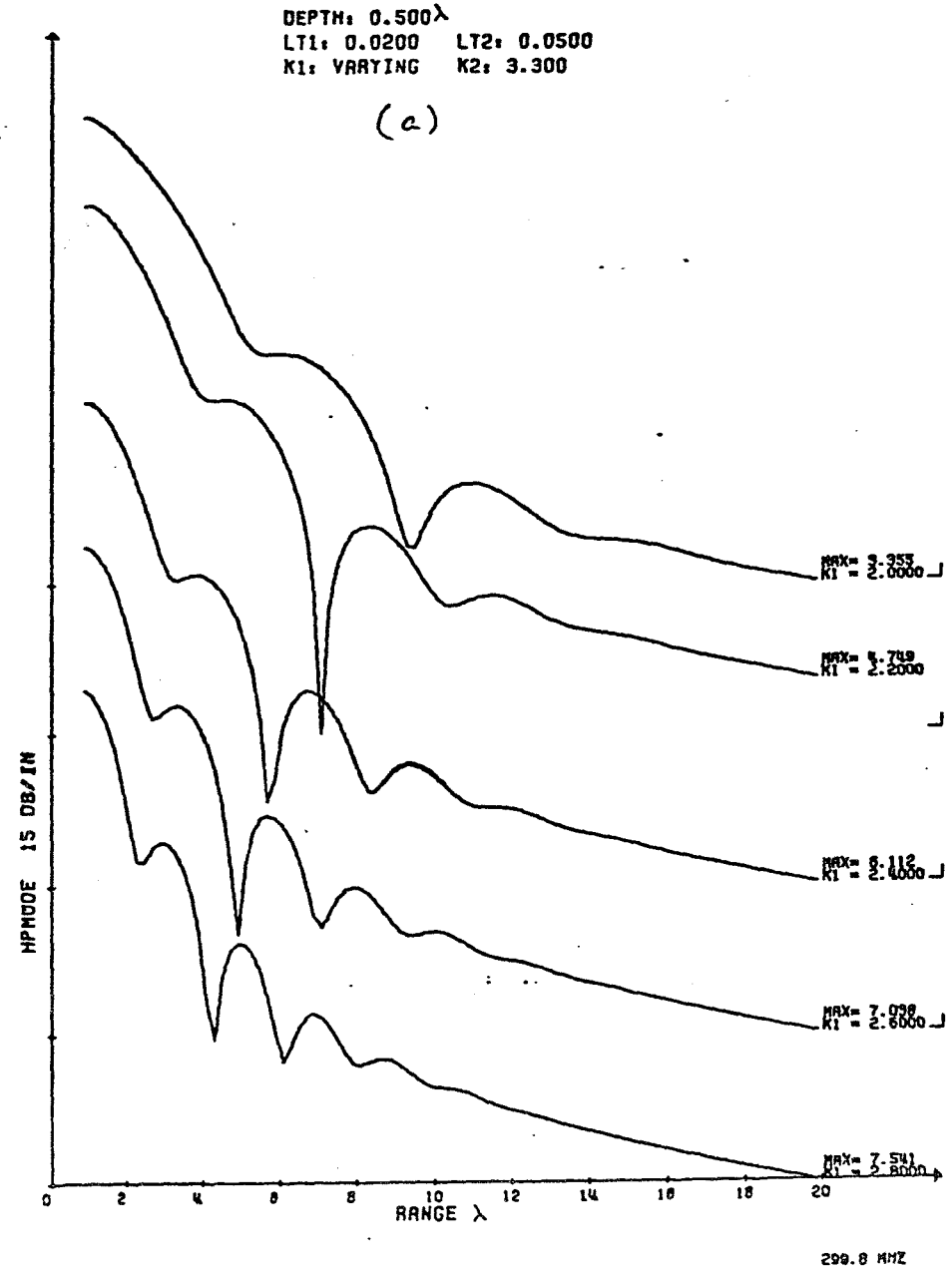
DEPTH: 0.500λ
LT1: 0.0200 LT2: 0.0500
K1: VARYING K2: 3.300
(a)
HPMODE 15 DB/IN
MAX= 8.355
K1 = 2.0000
MAX= 8.749
K1 = 2.2000
MAX= 8.112
K1 = 2.4000
MAX= 7.038
K1 = 2.6000
MAX= 7.541
K1 = 2.8000
0 2 4 6 8 10 12 14 16 18 20
RANGE λ
299.8 MHZ

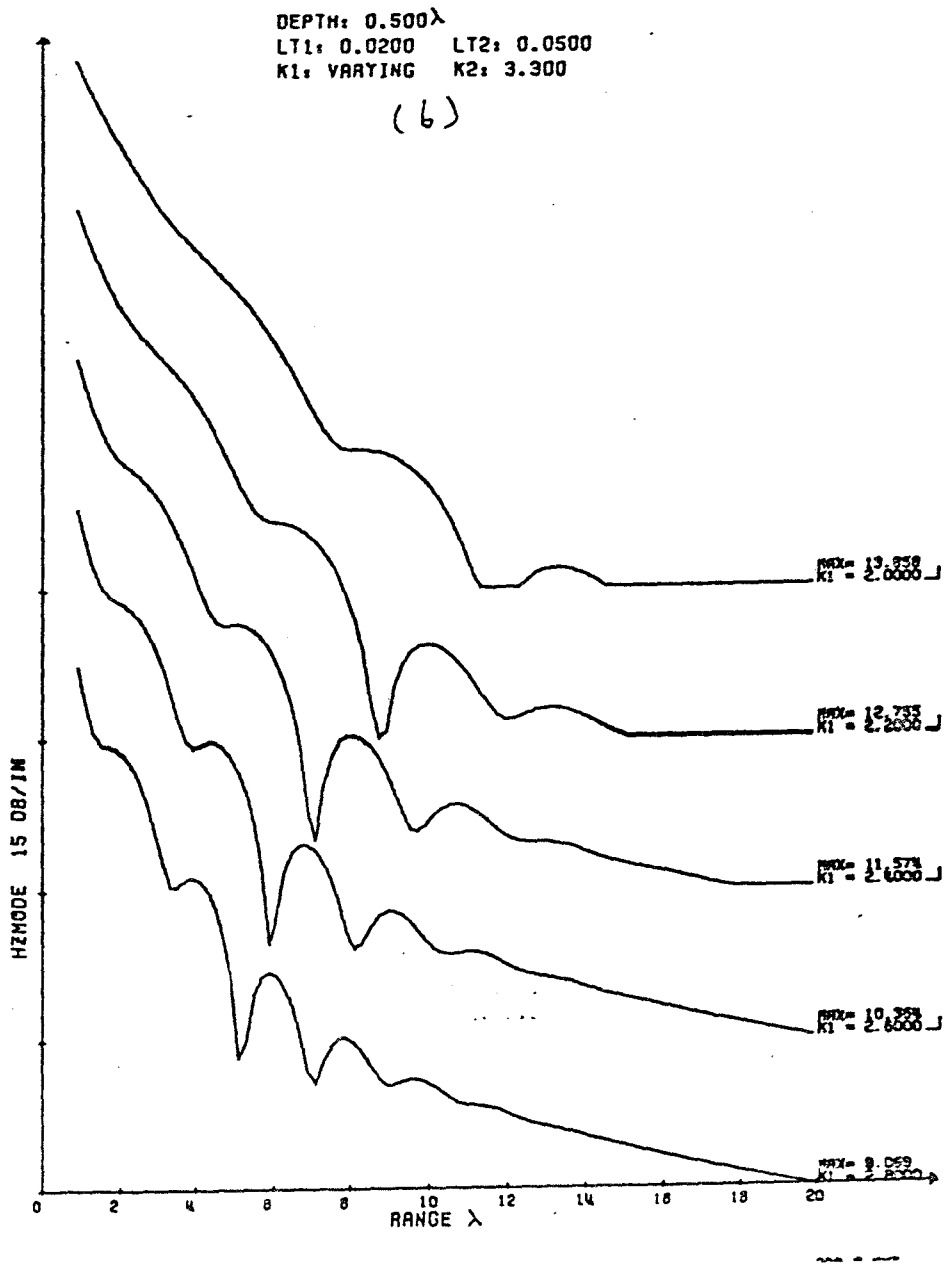
DEPTH: 0.500λ
LT1: 0.0200 LT2: 0.0500
K1: VARYING K2: 3.300
(b)
HZMODE 15 DB/IN
MAX= 13.958
K1 = 2.0000
MAX= 12.733
K1 = 2.2000
MAX= 11.574
K1 = 2.4000
MAX= 10.358
K1 = 2.6000
MAX= 9.069
K1 = 2.8000
0 2 4 6 8 10 12 14 16 18 20
RANGE λ

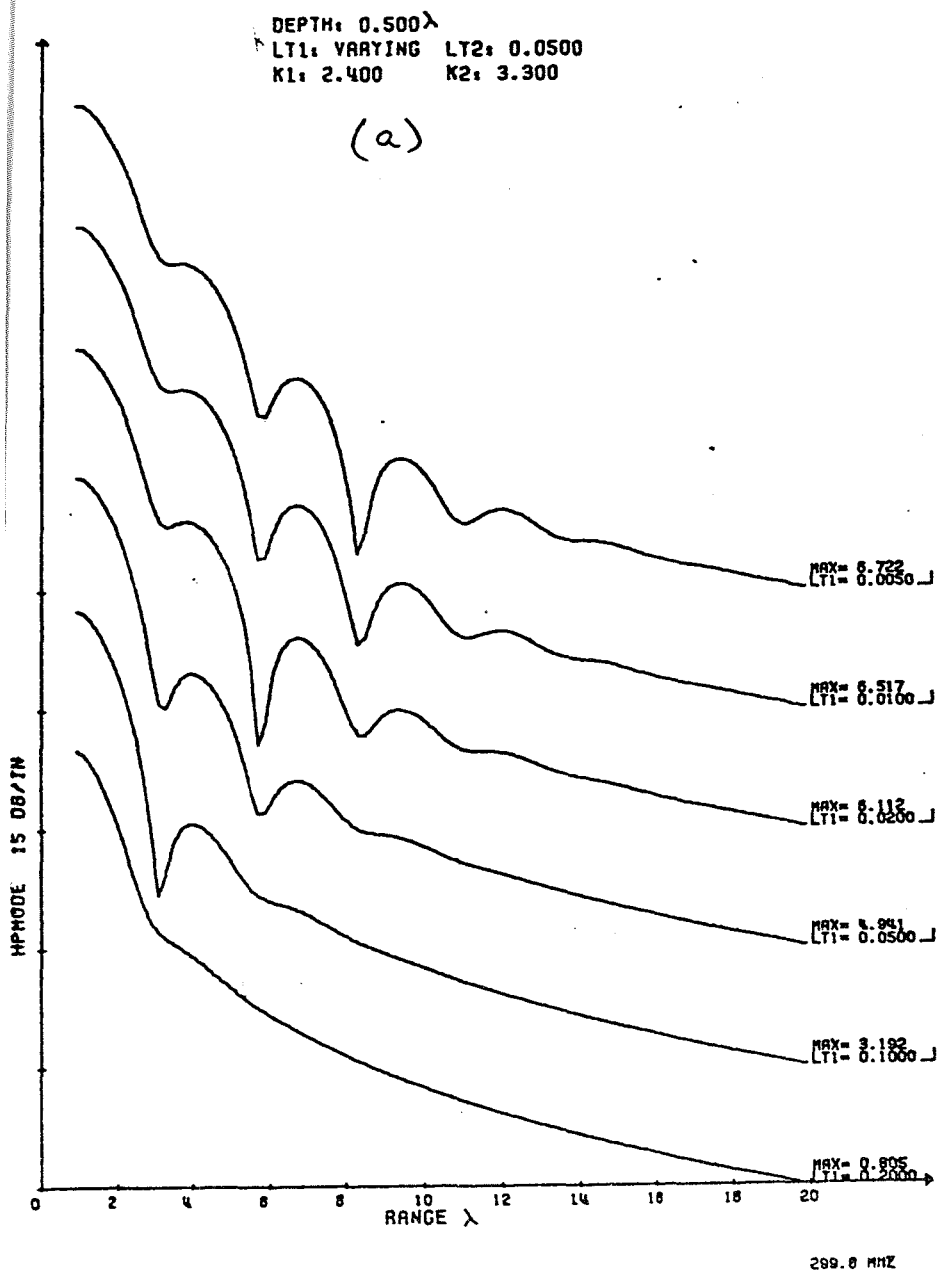
DEPTH: 0.500λ
LT1: VARYING LT2: 0.0500
K1: 2.400 K2: 3.300
(a)
MAX= 6.722
LT1= 0.0050
MAX= 6.517
LT1= 0.0100
MAX= 6.112
LT1= 0.0200
MAX= 5.941
LT1= 0.0500
MAX= 3.192
LT1= 0.1000
MAX= 0.805
LT1= 0.2000
HPMODE 15 DB/IN
0 2 4 6 8 10 12 14 16 18 20
RANGE λ
299.8 MHZ

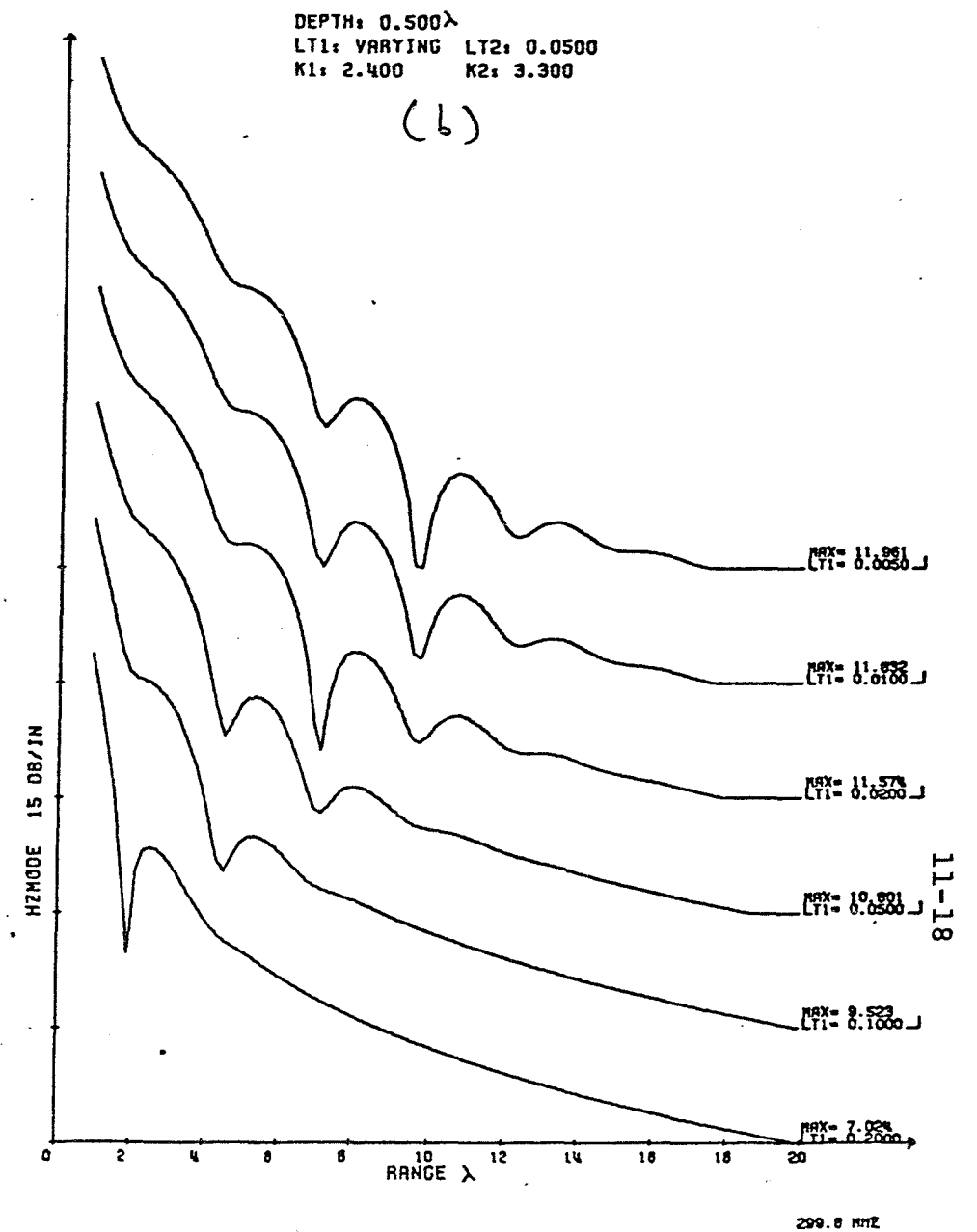
DEPTH: 0.500λ
LT1: VARYING LT2: 0.0500
K1: 2.400 K2: 3.300
(b)
MAX= 11.961
LT1= 0.0050
MAX= 11.632
LT1= 0.0100
MAX= 11.578
LT1= 0.0200
MAX= 10.801
LT1= 0.0500
MAX= 9.523
LT1= 0.1000
MAX= 7.02%
LT1= 0.2000
HZMODE 15 DB/IN
0 2 4 6 8 10 12 14 16 18 20
RANGE λ
299.8 MHZ

Fig. 7

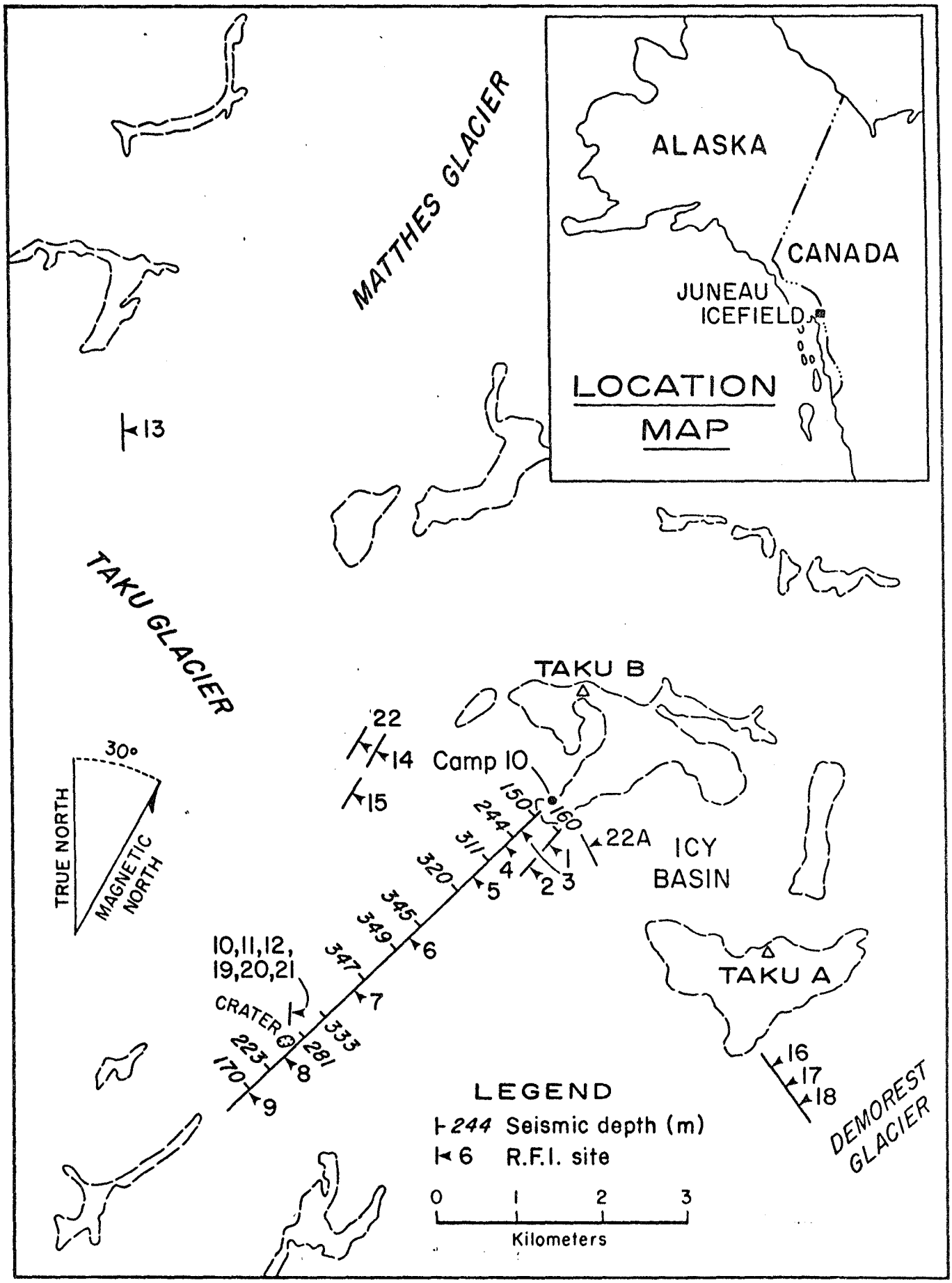
MATTHES GLACIER
ALASKA
CANADA
JUNEAU ICEFIELD
LOCATION MAP
13
TAKU GLACIER
TAKU B
22
14
Camp 10
15
150
160
244
311
320
345
349
347
333
281
223
170
1
2
3
4
5
6
7
8
9
22A
ICY BASIN
30°
TRUE NORTH
MAGNETIC NORTH
10,11,12,
19,20,21
CRATER
TAKU A
16
17
18
DEMOREST GLACIER
LEGEND
244 Seismic depth (m)
6 R.F.I. site
0 1 2 3
Kilometers

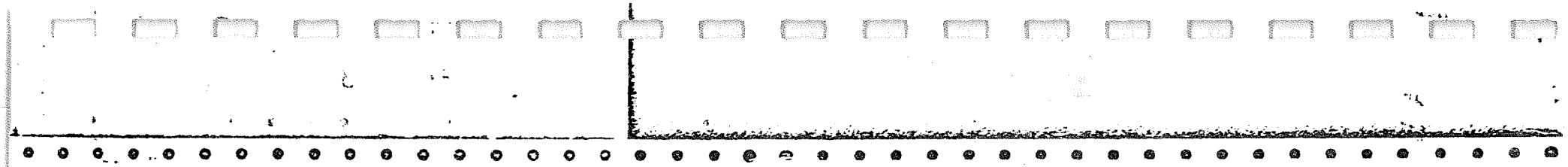

Fig 8

JUNEAU ICEFIELD - RUN 36

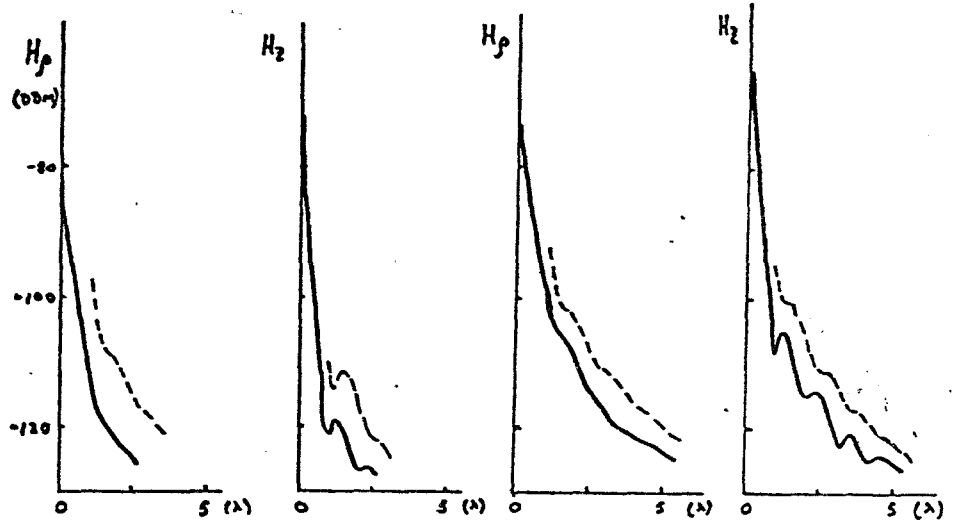

1 MHz.

2 MHz

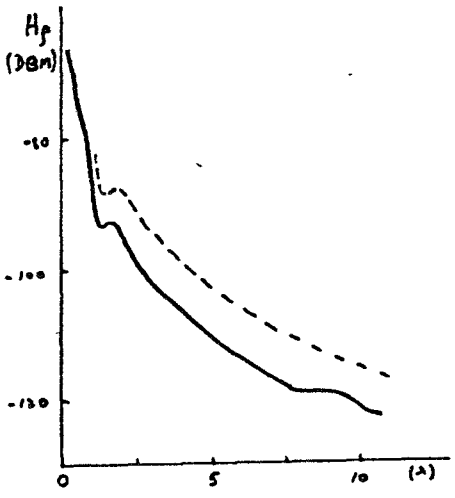

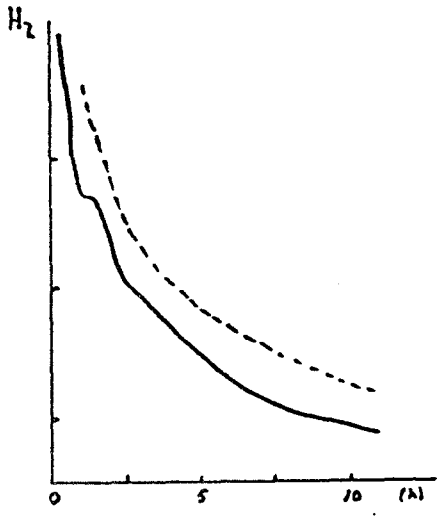

4 MHz

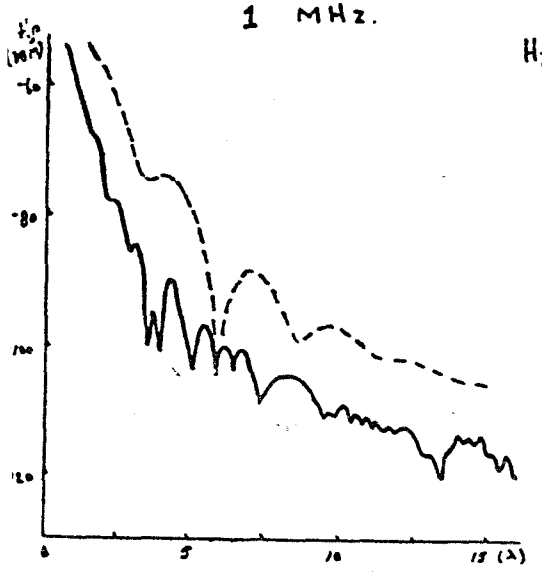

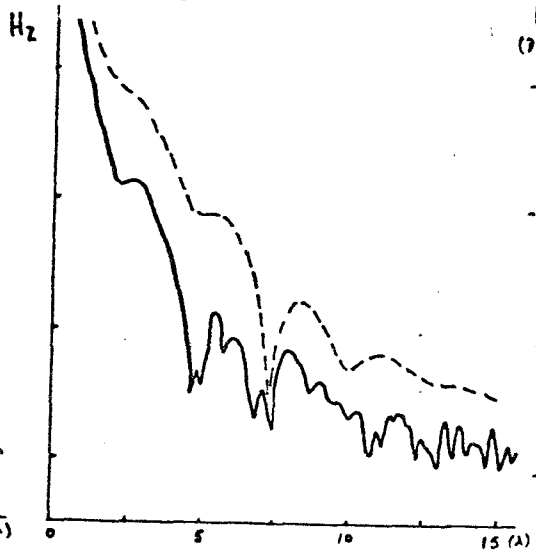

8 MHz

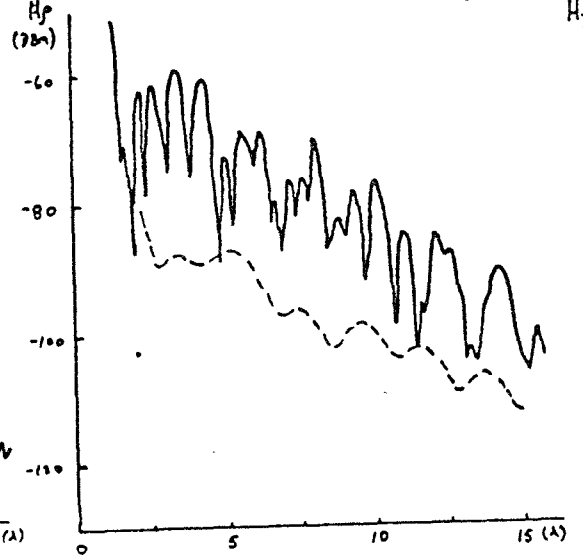

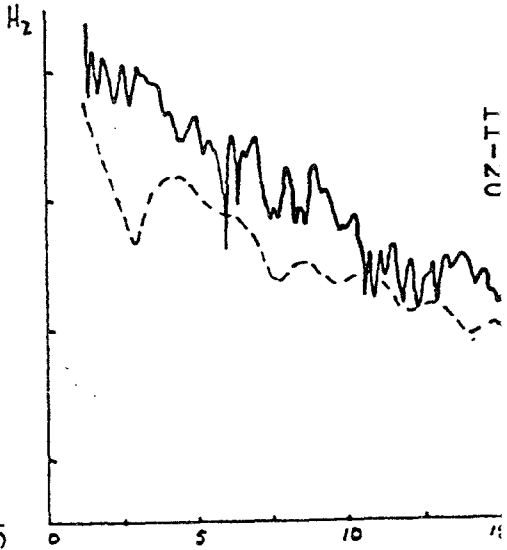

16 MHz

— Run 36

--- Mode Theory

JUNEAU ICEFIELD : RUN 092

Fig 9.

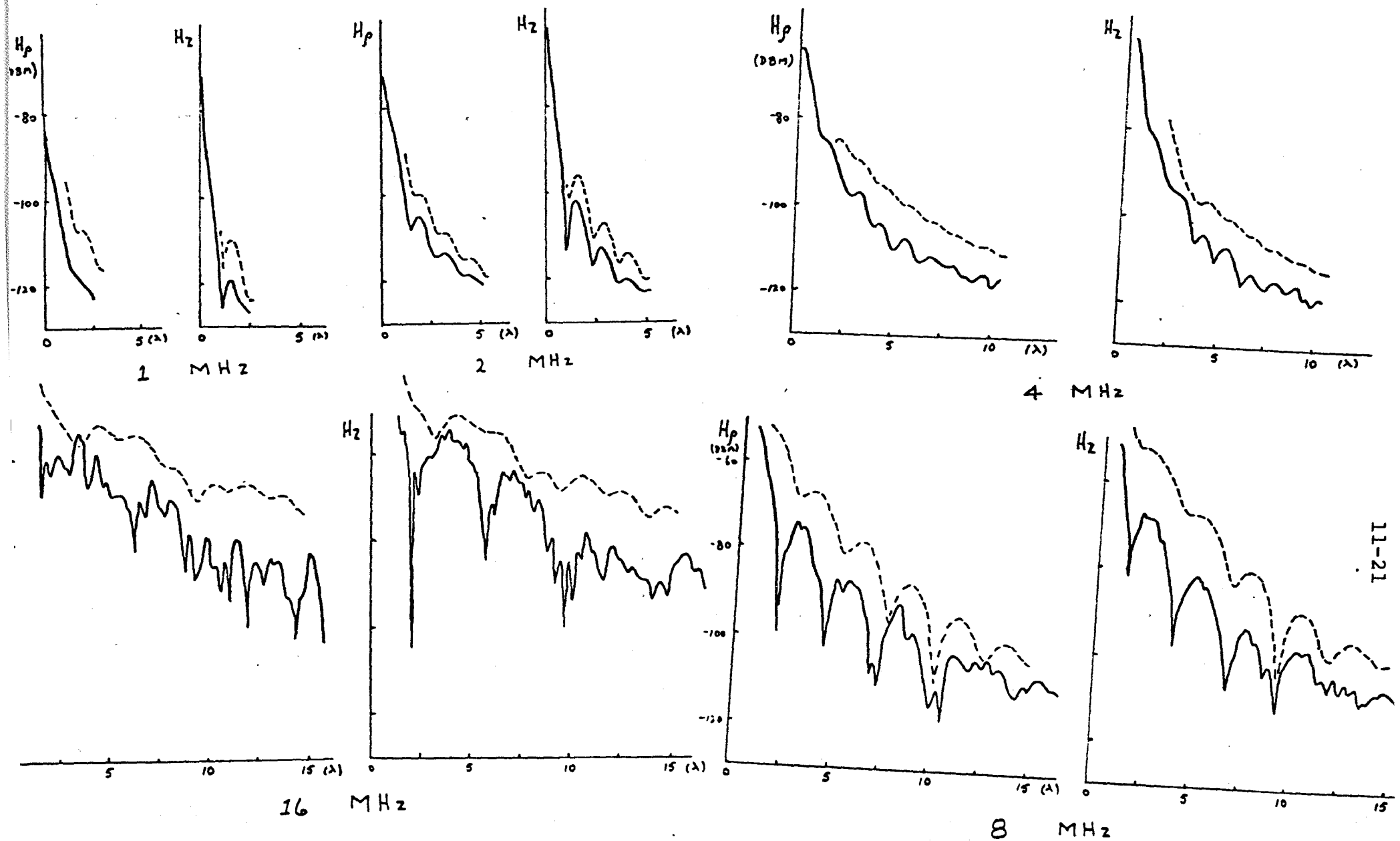

11-21

MASSACHUSETTS INSTITUTE OF TECHNOLOGY
CENTER FOR SPACE RESEARCH
CAMBRIDGE, MASSACHUSETTS 02139

May 6, 1974

TO: Distribution (list attached)

Enclosed is a revised sheet for inclusion in the SEP final report that was sent to you on April 17, 1974. Please substitute this page 1-1 for the original 1-1 included in the report.

Forwarded at the request of the Principal Investigator, Professor Gene Simmons.

2 Encls
1. Distribution List
2. Revised page 1-1

April 17, 1974

Final Report on the SURFACE ELECTRICAL PROPERTIES EXPERIMENT (NASA Contract NAS9-11540) - CSR TR-74-1, March 15, 1974 - mailed as follows:

No. of Copies	To
5	Dr. David Strangway, Univ. of Toronto, Dept. of Geology, Toronto, Canada
5	NASA, Lyndon B. Johnson Space Center, Houston, Texas 77058 (John Weber/ BC241)
1	Prof. John V. Harrington, Vice-President, Communications Satellite Corp., 950 L'Enfant Plaza SW, Washington, D.C. 20024
	Raytheon Company, Boston Post Road, Wayland, Mass. 01778 -
1	Joseph DeBettencourt
1	Joseph Urner, Program Manager, Equipment Div.
1	Dr. Dean Cubley, EE3 MSC, NASA 14-110, Houston, Texas 77058
1	Palmer Dyal, Ames Research Center, Moffett Field, Ca 94035
1	Dr. Tommy Gold, Center for Radiophysics & Space Research, Space Science Building, Cornell University, Ithaca, NY 14850
1	G. Hochn, Field Research Laboratory, P.O. Box 900, Dallas, Texas 75221
1	Dr. S. B. Jones, Chevron, La Habra, Ca 90631
1	Dr. Robert Kovach, Dept. Geophysics, Stanford University, Stanford, Ca 94305
1	Dr. Mark Langseth, Lamont Geol. Observatory, Palisades, N.Y. 10964
1	Jim Waitt, NOAA, University of Colorado, Boulder, Co 80302
1	Herb Wang, 6118 University Avenue, Geophysical & Polar Research, Middleton, WI 53562
	M.I.T.
3	Serials Dept., Sylvia A. McDowell, Room 14E-210
2	CSR Reading Room
5	L. E. Beckley
1	L. H. Bannister, N51-338
1	John Groener, N51-336
1	Richard H. Baker, N51-330
1	Prof. Jin-Au Kong, 20B-113
1	Gerry LaTorraca, N51-336
1	James Meyer, 26-147
1	Prof. Leung Tsang, 36-345